Mechanical interactions between water and the solid Earth: From quasi-static geodetic deformation to dynamic fault slip

Thesis by
Stacy Larochelle

In Partial Fulfillment of the Requirements for the
Degree of
Ph.D. in Geophysics

Caltech

CALIFORNIA INSTITUTE OF TECHNOLOGY
Pasadena, California

2022
Defended May 26, 2022

Stacy Larochelle
ORCID: 0000-0001-6161-5605

ACKNOWLEDGEMENTS

This thesis would not have been possible without the support, help and mentoring of my advisors, collaborators, friends and family.

First and foremost, I would like to express my deepest gratitude to my two incredible thesis advisors, Jean-Philippe Avouac and Nadia Lapusta, who welcomed me at Caltech with open arms, encouraged me to pursue my various research interests and gave me every opportunity to succeed as a graduate student and beyond. Jean-Philippe, thank you for your human, open-door and easygoing approach to advising; for sharing your extraordinary breadth of knowledge spanning all of geological and planetary sciences; and for allowing me to become part of the French scientific community (despite not always understanding my Québécois accent). Nadia, thank you for patiently teaching me the intricacies of earthquake physics and frictional processes, for always making sure I was happy and healthy before all else, and for always having valuable, wise and thoughtful advice about my career and life in general.

I am also extremely grateful to my long-distance, but close collaborators and mentors, Jean-Paul (Pablo) Ampuero and Kristel Chanard. Pablo, thank you for teaching me so much about earthquakes and fracture mechanics; for always being available to answer my numerous questions despite the distance; and for being an inspiring scientist and individual. Kristel, thank you for passing your passion and rich knowledge of geodesy on to me; for regularly blocking off your Friday evenings of the last 6 years to meet over skype/zoom; and for always listening and finding the right words when I felt stressed or overwhelmed. I feel truly lucky to consider you my academic big sister. Finally, I would like to thank you both for hosting me during my highly enlightening and memorable visits to France.

Morevoer, the work presented in this thesis would certainly not have been possible without the help, expertise and invaluable insights of my collaborators, Donald Argus, Frédéric Cappa, Manon Dalaison, Luce Fleitout, Jérome Fortin, Adriano Gualandi, Romain Jolivet, Valère Lambert, Laurent Longuevergne, Sylvain Michel, Paul Rebischung, Ares Rosakis, Vito Rubino, Krittanon (Pond) Sirorattanakul and Sophie Violette. I feel very privileged to have been able to learn from so many brilliant scientists throughout my graduate studies.

I am also thankful to my thesis committee members, Zachary Ross and Rob Clayton, for their generous time, valuable feedback and academic advice. Many thanks to Victor Tsai for offering academic guidance in the early years of my PhD, for teaching me how to teach through TAing, and for sparking my interest in glaciology. I would also like to recognize the Seismo Lab community as a whole for teaching me so much about geophysics and for the good times we have shared, both in and outside the office. Special thanks, in particular, to my amazing cohort — Celeste, Ollie, Valère, Vasilije, Zhe and Zhichao — and to our extraordinary administrative staff — Donna, Kim, Priscilla, Rosemary, and Sarah (and Carolina and Lisa outside the Seismo Lab) — for all their help and encouragement over the years. During my time at Caltech, I also had the great pleasure of working alongside many fellow students, postdocs and scientific staff in Jean-Philippe's and Nadia's groups; thank you all for your help, fruitful discussions and many fun lunches and potlucks.

I have to conclude the professional acknowledgements with my undergraduate research advisor, Yajing Liu, without who I certainly would not have been able to pursue a geophysics PhD at Caltech. Thank you Yajing for introducing me to the world of earthquake physics, for helping me navigate the academic world and for you kind support and guidance.

On a more personal note, I am incredibly grateful for the many friends I have made during my time at Caltech. A very special thanks to my classmates and housemates of the last 4 years, Ollie and Vasilije, for going through it all with me and to my dear friends, Katherine and Peishi, for being all-around amazing people. Thank you all for filling the last few years with countless laughters, adventures and excellent vibes. I am also deeply thankful for my fantastic, chaotic group of friends back home for having my back and making me laugh since 2005.

Lastly, I truly could not have undertaken and completed this journey without the love and support of my partner and family. Wilbur, thank you for travelling the world with me, for keeping me sane through tennis, hiking and yoga and for showing up for me every day. To my mom, dad, sister and grandparents, thank you for teaching me perseverance, courage and compassion, for being there for me no matter what, and for always supporting my dreams no matter how big. Merci pour tout.

ABSTRACT

Mechanical interactions between Earth's solid interior and its hydrosphere are central to many geophysical problems of crucial societal importance: Changing conditions in the global water cycle deform the solid Earth; the groundwater storage capacity of aquifer systems is controlled by its interaction with geological materials; and crustal water — either natural occurring or added through anthropogenic activities — affects earthquakes and fault slip processes. In this thesis, we investigate some of these interactions by harnessing recent developments in the fields of satellite geodesy, statistical data analysis, and elastodynamic earthquake modelling. We start by developing a procedure to identify and extract seasonal deformation signals associated with hydrological loading of the solid Earth from geodetic time series in Chapter 1. In Chapters 2 and 3, we consider the examples of the Ozarks Plateau (central United States) and Sacramento Valley (California) to establish a methodology for characterizing poroelastic deformation arising from groundwater variations with space-based geodesy. Then, in Chapter 4, we develop a model to simulate fault slip due to crustal water injections and calibrate it against a well-instrumented field experiment on a natural fault. We conclude by deriving a theoretical understanding of these fault slip simulations by considering the simple case of a fixed-length pressurized zone in Chapter 5. Overall, our work provides key insights for extracting and using different sources of hydrogeodetic signals as well as for modeling and understanding fluid-induced fault slip processes, which is becoming increasingly important in a world faced with water scarcity, a changing climate, and an increased reliance on groundwater and geoenergy resources.

PUBLISHED CONTENT

S. Larochelle, A. Gualandi, K. Chanard, and J. P. Avouac. Identification and extraction of seasonal geodetic signals due to surface load variations. *Journal of Geophysical Research: Solid Earth*, 123, 2018. doi: 10.1029/2018JB016607.
Contribution: S.L. performed the data analysis and participated in designing the study, interpreting the results and preparing the manuscript.

S. Larochelle, N. Lapusta, J.-P. Ampuero, and F. Cappa. Constraining fault friction and stability with fluid-injection field experiments. *Geophysical Research Letters*, 48, 2021. doi: 10.1029/2020GL091188.
Contribution: S.L. performed the numerical simulations and participated in designing the study, interpreting the simulations and preparing the manuscript.

S. Larochelle, K. Chanard, L. Fleitout, J. Fortin, A.Gualandi, L. Longuevergne, P. Rebischung, S. Violette, and J.-P. Avouac. Understanding the geodetic signature of large aquifer systems: Example of the Ozark Plateaus in central United States. *Journal of Geophysical Research: Solid Earth*, 127(3), 2022. doi: 10.1029/2021jb023097.
Contribution: S.L. performed the data analysis and modeling and participated in designing the study, interpreting the results and preparing the manuscript.

S. Larochelle, , J.-P. Ampuero, V. Lambert, and N. Lapusta. Fault reactivation and earthquake nucleation due to fluid injection. *To be submitted.*
Contribution: S.L. performed the numerical simulations and participated in designing the study, interpreting the results and preparing the manuscript.

S. Larochelle, K. Chanard, M. Dalaison, L. Fleitout, J. Fortin, R. Jolivet, L. Longuevergne, D. Argus, and J.-P. Avouac. Vertical and horizontal poroelastic deformation driven by groundwater extraction in the Sacramento Valley, California. *To be submitted*.
Contribution: S.L. performed the data analysis and modeling and participated in designing the study, interpreting the results and preparing the manuscript.

TABLE OF CONTENTS

INTRODUCTION

The solid Earth, encompassing our planet's geological interior and habitable surface, and the hydrosphere, composed of all water on Earth, are often studied as independent systems. Yet, mechanical interactions between these spheres are central to many geophysical problems of crucial societal importance, from sustainable water management to earthquake physics.

As a first example, changes in hydrospheric mass occurring near or at the Earth's surface have been linked to ground deformation on the order of a few millimeters to centimeters (Blewitt et al., 2001; van Dam et al., 2001). Because these mass variations reflect changing conditions in freshwater systems, oceans, and the cryosphere, characterizing this deformation has important implications for monitoring water resources and refining our understanding of the global water cycle (Figure 0.1a). At the same time, the associated changes in surface loading conditions offer an opportunity to constrain Earth's elastic and viscoelastic properties (Chanard et al., 2014, 2018; Drouin et al., 2016; Martens et al., 2016) as well as to evaluate the crust's sensitivity to small periodic stresses. Indeed, modulation of seismicity by hydrological loading has been reported in a variety of tectonic settings and geographical locations (Heki, 2003; Bettinelli et al., 2008; Craig et al., 2017; Johnson et al., 2017).

Moreover, in the first few kilometers below the surface, mechanical interactions between groundwater and the porous structure of geological materials control how much water aquifer systems can hold (Figure 0.1b). When fluctuations in groundwa-

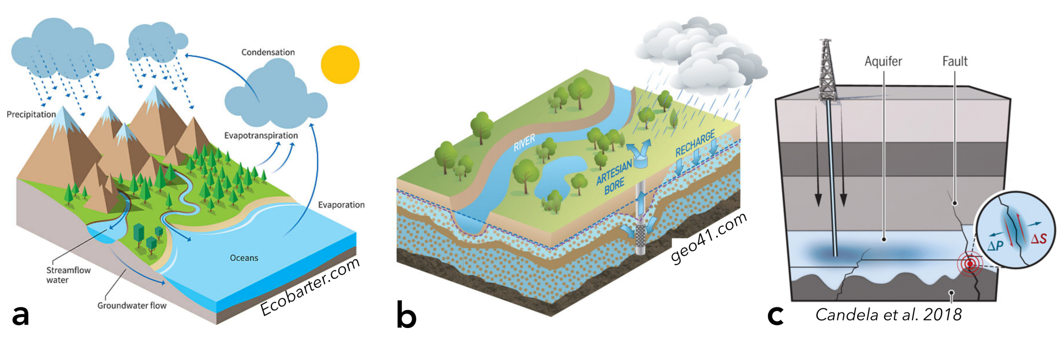

Figure 0.1: Schematic diagrams illustrating the different water-solid Earth interactions explored in this thesis. (a) Surface loading of the solid Earth by fluctuations in hydrospheric mass. (b) Poroelastic interactions between groundwater and the porous structure of geological materials. (c) Fault slip induced by injections of water into the crust.

ter levels resulting from the natural hydrologic cycle and anthropogenic extractions remain relatively small and slow, aquifers operate in a so-called poroelastic regime and their elastic storage capacity is preserved (Biot, 1941; Verruijt, 1969; Wang, 2017). In contrast, if groundwater extraction is too rapid and extensive, the system can enter an inelastic regime, causing irreversible loss of storage capacity as suggested by large land subsidence on the order of meters reported around critically drafted aquifer systems such California's San Joaquin Valley, the Basin of Mexico and Indonesia's Jakarta Basin (Poland and Davis, 1969; Galloway and Burbey, 2011). Hence, studying these hydromechanical couplings is essential to plan for the sustainable use of groundwater which is becoming an even more vital resource in a world faced with growing water scarcity (United Nations, 2022).

Going deeper into the crust, water naturally present at seismogenic depths is also thought to play a key role in the physics of earthquakes, notably by altering the shear resistance and loading conditions of fault zones via fluid pressure (Hubbert and Rubey, 1959; Sibson, 1992). In fact, the importance of fluids in fault slip processes has come to the forefront of the field in recent years due, in part, to the surge in seismicity associated with crustal injections of water used in the geoenergy industry (Ellsworth, 2013; Grigoli et al., 2017) (Figure 0.1c). Understanding how variations in fluid pressure and frictional fault interfaces interact is thus essential to decipher the mechanics of both tectonic and fluid-induced earthquakes, to develop physics-based forecasts of seismic hazard as well as to bolster the safe development of geoenergy technologies like enhanced geothermal systems and CO_2 sequestration.

Clearly, mechanical interactions between water and the solid Earth, whether naturally occurring or arising from human activities, lead to a wide array of important and interesting, but also complex, geophysical problems. Fortunately, the last two decades have seen the development of new techniques, datasets, and models with which to tackle these problems.

Notably, the rise of modern satellite techniques has enabled measurements of the Earth's evolving shape and gravity field at increasingly high spatial and temporal resolutions. As such, the emerging field of hydrogeodesy harnesses space-based techniques such as the Global Navigation Satellite System (GNSS), Interferometric Synthetic Aperture Radar (InSAR), and the Gravity Recovery and Climate Experiment (GRACE) to study hydrological processes. In particular, a number of studies have used GNSS and InSAR observations of the Earth's surface displacements to infer fluctuations in continental water storage (e.g., Argus et al., 2014, 2017; Borsa et al., 2014; Fu et al., 2015; Johnson et al., 2017) and monitor aquifer systems (e.g., Amelung et al., 1999; Wisely and Schmidt, 2010; Chaussard et al., 2014; Silverii et al., 2016; Riel et al., 2018; Ojha et al., 2018).

However, accurately extracting the different sources of hydrological signals from geodetic measurements is still challenging for a number of reasons. For one, geodetic datasets such as GNSS contain various sources of seasonal noise, systematic errors, and non-hydrologic deformation that make the recovery of primarily seasonal hydrologic signals difficult (Dong et al., 2002; Davis et al., 2012; Chanard et al., 2020). Another challenge in isolating the contribution of regional hydrology is the fact that surface deformation at a particular point results from both local loads and loads at larger spatial wavelengths, up to spherical harmonics degree 1 (Farrell, 1972). The related but distinct deformation fields associated with hydrological loading and poroelastic effects are also not easily separable given the high correlation between groundwater and continental water storage variations (the latter encompassing the former). In fact, relatively few hydrogeodetic studies have focused on characterizing the poroelastic response of aquifer systems compared to the well-documented inelastic porous response associated with permanent land subsidence. Yet, understanding and documenting both regimes is important to prevent healthy aquifer systems from becoming critically stressed by excessive groundwater pumping. Similarly, relatively little work has been done on horizontal displacements given their generally lower signal-to-noise ratio compared to vertical displacements. Further work to understand the composition of horizontal geodetic measurements is certainly warranted given that they could provide additional constraints on hydrologic variations (Wahr et al., 2013).

While satellite geodesy has also led to important observations for the field of induced seismicity — notably the detection of aseismic slip transients (Wei et al., 2015) — here we focus on recent advances on the modeling front. Indeed, numerical modeling promises to help answer key questions about fluid-induced fault slip, starting with what exactly controls its stability (i.e., seismic vs aseismic), frequency of occurrence, and spatial distribution. A number of recent studies have given insight into these questions through slip-weakening friction models (Garagash and Germanovich, 2012; Viesca and Rice, 2012; Galis et al., 2017; Bhattacharya and Viesca, 2019). However, laboratory experiments on various geological interfaces have shown that frictional strength depends on both instantaneous slip rates and slip history (Dieterich, 1979, 2007; Rice and Ruina, 1983; Marone, 1998). In fact, rate- and state-dependent friction laws are widely used in dynamic models of natural earthquake sequences which are now capable of resolving the entire spectrum of fault slip behavior, from earthquake nucleation, propagation and arrest to slow stable sliding over thousands of years (Ben-Zion and Rice, 1997; Lapusta et al., 2000; Jiang et al., 2022). There is thus an opportunity to further our understanding of induced earthquakes by building on the rate-and-state, elastodynamic framework of the natural earthquake modeling community. In particular, such modeling could help evaluate whether critical nucleation lengthscales derived for tectonically-loaded faults and thought to control their stability (Ruina, 1983; Dieterich, 1992; Uenishi and Rice, 2003; Rubin and Ampuero, 2005) apply in the case of fluid-induced slip.

This thesis is an attempt to address and explore some of these questions through state-of-the-art geodetic, data analysis, and numerical modeling tools.

In Chapter 1, we start by developing a methodology to identify and extract seasonal signals associated with fluctuations of continental water mass in vertical and horizontal GNSS time series. The approach relies on Independent Component Analysis (ICA) to extract the seasonal signals and a GRACE-based deformation model to identify which of the independent component are caused by hydrological loading. We test the approach in the Arabian Peninsula and Nepal Himalayas and show that it is robust to spatial heterogeneities inherent to geodetic measurements and that it can help extract systematic errors in geodetic products (e.g., draconitic errors). We also discuss how to handle the degree-1 deformation field present in the geodetic data set but not captured by the gravity-based model.

In Chapter 2, we focus on the Ozark Plateaus aquifer system to demonstrate a methodology for extracting poroelastic deformation signals from horizontal and vertical GNSS measurements. The procedure consists in characterizing the dominant temporal functions of in situ groundwater level measurements with ICA before projecting the geodetic time series corrected for hydrological loading effects onto these functions. We interpret the resulting displacements in light of a semi-analytical two-layer poroelastic model relating groundwater level variations to surface displacements and highlight key differences between the hydrological loading and poroelastic responses. We conclude the study by inferring a heterogeneous distribution of elastic moduli in the surficial aquifer layers.

In Chapter 3, we use the approach of Chapter 2 to characterize the large poroelastic displacements associated with pervasive groundwater pumping operations in the Sacramento Valley aquifer system. Applying ICA to the extensive network of groundwater monitoring wells provides a high-resolution picture of the dominant spatiotemporal variations in groundwater levels in the region. We relate the extracted vertical and horizontal poroelastic displacements to groundwater variations with the help of two different analytical poroelastic models. We find that elastic properties are relatively homogeneous within the aquifer layer but that the higher elastic moduli of the underlying crystalline basements of nearby mountain ranges are necessary to explain the small horizontal displacements at the aquifer boundaries.

In Chapter 4, we implement fluid injection and diffusion in the rate-and-state, elastodynamic model of Lapusta et al. (2000) and calibrate it against the observations of a well-instrumented fluid-injection experiment on a natural fault (Guglielmi et al., 2015). We show that a range of fault models with different intrinsic stabilities can reproduce the slip measured during pressurization. Upon depressurization, however, the most unstable scenario departs from the observations, suggesting that the fault is relatively stable. We discuss how the models could be further distinguished via optimized depressurization tests or spatially distributed monitoring. Our findings suggest that avoiding injection near low-residual-friction faults and depressurizing upon slip acceleration could help prevent large-scale earthquakes.

In Chapter 5, we focus on understanding the conditions that lead to the different slip behaviors observed in the simulations presented in Chapter 4 by considering the simpler case of a fixed-length pressurized zone. We first establish similarities between the simulated slip resulting from fixed-length and diffusive pressurized zones before focusing on the former. Then, we identify 3 distinct stages common to all simulations and explain the slip behavior observed at each stage with relevant lengthscales and additional closed-form solutions. In particular, we find that slip resulting from a simple linearly increasing pressure scenario is controlled by a combination of several stability lengthscales originally derived for tectonically-loaded faults.

We conclude the thesis by discussing directions of ongoing and future work.

Bibliography

F. Amelung, D. L. Galloway, J. W. Bell, H. A. Zebker, and R. J. Laczniak. Sensing the ups and downs of Las Vegas: InSAR reveals structural control of land subsidence and aquifer-system deformation. *Geology*, 27:483, 6 1999. ISSN 0091-7613. doi: 10.1130/0091-7613(1999)027<0483:STUADO>2.3.CO;2.

D. F. Argus, Y. Fu, and F. W. Landerer. Seasonal variation in total water storage in California inferred from GPS observations of vertical land motion. *Geophysical Research Letters*, 41(6):1971–1980, 2014. ISSN 00948276. doi: 10.1002/2014GL059570.

D. F. Argus, F. W. Landerer, D. N. Wiese, H. R. Martens, Y. Fu, J. S. Famiglietti, B. F. Thomas, T. G. Farr, A. W. Moore, and M. M. Watkins. Sustained water loss in California's mountain ranges during severe drought from 2012 to 2015 inferred from GPS. *Journal of Geophysical Research: Solid Earth*, 122(12): 10–559, 2017.

Y. Ben-Zion and J. R. Rice. Dynamic simulations of slip on a smooth fault in an elastic solid. *Journal of Geophysical Research: Solid Earth*, 102(B8):17771–17784, 1997.

P. Bettinelli, J.-P. Avouac, M. Flouzat, L. Bollinger, G. Ramillien, S. Rajaure, and S. Sapkota. Seasonal variations of seismicity and geodetic strain in the Himalaya induced by surface hydrology. *Earth and Planetary Science Letters*, 266(3-4): 332–344, 2008. ISSN 0012-821X. doi: 10.1016/J.EPSL.2007.11.021.

P. Bhattacharya and R. Viesca. Fluid-induced aseismic fault slip outpaces pore-fluid migration. *Science*, 364(6439):464–468, 2019. doi: 10.1126/science.aaw7354. URL `https://doi.org/10.1126/science.aaw7354`.

M. A. Biot. General theory of three-dimensional consolidation. *Journal of Applied Physics*, 12, 1941. ISSN 00218979. doi: 10.1063/1.1712886.

G. Blewitt, D. Lavallée, P. Clarke, and K. Nurutdinov. A new global mode of Earth deformation: Seasonal cycle detected. *Science (New York, N.Y.)*, 294(5550): 2342–5, 2001. ISSN 0036-8075. doi: 10.1126/science.1065328.

A. A. Borsa, D. C. Agnew, and D. R. Cayan. Ongoing drought-induced uplift in the western United States. *Science*, 345(6204):1587–1590, sep 2014. doi: 10.1126/SCIENCE.1260279.

K. Chanard, J. P. Avouac, G. Ramillien, and J. Genrich. Modeling deformation induced by seasonal variations of continental water in the himalaya region: Sensitivity to earth elastic structure. *Journal of Geophysical Research: Solid Earth*, 119:5097–5113, 6 2014. ISSN 21699313. doi: 10.1002/2013JB010451. URL `http://doi.wiley.com/10.1002/2013JB010451`.

K. Chanard, L. Fleitout, E. Calais, S. Barbot, and J.-P. Avouac. Constraints on transient viscoelastic rheology of the asthenosphere from seasonal deformation. *Geophysical Research Letters*, 45(5):2328–2338, 2018.

K. Chanard, M. Métois, P. Rebischung, and J.-P. Avouac. A warning against over-interpretation of seasonal signals measured by the Global Navigation Satellite System. *Nature Communications*, 11(1):1375, 2020. ISSN 2041-1723. doi: 10.1038/s41467-020-15100-7.

E. Chaussard, R. Bürgmann, M. Shirzaei, E. J. Fielding, and B. Baker. Predictability of hydraulic head changes and characterization of aquifer-system and fault properties from InSAR-derived ground deformation. *Journal of Geophysical Research: Solid Earth*, 119(8):6572–6590, 2014. ISSN 21699313. doi: 10.1002/2014JB011266.

T. J. Craig, K. Chanard, and E. Calais. Hydrologically-driven crustal stresses and seismicity in the New Madrid Seismic Zone. *Nature Communications*, 8(1):2143, 2017. ISSN 2041-1723. doi: 10.1038/s41467-017-01696-w.

J. L. Davis, B. P. Wernicke, and M. E. Tamisiea. On seasonal signals in geodetic time series. *Journal of Geophysical Research: Solid Earth*, 117, 2012. ISSN 21699356. doi: 10.1029/2011JB008690.

J. H. Dieterich. Modeling of rock friction: 1. Experimental results and constitutive equations. *Journal of Geophysical Research*, 84(B5):2161, 1979. doi: 10.1029/JB084iB05p02161. URL `https://doi.org/10.1029/JB084iB05p02161`.

J. H. Dieterich. Earthquake nucleation on faults with rate-and state-dependent strength. *Tectonophysics*, 211(1–4):115–134, 1992. doi: 10.1016/0040-1951(92)90055-B. URL `https://doi.org/10.1016/0040-1951(92)90055-B`.

J. H. Dieterich. Applications of rate- and state-dependent friction to models of fault slip and earthquake occurrence. *Treatise on Geophysics*, page 107–129, 2007. doi: 10.1016/B978-044452748-6.00065-1. URL `https://doi.org/10.1016/B978-044452748-6.00065-1`.

D. Dong, P. Fang, Y. Bock, M. K. Cheng, and S. Miyazaki. Anatomy of apparent seasonal variations from GPS-derived site position time series. *Journal of Geophysical Research: Solid Earth*, 107(B4):ETG 9–1–ETG 9–16, 2002. ISSN 01480227. doi: 10.1029/2001JB000573.

V. Drouin, K. Heki, F. Sigmundsson, S. Hreinsdóttir, and B. G. Ófeigsson. Constraints on seasonal load variations and regional rigidity from continuous gps measurements in iceland, 1997–2014. *Geophysical Journal International*, 205: 1843–1858, 6 2016. ISSN 0956-540X. doi: 10.1093/gji/ggw122. URL `https://academic.oup.com/gji/article-lookup/doi/10.1093/gji/ggw122`.

W. L. Ellsworth. Injection-induced earthquakes. *Science*, 341:1225942, 7 2013. doi: 10.1126/science.1225942. URL `http://science.sciencemag.org/content/341/6142/1225942.abstract`.

W. E. Farrell. Deformation of the Earth by surface loads. *Reviews of Geophysics*, 10(3):761, 1972. ISSN 8755-1209. doi: 10.1029/RG010i003p00761.

Y. Fu, D. F. Argus, and F. W. Landerer. GPS as an independent measurement to estimate terrestrial water storage variations in Washington and Oregon. *Journal of Geophysical Research: Solid Earth*, 120(1):552–566, 2015. ISSN 21699313. doi: 10.1002/2014JB011415.

M. Galis, J. Ampuero, P. Mai, and F. Cappa. Induced seismicity provides insight into why earthquake ruptures stop. *Science Advances*, 3(12):7528, 2017. doi: 10.1126/sciadv.aap7528. URL `https://doi.org/10.1126/sciadv.aap7528`.

D. L. Galloway and T. J. Burbey. Review: Regional land subsidence accompanying groundwater extraction. *Hydrogeology Journal*, 19(8):1459–1486, 2011. ISSN 1431-2174. doi: 10.1007/s10040-011-0775-5.

D. Garagash and L. Germanovich. Nucleation and arrest of dynamic slip on a pressurized fault. *Journal of Geophysical Research: Solid Earth*, 117(B10), 2012. doi: 10.1029/2012JB009209. URL `https://doi.org/10.1029/2012JB009209`.

F. Grigoli, S. Cesca, E. Priolo, A. P. Rinaldi, J. F. Clinton, T. A. Stabile, B. Dost, M. G. Fernandez, S. Wiemer, and T. Dahm. Current challenges in monitoring, discrimination, and management of induced seismicity related to underground industrial activities: A European perspective. *Reviews of Geophysics*, 55:310–340, 6 2017. ISSN 87551209. doi: 10.1002/2016RG000542. URL `http://doi.wiley.com/10.1002/2016RG000542`.

Y. Guglielmi, F. Cappa, J. Avouac, P. Henry, and D. Elsworth. Seismicity triggered by fluid injection-induced aseismic slip. *Science*, 348(6240), 2015. doi: 10.1126/science.aab0476. URL `https://doi.org/10.1126/science.aab0476`.

K. Heki. Snow load and seasonal variation of earthquake occurrence in Japan. *Earth and Planetary Science Letters*, 207, 2003. ISSN 0012821X. doi: 10.1016/S0012-821X(02)01148-2.

M. Hubbert and W. W. Rubey. Role of fluid pressure in mechanics of overthrust faulting: I. Mechanics of fluid-filled porous solids and its application to overthrust faulting. *Geological Society of America Bulletin*, 70(2):115–166, 1959.

J. Jiang, B. A. Erickson, V. R. Lambert, J. Ampuero, R. Ando, S. D. Barbot, C. Cattania, L. D. Zilio, B. Duan, E. M. Dunham, A. Gabriel, N. Lapusta, D. Li, M. Li, D. Liu, Y. Liu, S. Ozawa, C. Pranger, and Y. Dinther. Community-driven code comparisons for three-dimensional dynamic modeling of sequences of earthquakes and aseismic slip. *Journal of Geophysical Research: Solid Earth*, 127, 2022. ISSN 2169-9313. doi: 10.1029/2021jb023519.

C. W. Johnson, Y. Fu, and R. Bürgmann. Seasonal water storage, stress modulation, and California seismicity. *Science (New York, N.Y.)*, 356(6343):1161–1164, 2017. ISSN 1095-9203. doi: 10.1126/science.aak9547.

N. Lapusta, J. R. Rice, Y. Ben-Zion, and G. Zheng. Elastodynamic analysis for slow tectonic loading with spontaneous rupture episodes on faults with rate-and state-dependent friction. *Journal of Geophysical Research*, 105(B10): 765–788, 2000. doi: 10.1029/2000JB900250. URL `https://doi.org/10.1029/2000JB900250`.

C. Marone. Laboratory-derived friction laws and their application to seismic faulting. *Annual Review of Earth and Planetary Sciences*, 26, 1998. Retrieved from www.annualreviews.org.

H. R. Martens, L. Rivera, M. Simons, and T. Ito. The sensitivity of surface mass loading displacement response to perturbations in the elastic structure of the crust and mantle. *Journal of Geophysical Research: Solid Earth*, 121, 2016. ISSN 21699356. doi: 10.1002/2015JB012456.

C. Ojha, M. Shirzaei, S. Werth, D. F. Argus, and T. G. Farr. Sustained groundwater loss in California's Central Valley exacerbated by intense drought periods. *Water Resources Research*, 54(7):4449–4460, 2018. ISSN 0043-1397. doi: 10.1029/2017WR022250.

J. F. Poland and G. H. Davis. Land subsidence due to withdrawal of fluids. *GSA Reviews in Engineering Geology*, 2, 1969. ISSN 00802018. doi: 10.1130/REG2-p187.

J. R. Rice and A. Ruina. Stability of steady frictional slipping. *Journal of Applied Mechanics*, 50(2):343, 1983. doi: 10.1115/1.3167042. URL `https://doi.org/10.1115/1.3167042`.

B. Riel, M. Simons, D. Ponti, P. Agram, and R. Jolivet. Quantifying ground deformation in the Los Angeles and Santa Ana coastal basins due to groundwater withdrawal. *Water Resources Research*, 54(5):3557–3582, 2018. ISSN 0043-1397. doi: 10.1029/2017WR021978.

A. Rubin and J.-P. Ampuero. Earthquake nucleation on (aging) rate and state faults. *Journal of Geophysical Research: Solid Earth*, 110(B11), 2005. doi: 10.1029/2005JB003686. URL `https://doi.org/10.1029/2005JB003686`.

A. Ruina. Slip instability and state variable friction laws. *Journal of Geophysical Research: Solid Earth*, 88(B12):10359–10370, 1983. doi: 10.1029/JB088iB12p10359. URL `https://doi.org/10.1029/JB088iB12p10359`.

R. H. Sibson. Implications of fault-valve behaviour for rupture nucleation and recurrence. *Tectonophysics*, 211(1-4):283–293, 1992.

F. Silverii, N. D'Agostino, M. Métois, F. Fiorillo, and G. Ventafridda. Transient deformation of karst aquifers due to seasonal and multiyear groundwater variations observed by GPS in southern Apennines (Italy). *Journal of Geophysical Research: Solid Earth*, 121(11):8315–8337, nov 2016. ISSN 2169-9313. doi: 10.1002/2016JB013361.

K. Uenishi and J. R. Rice. Universal nucleation length for slip-weakening rupture instability under nonuniform fault loading. *Journal of Geophysical Research: Solid Earth*, 108(B1), 2003. doi: 10.1029/2001JB001681. URL `https://doi.org/10.1029/2001JB001681`.

United Nations. *The United Nations World Water Development Report 2022: Groundwater: Making the invisible visible*. UNESCO, Paris, 2022.

T. van Dam, J. Wahr, P. C. D. Milly, A. B. Shmakin, G. Blewitt, D. Lavallée, and K. M. Larson. Crustal displacements due to continental water loading. *Geophysical Research Letters*, 28(4):651–654, 2001. ISSN 00948276. doi: 10.1029/2000GL012120.

A. Verruijt. Elastic storage of aquifers in *Flow through Porous Media*, 1969.

R. Viesca and J. R. Rice. Nucleation of slip-weakening rupture instability in landslides by localized increase of pore pressure. *Journal of Geophysical Research: Solid Earth*, 117(B3), 2012. doi: 10.1029/2011JB008866. URL `https://doi.org/10.1029/2011JB008866`.

J. Wahr, S. A. Khan, T. van Dam, L. Liu, J. H. van Angelen, M. R. van den Broeke, and C. M. Meertens. The use of GPS horizontals for loading studies, with applications to northern California and southeast Greenland. *Journal of Geophysical Research: Solid Earth*, 118(4):1795–1806, apr 2013. ISSN 21699313. doi: 10.1002/jgrb.50104.

H. F. Wang. Theory of linear poroelasticity with applications to geomechanics and hydrogeology. In *Theory of Linear Poroelasticity with Applications to Geomechanics and Hydrogeology*. Princeton University Press, 2017.

S. Wei, J.-P. Avouac, K. Hudnut, A. Donnellan, J. Parker, and R. Graves. The 2012 brawley swarm triggered by injection-induced aseismic slip. *Earth and Planetary Science Letters*, 422:115–125, 2015. doi: 10.1016/j.epsl.2015.03.054. URL `https://doi.org/10.1016/j.epsl.2015.03.054`.

B. A. Wisely and D. Schmidt. Deciphering vertical deformation and poroelastic parameters in a tectonically active fault-bound aquifer using insar and well level data, san bernardino basin, california. *Geophysical Journal International*, 181:1185–1200, 3 2010. ISSN 0956540X. doi: 10.1111/j.1365-246X.2010.04568.x. URL `https://academic.oup.com/gji/article-lookup/doi/10.1111/j.1365-246X.2010.04568.x`.

Chapter 1

IDENTIFICATION AND EXTRACTION OF SEASONAL GEODETIC SIGNALS DUE TO HYDROLOGICAL LOADING

Published as:

S. Larochelle, A. Gualandi, K. Chanard, and J. P. Avouac. Identification and extraction of seasonal geodetic signals due to surface load variations. *Journal of Geophysical Research: Solid Earth*, 123, 2018. doi: 10.1029/2018JB016607.

1.1 Introduction

Seasonal signals are observed in geodetic position time series of Global Navigation Satellite System (GNSS) stations at a global scale (Blewitt et al., 2001). These annual displacements can be explained, to first order, by the Earth's response to variations in surface loads mostly due to redistributions of continental water mass(Blewitt et al., 2001; van Dam et al., 2001; Dong et al., 2002). Identifying and extracting non-tectonic seasonal signals from geodetic measurements is critical to detect potential tectonic signals of small amplitude, key to our understanding of the seismic cycle (e.g., slow slip events and tremors, postseismic slip and interseismic strain). Characterizing geodetic seasonal signals is also important to study the possible relationship between small periodic stresses and earthquake nucleation (Bettinelli et al., 2008; Bollinger et al., 2007; Craig et al., 2017; Johnson et al., 2017), invert for continental water storage fluctuations (Argus et al., 2014; Borsa et al., 2014; Fu et al., 2015) and constrain the elastic (Chanard et al., 2014; Drouin et al., 2016) and viscoelastic (Chanard et al., 2018a) properties of the Earth.

In recent years, two promising strategies to isolate geodetic seasonal signals have been developing in parallel. On one hand, a large effort has been made towards developing accurate models of the Earth's surface displacements induced by surface load variations measured by the Gravity Recovery and Climate Experiment (GRACE) satellites (Figure 1.1). Several studies (Bettinelli et al., 2008; Chanard et al., 2014, 2018b; Davis et al., 2004; Fu et al., 2012; Fu and Freymueller, 2012) have demonstrated that GRACE-based deformation models can explain a large part of the GNSS annual observations. Although such models are essential to establish the hydrological origin of seasonal geodetic signals, discrepancies remain between model and data (e.g., Figures 1.2(a,b)).

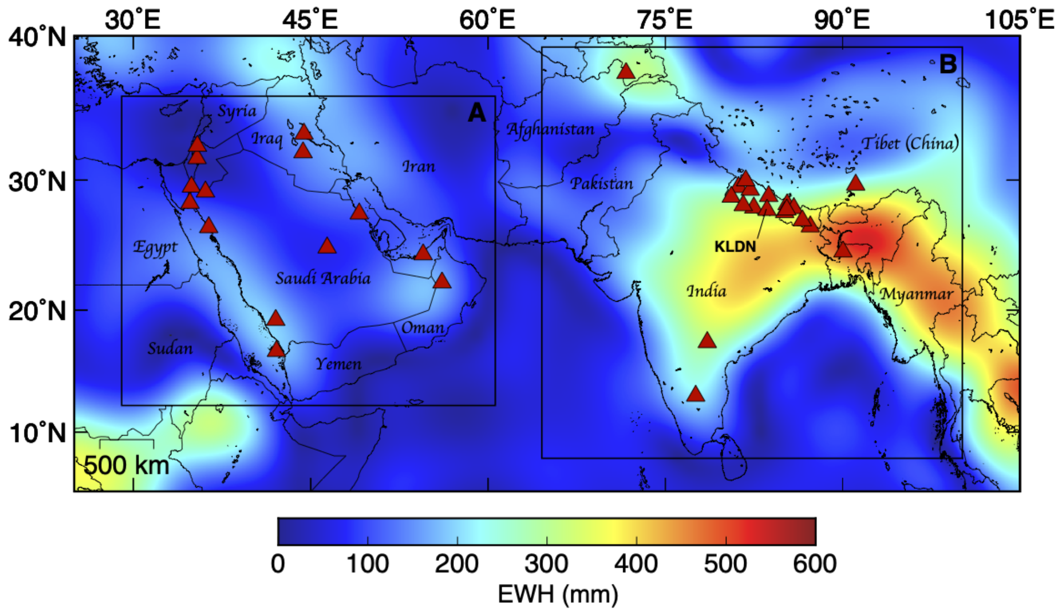

Figure 1.1: Average peak-to-peak GRACE-derived surface load distribution for the period 2007 to 2012.5 expressed in Equivalent Water Height (EWH). Boxes A and B delineate the two study areas: the Arabian Peninsula and the Nepal Himalaya. The triangles indicate the locations of GNSS stations used in each study area. Station KLDN for which time series are shown in Figure 1.2 is also identified.

On the other hand, the task of isolating seasonal signals from geodetic time series can be approached as a blind-source separation problem where the observed displacements are the result of several, mixed sources. To this end, an Independent Component Analysis (ICA) can be applied to the displacement dataset to untangle, in a purely statistical manner, the different physical processes beneath the observations (Comon, 1994). Notably, Gualandi et al. (2017a,b); Serpelloni et al. (2018) showed that the variational Bayesian form of the ICA (vbICA) can objectively extract seasonal signals from GNSS time series. Being a data-driven approach, ICA-reconstructed seasonal signals have the ability to satisfactorily reproduce the observations, capturing also the effects of local heterogeneities that are otherwise averaged out in the aforementioned models. While the independence of components required by ICA suggests that these seasonal components are physical signals, the technique alone provides no information about their origins.

In light of the strengths and limitations of these two parallel strategies, we here propose a procedure that combines the physical robustness of a GRACE-based model (Chanard et al., 2014, 2018b) with the statistical precision of the vbICA algorithm (Gualandi et al., 2016) to (1) decompose the displacement datasets (GNSS and

GRACE-derived deformation) into a finite number of components, (2) retain the seasonal signals and (3) describe them in terms of underlying physical processes. Hereafter, we first present the GNSS data and GRACE-derived deformation model used in this study and provide an overview of the vbICA technique and the proposed procedure. In Section 1.3, we test the procedure in two study areas: the Arabian Peninsula and the Nepal Himalaya. Each case study presents its own complexities and provides complementary insight on the robustness of the approach to spatial heterogeneities and how it can help extract systematic errors in geodetic products (e.g., draconitic errors). In Section 1.4, we explore two variations to the input time series in order to identify the most robust procedure, which we summarize in Section 1.5. We conclude with final remarks on the applicability of the procedure.

1.2 Data and Methods

1.2.1 Datasets

1.2.1.1 GNSS displacement time series

We use 24-hour final solution time series processed by the Nevada Geodetic Laboratory (NGL) (Blewitt et al., 2018). The solutions are aligned with ITRF2008 whose origin linearly tracks the mean of the total Earth system's center of mass but corresponds to the center of the IGS08b network which is close to the center of figure of the Earth for sub-secular time scales (Dong et al., 2003). Most of the available continuous GNSS stations in the regions of interest were deployed in 2007 or later. To minimize missing data across the GNSS and GRACE datasets, we consider the time range [2007.0, 2012.5] since the GRACE data started showing more frequent gaps in 2012 as the satellites neared the end of their lifespan (Jean et al., 2015). Of the 72 GNSS stations available in the Arabian Peninsula and of the 59 available in Nepal, for each area we select 14 stations with recordings during the time range [2007.0, 2012.5] in such a way that the stations are approximately evenly distributed across the studied region. Five stations outside of Nepal are also included to ensure that loads with a spatial wavelength larger than Nepal are fully captured. The selected stations are indicated by triangles in Figure 1.1.

The geodetic time series are simultaneously detrended and corrected for step discontinuities by least-square fitting of a linear trend, annual and semi-annual sinusoids and offsets terms where visually obvious (see Table A.1), at epochs corresponding to equipment changes, and coseismic displacements as reported by NGL (`http://geodesy.unr.edu/NGLStationPages/steps.txt`). Note that

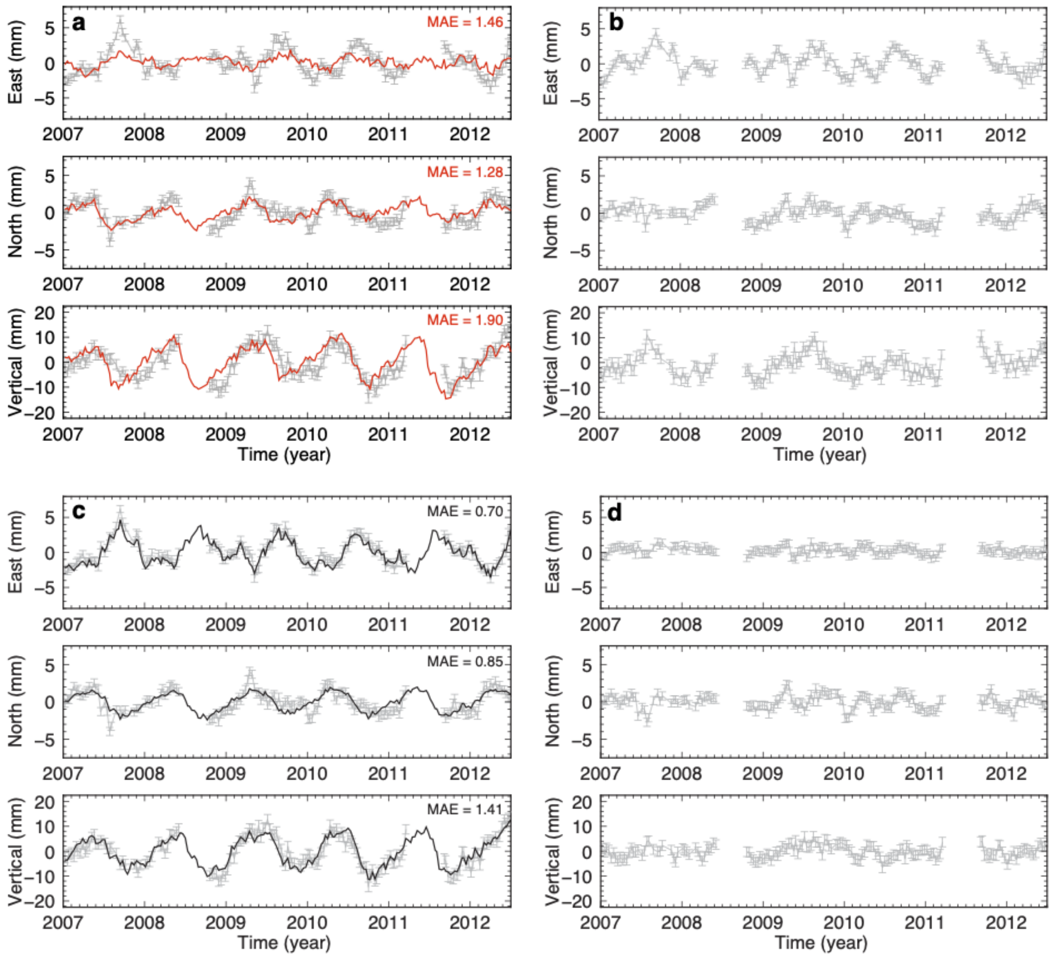

Figure 1.2: Comparison of seasonal correction at GNSS station KLDN in Nepal from the GRACE model and the recommended vbICA reconstruction with 2 ICs. (a) East, north and vertical components of detrended 10-day moving-average geodetic (grey) and GRACE model (red) with the mean absolute error (MAE) indicated at the top right corner. (b) GPS time series corrected for seasonal signal (via subtraction of GRACE model). (c,d) Same as (a,b) but for the ICA reconstruction (black) proposed in this study. As indicated by the MAE values and the residuals in (b) and (d), the vbICA reconstruction performs better at removing the seasonal signals in the original GNSS time series.

detrending is necessary when comparing GNSS and GRACE-derived datasets as they may not exhibit the same long-term trends (e.g., interseismic deformation might be present in the GNSS dataset but not in GRACE). This means that, here, we are only comparing the variations from the relative linear trends of the two datasets. Note, however, that the technique does not require the linear trend in the GNSS time series to be of tectonic origin only. Outliers, defined as data points that exceed three times the average deviation from the mean within a 90-day sliding window in any of the directions (east, north, and vertical), are then removed from all three time series relative to a given station. The daily position solutions are also averaged over a 10-day period to match the GRACE data temporal resolution.

The final step consists in removing the spherical harmonics degree-1 contribution from the time series to allow comparison with the GRACE dataset which does not contain degree-1 deformations (Swenson et al., 2008). We estimate and retrieve the degree-1 deformation field using a dataset of 689 globally distributed GNSS time series processed by NGL (Blewitt et al., 2018), as described in Chanard et al. (2018b). The importance of the degree-1 deformation field and the necessity of correcting for its effect in the GNSS time series are discussed in further details in Section 1.4.1. These final time series are referred to as the GNSS dataset. Figure 1.2 shows an example of cleaned GNSS time series at station KLDN in Nepal. Additional time series at other stations are also available in Figure A.1.

1.2.1.2 GRACE gravimetric time series

To quantify surface mass variations, we start with the 10-day Level-2 CNES/CRGS solutions (`http://grgs.obs-mip.fr`, last accessed on July 1st, 2017) of the Earth's time-varying gravitational field as measured by the GRACE twin satellites. The CNES/CRGS processing methodology, which includes removal of the static geoid and of well-characterized gravimetric contributions (e.g., solid earth and oceanic tides), is described in Bruinsma et al. (2010). We add back atmospheric and non-tidal oceanic contributions as these are not corrected for in the GNSS dataset (Carrère and Lyard, 2003). The solutions expressed in terms of Stokes coefficients of degree 2 to 50 are converted, via isotropic filtering (Ramillien et al., 2005), to a spatial load distribution in units of equivalent water height (EWH). The EWH time series are then detrended to allow comparison with the geodetic dataset. Figure 1.1 shows the resulting peak-to-peak surface load distribution averaged over the study period of 2007 to 2012.5.

1.2.1.3 GRACE-derived displacement time series

To enable comparison between the GRACE and GNSS datasets, we compute the displacements expected at the GNSS site locations from the GRACE-derived surface load distribution by using the numerical model developed by Chanard et al. (2018b). The model first decomposes the loads in the temporal and spatial domains and generates load Love numbers (Farrell, 1972) for an elastic Earth structure with continental crust (Bassin et al., 2000) and PREM parameters (Dziewonski and Anderson, 1981). The spatially- and temporally-separated loads are then convolved with the appropriate load Love numbers to form the desired displacement time series. Figure 1.2a shows an example of a GRACE-derived time series at station KLDN. Hereafter, we refer to this dataset as the GRACE dataset.

1.2.2 Variational Bayesian Independent Component Analysis (vbICA)

The goal of any ICA algorithm is to isolate a set of Independent Components (ICs) that, when mixed together, can explain the observations. As is usual of ICA algorithms (e.g., JADE, Cardoso and Souloumiac (1993) or FastICA, Hyvärinen and Oja (1997)), the vbICA framework is set up as a linear mixing problem of non-moving sources, i.e.,

$$X = A\Sigma + N \tag{1.1}$$

where X is the matrix of the input time series, A the mixing matrix, Σ the sources matrix and, N the Gaussian noise. The mixing matrix A only depends on the relative position between the stations and the sources, while matrix Σ contains the temporal functions characterizing the sources. Differently from conventional ICA algorithms, however, vbICA follows a modeling approach, i.e., it searches for some best (in a sense to be defined) model parameters. This offers two advantages: (1) Data gaps can be handled without any interpolation of the missing data (Chan et al., 2003; Gualandi et al., 2016) and (2) we gain flexibility in the description of the sources. In particular, the sources are modeled by a mixture of Gaussians (MoG). Since any probability density function (pdf) can be expressed as a MoG, given a sufficient number of Gaussians, the technique is capable of generating multimodal pdfs commonly observed in geophysical signals (Gualandi et al., 2016).

Under the Bayesian framework, the modeling approach attempts to maximize the posterior pdf of the model parameters, that in our case are random variables related to the mixing matrix, the noise and the sources. We refer to Gualandi et al. (2016) for a list of all the parameters W involved in the model. The best model parameter set is that which simultaneously maximizes the statistical independence of the sources' pdfs and the fit to the data. Maximizing the parameters' posterior pdf is a challenging task that vbICA accomplishes by using a variational approximation approach consisting in introducing an approximating pdf ($p'(W)$) to the real posterior pdf ($p(W|X)$). The best approximation is the one that minimizes the Kullback-Leibler (KL) divergence between $p'(W)$ and $p(W|X)$, defined as:

$$D_{KL}[p'(W)||p(W|X)] = \int p'(W) \ln \frac{p'(W)}{p(W|X)} dW. \tag{1.2}$$

Since the true posterior pdf is unknown, we resort to variational inference and Bayes theorem to rewrite equation (1.2) as:

$$D_{KL}[p'(W)||p(W|X)] = \int p'(W) \ln \frac{p'(W)}{p(W,X)} dW + \int p'(W) \ln p(X) dW \tag{1.3}$$

$$D_{KL}[p'(W)||p(W|X)] = \int p'(W) \ln \frac{p'(W)}{p(W,X)} dW + \ln p(X). \tag{1.4}$$

Since the log-evidence $\ln p(X)$ does not depend on W, we can maximize the integral term (called the Negative Free Energy) with respect to $p'(W)$ in order to minimize the KL divergence on the left-hand side of (1.4).

The Bayesian framework also requires that a priori parameters (or hyper-parameters) be specified for the pdfs governing the model parameters W. In practice, the choice of priors affects how much the model is allowed to adapt to the observations. However, since the GNSS dataset under study here is not particularly affected by the choice of prior on the mixing matrix and sources, we select a priori hyper-parameters that let the data dominate the a posteriori pdf. For the GRACE dataset, we use the same priors on the mixing matrix and sources precision but select modified values for the noise precision to account for the increased signal-to-noise ratio (SNR) inherent to modeled datasets. These sets of hyper-parameter values are specified in Table A.2. A brief description of these hyper-parameters is also presented in the footnote of Table A.2.

We aggregate the time series from the two datasets into matrices $X_{(M \times T)}$ where M is the number of time series (equal to three times the number of stations to account for the east, north and vertical directions) and T the number of epochs. We follow the notation of Gualandi et al. (2016) where, similarly to a Singular Value Decomposition (SVD) notation, the dataset is decomposed into three matrices:

$$X_{(M \times T)} \sim U_{(M \times R)} S_{(R \times R)} V^T_{(R \times T)} \tag{1.5}$$

where R is the number of components, $U_{(M\times R)}$ the matrix of spatial distributions, $S_{(R\times R)}$ a weighting diagonal matrix and $V_{(T\times R)}$ the matrix of temporal functions. The only difference between the notation of equations (1.1) and (1.5) is the introduction of the diagonal matrix S which is obtained after setting the columns of U and V to unit norm. Contrary to SVD and the commonly used Principal Component Analysis (PCA), the columns of U and V are not orthogonal and the weights in S do not directly relate to the variance of the dataset. Hereafter, we refer to the spatial distribution, weight and temporal function of the i-th component as U_i, S_i and V_i, respectively, with $i = 1, \ldots, R$.

To decide on the number of components to retain, we resort to the Automatic Relevance Determination (ARD) criterion posed in Gualandi et al. (2016). The ARD criterion relies on the variances of the mixing matrix columns which can be computed from the derived mixing matrix posterior pdf. If the posterior variance of one column is small (<10 times) compared to the variance of the other columns, this implies that the corresponding IC contributes very little to the data reconstruction as its mixing values remain close to the null a priori. We thus select the number of components to be one less than the number of ICs at which one IC becomes unimportant for the data reconstruction.

1.2.3 Proposed Procedure

The procedure we propose to extract geodetic seasonal signals aims to identify components that share the same physical mechanism in the GNSS and GRACE-derived datasets. The step-by-step procedure can be summarized as follows:

1. Generate GRACE-derived displacement time series using the model presented in Chanard et al. (2018b).
2. Perform vbICA with an increasing number of ICs on the GNSS dataset until the ARD criterion is satisfied.
3. Perform vbICA on the GRACE dataset with the number of ICs identified in step 2.
4. a) Starting with the GNSS IC with the highest weight S_i, compare the temporal function V_i with the remaining unmatched GRACE temporal functions by computing correlation coefficients (ρ).

   b) Pair GNSS IC$_i$ with the GRACE IC with which it has the highest ρ.

c) If the correlation is higher than 0.50, consider the match a good one.

Tables A.3 and A.4 demonstrate how this pairing process is done in the Arabian Peninsula and the Nepal Himalaya, respectively.

5. Reconstruct the geodetic seasonal signal from the GNSS ICs having a good match with GRACE ICs.

Note that the above procedure is only meant as a general guideline for potential users of this technique and can be modified as needed. The 0.50 correlation coefficient criterion, for example, is somewhat arbitrary and could be modified, as long as there is some methodology in place to match the ICs across the two datasets.

1.3 Case Studies

1.3.1 Arabian Peninsula

As a first test case, we apply the proposed technique to the Arabian Peninsula — a region with a relatively simple but important seasonal loading pattern (e.g., Figures A.1(v) – A.1(viii)). The first two ICs (shown in Figure 1.3) explain about 55% of the data variance in the GNSS dataset and are found to be sufficient to satisfy step 2) of the procedure. Looking at the temporal functions of the ICs, we find that V_1^{GNSS} and V_1^{GRACE} are both seasonal and agree well with one another ($\rho = 0.692$; Table 1.1; Figure 1.3a), providing strong evidence to conclude that the seasonal signal in Arabia is of hydrological origin. Although establishing the exact hydrological cause(s) of the signal is outside the scope of this study, we expect the hydrological seasonality to be at least partially caused by the inflow of water in the Red Sea (from the Gulf of Aden) in the fall and the subsequent outflow in the spring, both resulting from the Monsoon climate (Smeed, 2004; Wahr et al., 2014).

As for the spatial distributions U_1^{GNSS} and U_1^{GRACE}, there is good agreement in the vertical direction but discrepancies are visible in the horizontal directions. We see two potential reasons for these discrepancies. 1) The GRACE dataset is derived from long-wavelength gravity measurements (> 200 km) whereas GNSS observations are local measurements. Geodetic measurements can thus be affected by local heterogeneities (e.g., in mass, Earth rheology or in surface load due to basins and rivers) that are averaged out in the GRACE dataset. This is especially true for horizontal GNSS measurements which are more sensitive to small-wavelength heterogeneities than vertical measurements. For example, the large amplitude observed at GNSS station HALY (Figure 1.3c) could be due to a nearby body of groundwater with

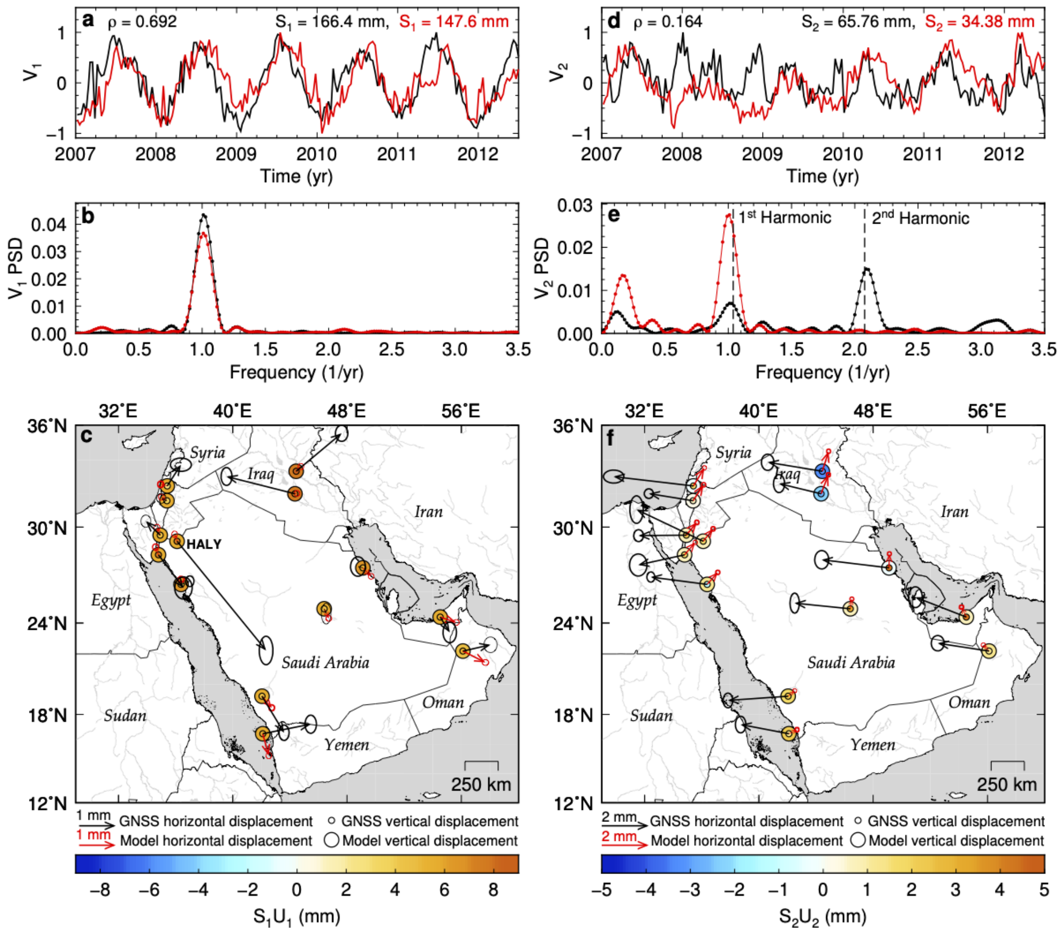

Figure 1.3: ICA results for the Arabian Peninsula case for degrees > 1. (a and d) Time evolutions (V) for IC_1 and IC_2 from the GNSS dataset (black) and the GRACE model (red). The correlation coefficients and S values are reported in each case in the top left and right corners, respectively. (b and e) PSDs associated with the time evolutions in (a) and (d). The 1st and 2nd draconitic harmonics are indicated by the dashed lines. (c and f) Spatial distribution (U) for IC_1 and IC_2. Arrows are the horizontal displacement for the GNSS data (black) and the GRACE model (red). Uncertainty ellipses for the spatial distributions correspond to 1σ confidence intervals. Circles are the vertical displacement for the GNSS data (inner circle) and the GRACE model (outer circle). U has been multiplied by the appropriate S in order to express the spatial distribution in mm. While IC_1^{GNSS} and IC_1^{GRACE} are seasonal and matching, IC_2^{GNSS} and IC_2^{GRACE} are not. IC_2^{GNSS} is instead attributed to draconitic effects.

Table 1.1: Correlation coefficients between the GNSS – GRACE Model IC pairs shown in Figures 1.3, 1.5 1.7-1.10. Note that the combined approach refers to the original analysis performed in Section 1.3. The all-degrees and horizontal/vertical analyses are presented in Sections 1.4.1 and 1.4.2, respectively.

	Degrees > 1		All Degrees	
	IC_1	IC_2	IC_1	IC_2
		Arabian Peninsula		
Combined	0.692	0.164	0.747	0.115
Horizontal	-0.012	- 0.030	0.523	0.208
Vertical	0.623	0.039	0.581	-0.013
		Nepal Himalaya		
Combined	0.823	0.628	0.843	0.528
Horizontal	0.837	0.667	0.699	0.019
Vertical	0.841	0.745	0.847	0.747

high seasonality. 2) The signal extracted from the GNSS dataset is still mixed with other physical effects (e.g., poroelastic and thermoelastic) or potential systematic GNSS processing errors, both not captured by gravimetric measurements. In other words, there might be cross-talk (i.e., leakage of one IC into another) between the ICs. However, given the high correlation between V_1^{GNSS} and V_1^{GRACE}, we argue that cross-talk is negligible in this case.

To investigate the first possibility, in Figure 1.4, we demonstrate how an heterogeneous load distribution, for example, can result in different horizontal Us for datasets of different spatial resolutions. Figure 1.4b shows an heterogeneous load distribution and the resulting deformation at 10 fictive GNSS stations computed using a simple Boussinesq forward model (Boussinesq, 1885). In Figure 1.4a, the same total load is instead averaged out over the entire 400 x 400 km area to simulate the resolution of the GRACE dataset. Calculating the deformation induced at these same 10 stations, we find that the horizontal displacements are different than in (b), even though these two scenarios present the same total load. Discrepancies in displacements are observed in the horizontal direction but the vertical distributions display a similar pattern independent of load heterogeneity. This is consistent with what we observe in real GNSS datasets. Note that discrepancies only arise for the stations inside the loaded area; stations outside the loaded patch feel a similar effective load whether the distribution is averaged out or not.

Modeling these local effects goes beyond the goals of this paper and requires a more refined surface load distribution that can be achieved through integrated models

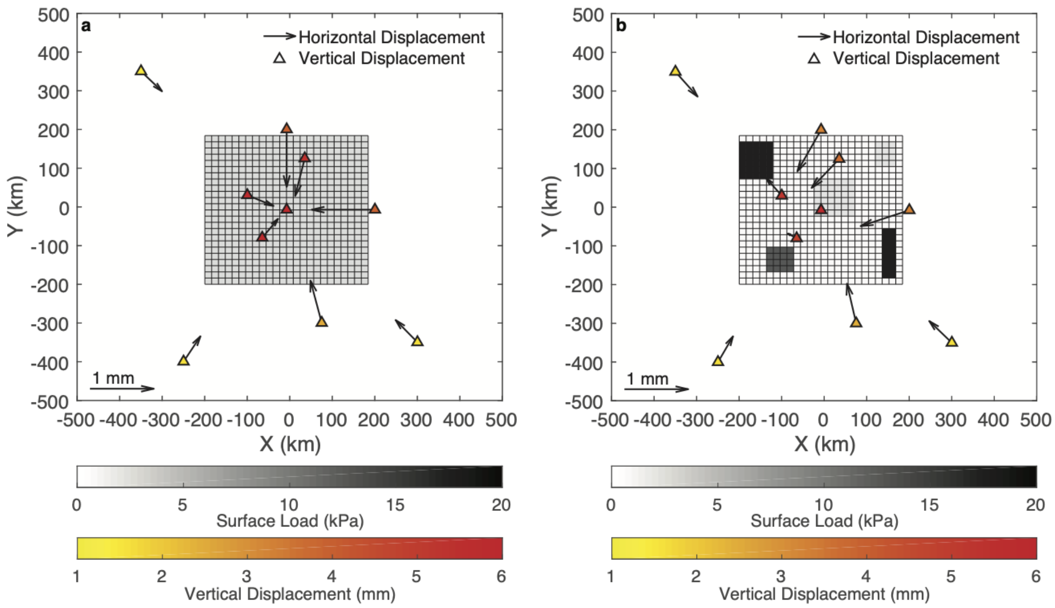

Figure 1.4: Deformation induced by (a) homogeneous and (b) heterogeneous load distribution (grey scale), measured at 10 fictive GNSS stations (triangles). Scenarios (a) and (b) are representative of the spatial resolution of GNSS and GRACE measurements, respectively.

relying on local meteorological data for example. Ultimately, since we use the Us from the GNSS dataset to reconstruct the desired signal from the seasonal Vs, such local effects are inherently modeled by the technique. Thus, our conclusions regarding the origin of the seasonal geodetic signal remain unchanged in light of these diverging Us.

As for the second IC, the correlation between V_2^{GNSS} and V_2^{GRACE} ($\rho = 0.164$; Table 1.1; Figure 1.3d) does not satisfy the criterion in Step 4c). The quasi-perpendicularity of the directions of the horizontal responses of U_2^{GNSS} and U_2^{GRACE} reinforces the idea that the two signals are not related, i.e., $\mathrm{IC}_2^{\mathrm{GNSS}}$ cannot be attributed to surface load variations. Considering the power spectral density (PSD) distribution of the temporal functions in Figure 1.3e, V_2^{GNSS} displays a mix of quasi-annual and quasi-biannual signals, whereas V_2^{GRACE} shows annual and multi-annual signals (Figure 1.3e). Given that the PSD of V_2^{GNSS} peaks around the first and second draconitic harmonics, we instead attribute $\mathrm{IC}_2^{\mathrm{GNSS}}$ to draconitic effects known to affect GNSS measurements (Ray et al., 2008). Draconitic effects are systematic errors in geodetic products most likely due to orbit modeling deficiencies. The resulting signals being spatially correlated, with a spatial correlation a priori

Table 1.2: Mean absolute errors (MAE) between GNSS data and different ICA reconstructions

	Degrees > 1			All Degrees		
	East	North	Vertical	East	North	Vertical
			Arabian Peninsula			
Combined	18.89	12.44	55.80	22.99	16.13	52.98
Horizontal/Vertical	18.28	12.53	54.82	21.01	17.93	53.38
			Nepal Himalaya			
Combined	34.38	31.87	115.70	31.66	34.70	112.99
Horizontal/Vertical	35.66	32.73	115.73	32.76	35.49	113.93

distinct from the loading processes, we expect vbICA to be able to discriminate them from true deformation signals. Figure A.2 shows that V_2^{GNSS} can indeed be explained by a sum of sinuisoids with periods corresponding to the first 6 draconitic harmonics (351.6, 175.8, 87.9, 44.0, 22.0, and 11.0 days). Mean absolute errors (MAE) between the GNSS dataset and the ICA time series reconstructed with the seasonal $\mathrm{IC}_1^{\mathrm{GNSS}}$ and the draconitic $\mathrm{IC}_2^{\mathrm{GNSS}}$ are listed in Table 1.2. MAE values are considerably higher in the vertical because the signal is stronger in this direction.

1.3.2 Nepal Himalaya

The Nepal Himalaya represents a more intricate case due to its more complex hydrological loading pattern. The procedure once again prescribes a two components ICA as presented in Figure 1.5. In this case, the temporal functions from both datasets are all seasonal and the correlation coefficients are highest for the pairs V_1^{GNSS} - V_1^{GRACE} (ρ = 0.825; Table 1.1; Figure 1.5a) and V_2^{GNSS} - V_2^{GRACE} (ρ = 0.628; Table 1.1; Figure 1.5d). We thus argue that both $\mathrm{IC}_1^{\mathrm{GNSS}}$ and $\mathrm{IC}_2^{\mathrm{GNSS}}$ should be related to hydrological processes. The vertical patterns of U_1^{GNSS} and U_1^{GRACE} are in good agreement, while the horizontal distribution of U_1^{GNSS} is again quite heterogeneous compared to U_1^{GRACE}. Considering U_2^{GNSS} and U_2^{GRACE}, we notice a substantial improvement and degradation in the agreement of the horizontal and vertical patterns, respectively. In light of these observations, it is useful to consider the nature of the load by considering the gravimetric data presented in Section 1.2.1.2. Movie A.1 in the appendix shows a migration of the load distribution over time, from south-east to central Asia. This trend corresponds to the Indian Monsoon regime which causes heavy precipitations during the summer months (Bettinelli et al., 2008). This load pattern cannot be considered stationary as the Monsoon first hits the eastern Himalaya and gradually sweeps westwards over the whole arc during the summer.

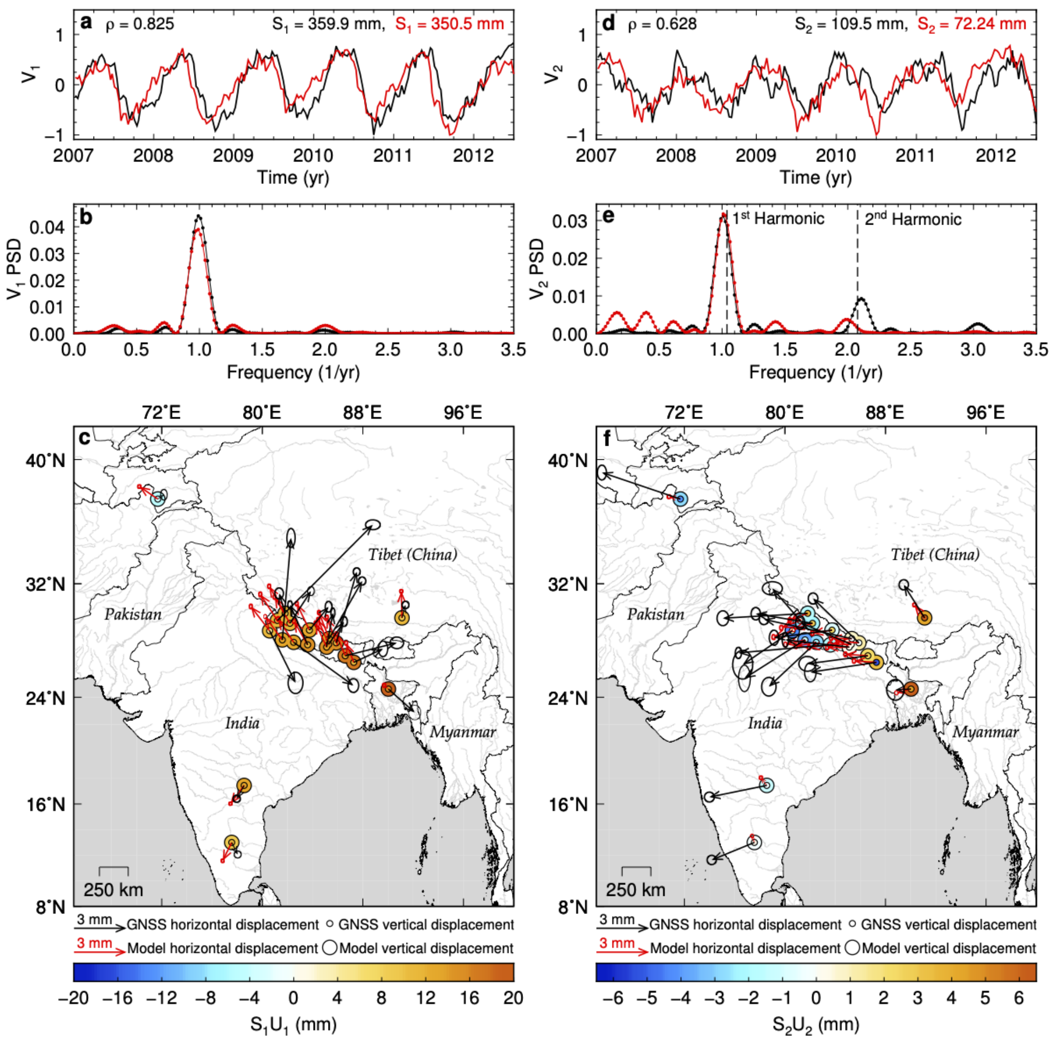

Figure 1.5: Same as Figure 1.3 but for the Himalayan case. In this case, both pairs of ICs are seasonal and matching.

This process results in a westward moving source of load. Since vbICA assumes non-moving sources (Section 1.2.2), multiple components are necessary to fully recover the effects of the propagating Monsoon load. For the special case of a source moving at a constant speed in a constant direction, we find that two components are sufficient to explain the observations and that these two components must be derivatives of one another.

Section A.1 in Appendix A presents an analytical proof of these results valid for simple harmonic loads and the Boussinesq forward model in Figure 1.6 demonstrates that these findings might hold for a broader category of deformation fields (i.e., the temporal functions do not need to be simple sinusoids and the temporal mixing

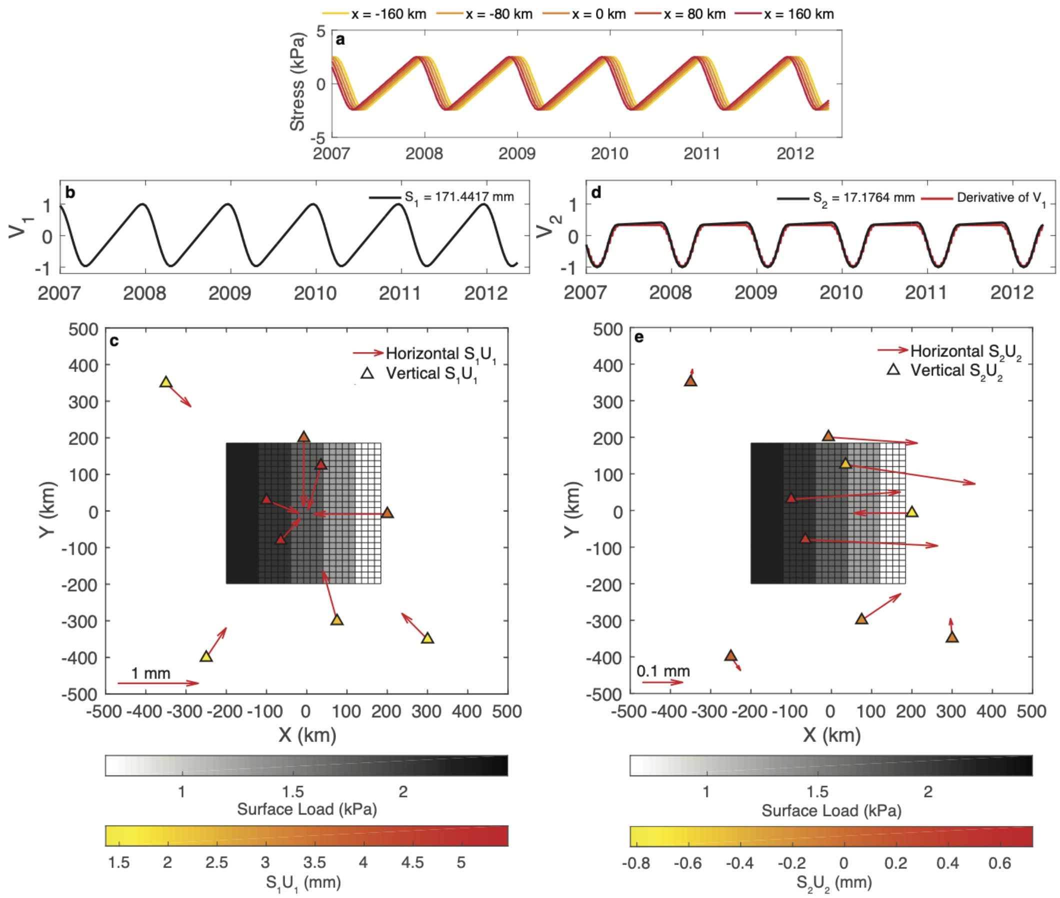

Figure 1.6: 2-component vbICA decomposition of a load pattern moving to the right at a constant velocity with a non-symmetric temporal function. (a) Temporal load evolution at different point along the loaded patch. (b and d) Temporal functions corresponding to IC_1 and IC_2. The red curve in (d) corresponds to the derivative of IC_1. (c and e) Load distribution (in shades of grey) and vbICA spatial distribution (in yellow to red colors).

factors need not be harmonic). In Figure 1.6, we first compute the deformation induced by a load propagating to the right with the temporal function shown in Figure 1.6a. After performing a vbICA on the resulting deformation field, we find that 2 components are indeed sufficient to explain all of the data variance and that the second component is the derivative of the first component as indicated by the excellent fit between the black and red lines in Figure 1.6d. Moreover, IC_1 is associated with the loading pattern itself whereas IC_2 is related to the motion of the loading pattern, which is consistent with what we observe in the Nepal Himalaya. Since in the Himalaya we indeed find that V_2^{GNSS} approximates the derivative of V_1^{GNSS} (Figure A.3), we conclude that the two ICs are likely expressing the moving nature of the Monsoonal load. The fact that the horizontal patterns of U_2^{GNSS} and U_2^{GRACE} both point in the direction of load migration further supports this conclusion. Discrepancies in amplitudes between the two datasets (e.g., $S_2^{\mathrm{GNSS}} > S_2^{\mathrm{GRACE}}$) could be due to thermal, poroelastic and atmospheric effects not captured by the GRACE satellites (Dong et al., 2002).

As for the draconitic effect in the Nepal Himalaya, there is a quasi-biannual signal present in V_2^{GNSS} which approximately corresponds to the 2nd draconitic harmonic, meaning that the draconitic effect might have infiltrated $\mathrm{IC}_2^{\mathrm{GNSS}}$. A decomposition with three ICs (Figure A.4) still shows the same features for the first two ICs but V_3^{GNSS} and V_3^{GRACE} do not display an acceptable correlation ($\rho = 0.346$; Figure A.4g), indicating that $\mathrm{IC}_3^{\mathrm{GNSS}}$ is likely not related to surface loading. An analysis of the associated PSD (Figure A.4h) reveals that V_3^{GNSS} peaks around the 2nd draconitic harmonic but not around the 1st. Given that S_2^{GNSS} is considerably higher than S_2^{GRACE}, it is possible that part of the annual signal in $\mathrm{IC}_2^{\mathrm{GNSS}}$ is due to 1st harmonic draconitic effects. Draconitic errors usually exhibit a long-wavelength spatial pattern. Thus, one reason why the first draconitic harmonic signal may be absorbed into the annual component in the Himalaya but not in Arabia is because the hydrological signal is of longer wavelength in the Himalaya. Moreover, looking at the sum of sinusoids fit of V_2^{GNSS} in Figure A.5, we see that, in addition to the annual and biannual periods, the first 2 draconitic harmonics play the most important role in reconstructing the signal. V_3^{GNSS} in Figure A.6, on the other hand, can be mostly explained by the first 2 draconitic harmonics alone. We conclude that $\mathrm{IC}_3^{\mathrm{GNSS}}$ is probably mostly draconitic and that there might be some leakage of $\mathrm{IC}_3^{\mathrm{GNSS}}$ into $\mathrm{IC}_2^{\mathrm{GNSS}}$. MAE values from the ICA reconstruction with $\mathrm{IC}_1^{\mathrm{GNSS}}$ and $\mathrm{IC}_2^{\mathrm{GNSS}}$ are presented in Table 1.2.

1.4 Variations to the General Procedure

1.4.1 Inclusion of the degree-1 contribution

Although we have previously removed the degree-1 contribution from the GNSS time series for comparison purposes, the degree-1 spherical harmonic deformation is important to consider since a significant portion of it is due to redistributions in very long wavelength hydrological mass. Identifying the origin of the degree-1 deformation field as recorded by GNSS stations has large implication for reference frame definitions. If the extracted seasonal signal is meant for hydrological studies, it would be preferable to perform the analysis directly on the original GNSS time series (i.e., not corrected for degree-1) and on the GRACE-derived time series to

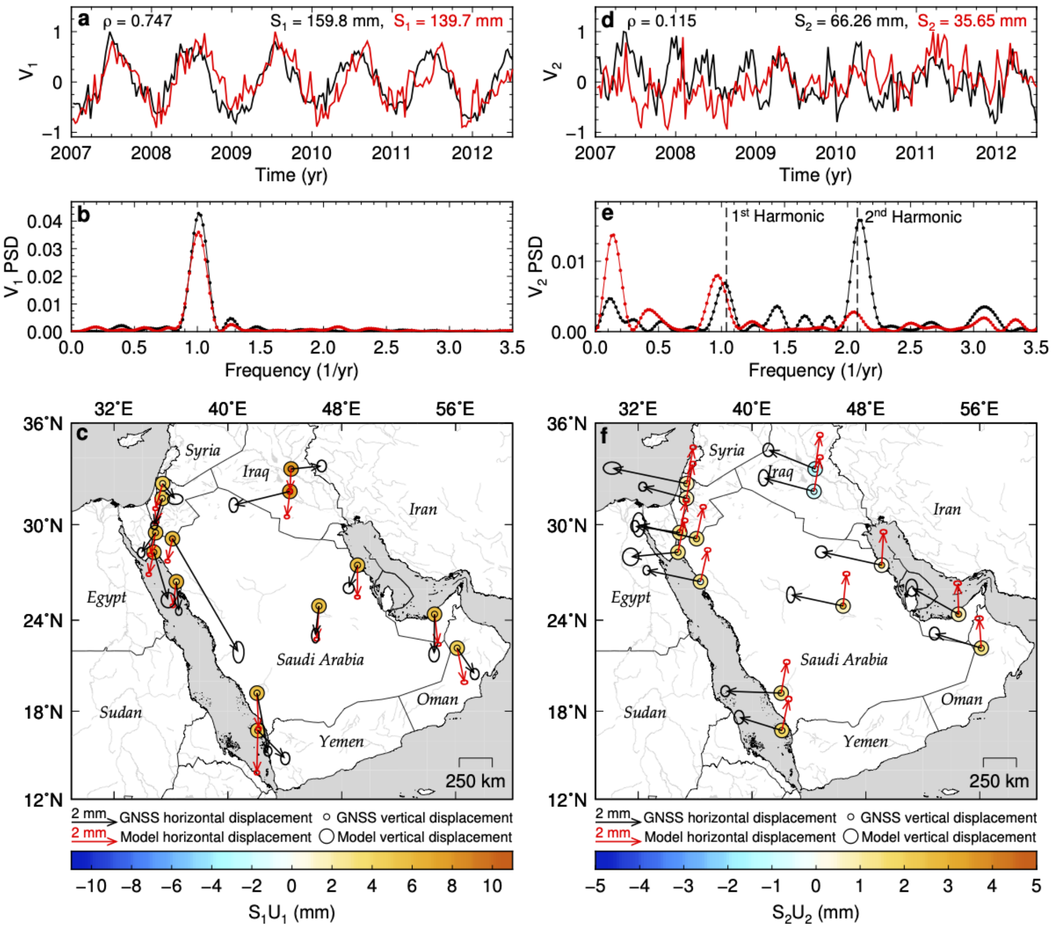

Figure 1.7: Same as Figure 1.3 but for the all-degrees case.

which the degree-1 contribution has been added as described in Chanard et al. (2018b). The results from such analyses are presented in Figures 1.7 and 1.8 (and A.7) and the correlation coefficients and MAEs in Tables 1 and 2, respectively.

Unsurprisingly, the correlation coefficients for the IC_1's are larger for the all-degrees case than the degrees > 1 analysis for both the Arabian Peninsula and the Nepal Himalaya. This is to be expected since a portion of the vbICA input, namely the degree-1 contribution, is correlated in both datasets. The spatial correlations between the matching U^{GNSS} and U^{GRACE} are also better, especially in the Arabian Peninsula where the degree-1 contribution is a comparatively more important part of the seasonal signal. Although the correlation between U_2^{GNSS} and U_2^{GRACE} in the Himalaya is noticeably improved for the all-degrees case, the correlation coefficient between V_2^{GNSS} and V_2^{GRACE} is actually smaller in that case. We hypothesize that this may be due to the relative stationarity of the degree-1 deformation field compared

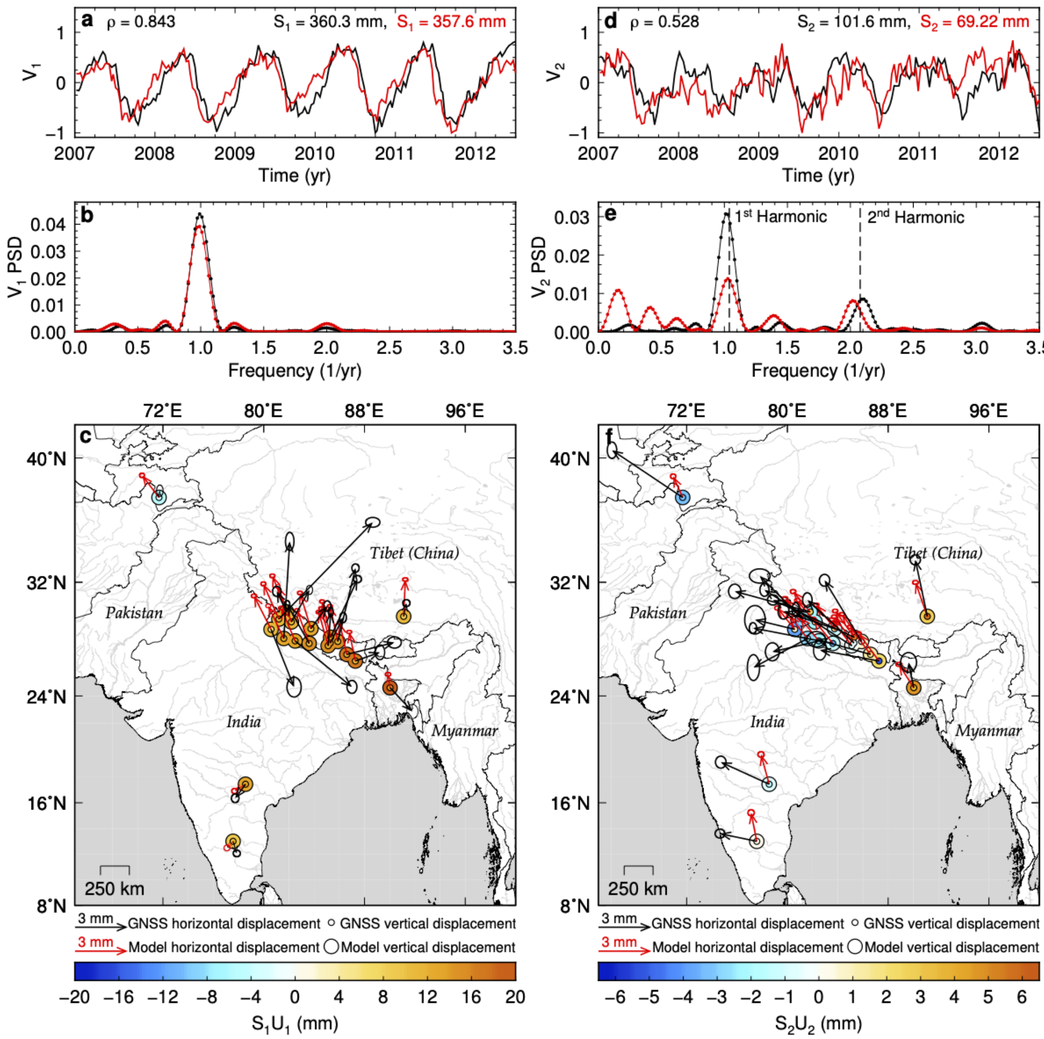

Figure 1.8: Same as Figure 1.5 but for the all-degrees case. See Figure A.7 in Appendix A for a close-up view on Nepal.

to that of higher degrees, diminishing the importance of the propagation signal and thus making it harder to resolve by the vbICA. Nonetheless, given that the correlation coefficient is above the threshold of 0.50 and V_2^{GNSS} and V_2^{GRACE} are visibly matching, we still conclude that $\mathrm{IC}_1^{\mathrm{GNSS}}$ and $\mathrm{IC}_2^{\mathrm{GNSS}}$ for the Himalaya are most likely of hydrological origin.

Since we reach the same conclusions whether we apply the procedure to the datasets with or without the degree-1 contribution, we recommend doing the analysis without correcting the GNSS time series for the degree-1 deformation. This way, the resulting ICA reconstruction will not depend on the choice of degree-1 field and will be readily useable for hydrological studies. Going through the procedure without the degree-1 contribution was still necessary, however, to demonstrate that the correlation between the IC^{GNSS} and IC^{GRACE} is not solely due to the GNSS-derived degree-1 contribution added to the GRACE dataset. For reference, Figures A.2, A.3 and A.5 are also presented for the all-degrees analysis to show that the discussion from Section 1.3 still holds in this case.

1.4.2 Analysis on the vertical and horizontal time series separately

Up to this point, we have applied the procedure to the vertical and horizontal time series simultaneously without questioning the validity of this combined approach. The intuitive reasoning behind this approach is that the vertical and horizontal deformation fields should have the same source. To evaluate the validity of our combined approach, we compare our results so far to that obtained through vbICAs performed separately on the vertical and horizontal time series (with degree-1) (Figures 1.9 and 1.10). In both Arabia and Himalaya, we find that IC_1^{GNSS} and IC_1^{GRACE} from the vertical decomposition are quite similar to those from the combined analysis. This is expected because vertical seasonal deformation is the dominant signal in these time series. For the horizontal analysis in Arabia, the decomposition does not seem to be separating the seasonal loading from the draconitic effect in the GNSS dataset, thus resulting in a lower correlation coefficient between V_1^{GNSS} and V_1^{GRACE}. The horizontal decomposition also does not perform as well in Nepal as V_2^{GRACE} does not match V_2^{GNSS}, possibly because the horizontal direction is largely affected by localized loads in the mid/high range (e.g., rivers) that GRACE averages out. This effect is smoothed out in the combined approach because the vertical direction is much less affected by small scale loads and therefore consistent with GRACE.

In terms of MAEs (Table 1.2), in the Himalaya, all values are smaller for the combined analyses than for the horizontal/vertical analyses. In the Arabian Peninsula, only about half the values are smaller for the combined analyses. However, looking at the sample GNSS time series and vbICA reconstructions from a combined and a vertical/horizontal analysis in Figure A.8, the fit to the east and north directions is visually better for the combined case. This is because the separated analysis does a poor job at capturing the weak but still existent seasonal signal in the east and north time series. We hypothesize that this is because the signal is too weak to be captured by the vbICA in the horizontal time series alone. Thus, unless the approach in which the horizontals and verticals are separated is improved, we advocate for the combined approach.

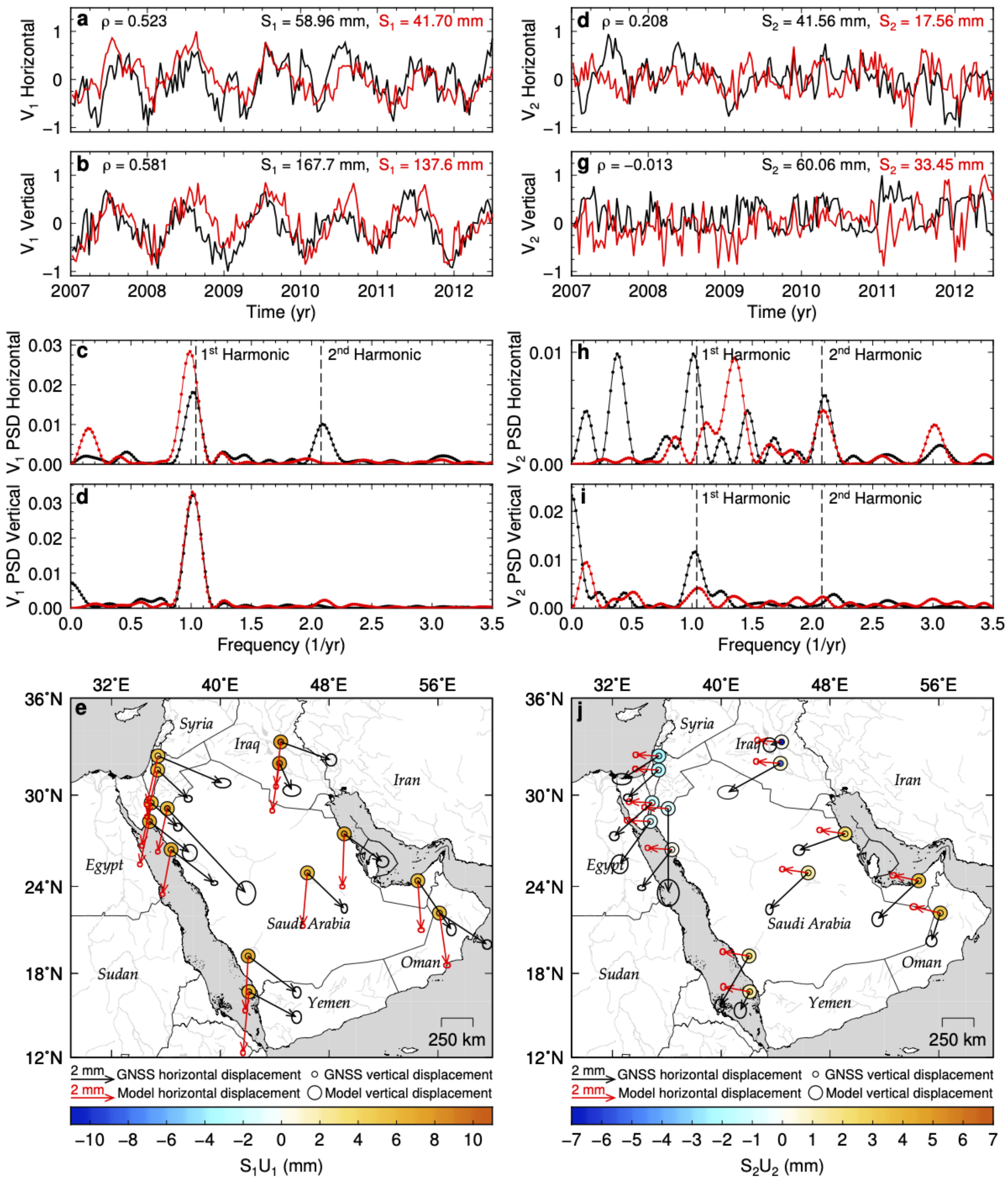

Figure 1.9: Same as Figure 1.3 but for the vertical/horizontal, all-degrees analysis.

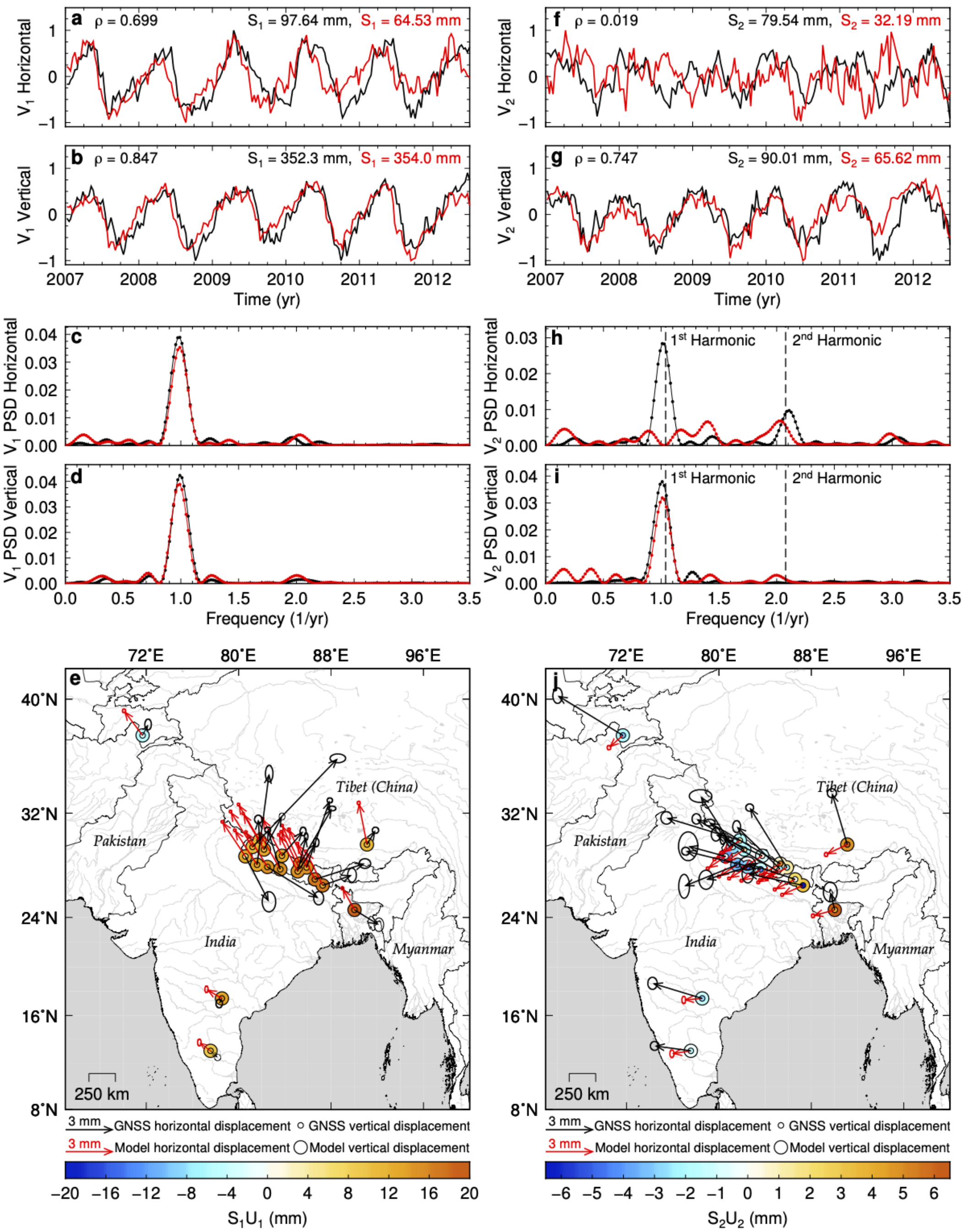

Figure 1.10: Same as Figure 1.5 but for the vertical/horizontal, all-degrees analysis.

1.5 Discussions and Conclusions

We have shown that supplementing a GRACE-based deformation model with a vbICA provides an efficient and accurate means of isolating surface load contributions from geodetic time series. We used the fact that GNSS and GRACE-derived displacements yield consistent time functions in both the Arabian Peninsula and the Nepal Himalaya to validate the origin of the ICs$^{\text{GNSS}}$s related to continental water mass variations. Specifically, we recommend following the proposed procedure presented in Section 1.2.3 with the vbICA performed simultaneously on the horizontal and vertical time series including the degree-1 deformation field (as presented in Figures 1.7 and 1.8) since, of the different analyses presented in this work, it is the simplest and most robust approach to recover the complete surface load variation signal from the GNSS time series.

To correct the GNSS dataset for these seasonal effects, we suggest to directly subtract the matched ICs$^{\text{GNSS}}$ from the geodetic time series as opposed to subtracting the associated ICs$^{\text{GRACE}}$. We argue that this approach is more accurate in filtering out the non-tectonic seasonal signals than the latter as GNSS stations are sensitive to local effects that are smoothed out by the GRACE data acquisition and processing. Figures A.1 show examples of ICA reconstructions and corrected GNSS time series using this approach. MAE values are also presented in map format in Figures A.9 and A.10. Moreover, once an IC$^{\text{GNSS}}$ in a given region has been identified as being caused by surface load variations by comparison with the GRACE-derived dataset over a sufficiently long timespan, redoing the comparison would not be strictly necessary if a similar IC$^{\text{GNSS}}$ is obtained from a vbICA in the same region but over a longer time span. In other words, the method could still be useful for epochs with missing GRACE data.

Although both study areas display a single hydrological seasonal source, we retain two ICs to correct the GNSS time series to account for (1) draconitic errors in the case of Arabia and (2) the migratory behavior of the load in Nepal. In the latter case, a third IC is related to the GNSS draconitic error, here considered as noise. Since the SNR between the hydrological signal and the draconitic error is larger in Nepal than Arabia, it is reasonable to expect this noise to appear in higher components, although not strictly necessary to reproduce the observations to first order as seen in Figure 1.2c. Nonetheless, the fact that vbICA is able to discriminate at least part of the draconitic error from the hydrological signal for the low SNR scenario is a major strength of the proposed procedure. Moreover, we recognize that the decision to retain only two components for the decompositions is influenced by our choice of a priori hyper-parameters in the vbICA. Even if ICA is not meant to decompose the dataset in terms of variance maximization, an alternative approach could be to select the number of components by setting a minimum threshold on the amount of variance explained. In either case, selecting the number of components remains a case-dependent decision in which expert judgment still plays an important role.

The two complementary examples shown in this work demonstrate that the procedure is robust to complexities associated with spatial heterogeneities (e.g., local mass anomaly, poro- and thermoelastic deformation and regional deviation from PREM) and simple moving loads. The technique can also help to isolate systematic errors in geodetic products, especially in low SNR ratio scenarios as is the case in Arabia. In a tectonically active region like Nepal, the technique can be used to investigate the link between seasonal loading and seismic activity.

It should be noted that although the technique aims to identify components that share the same physical mechanism across the two datasets, what the procedure is actually doing is identifying GNSS components that follow the same temporal pattern as surface load variations measured with GRACE. If there happened to be a source of deformation different but in phase with the GRACE components, then the seasonal signal extracted from the GNSS data might not be entirely caused by surface loading. A prime candidate for this is thermoelastic deformation of solid Earth (Ben-Zion and Leary, 1986; Fang et al., 2014; Tsai, 2011) and or eventually of the GNSS monuments (Yan et al., 2009). Since, in the two study areas presented here, the temporal pattern and the amplitude of the GNSS seasonal signal agree fairly well with the prediction made from GRACE, we are confident that thermoelastic deformation is not a dominant effect in these regions. It could however be more significant in other regions, and the geodetic signal could then represent the combined effect of surface load and surface temperature variations if both signals were in phase.

Now that this methodology has been benchmarked for seasonal signals, a similar technique could be developed to capture multiannual hydrological trends which could provide new insights into Earth's rheology (Chanard et al., 2018a). When additional ICs are included in the analysis, the technique can also be used to compare them with non-hydrological sources of known temporal behavior to help validate their physical causes. In fact, any dataset with a spatio-temporal structure can be analyzed with the vbICA algorithm, making the approach suitable for the study of other geophysical problems. For example, a similar procedure could be applied to seismological data to study the effects of hydrology on seismic velocities. The kind of techniques describe in this study will also be particularly useful in exploiting the upcoming dataset from the GRACE Follow-On mission which will benefit from better procedures to relate surface hydrology and transient geodetic strain.

Bibliography

D. Argus, Y. Fu, and F. Landerer. Seasonal variation in total water storage in California inferred from GPS observations of vertical land motion. *Geophysical Research Letters*, 41(6):1971–1980, 2014. doi: 10.1002/2014GL059570. URL `https://doi.org/10.1002/2014GL059570`.

C. Bassin, G. Laske, and G. Masters. The current limits of resolution for surface wave tomography in North America. *Eos Transactions American Geophysical Union*, 81:897, 2000.

Y. Ben-Zion and P. Leary. Thermoelastic strain in a half-space covered by unconsolidated material. *Bulletin of the Seismological Society of America*, 76:1447–1460, 1986.

P. Bettinelli, J. Avouac, M. Flouzat, L. Bollinger, G. Ramillien, S. Rajaure, and S. Sapkota. Seasonal variations of seismicity and geodetic strain in the Himalaya induced by surface hydrology. *Earth and Planetary Science Letters*, 266:332–344, 2008. doi: 10.1016/j.epsl.2007.11.021. URL `https://doi.org/10.1016/j.epsl.2007.11.021`.

G. Blewitt, D. Lavallée, P. Clarke, and K. Nurutdinov. A new global mode of Earth deformation: Seasonal cycle detected. *Science*, 294:2342–2345, 2001. doi: 10.1126/science.1065328. URL `https://doi.org/10.1126/science.1065328`.

G. Blewitt, W. Hammond, and C. Kreemer. Harnessing the GPS data explosion for interdisciplinary science. *Eos*, 99, 2018. doi: 10.1029/2018EO104623. URL `https://doi.org/10.1029/2018EO104623`.

L. Bollinger, F. Perrier, J. Avouac, S. Sapkota, U. Gautam, and D. Tiwari. Seasonal modulation of seismicity in the Himalaya of Nepal. *Geophysical Research Letters*, 34:08304, 2007. doi: 10.1029/2006GL029192. URL `https://doi.org/10.1029/2006GL029192`.

A. Borsa, D. Agnew, and D. Cayan. Ongoing drought-induced uplift in the western United States. *Science*, 345:1587–1590, 2014. doi: 10.1126/science.1260279. URL `https://doi.org/10.1126/science.1260279`.

J. Boussinesq. *Application des potentiels à l'étude de l'équilibre et du mouvement des solides élastiques*. Blanchard, Paris, reprint edition, 1885.

S. Bruinsma, J.-M. Lemoine, R. Biancale, and N. Valès. Cnes/grgs 10-day gravity field models (release 2) and their evaluation. *Advances in Space Research*, 4(45): 587–601, 2010. doi: 10.1016/j.asr.2009.10.012. URL `https://doi.org/10.1016/j.asr.2009.10.012`.

J.-F. Cardoso and A. Souloumiac. Blind beamforming for non-gaussian signals. In *IEE Proceedings F (Radar and Signal Processing)*, volume 140, pages 362–370. IET, 1993.

L. Carrère and F. Lyard. Modeling the barotropic response of the global ocean to atmospheric wind and pressure forcing - comparisons with observations. *Geophysical Research Letters*, 30(6):1275, 2003. doi: 10.1029/2002GL016473. URL `https://doi.org/10.1029/2002GL016473`.

K. Chan, T.-W. Lee, and T. J. Sejnowski. Variational Bayesian learning of ICA with missing data. *Neural Computation*, 15(8):1991–2011, 2003.

K. Chanard, J. Avouac, G. Ramillien, and J. Genrich. Modeling deformation induced by seasonal variations of continental water in the Himalaya region: Sensitivity to Earth elastic structure. *Journal of Geophysical Research-Solid Earth*, 119: 5097–5113, 2014. doi: 10.1002/2013jb010451. URL `https://doi.org/10.1002/2013jb010451`.

K. Chanard, L. Fleitout, E. Calais, S. Barbot, and J.-P. Avouac. Constraints on transient viscoelastic rheology of the asthenosphere from seasonal deformation. *Geophysical Research Letters*, 45:2328–2338, 2018a. doi: 10.1002/2017GL076451. URL `https://doi.org/10.1002/2017GL076451`.

K. Chanard, L. Fleitout, E. Calais, P. Rebischung, and J.-P. Avouac. Toward a global horizontal and vertical elastic load deformation model derived from GRACE and GNSS station position time series. *Journal of Geophysical Research: Solid Earth*, 123:3225–3237, 2018b. doi: 10.1002/2017JB015245. URL `https://doi.org/10.1002/2017JB015245`.

P. Comon. Independent component analysis, a new concept? *Signal Processing*, 36:287–314, 1994. doi: 10.1016/0165-1684(94)90029-9. URL `https://doi.org/10.1016/0165-1684(94)90029-9`.

T. Craig, K. Chanard, and E. Calais. Hydrologically-driven crustal stresses and seismicity in the New Madrid seismic zone. *Nature Communications*, 8(1):2143, 2017. doi: 10.1038/s41467-017-01696-w. URL `https://doi.org/10.1038/s41467-017-01696-w`.

J. Davis, P. Elósegui, J. Mitrovica, and M. Tamisiea. Climate-driven deformation of the solid Earth from GRACE and GPS. *Geophysical Research Letters*, 31 (24):24605, 2004. doi: 10.1029/2004GL021435. URL `https://doi.org/10.1029/2004GL021435`.

D. Dong, P. Fang, Y. Bock, M. Cheng, and S. Miyazaki. Anatomy of apparent seasonal variations from GPS-derived site position time series. *Journal of Geophysical Research-Solid Earth*, 107(B4), 2002. doi: 10.1029/2001JB000573. URL `https://doi.org/10.1029/2001JB000573`.

D. Dong, T. Yunck, and M. Heflin. Origin of the international terrestrial reference frame. *Journal of Geophysical Research: Solid Earth*, 108(B4), 2003. doi: 10.1029/2002JB002035. URL `https://doi.org/10.1029/2002JB002035`.

V. Drouin, K. Heki, F. Sigmundsson, S. Hreinsdóttir, and B. Ófeigsson. Constraints on seasonal load variations and regional rigidity from continuous GPS measurements in Iceland, 1997–2014. *Geophysical Journal International*, 205 (3):1843–1858, 2016. doi: 10.1093/gji/ggw122. URL `https://doi.org/10.1093/gji/ggw122`.

A. Dziewonski and D. Anderson. Preliminary reference Earth model. *Physics of the Earth and Planetary Interiors*, 25:297–356, 1981. doi: 10.1016/0031-9201(81)90046-7. URL `https://doi.org/10.1016/0031-9201(81)90046-7`.

M. Fang, D. Dong, and B. Hager. Displacements due to surface temperature variation on a uniform elastic sphere with its centre of mass stationary. *Geophysical Journal International*, 196:194–203, 2014. doi: 10.1093/gji/ggt335. URL `https://doi.org/10.1093/gji/ggt335`.

W. Farrell. Deformation of the Earth by surface loads. *Reviews of Geophysics and Space Physics*, 10:761–797, 1972. doi: 10.1029/RG010i003p00761. URL `https://doi.org/10.1029/RG010i003p00761`.

Y. Fu and J. Freymueller. Seasonal and long-term vertical deformation in the Nepal Himalaya constrained by GPS and GRACE measurements. *Journal of Geophysical Research-Solid Earth*, 117:03407, 2012. doi: 10.1029/2011jb008925. URL `https://doi.org/10.1029/2011jb008925`.

Y. Fu, J. Freymueller, and T. Jensen. Seasonal hydrological loading in southern Alaska observed by GPS and GRACE. *Geophysical Research Letters*, 39(15): 15310, 2012. doi: 10.1029/2012GL052453. URL `https://doi.org/10.1029/2012GL052453`.

Y. Fu, D. Argus, and F. Landerer. GPS as an independent measurement to estimate terrestrial water storage variations in Washington and Oregon. *Journal of Geophysical Research-Solid Earth*, 120:552–566, 2015. doi: 10.1002/2014jb011415. URL `https://doi.org/10.1002/2014jb011415`.

A. Gualandi, E. Serpelloni, and M. Belardinelli. Blind source separation problem in GPS time series. *Journal of Geodesy*, 90:323–341, 2016. doi: 10.1007/s00190-015-0875-4. URL `https://doi.org/10.1007/s00190-015-0875-4`.

A. Gualandi, J. Avouac, J. Galetzka, J. Genrich, G. Blewitt, and L. Adhikari. Pre- and post-seismic deformation related to the 2015, M(w)7.8 Gorkha earthquake. *Nepal. Tectonophysics*, 714:90–106, 2017a. doi: 10.1016/j.tecto.2016.06.014. URL `https://doi.org/10.1016/j.tecto.2016.06.014`.

A. Gualandi, C. Nichele, E. Serpelloni, L. Chiaraluce, L. Anderlini, and D. Latorre. Aseismic deformation associated with an earthquake swarm in the northern Apennines (Italy). *Geophysical Research Letters*, 44:7706–7714, 2017b. doi: 10.1002/2017gl073687. URL `https://doi.org/10.1002/2017gl073687`.

A. Hyvärinen and E. Oja. A fast fixed-point algorithm for independent component analysis. *Neural Computation*, 9(7):1483–1492, 1997.

J. Jean, U. Meyer, and A. Jäggi. Combination of monthly gravity field solutions from different processing centers. In *EGU General Assembly*, volume 17, page 5879. Vienna, Austria, 2015.

C. Johnson, Y. Fu, and R. Burgmann. Seasonal water storage, stress modulation, and California seismicity. *Science*, 356(6343):1161–1164, 2017. doi: 10.1126/science.aak9547. URL `https://doi.org/10.1126/science.aak9547`.

G. Ramillien, F. Frappart, A. Cazenave, and A. Guntner. Time variations of land water storage from an inversion of 2 years of GRACE geoids. *Earth and Planetary Science Letters*, 235:283–301, 2005. doi: 10.1016/j.epsl.2005.04.005. URL `https://doi.org/10.1016/j.epsl.2005.04.005`.

J. Ray, Z. Altamimi, X. Collilieux, and T. Dam. Anomalous harmonics in the spectra of GPS position estimates. *GPS Solutions*, 12(1):55–64, 2008. doi: 10.1007/s10291-007-0067-7. URL `https://doi.org/10.1007/s10291-007-0067-7`.

E. Serpelloni, F. Pintori, A. Gualandi, E. Scoccimarro, A. Cavaliere, and L. Anderlini. Hydrologically-induced karst deformation: insights from GPS measurements in the Adria-Eurasia plate boundary zone. *Journal of Geophysical Research: Solid Earth*, 123:4413–4430, 2018. doi: 10.1002/2017JB015252. URL `https://doi.org/10.1002/2017JB015252`.

D. Smeed. Exchange through the Bab el Mandab. Deep sea research, Part II. *Topical Studies in Oceanography*, 51(4):455–474, 2004. doi: 10.1016/j.dsr2.2003.11.002. URL `https://doi.org/10.1016/j.dsr2.2003.11.002`.

S. Swenson, D. Chambers, and J. Wahr. Estimating geocenter variations from a combination of GRACE and ocean model output. *Journal of Geophysical Research: Solid Earth*, 113:08410, 2008. doi: 10.1029/2007JB005338. URL `https://doi.org/10.1029/2007JB005338`.

V. Tsai. A model for seasonal changes in GPS positions and seismic wave speeds due to thermoelastic and hydrologic variations. *Journal of Geophysical Research-Solid Earth*, 116, 2011. doi: 10.1029/2010jb008156. URL `https://doi.org/B04404`.

T. van Dam, J. Wahr, P. Milly, A. Shmakin, G. Blewitt, D. Lavallee, and K. Larson. Crustal displacements due to continental water loading. *Geophysical Research Letters*, 28:651–654, 2001. doi: 10.1029/2000GL012120. URL `https://doi.org/10.1029/2000GL012120`.

J. Wahr, A. S. D., E. Leuliette, and S. Swenson. Seasonal variability of the Red Sea, from satellite gravity, radar altimetry, and in situ observations. *Journal of Geophysical Research: Oceans*, 119(8):5091–5104, 2014. doi: 10.1002/2014JC010161. URL `https://doi.org/10.1002/2014JC010161`.

H. Yan, W. Chen, Y. Zhu, W. Zhang, and M. Zhong. Contributions of thermal expansion of monuments and nearby bedrock to observed GPS height changes. *Geophysical Research Letters*, 36(13), 2009. doi: 10.1029/2009GL038152. URL `https://doi.org/10.1029/2009GL038152`.

Chapter 2

UNDERSTANDING THE GEODETIC SIGNATURE OF LARGE AQUIFER SYSTEMS: EXAMPLE OF THE OZARK PLATEAUS IN CENTRAL UNITED STATES

Published as:

S. Larochelle, K. Chanard, L. Fleitout, J. Fortin, A.Gualandi, L. Longuevergne, P. Rebischung, S. Violette, and J.-P. Avouac. Understanding the geodetic signature of large aquifer systems: Example of the Ozark Plateaus in central United States. *Journal of Geophysical Research: Solid Earth*, 127(3), 2022. doi: 10.1029/2021jb023097.

2.1 Introduction

Hydrological processes occurring at the surface of the Earth redistribute continental water mass and the resulting load variations deform the solid Earth. The primarily seasonal deformation can be measured with space-based geodetic techniques such as GNSS (Global Navigation Satellite System) (Blewitt et al., 2001; van Dam et al., 2001; Dong et al., 2002). It is thus possible to infer fluctuations in continental water storage from GNSS time series (Ouellette et al., 2013; Argus et al., 2014, 2017; Borsa et al., 2014; Fu et al., 2015; Adusumilli et al., 2019; Ferreira et al., 2019) assuming that the regional deformation field induced by hydrology can be separated from other geodetic signals and/or systematic errors (Chanard et al., 2020). Such regional-scale constraints on hydrological fluctuations help bridge the gap between *in situ* measurements (e.g., groundwater monitoring wells, stream gauges) and continental-scale observations from the Gravity Recovery and Climate Experiment (GRACE) mission (Tapley et al., 2004).

At a global scale, seasonal signals in GNSS time series are not entirely explained by GRACE-measured hydrological loading (Chanard et al., 2018). Additional deformation mechanisms related to groundwater and temperature variations are thought to explain a significant fraction of this seasonal variance (Tsai, 2011). In particular, aquifer basins — which store roughly 30% of Earth's freshwater reserves (Shiklomanov, 1993) — are prone to poroelastic swelling in addition to hydrological loading (Wang, 2000). An increase in surface and groundwater mass (Figure 2.1A) translates to an increase of load which leads to subsidence and horizontal displace-

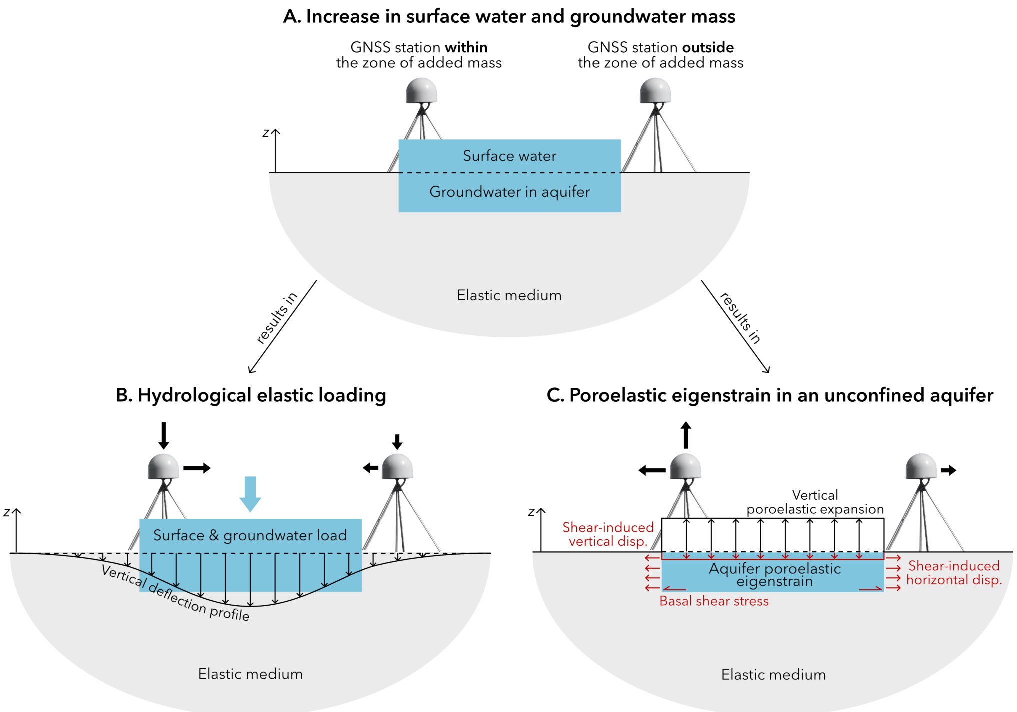

Figure 2.1: Deformation due to hydrological elastic loading vs poroelastic eigenstrain. (A) Schematic representation of an increase in surface and groundwater mass in the vicinity of GNSS stations. (B) The added mass, whether at the surface or in the ground, causes subsidence and horizontal motion towards the added load. The surface vertical displacement expected from a circular load on an elastic half-space is shown in black. (C) At the same time, groundwater recharge increases pore water pressure within the aquifer, leading to upward vertical and outward horizontal displacements. While most of the vertical deformation comes from poroelastic expansion (black), horizontal and vertical displacements also result from basal shear stresses (red).

ments towards the added load (Boussinesq, 1885; Verruijt, 2009) (Figure 2.1B). At the same time, the increase in groundwater storage rises pore pressure levels and generates eigenstrains within the aquifer and hence induces uplift and radially outward surface displacements (King et al., 2007; Galloway and Burbey, 2011) (Figure 2.1C).

Separating the contributions of hydrological loading and poroelasticity in geodetic time series is crucial to better understand the physics of either deformation processes and quantify fluctuations in total water storage. Extracting the poroelastic deformation field has direct implications for inferring, at the field scale, the hydromechanical properties of aquifer systems which are tightly linked to hydrodynamical properties.

Indeed, surface deformation provides information about internal aquifer processes which are generally not accessible otherwise. Such insight could improve the representation of groundwater within global and regional hydrological models and hence strengthen their predictive ability (Gleeson et al., 2021). Estimates of effective elastic moduli obtained through geodesy also provide measurements at a scale and loading rate (i.e., quasi-static) relevant for geohydrologic processes and complementary to those obtained through seismology and laboratory experiments (Carlson et al., 2020). Beyond hydrological applications, characterizing the seasonal content of geodetic time series is also essential to isolate the deformation associated with tectonic processes (Michel et al., 2019; Vergnolle et al., 2010) and to investigate the response of seismicity to seasonal forcings (Bettinelli et al., 2008; Craig et al., 2017; Johnson et al., 2017).

A number of studies, mostly using Interferometric Synthetic Aperture Radar (InSAR), have demonstrated the feasibility of documenting aquifer dynamics and inferring their mechanical properties based on remote sensing measurements of surface deformation and *in situ* measurements of groundwater levels (Amelung et al., 1999; Bell et al., 2008; Wisely and Schmidt, 2010; Galloway and Burbey, 2011; Chaussard et al., 2014, 2017; Miller et al., 2017; Ojha et al., 2018; Riel et al., 2018; Alghamdi et al., 2020; Hu and Bürgmann, 2020; Gualandi and Liu, 2021). Most of these studies focused on aquifer basins where the poroelastic response dominates the local deformation field. At a regional scale, however, both deformation fields vary spatially and are not easily separated given the codependency of these deformation processes.

Here, we describe a new methodology to extract poroelastic deformation from GNSS time series by harnessing observations from the GRACE satellites and *in situ* groundwater monitoring wells as well as a blind source separation technique (Gualandi et al., 2016). Focusing on GNSS data as opposed to InSAR provides (1) a complementary set of geodetic observations with different systematic errors, (2) the opportunity to study larger aquifer systems at which InSAR processing becomes challenging and (3) a means to correct for known hydrological effects in GNSS time series extensively used in tectonic studies. Indeed, GNSS provides insight into the 3D surface deformation field complementary to InSAR, particularly when it comes to horizontal displacements. This is important because, as we emphasize in this work, horizontal and vertical deformation fields arising from different mechanisms can have distinct spatial signatures.

Previous studies have described poroelastic deformation fields using a number of modeling frameworks, including the USGS modular finite-difference groundwater flow model (MODFLOW) (Hoffmann and Wilson, 2003), finite strain cuboids in a homogeneous elastic half-space (Barbot et al., 2017; Silverii et al., 2019; Hu and Bürgmann, 2020), and mixed finite element models (Ferronato et al., 2010; Alghamdi et al., 2020). In this work, we present an alternative framework to characterize the vertical and horizontal surface displacements arising from poroelastic eigenstrains in an unconfined aquifer with heterogeneous elastic properties (Fleitout and Chanard, 2018). We hope that the resulting (semi-)analytical solutions can serve as an intermediate between models with homogeneous elastic properties and more involved numerical models, and hence provide further insight into the complex, three-dimensional deformation field of aquifer systems.

The manuscript is organized as follows: We first introduce the geohydrological setting and data sets of our study area in Section 2.2. We selected the Ozark Plateaus Aquifer System (OPAS) in central United States to test the method because of the relatively quiescent tectonic setting (Craig and Calais, 2014; Calais et al., 2016), the data availability and the well-documented geohydrological setting (e.g., Imes and Emmett, 1994; Hays et al., 2016; Westerman et al., 2016; Knierim et al., 2017). In Section 2.3, we characterize the heterogeneous groundwater level dataset with an Independent Component Analysis (ICA). We then present analytical solutions for simple disk loading and aquifer scenarios before extracting the 3D poroelastic deformation field from the GNSS time series in Section 2.4. We conclude the study by inferring the heterogeneous distribution of elastic moduli in OPAS from the extracted groundwater level variations and vertical poroelastic displacements in Section 2.5.

2.2 Regional Setting and Data Sets

2.2.1 The Ozark Plateaus Aquifer System (OPAS)

OPAS is a large system of aquifers and confining units in the Mississippi River basin in central United States (Figure 2.2). The system is bounded by the Mississippi River and its alluvial plain, the Missouri River and Arkansas River to the east, north and south, respectively, and by a saline to freshwater transition zone to the west (Imes and Emmett, 1994) (Figure 2.2A). Although it is a significant source of water for agricultural and public supply in the region, groundwater use in OPAS represents a relatively small portion of the hydrologic budget – about 2% of aquifer recharge (Hays et al., 2016). Most groundwater recharge flows laterally, feeding other aquifers

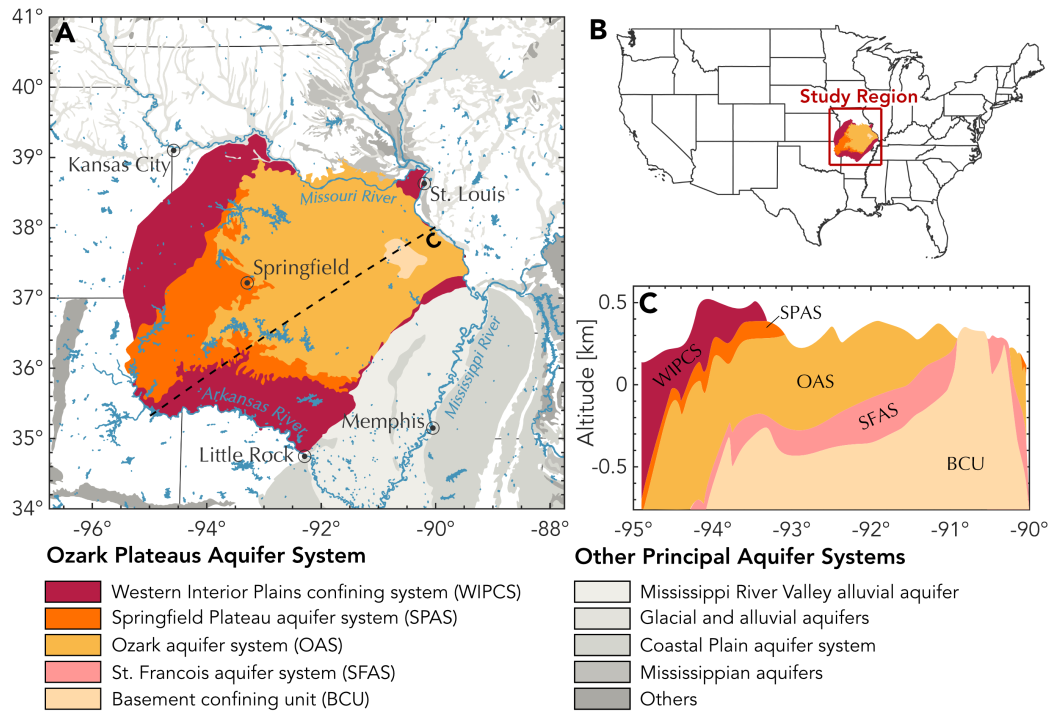

Figure 2.2: Regional hydrogeological setting. (A) Simplified outcrop map of the Ozark Plateaus Aquifer System (OPAS) based on physiographic sections (modified from Hays et al. (2016) and Knierim et al. (2017)) and neighbouring aquifer systems (from USGS map of Principal Aquifers). (B) Geographical location of OPAS. (C) Hydrogeological cross-section at the dashed line in A based on Westerman et al. (2016).

and sustaining streams, lakes and wetlands (Hays et al., 2016). Nonetheless, groundwater pumping does cause localized cones of depression around certain urban areas such as Springfield, Missouri (Imes, 1989).

OPAS is composed of interbedded layers of carbonate and clastic deposits around the topographic high Ozark dome (Hays et al., 2016; Westerman et al., 2016). The system is underlaid by a basement confining unit which outcrops at the Ozark dome in east-central Missouri (Figure 2.2AC). The Ozark aquifer system (OAS) – the most important water-bearing unit of the system – crops out at the center of the system and is otherwise overlaid by the Springfield Plateau aquifer system (SPAS) and/or the Western Interior Plains confining system (WIPCS). North of the Missouri - Arkansas border, carbonate-rich units such as SPAS and OAS present rich karst features (Hays et al., 2016).

Other aquifer systems surrounding OPAS are also shown in Figure 2.2. The Mississippi Embayment Aquifer System and the shallower Mississippi River Valley Aquifer southeast of OPAS supply much of the irrigation water for the agriculture-intensive region (Hart et al., 2008). The Mississippian Aquifers and glacial deposits from the Laurentide Ice Sheet occupy the north and northeastern boundaries of the study area (Bayless et al., 2017).

2.2.2 Data Sets

2.2.2.1 Groundwater level time series

Groundwater monitoring wells (i.e., piezometers) record the temporal evolution of hydraulic head at a given depth. In this study, we take advantage of the piezometric network maintained by the United States Geological Survey which provides daily observations of water level depth (USGS Water Services; https://waterservices.usgs.gov). Of the 312 wells in the study area, we retain the 167 sites with 60% or more data completeness during the 2007 to 2017 timespan and further exclude seven stations classified as anomalous after visual inspection (Figure B.1). For example, two time series with a typical groundwater pumping signature (Figure B.1) are excluded from the analysis because these signals are expected to be very local (tens of meters) — as they represent the aquifer response to local forcings — and to bias the analysis due to their large amplitudes. We subtract the altitude at each well location to obtain the hydraulic head, detrend the time series and compute monthly averages to facilitate comparison with the other data sets used in this study. The positions of the 160 selected wells are shown in Figure 2.3A and examples of retained time series are presented in Figure 2.3B. They present seasonal and multi-annual water level oscillations from a few to tens of meters in amplitude.

2.2.2.2 GRACE-derived displacement time series

GRACE satellites monitor space and time variations in Earth's gravity field from which changes in continental water storage — which include both surface and groundwater mass (Figure 2.1A) — can be inferred and expressed in units of equivalent water height (EWH). At the global scale, GRACE-based models have been shown to better explain the seasonal signals in GNSS datasets than hydrology-based models (Li et al., 2016). Here, we make use of the Level 2 Release 06 spherical harmonics GRACE solution up to degree 96 where low degree harmonics C_{20} have been replaced by SLR-derived values provided by the Center for Space Research (CSR)

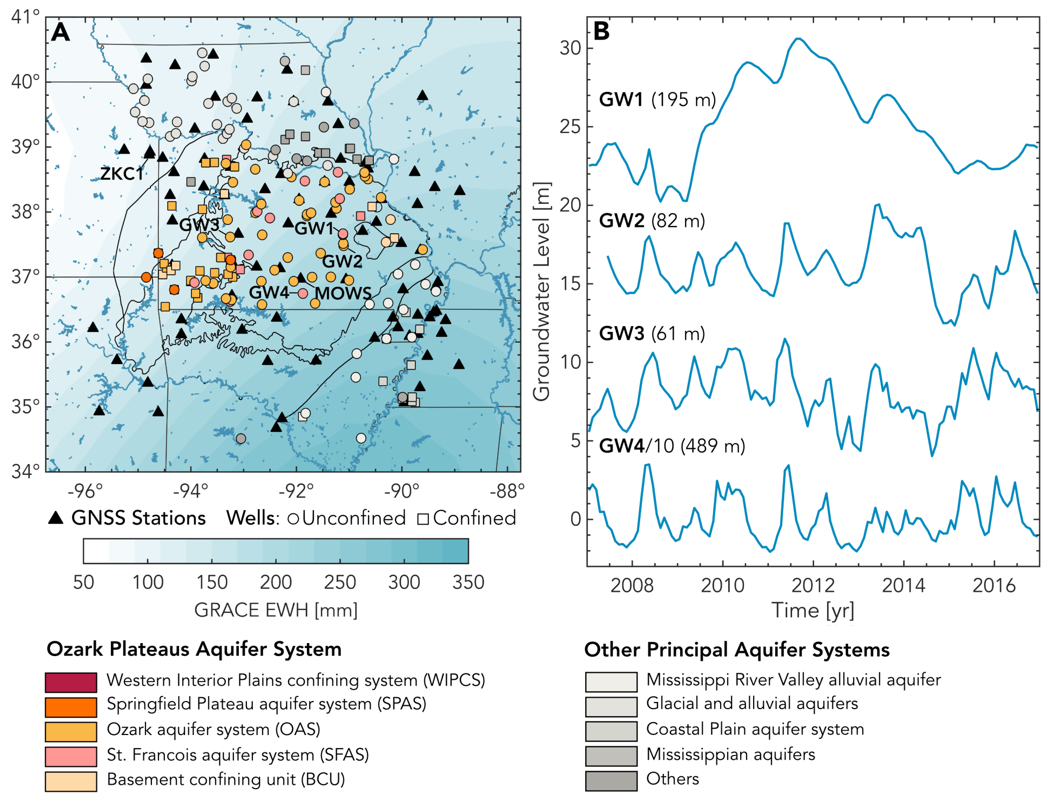

Figure 2.3: GNSS, GRACE, and groundwater data sets. (A) Annual EWH peak-to-peak amplitudes derived from GRACE and locations of GNSS stations and groundwater monitoring wells used in this study. The color of the well markers indicates the aquifer system at the base of a well and the shape describes the type of aquifer(s) — i.e., confined or unconfined — encountered by a well (as classified by the USGS). (B) Example of groundwater time series at different locations across OPAS. Note that the time series are offsetted and that GW4 is divided by a factor of 10 for illustration purposes. Well depths are indicated in parenthesis. The featured wells correspond to USGS site numbers 373955091065901 (GW1), 372853091061801 (GW2), 373701093151601 (GW3) and 364324091515001 (GW4).

(Bettadpur, 2018; GRACE, 2018) and DDK5-filtered to minimize north-south striping noise (Kusche et al., 2009). We add back the atmospheric and non-tidal oceanic contributions as these effects are not corrected in the GNSS data set and detrend the resulting time series. The colormap in Figure 2.3A shows the average annual EWH peak-to-peak amplitudes observed during the 2007 to 2017 timespan and reveals an important large-scale NW to SE gradient in regional water storage changes, with higher amplitudes concentrated around the Mississippi Alluvial Valley.

To quantify the large-scale hydrological elastic loading deformation resulting from changes in surface water and groundwater mass (Figure 2.1B), we compute the deformation expected from GRACE-inferred loads at the GNSS sites using a spherical elastic layered Earth model based on the Love number formalism (Farrell, 1972; Chanard et al., 2018). Note that while hydrological loading can, in theory, produce both elastic and viscoelastic deformation fields, here we limit our analysis to a purely elastic model given that the Earth's response is in phase with loading at the annual and multiannual timescales. Moreover, while changes in groundwater mass do not occur exactly at the surface of the Earth, the depth at which those changes occur (on the order of 1 km at most) is negligible compared to the radius of the Earth, which is the key quantity in elastic loading equations on a spherical Earth (Farrell, 1972). For example, using a radius of 6370 km instead of 6371 km would result in a 0.01% change in the computed surface displacements. We therefore neglect this depth dependency in our calculations. Given the relatively large spatial wavelengths considered here, we also neglect the effect of relatively weak aquifer layers. Examples of the resulting time series are compared to the corresponding GNSS measurements in Figure B.2. In Figure B.3, we show that the modeled displacements in this region are relatively insensitive to the particular choice of GRACE solution as solutions from the CSR, JPL and GFZ centers all produce displacements with mean absolute differences smaller than 1 mm (the approximate uncertainty of GNSS measurements).

2.2.2.3 GNSS displacement time series

GNSS tracks the vertical and horizontal displacements of geodetic monuments anchored a few meters below the ground surface (or on top of buildings for fewer than 15% of stations). In this analysis, we start from the time series processed by the Nevada Geodetic Laboratory and expressed in the IGS14 reference frame (International GNSS Service), based on the latest release of the International Terrestrial Reference Frame (ITRF2014), (Altamimi et al., 2016; Blewitt et al., 2018, http://geodesy.unr.edu). Of the 315 stations located in the study area which is delimited by longitudes -96º to -89º and latitudes 34.5º to 40.5º, we retain the 92 stations with at least 60% of daily data between 2007 and 2017. After visual inspection, six additional stations (CVMS, MOGF, MOMK, MOSI, NWCC, and SAL5) are discarded due to spurious large amplitude signals. The positions of the remaining 86 stations are shown in Figures 2.3A and B.4.

For each time series, we fit a trajectory model (Bevis and Brown, 2014) with a linear trend, annual and semi-annual terms and step functions to account for material changes and potential coseismic displacements (http://geodesy.unr.edu/NGLStationPages/steps.txt) as well as visually obvious offsets. We subtract the best-fit linear trend and step functions from the time series but do not correct for the periodic terms. Next, we identify and eliminate outliers defined as points that exceed three times the average deviation from the 90-day median for any of the three directions (east, north, vertical). The time series are then monthly averaged to match the GRACE temporal resolution. Finally, the spherical harmonic degree-1 deformation field is estimated from a global network of 1150 GNSS stations and subtracted from retained GNSS time series to allow for a direct comparison with GRACE observations which do not capture degree-1 mass changes (Chanard et al., 2018). Examples of the resulting time series are provided in Figure B.2.

2.3 Fluctuations in groundwater levels

The first step towards extracting poroelastic signals from our GNSS dataset is to characterize the groundwater fluctuations responsible for the deformation. This requires some form of spatial interpolation since piezometers only probe groundwater levels at discrete points in space and are generally not co-located with GNSS stations. We determine that directly interpolating between the piezometric sensors is not warranted in this case given the heterogeneous nature of aquifers and the variable depth of wells (Figure 2.3). For example, neighboring piezometers GW1 and GW2 in Figure 2.3B reveal very different temporal signatures. On the other hand, GW2 and GW3 — which are over 200 km apart — have highly correlated time series. Groundwater fluctuations at GW4 also correlate with GW2 and GW3 but are of much higher amplitude. The groundwater dataset thus contains both regional- and local-scale signals with peak-to-peak amplitudes that span two orders of magnitude (~0.5 to 50 m).

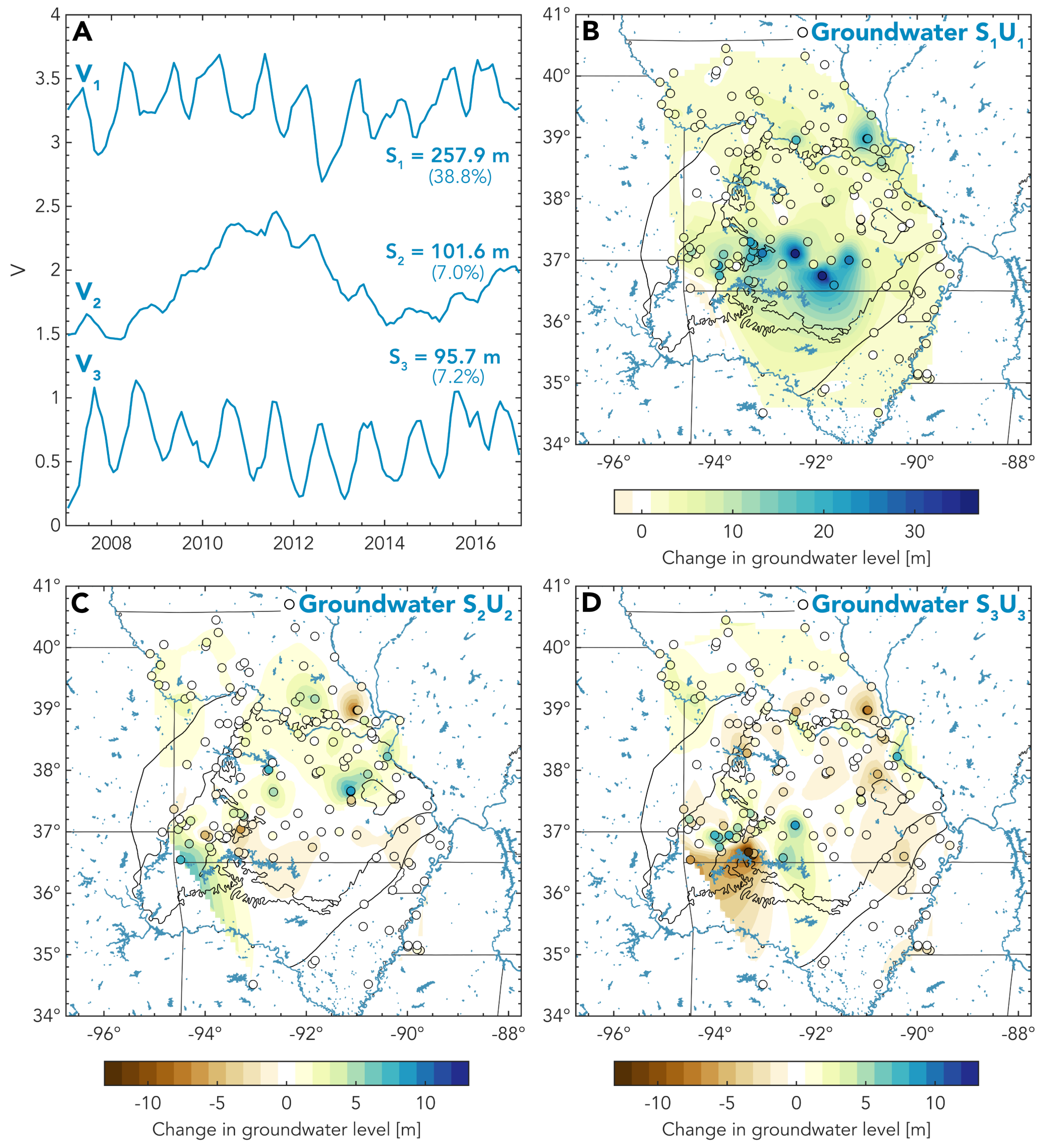

Figure 2.4: ICA decomposition of the groundwater dataset. (A) Temporal evolution and weighting factors of the three components ICA. The temporal functions are offsetted for illustration purposes. The variance of the groundwater dataset explained by each component is also indicated in parenthesis. (B-D) Weighted spatial distributions of the three components (circles). Spatial interpolation of the distributions is also shown.

2.3.1 Extracting Groundwater Signals with ICA

In light of these observations, we perform an Independent Component Analysis (ICA) on the groundwater dataset to extract the main modes of variability before proceeding with the spatial interpolation. ICA algorithms seek to recover the statistically independent sources of signal assumed to generate the linearly mixed time series at each sensor (Roberts and Everson, 2001). In particular, variational Bayesian ICA (vbICA) (Choudrey, 2002) has been shown to perform well to recover geophysical signals (e.g., postseismic, hydrology-induced and common mode error) from synthetic and real GNSS data sets (Gualandi et al., 2016; Larochelle et al., 2018). Once an independent component (IC) — i.e. a source of signal — i is isolated, it can be expressed with space and time vectors as $\mathrm{IC}_i = U_i S_i V_i^T$ where U_i is a normalized spatial distribution, S_i is a weighting factor and V_i is a normalized temporal function.

Figure 2.4 shows the temporal functions (A), weighting factors (A) and spatial distributions (B-D) obtained from a 3 components vbICA of the groundwater dataset. We use a triangulation-based natural neighbor algorithm (MATLAB, 2017) to interpolate the spatial distributions from the discrete data points (Figure 2.4B-D). We choose to limit our analysis to 3 components since analyses with more components (e.g., see Figure B.5 for a 5 components analysis) yield similar IC1-3 and additional lower-amplitude ICs with spurious temporal functions that only explain a limited portion of data variance. The retained temporal functions all display a mix of multiannual and seasonal frequencies.

IC_1, the component which explains the greatest share of data variance, has an overall positive spatial distribution and is observed at almost all wells including those outside OPAS (Figure 2.4B). This spatial distribution is indicative of a regional income of water linked to recharge processes (Longuevergne et al., 2007). The large fluctuations occurring in southern Missouri (e.g., at station GW4 (Figure 2.3)) are likely linked to the high storage capacity of thick limestone layers with limited karstification (Figure 2.4B). Figure B.6 also reveals a crude spatial correlation between sinkhole density, which suggests a higher ability to recharge the aquifer system, and wells with high $S_1 U_1$ values. IC_2 and IC_3 represent seasonal and multi-annual signals with different phases than IC_1 and exhibit heterogeneous spatial distributions with positive and negative values (Figure 2.4CD). These components probably compensate for local deviations from the regional behavior due to the

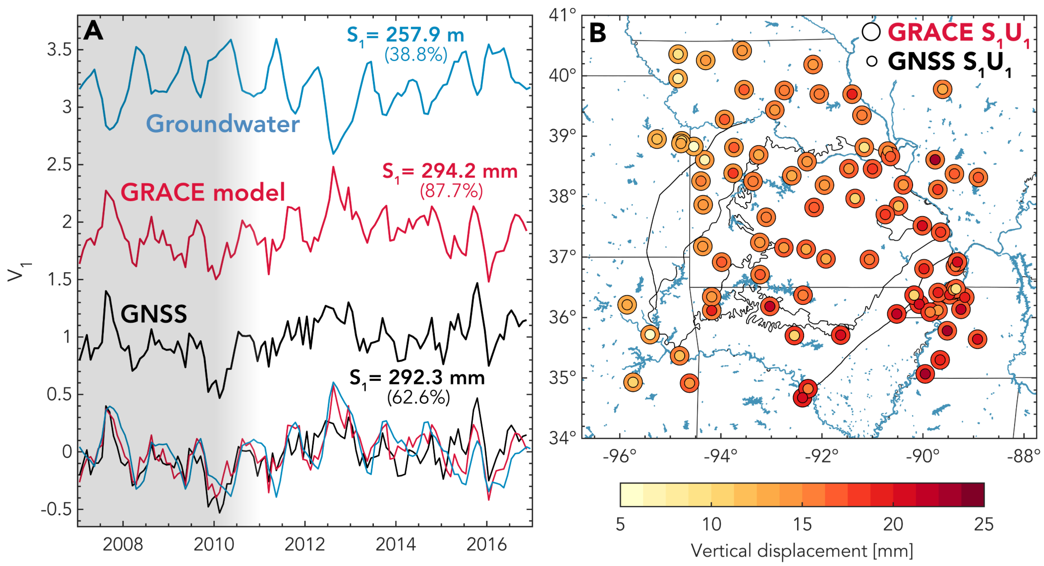

Figure 2.5: Temporal correlation between the first independent component of groundwater and the GRACE-predicted and GNSS vertical displacements. (A) Temporal functions (offsetted), weighting factor and variance explained for each dataset. The 3 temporal functions are replotted at the bottom of the figure (note that the groundwater function is flipped) to facilitate visual comparison. The grey shaded area indicates the timespan prior to the installation of most GNSS stations sitting on top of OPAS from 2010 to 2011. (B) Spatial distribution of the GRACE-predicted (outer circles) and GNSS (inner circles) vertical displacement datasets.

delayed response of deeper aquifers, differing recharge and discharge mechanisms and groundwater pumping.

2.3.2 Comparing Regional-Scale Hydrological Signals Across Datasets

Given that IC_1 spans the entire study region, we expect to find a similar signal in the GRACE dataset. Performing a vbICA on the GRACE-predicted vertical displacements — completely independently from the groundwater ICA — the temporal function of the first and most important component indeed correlates very well with V_1^{GW}, as evidenced by the correlation coefficient ρ of -0.81 (Figure 2.5A). Downward motion occurs concurrently with rising groundwater levels because GRACE-derived vertical displacements solely reflect the hydrological loading deformation due to changes in continental water storage (Figure 2.1B), not the poroelastic deformation (Figure 2.1C). The associated spatial response (Figure 2.5B) reflects the northwest to southeast gradient of hydrological loads.

By contrast, GNSS vertical time series should comprise both deformation fields. Performing a similar analysis on the GNSS dataset independently from the groundwater and GRACE analyses results in a lower but still significant correlation of $\rho = -0.52$ with V_1^{GW} (Figure 2.5A). Note that a significant portion of GNSS stations sitting on top of OPAS were not installed until 2010 or 2011 as indicated by the grey shading in Figure 2.5A. Although the GNSS spatial distribution displays the same overall gradient as the GRACE-derived model with generally higher amplitudes around the Mississippi Alluvial Valley, the response is more heterogeneous (Figure 2.5B).

This comparison exercise demonstrates that the dominant temporal functions of all three datasets are in phase on a monthly timescale. This is consistent with a relatively uniform regional recharge of the aquifer system (Figure 2.4B) and with the system's karstic nature which allows for rapid communication between surface water and groundwater (Hays et al., 2016), suggesting that the aquifer's global behavior can be considered as unconfined. We recognize that OPAS is a complex aquifer system with both confined and unconfined units (Figure 2.3A) and that different hydrogeologic processes might interact to generate surface displacements. However, in this work, we choose to treat OPAS as an effectively unconfined system and infer mechanical properties under this assumption.

2.4 Poroelastic Deformation

2.4.1 Hydrological Elastic Loading vs Poroelastic Eigenstrain: Insights about Surface Displacements from Simple Analytical Solutions

To gain intuition about the elastic and poroelastic deformation fields we expect to find in the vicinity of an unconfined aquifer, we first develop and compare analytical solutions for surface displacements associated with the simple disk scenarios shown in Figure 2.1BC, assuming an elastic half-space medium. In B.1, we extend the poroelastic solution to an arbitrary 2D eigenstrain distribution which we later use to predict horizontal poroelastic displacements. While we rely on this elastic half-space model with an aquifer layer to analyse and model poroelastic displacements in later sections, we only show the equivalent elastic half-space loading model in this section for illustration and comparison purposes.

2.4.1.1 Disk loading of an elastic half-space

We first consider a disk load of radius a and uniform pressure P at the surface of an elastic half-space with Young's modulus E_{deep}, representative of hydrological loading from surface water (Figure 2.1B). The corresponding vertical and horizontal surface displacements were derived by Johnson (1987) and Verruijt (2009) as:

$$u_z(r) = \begin{cases} -\dfrac{4(1-\nu^2)}{\pi E_{deep}} Pa\mathcal{E}\left(\dfrac{r^2}{a^2}\right), & r \leq a \\ -\dfrac{4(1-\nu^2)}{\pi E_{deep}} Pr\left(\mathcal{E}\left(\dfrac{a^2}{r^2}\right) - \left(1-\dfrac{a^2}{r^2}\right)\mathcal{K}\left(\dfrac{a^2}{r^2}\right)\right), & r > a \end{cases} \tag{2.1}$$

$$u_r(r) = \begin{cases} -\dfrac{(1-2\nu)(1+\nu)}{2E_{deep}} Pr, & r \leq a \\ -\dfrac{(1-2\nu)(1+\nu)}{2E_{deep}} P\dfrac{a^2}{r}, & r > a \end{cases} \tag{2.2}$$

where $u_z(r)$ and $u_r(r)$ are the vertical and horizontal displacements as a function of radial distance r and $\mathcal{K}$ and $\mathcal{E}$ are the complete elliptic integral of the first and second kind, respectively.

Figure 2.6A shows the deformation resulting from 10 km and 25 km-radius disks uniformly loaded with 5 m of water. Both the vertical and horizontal displacements extend beyond the loaded region with the maximum vertical and horizontal displacements occurring at the center of the disk and at the load boundary, respectively. Note that the amplitude of deformation is proportional to the spatial wavelength of the load.

2.4.1.2 Poroelastic eigenstrain in a disk within an elastic half-space

Poroelastic deformation arises from dilational eigenstrains (Mura, 1982) associated with changes in pore pressure, analogous to thermoelastic deformation resulting from changes in temperature. In fact, the solutions derived here are directly applicable to the equivalent thermoelastic problem (Fleitout and Chanard, 2018). Eigenstrains refer to internal strains which, in the absence of external stresses resisting them, would lead to isotropic expansion or contraction of the body. In the poroelastic case, eigenstrains are related to changes in pore pressure, Δp, and hence in groundwater level, Δh, as:

$$\varepsilon_{eig} = \frac{\beta \Delta p(1-2\nu)}{E_{aq}} = \frac{\beta \rho g \Delta h(1-2\nu)}{E_{aq}} \tag{2.3}$$

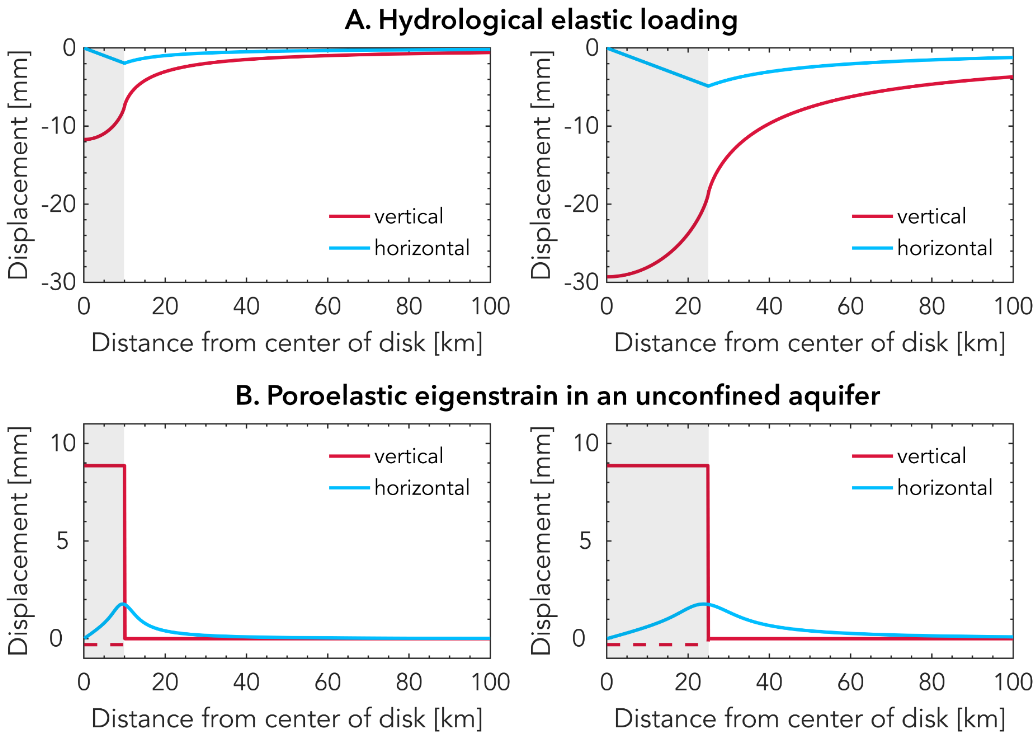

Figure 2.6: Surface displacements due to hydrological elastic loading vs poroelastic eigenstrain. Vertical and horizontal surface displacements induced by (A) a disk load at the surface of an elastic half-space and (B) poroelastic eigenstrain in a circular unconfined aquifer as illustrated in Figure 2.1 for disks of radius a = 10 km (left) and a = 25 km (right) as indicated by the grey-shaded areas. For the vertical poroelastic deformation, the dashed line represents the shear-induced deformation while the solid line represents the total poroelastic displacement. The increase in surface water level, P, and groundwater level, Δh, are set at 5 and 20 m, respectively, consistent with a 25% porosity. Other parameter values are: $\nu = 0.25$, $E_{deep} = 80$ GPa, $E_{aq} = 10$ GPa, $\beta = 0.8$, $b = 1000$ m.

where β, ν and E_{aq} are the Biot-Willis coefficient, Poisson's ratio and Young's modulus of the aquifer layers, respectively, while ρ is water density and g is the gravitational acceleration.

Given the relatively high hydraulic conductivity of karstified sedimentary rocks (Domenico and Schwartz, 1998; Hays et al., 2016), in this work we assume that there is no significant time delay between changes in pore pressure and the resulting deformation. We also assume that deformation is entirely (poro)elastic and neglect permanent deformation as clay minerals often responsible for inelastic processes are seldom found in OPAS (Westerman et al., 2016).

Linear elastic constitutive equations accounting for eigenstrains are as follows (Wang, 2000):

$$\varepsilon_{zz} = \frac{1}{E_{aq}} \left[(1+\nu)\sigma_{zz} - \nu(\sigma_{rr} + \sigma_{\theta\theta} + \sigma_{zz}) \right] + \varepsilon_{eig} \tag{2.4}$$

$$\varepsilon_{rr} = \frac{1}{E_{aq}} \left[(1+\nu)\sigma_{rr} - \nu(\sigma_{rr} + \sigma_{\theta\theta} + \sigma_{zz}) \right] + \varepsilon_{eig} \tag{2.5}$$

$$\varepsilon_{\theta\theta} = \frac{1}{E_{aq}} \left[(1+\nu)\sigma_{\theta\theta} - \nu(\sigma_{rr} + \sigma_{\theta\theta} + \sigma_{zz}) \right] + \varepsilon_{eig}. \tag{2.6}$$

Given that lateral motion is restrained by the elastic medium below, it can be shown that horizontal strains within the aquifer layers, ε_{rr} and $\varepsilon_{\theta\theta}$, although not strictly null, are negligible compared to ε_{eig} in this case (Fleitout and Chanard, 2018). Under this assumption, lateral stresses, σ_{rr} and $\sigma_{\theta\theta}$, can be approximated as:

$$\sigma_{rr} = \sigma_{\theta\theta} = \frac{-E_{aq}\varepsilon_{eig} + \nu\sigma_{zz}}{1-\nu} \tag{2.7}$$

where σ_{zz} is the change in total vertical stress associated with a change in groundwater level Δh:

$$\sigma_{zz} = -\phi\rho g \Delta h \tag{2.8}$$

where ϕ is the porosity of the aquifer layers and the negative sign indicates compressive stresses. Substituting Equations (2.3), (2.7) and (2.8) into (2.4) and integrating the vertical strain over the saturated aquifer thickness b and radius a yields the following vertical deformation field at the surface:

$$u_{z,exp}(r) = \begin{cases} \dfrac{(1+\nu)(1-2\nu)}{(1-\nu)} \dfrac{(\beta-\phi)\rho g \Delta h(r) b}{E_{aq}}, & r \leq a \\ 0, & r > a. \end{cases} \tag{2.9}$$

Here we must integrate over the entire saturated thickness b since pore pressure increases over the entire depth of the hydraulically-connected aquifer when it is recharged with additional water. Equation (2.9) describes the vertical poroelastic expansion of the aquifer layers in excess of the elastic loading deformation resulting from the added groundwater load ($\phi\rho g\Delta h$) within these elastically weak layers.

The total horizontal strain, sum of the elastic and eigenstrain, has to be small compared to the eigenstrain because it requires deformation of the elastic medium below the aquifer. In fact, compensation of horizontal eigenstrain by elastic strain requires strong variations in lateral stress σ_{rr} within the aquifer (Equation (2.7)).

These variations in σ_{rr} necessarily induce shear stresses at the base of the aquifer, which results in both horizontal and vertical displacements within the medium below the aquifer. We can see this effect by solving for this basal shear stress, $\sigma_{rz}(z = b)$, considering the stress equilibrium equations for an axisymmetric problem in cylindrical coordinates (Wang, 2000):

$$\frac{\partial \sigma_{rz}}{\partial r} + \frac{\partial \sigma_{zz}}{\partial z} + \frac{\sigma_{rz}}{r} = 0 \tag{2.10}$$

$$\frac{\partial \sigma_{rz}}{\partial z} + \frac{\partial \sigma_{rr}}{\partial r} + \frac{\sigma_{rr} - \sigma_{\theta\theta}}{r} = 0. \tag{2.11}$$

Substituting Equation (2.7) into (2.11), integrating with respect to z and applying a zero shear stress boundary condition at the surface ($\sigma_{rz}(z = 0) = 0$) yields:

$$\sigma_{rz}(z = b) = -\int_0^b \frac{\partial}{\partial r}\left[\frac{-E_{aq}\varepsilon_{eig} + \nu\sigma_{zz}}{1-\nu}\right]\partial z \tag{2.12}$$

$$= \frac{\partial}{\partial r} I(r) \tag{2.13}$$

where

$$I(r) = \int_0^b \frac{E_{aq}\varepsilon_{eig} - \nu\sigma_{zz}}{1-\nu}\partial z \tag{2.14}$$

is the fundamental quantity driving poroelastic deformation (Fleitout and Chanard, 2018). For the simple disk aquifer considered here, E_{aq}, ε_{eig}, ν and σ_{zz} are uniform within the aquifer and ε_{eig} and σ_{zz} are equal to zero outside the aquifer such that:

$$I(r) = \frac{(E_{aq}\varepsilon_{eig} - \nu\sigma_{zz})b}{1-\nu}\mathcal{H}(a-r) \tag{2.15}$$

$$= \frac{(\beta(1-2\nu) + \phi\nu)\rho g \Delta h b}{(1-\nu)}\mathcal{H}(a-r) \tag{2.16}$$

$$= I_{disk}\mathcal{H}(a-r) \tag{2.17}$$

and

$$\sigma_{rz}(z = b) = I_{disk}\delta(r-a) \tag{2.18}$$

where $\mathcal{H}$ and δ are the Heaviside and Dirac delta functions, respectively. Finally, we predict the deformation induced by $\sigma_{rz}(z = b)$ with the expressions derived by Johnson (1987) for surface displacements due to an axisymmetric shear stress distribution, $q(t)$:

$$u_{z,shear}(r) = \begin{cases} -\dfrac{(1-2\nu)(1+\nu)}{\pi E_{deep}}\displaystyle\int_r^a q(t)dt, & r \leq a \\ 0, & r > a \end{cases} \tag{2.19}$$

$$u_{r,shear}(r) = \frac{4(1-\nu^2)}{\pi E_{deep}}\int_0^a \frac{t}{t+r}q(t)\left[\left(\frac{2}{k^2}-1\right)\mathcal{K}(k) - \frac{2}{k^2}\mathcal{E}(k)\right]dt \tag{2.20}$$

where $k^2 = 4tr/(t+r)^2$. Using $\sigma_{rz}(z = b)$ as $q(t)$, inclusive limits of integration and the sifting property of the Dirac delta function results in:

$$u_{z,shear}(r) = \begin{cases} -\dfrac{(1-2\nu)(1+\nu)}{\pi E_{deep}} I_{disk}, & r \leq a \\ 0, & r > a \end{cases} \tag{2.21}$$

$$u_{r,shear}(r) = \frac{4(1-\nu^2)}{\pi E_{deep}} I_{disk} \frac{a}{a+r} \left[\left(\frac{2}{k^2} - 1 \right) \mathcal{K}(k) - \frac{2}{k^2} \mathcal{E}(k) \right] \tag{2.22}$$

where $k^2 = 4ar/(a+r)^2$. At $r = a$, $u_{r,shear}$ has an infinite value. Our mathematical framework is derived in a "thin layer" approximation, and therefore only valid for spatial wavelengths larger than the aquifer thickness. It would be possible to derive analytical solutions in a more complex mathematical framework for shorter wavelengths. However, for simplicity, we choose to numerically approach the diverging solution of Equation (2.22) at $r = a$ by truncating its expansion series (B.2), which has no impact at distances larger than the aquifer thickness.

To obtain an order of magnitude estimate of the poroelastic displacements expected in OPAS, we compute the poroelastic deformation generated by a 20 m increase in groundwater level in unconfined disk aquifers with radii of 10 km and 25 km and a thickness of 1000 m (Figure 2.6B). These parameter values are representative of the localized zone of elevated groundwater variations observed at the center of OPAS (Figure 2.4B) and are consistent with the equivalent elastic loading scenarios shown in Figure 2.6A, assuming a porosity of 25%. The vertical displacement is largely due to poroelastic expansion and is bounded by the aquifer. The horizontal poroelastic displacement, on the other hand, is entirely due to the shear stress imposed at the base of the aquifer and extends beyond the aquifer. Moreover, the amplitude of deformation is independent of the wavelength of pore pressure perturbation in contrast to the hydrological loading case. Indeed, the 10 and 25 km disks result in displacements of the same amplitude.In fact, expressions for horizontal displacements given by Equations (2.2) and (2.22) become independent of the disk radius a when evaluated for distances $r = r/a$. We rely on the observation that poroelastic displacements only depend on local changes in pore pressure to justify the use of elastic half-space models — as opposed to a spherical Earth model — for the upcoming analysis.

2.4.2 Extraction of Geodetic Poroelastic Displacements

In order to extract poroelastic deformation from GNSS time series, we first assume that deformation from hydrological loading is well reproduced by the GRACE model

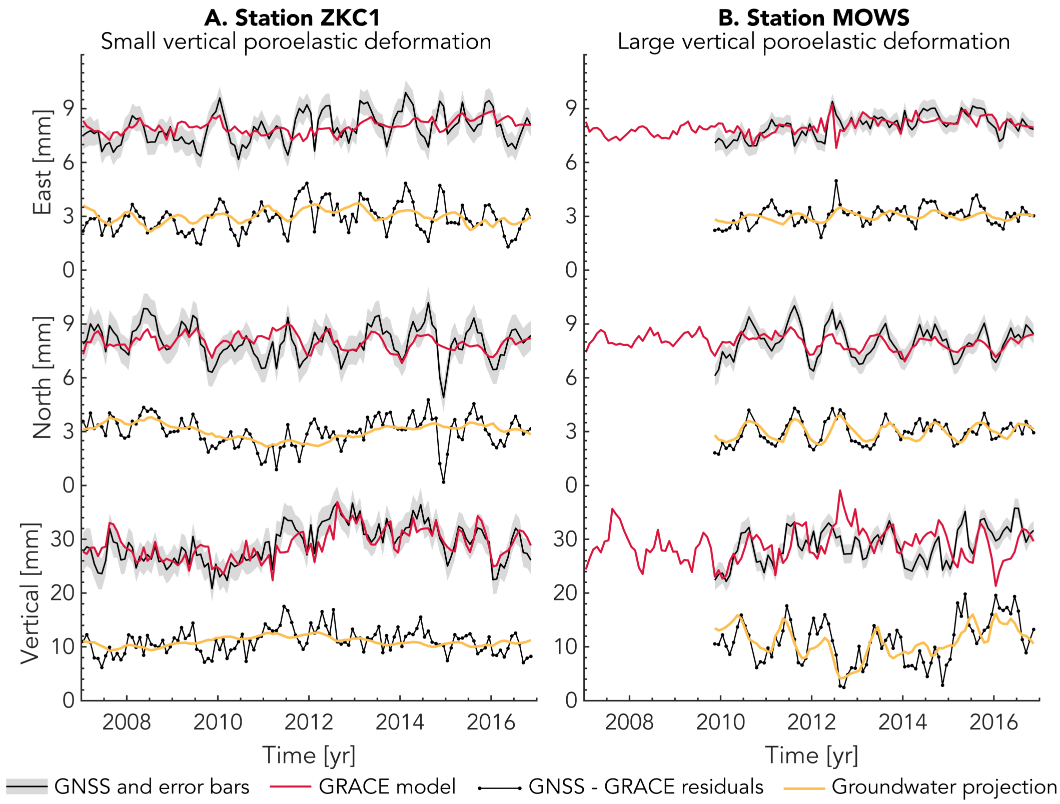

Figure 2.7: Extracting the OPAS's poroelastic signal from GNSS time series. Black lines with grey error bars are GNSS time series (corrected for degree 1). A common mode has been removed in the East and North components. Red lines are the GRACE model predictions. Black dots are the GNSS-GRACE residuals. Yellow lines are the projection of the GNSS-GRACE residuals onto the W_i from the groundwater ICA.

and hence focus on the GNSS — GRACE residual time series. This assumption is supported by a comparison of the vertical time series in Figures 2.7 and B.2. The geodetic deformation at station ZKC1 located outside OPAS and other aquifer systems (Figure 2.3A) is well explained by the GRACE model and presents very little residual seasonal displacements (Figure 2.7A). This is consistent with Chanard et al. (2018)'s finding that vertical displacements observed by GNSS are generally well explained by a GRACE loading model at a global scale because most stations are located at bedrock sites. At station MOWS at the center of OPAS, on the other hand, the GNSS vertical displacements deviate from that predicted from loading effects and the residuals show clear seasonal and multiannual features (Figure 2.7B).

For the horizontal components, we first estimate and remove the common mode deformation from the GNSS-GRACE residual time series to isolate OPAS's poroelastic response. We estimate the common mode by taking a spatial average of all horizontal GNSS-GRACE residual time series within the study area. This step is necessary as Figure B.7 illustrates that neighbouring aquifers can induce significant horizontal poroelastic deformation within the study region. Although the horizontal displacements in OPAS caused by the synthetic poroelastic eigenstrains in Figure B.7D are affected by boundary effects and vary with distance from the perturbed zone, most stations do move in the same direction, similar to the displacements extracted through our methodology but without removing the common mode (Figure B.7C). Subtracting the common mode from GNSS-GRACE residual time series should thus account for the first order effects of neighbouring aquifers.

We posit that at least part of these seasonal and multiannual residuals can be attributed to instantaneous poroelastic deformation and should therefore be proportional to and in phase with groundwater fluctuations. Since we know the dominant temporal functions that make up the groundwater fluctuations, we can test this hypothesis by projecting the residual geodetic time series onto these functions. However, unlike the related Principal Component Analysis (PCA) technique, ICA yields independent components which are not constrained to be orthogonal. Before proceeding with the projection, we must thus orthogonalize vectors V_1^{GW}, V_2^{GW} and V_3^{GW} from Section 2.3.1 via the Gram-Schmidt process to produce an orthogonal basis, enabling us to sum the contribution of each basis vector as follows:

$$P_j = \frac{R_j \cdot W_1}{\|W_1\|^2} W_1 + \frac{R_j \cdot W_2}{\|W_2\|^2} W_2 + \frac{R_j \cdot W_3}{\|W_3\|^2} W_3 \tag{2.23}$$

where P_j is the inferred poroelastic displacement for direction j (i.e., east, north or up), R_j is the GNSS-GRACE residual time series and W_1, W_2, W_3 are the orthogonalized versions of $V_1^{GW}, V_2^{GW}, V_3^{GW}$. Figure B.8 reveals that the V_i^{GW}'s were not far from orthogonality to start with since W_2 and W_3 only differ marginally from V_2^{GW} and V_3^{GW}, respectively.

The resulting P_j's are shown in yellow in Figure 2.7 and Figure B.2. The recovered vertical poroelastic deformation is relatively small at station ZKC1 outside of aquifer systems and relatively large at station MOWS at the center of OPAS. However, both stations exhibit similar amplitudes of horizontal poroelastic deformation. This behavior is consistent with the analytical solutions developed in Section 2.4.1.

2.4.3 Vertical Poroelastic Displacements

Figure 2.8 illustrates the amplitudes of the poroelastic signals extracted with each groundwater temporal function W_i. Similar to the groundwater spatial distributions in Figure 2.4, the vertical poroelastic signal recovered with W_1 is mostly positive and is more extensive and of higher amplitude than the signals recovered with W_2 and W_3. The poroelastic signals associated with W_2 and W_3 present both positive and negative values like the S_2U_2 and S_3U_3 distributions of groundwater.

Focusing on this regional signal, Figure 2.8A shows that many stations outside OPAS exhibit amplitudes comparable to those inside OPAS. We attribute these poroelastic displacements to the other major aquifer systems present in the region (Figure 2.2). Westernmost stations (e.g., ZKC1) where major aquifer structures are sparse or non-existent display some of the smallest amplitudes. However, it is difficult to evaluate whether or not a GNSS station is sitting on top of an aquifer system since the map in Figures 2.2 and B.4 only indicates the surface outcrops of these aquifer systems. The particularly large seasonal displacements at station OKMU (Figure B.2C) at the southwestern edge of OPAS might be due to intensive groundwater pumping. Unfortunately there is no nearby groundwater monitoring well active during this time period to test this hypothesis. Finally, as Eq. (2.9) suggests, the range of vertical poroelastic amplitudes observed within OPAS — from about 2 to 14 mm — may reflect differences in poroelastic (β, ϕ, E_{aq}) properties, groundwater variations (Δh) or saturated aquifer thickness (b). We discuss this further in Section 2.5.

2.4.4 Horizontal Poroelastic Displacements

As for horizontal displacements, Figure 2.8D-F suggests that all three temporal functions W_i's are associated with spatially heterogeneous poroelastic deformation on the order of a few millimeters. According to Equation (2.22), poroelastic horizontal displacements are governed by deep elastic parameters as opposed to the aquifer properties relevant for vertical poroelastic expansion. Elastic properties are believed to be more laterally homogeneous at depth than at the surface. Indeed, as discussed in Section 2.5.2, surficial layers are more prone to fracturing which can alter elastic moduli. We thus approximate E_{deep} with a constant value of 80 GPa and use Equations (B.3) and (B.4) for a spatially variable 2D distribution $I(x, y)$ (B.1) to predict the horizontal poroelastic deformation induced by the observed groundwater fluctuations.

The colormaps in Figure 2.8D-F show the spatial distributions of $I(x, y)$ interpolated within OPAS for each groundwater IC as well as the resulting displacements at the GNSS sites (red arrows). Although the model predictions associated with W_1 match the observed displacements to first order at a handful of stations within OPAS, the

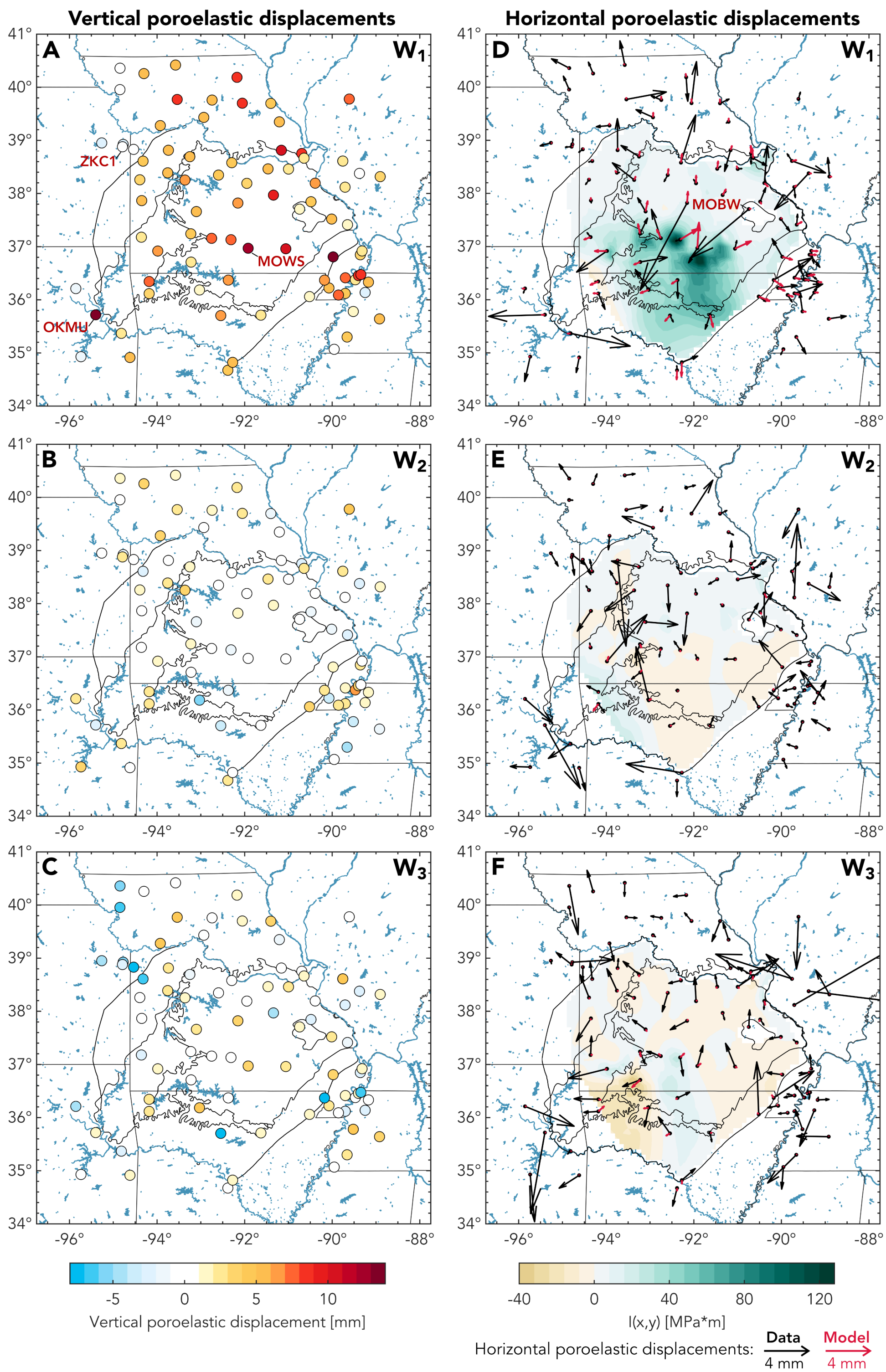

Figure 2.8: Inferred poroelastic displacements and model predictions of poroelastic horizontal displacements. Vertical (A-C) and horizontal (D-F) poroelastic displacement extracted by projecting onto the different temporal functions W_i. (D-F) Distribution of $I(x, y)$ from each groundwater IC and resulting horizontal poroelastic displacement (red arrows).

observations are more heterogeneous than predicted (Figure 2.8D). For example, station MOBW undergoes a 7 mm displacement to the southwest whereas the model predicts a sub-millimetric eastward displacement (Figure B.2D). The models for W_2 and W_3, on the other hand, fail to match the extracted displacements (Figure 2.8EF).

There are a number of potential reasons for these discrepancies. First and foremost, horizontal poroelastic displacements are highly sensitive to local variations in groundwater levels since they depend on the gradient of the groundwater field (e.g., Equation (2.13)) and do not attenuate with decreasingly small perturbation wavelengths. Hence, the spatial resolution of the piezometric network might be insufficient to accurately model the horizontal deformation. One way to improve the analysis would be to refine the spatial resolution of surface deformation measurements using InSAR (with the caveat that InSAR is mostly sensitive to east-west and vertical deformation). The model could also be extended to account for perturbation wavelengths smaller than the thickness of the aquifer. Some of the large horizontal displacements might also be due to hydrogeologic phenomena not included in the present model. For example, Silverii et al. (2016) and Serpelloni et al. (2018) explain horizontal transient signals observed around karstic aquifers with the opening and closing of vertical tensile dislocations due to groundwater variations. Groundwater pumping and the associated cones of depression might also be inducing horizontal deformation within the aquifer system itself (Helm, 1994).

Finally, our projection methodology might be capturing sources of seasonal and multi-annual signals not associated with groundwater. In particular, Fleitout and Chanard (2018) show that important horizontal thermoelastic displacements can result from sharp variations in elastic properties. Heterogeneities in hydrological loading from surface water not captured by GRACE might also be responsible for some of the discrepancy. However, this would require relatively strong heterogeneities in surface water variations since, as demonstrated in Figure 2.6A and as opposed to poroelastic deformation, the amplitude of deformation associated with hydrological elastic loading decreases with decreasing load size. In the next section, we present a preliminary analysis to quantify the displacements induced by surface hydrological fluctuations not detected by GRACE.

2.4.5 Hydrological Loading from Small-Scale Surface Water Heterogeneities

As the GRACE model only captures long-wavelength hydrological loads, our GNSS-GRACE residuals may contain signals from small-scale hydrological surface loads

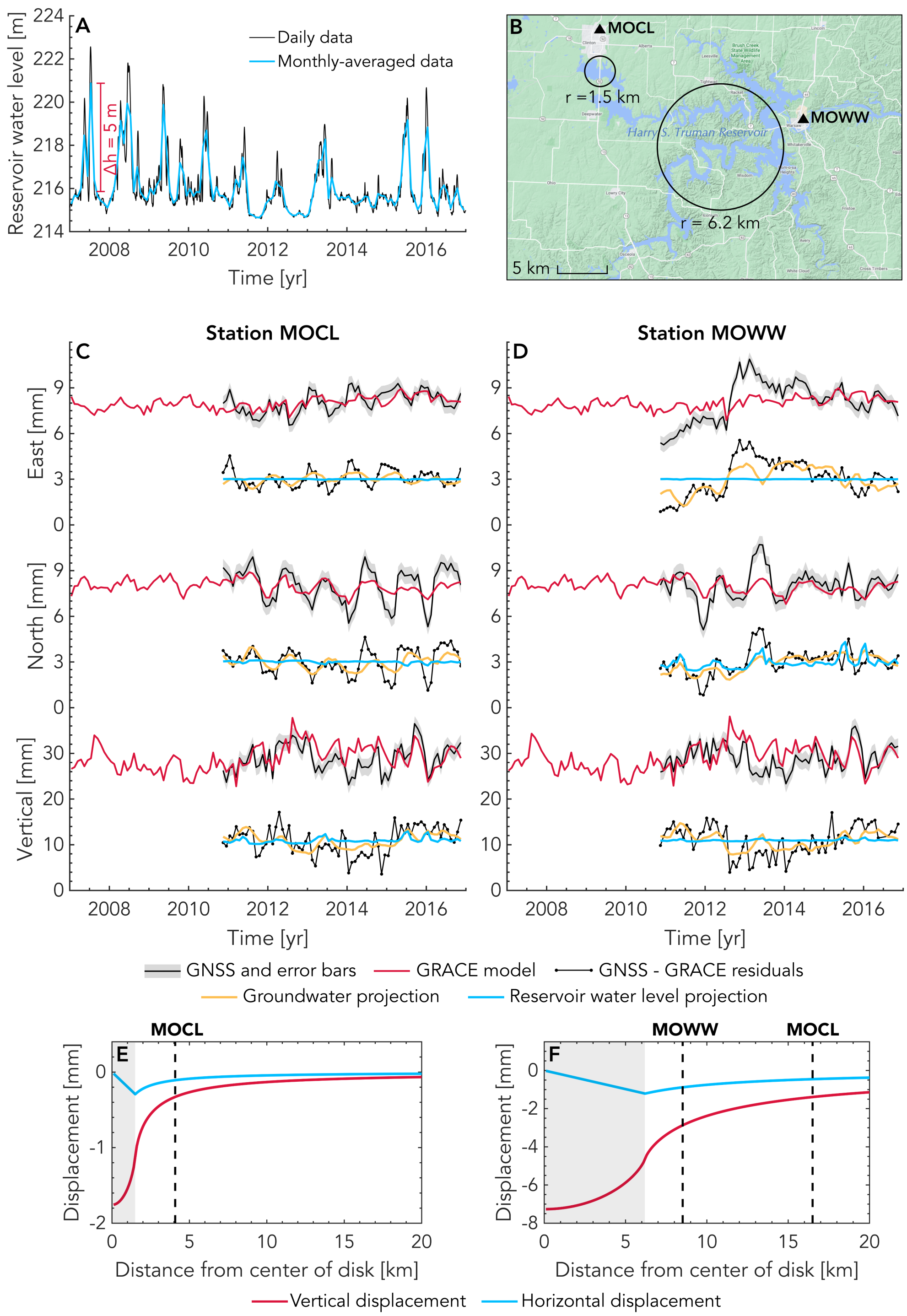

Figure 2.9: Estimating the elastic loading contribution from a surface water reservoir. (A) Daily and monthly-averaged temporal evolution of water levels at the Harry S. Truman Reservoir. (B) Location of GNSS stations MOCL and MOWW with respect to the reservoir. (C,D) Same as Figures 2.7 and B.2 but with projections of the GNSS-GRACE residuals onto reservoir water levels (blue). (E,F) Displacements associated with the analytical elastic loading model (as in Figure 2.6A) for the circular regions shown in (B) and a 5m increase in water level.

in addition to groundwater-related deformation. Thoroughly quantifying the role of these small-scale heterogeneities in GNSS time series would require a sufficiently resolved spatiotemporal characterization of surface water variations throughout OPAS. We can, however, assess how important this effect is in our study area by considering the illustrative case of the Harry S. Truman Reservoir in central Missouri for which we have a record of the water levels (`https://waterdata.usgs.gov/nwis/dv?referred_module=sw&site_no=06922440`) (Figure 2.9AB). If fluctuations in the lake reservoir were causing important solid Earth deformation, we would expect that projecting GNSS-GRACE residuals of nearby stations onto the water level time series would result in significant projection signals, similar to the poroelastic case. In the case of vertical displacements, we would also expect the recovered signal to be in phase opposition with the water levels given the elastic loading nature of the deformation.

However, Figure 2.9CD reveals that performing such a projection at nearby stations MOCL and MOWW results in vertical signals of relatively small amplitudes and in phase with water levels. As for the horizontals, we do find a significant signal in the north component of station MOWW. The fact that the recovered signal is in phase with the groundwater projection suggests that the residuals could be due to elastic loading from the reservoir, poroelastic effects or a mix of both.

We can also use the analytical model from Section 2.4.1.1 to compute the elastic loading displacements expected from water level variations in the Truman Reservoir. In Figure 2.9E, we show that the displacements expected from a 5 m increase in water level over a circular region of radius 1.5 km — representative of the small portion of the Truman Reservoir closest to station MOCL — are below the 1 mm threshold of GNSS accuracy. Using a circular region with the same total surface area as that of the reservoir, on the other hand, does result in significant millimetric displacements at both stations MOWW and MOCL (Figure 2.9F). If the north displacements at station MOWW were indeed caused by elastic loading from the Truman reservoir, Figure 2.9F suggests that we should observe even larger displacements in the vertical direction. Since this is not what we observe in Figure 2.9D, we conclude that elastic loading from the Truman reservoir must be relatively small compared to the poroelastic effect. Although this analysis is limited to a single reservoir due to the paucity of water level data, we assume these findings to be representative of other lakes and reservoirs in the study area.

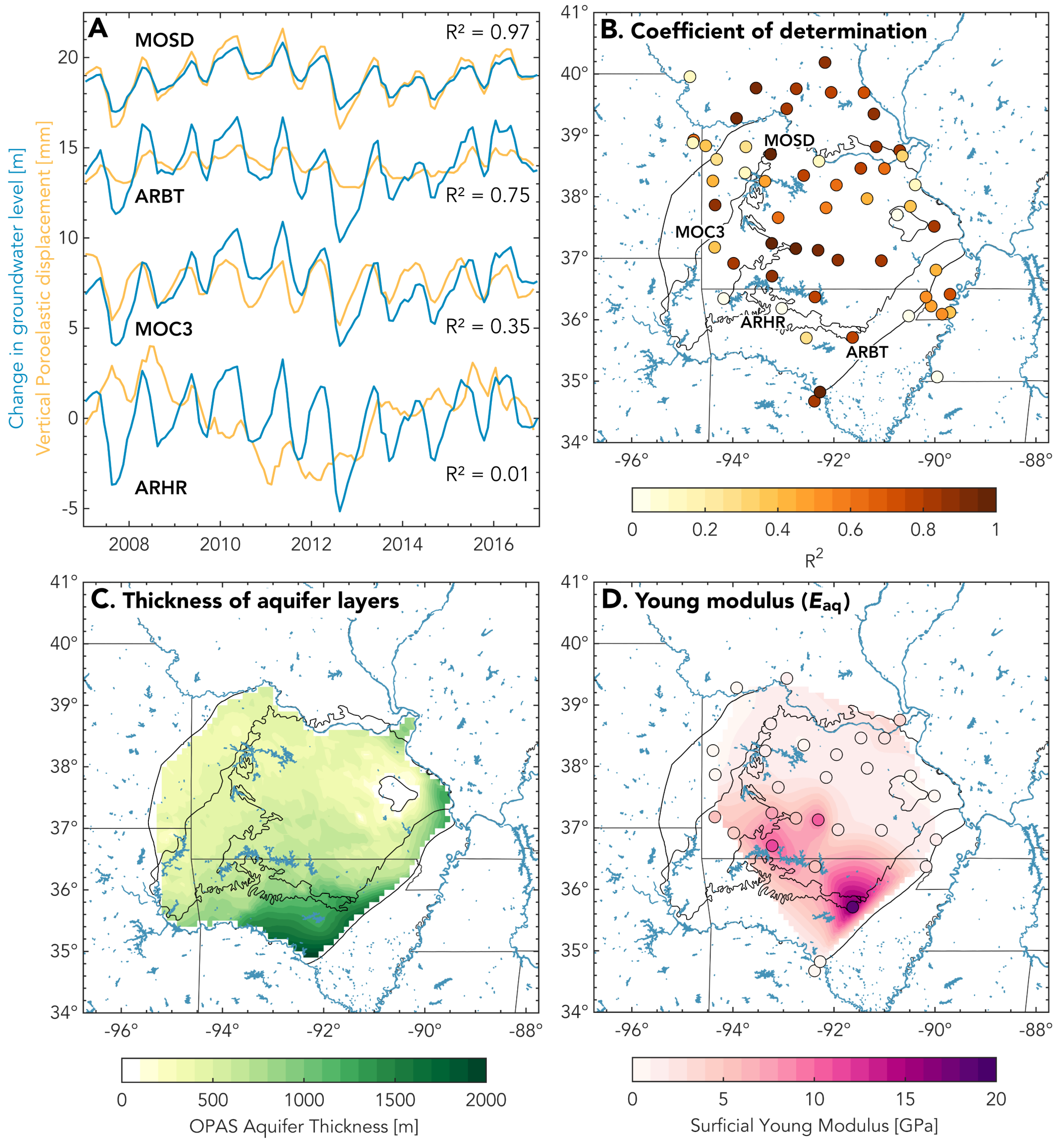

Figure 2.10: Estimating aquifer Young modulus from vertical poroelastic displacement and groundwater level variations. (A) Examples of vertical poroelastic displacement time series and groundwater level change extracted with ICA and interpolated at the GNSS stations location. Note that the time series are offsetted for illustration purposes. (B) Coefficient of determination (R^2) of a linear fit through poroelastic displacement vs change in groundwater level. The higher R^2, the better the E_{aq} estimate. (C) Total thickness of the aquifer layers. (D) Young's Modulus computed for $R^2 > 0.35$ and where all three input variables are available.

2.5 Aquifer Mechanical Properties

2.5.1 Estimating Aquifer Elastic Parameters from Vertical Geodetic Measurements

As discussed in Section 2.4, vertical poroelastic displacement is primarily due to the expansion and contraction of aquifer layers in response to groundwater fluctuations. Assuming that the system is effectively unconfined and that the ICs extracted in Section 2.3 indeed capture the groundwater variations responsible for the poroelastic deformation, we can estimate an effective aquifer Young modulus E_{aq} directly below each GNSS station by rearranging Eq. (2.9) as:

$$E_{aq} = \frac{(1+\nu)(1-2\nu)}{(1-\nu)} \frac{(\beta - \phi)\rho g \Delta h b}{u_{z,exp}}. \tag{2.24}$$

To this end, we compare the interpolated groundwater fluctuations from Section 2.3 to the inferred vertical poroelastic deformation from Section 2.4. Note that E_{aq} only depends on the vertical displacement in Eq. (2.24) and, as such, poroelastic horizontal displacements are not used in constraining the elastic modulus. For each GNSS station where both datasets are available, we consider the slope and coefficient of determination, R^2, of the best-fit line through the displacement vs groundwater level space (Figure B.9). The slope represents the ratio of vertical displacement to groundwater variation, $u_{z,exp}/\Delta h$, whose inverse enters Eq. (2.24) and R^2 quantifies the fit of the linear regression. The higher R^2 is, the more correlated the two datasets are and, hence, the more confident we are in the E_{aq} estimate. Figure 2.10A shows examples of vertical displacement and groundwater level time series with different R^2 values and Figure 2.10B illustrates the spatial distribution of R^2. We only retain stations with $R^2 > 0.35$ such as MOC3, ARBT and MOSD to estimate E_{aq}. Station ARHR illustrates a case where the time series are too incoherent to infer a meaningful value of E_{aq}. Stations with low R^2 might reflect localities where spatial interpolation of the groundwater ICs fails to reproduce the actual variations in groundwater levels. For example, station ARHR and two of its neighbours which also display low R^2 values are all located in a region with relatively few piezometric measurements.

For the thickness b, we assume that there is significant hydraulic connectivity between the different aquifer units making up OPAS (as evidenced by the temporal correlation in Figure 2.5A) and sum their thicknesses. We also assume that the aquifer is saturated over its entire thickness. Figure 2.10C shows the total thickness, b_{model}, derived from Westerman et al. (2016)'s hydrogeological model. We extrap-

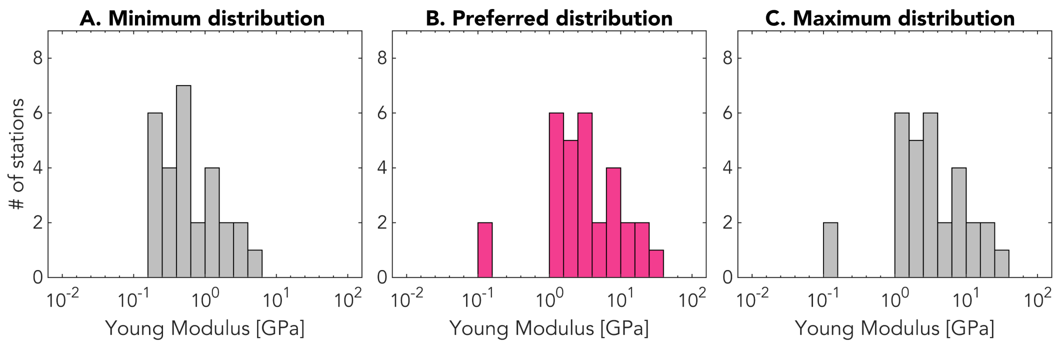

Figure 2.11: Inferred distributions of aquifer Young modulus. The preferred distribution (B) is computed with $\nu = 0.25$, $\beta = 0.80$, $\phi = 0.25$, and $b = b_{model}$ while the minimum (A) and maximum (C) distributions are computed with $\nu = 0.33$ and 0.25, $\beta = 0.6$ and 0.9, $\phi = 0.40$ and 0.00, and $b = b_{model} \mp 36$ m, respectively. Note that two stations were removed for the minimum distribution as the aquifer thickness becomes negative when subtracting 36 m.

olate this thickness distribution for GNSS stations that are within 0.2°of the OPAS surface trace. Assuming representative constant values of $\nu = 0.25$, $\beta = 0.80$, and $\phi = 0.25$ (Domenico and Schwartz, 1998), we obtain estimates of E_{aq} at the 30 retained sites where all three datasets (Δh, b_{model} and $u_{z,exp}$) are available (Figure 2.10D). We also interpolate between stations given that the vertical poroelastic field is governed by the relatively homogeneous spatial distribution associated with W_1 (Figure 2.8A). Figure 2.11 reveals that this (preferred) distribution of E_{aq} mostly falls between 1 and 10 GPa. We discuss these values further in Section 2.5.2.

2.5.2 Explaining Low Field Estimates of E_{aq}

In Section 2.5.1, we estimated a distribution for E_{aq} with values ranging from 0.04 to 18 GPa and a median of 1.58 GPa (Figure 2.11). These values are lower than the laboratory-constrained elastic moduli of the principal rocks found in OPAS: limestone, dolomite, sandstone and shale (Westerman et al., 2016). For example, Ge and Garven (1992) suggest values of 125, 68, 9 and 11 GPa for the Young modulus of Blair Dolomite, Maxville Limestone, Berea Sandstone and Chattanooga Shale, respectively (see Table B.1), pointing to an average Young modulus of the order of 50 GPa.

Here we investigate whether this order of magnitude discrepancy could be due to uncertainties on the various parameters involved in estimating E_{aq}. We evaluate the uncertainty on parameter b at ± 36 m based on the root mean square errors reported by Westerman et al. (2016). For the poroelastic constants, Domenico and Schwartz

(1998) states that the Poisson ratio ν falls within 0.25 and 0.33 for most rocks and that the porosity ϕ of limestone (including karst limestone), dolomite, sandstone and shale ranges from 0 to 0.40. As for the Biot-Willis coefficient β, we infer a range of 0.60 to 0.90 based on the reported values of 0.69, 0.76 and 0.95 for limestone, sandstone and mudstone, respectively (Domenico and Schwartz, 1998).

We then compute the minimum and maximum expected distributions of E_{aq} in Figure 2.11 by considering the parameter values within these uncertainty ranges that minimize and maximize the factor $(1+\nu)(1-2\nu)/(1-\nu)(\beta-\phi)b$ in Equation (2.24). The medians of the resulting distributions are 0.43 and 2.73 GPa, respectively. Since the maximum estimated values of E_{aq} are still generally an order of magnitude smaller than those observed in the laboratory, we argue that there is a robust discrepancy between elastic modulus measured at these different scales.

Lower-than-expected elastic modulus cannot be explained by the potential underestimation of hydrological loading displacements associated with small-scale heterogeneities in surface water discussed in Section 2.4.5. Indeed, if the loading deformation is underestimated by GRACE, the vertical poroelastic response would be underestimated as well and hence the Young modulus would be overestimated. This is because vertical poroelastic and elastic loading displacements act in opposite directions. For example, if the actual loading induces a -5 mm deformation and the poroelastic displacement is 10 mm, GNSS would record a net signal of 5 mm (since GNSS = poroelastic + loading). Now if GRACE underestimates the loading deformation at -3 mm instead of -5 mm, we would underestimate the poroelastic signal at 8 mm instead of 10 mm and, thus, overestimate the Young modulus.

There is, however, a growing body of evidence that laboratory-based values overpredict *in situ* estimates of effective elastic moduli (e.g., Matonti et al., 2015; Bailly et al., 2019). Matonti et al. (2015), for instance, report seismic velocities, V_p, measured on carbonate rock outcrops that are up to 70% smaller than those obtained on rock samples in the laboratory, implying a tenfold reduction in elastic moduli. Although part of the discrepancy is probably due to the greater porosity observed in the field (e.g., due to karstic features in this case), Fortin et al. (2007) and Bailly et al. (2019) have shown that seismic velocities — and hence elastic moduli — are more sensitive to geological features with high aspect ratios such as cracks, fractures, bedding plane, and faults because they are more compliant to deformation than spherical pores.

Following the effective medium theory framework of Fortin et al. (2007), the ratio of effective bulk modulus K to bulk modulus of the intact rock, K_o, can be described in terms of porosity, ϕ, and fracture density, f, defined as $f = Nc^3/V$, where N is the number of penny-shaped cracks with radius c, embedded in a volume V (Walsh, 1965):

$$\frac{K_o}{K} = 1 + \frac{3}{2}\frac{(1-\nu_o)}{(1-2\nu_o)}\phi + \frac{16}{9}\frac{(1-\nu_o^2)}{(1-2\nu_o)}f \tag{2.25}$$

where ν_o is the Poisson ratio of the intact rock. Assuming $\nu_o = 0.25$, Eq. (2.25) reduces to:

$$\frac{K_o}{K} = 1 + 2.25\phi + 3.33f. \tag{2.26}$$

Thus, a fourfold reduction in elastic modulus ($K_o/K = 4$) for example would require — assuming a spherical pore porosity of 25% — a fracture density f of 0.7, a common value reported in fractured reservoirs (Bailly et al., 2019). We thus conclude that the reduction in elastic moduli is mostly due to the presence of fracture-like geological features as in previous studies (Matonti et al., 2015; Bailly et al., 2019).

2.6 Conclusions

To summarize, in this study, we characterized the spatiotemporal variations of OPAS's groundwater levels with three independent components. In particular, we uncovered a regional-scale groundwater signal that is temporally correlated with geodetic observations. Then, by assuming that large-scale hydrological loading displacements are well described by a GRACE-based model and that poroelastic deformation is in phase with groundwater fluctuations, we extracted vertical and horizontal poroelastic displacement fields from GNSS time series by projecting onto the groundwater temporal functions. We also quantified the amplitudes of displacements induced by hydrological loading vs poroelastic effects with analytical solutions and developed a 2D poroelastic model to relate groundwater perturbations in an unconfined aquifer system to surface displacements. Finally, we found that the extracted groundwater variations and vertical poroelastic displacements imply a heterogeneous spatial distribution of Young modulus with values no larger than a few GPa's.

Our findings have important implications in the fields of hydrology, geodesy and seismology. First, the excellent correlation between the GRACE and groundwater temporal functions indicates that there is consistency between the water mass fluctuations observed at the local and continental scales. Filtering groundwater levels dataset with ICA could also lead to improved piezometric maps free of aberrant local signals. In terms of poroelastic displacements, the OPAS example clearly demonstrates that both hydrological loading and poroelastic effects can induce significant geodetic deformation in the vertical and horizontal directions — hence the need to account for both deformation fields when correcting GNSS time series for hydrological effects. Since the two types of deformation can interfere destructively, failing to account for poroelastic effects in hydrogeodetic inversions could result in large errors in estimates of total water storage variations. The notion that poroelastic stresses may be locally stronger than those generated from hydrological loading (due to their relative amplitudes at small perturbation wavelengths) also warrants revisiting the role of both sources of stress in triggering seasonal seismicity (Craig et al., 2017). Lastly, our relatively low geodetic estimates of Young modulus motivates further investigation into surficial elastic parameters and their effect on global hydrological loading models (Chanard et al., 2018).

While this study is clarifying the signature of large aquifer systems in GNSS time series, further work is certainly necessary to address the current limitations of our methodology, starting with testing the validity of the method in other aquifer settings. In particular, the methodology should be evaluated in non-karstic and/or confined aquifer environments as well as in systems undergoing inelastic deformation. Furthermore, the poroelastic model presented here neglects horizontal strains within the aquifer layers which may be more important in confined systems. We also recognize that the signals we attribute to poroelastic origins may be contaminated by other sources of seasonal signals, either due to deformation from thermal, atmospheric and residual hydrological loading effects or to systematic errors in the GRACE and GNSS data processing. Chanard et al. (2020) report draconitic signals, aliasing from mismodelled tides, tropospheric delays and other environmental effects as potential sources of seasonal noise and systematic errors in GNSS datasets. Perhaps most importantly, our work suggests that horizontal poroelastic displacements are highly sensitive to spatial variations in groundwater, making it difficult to accurately extract them from GNSS time series without a sufficient resolution of the piezometric surface.

Future work will thus focus on characterizing the horizontal deformation field that would help identify possible local effects in the vicinity of groundwater monitoring wells using InSAR displacement time series. Accurately measuring aquifer deformation is essential to understand its mechanics at the system scale, which is not possible from piezometric monitoring alone given the hydromechanical couplings involved. In particular, a more complete characterization of surface horizontal displacements should lead to an improved understanding of how water is stored in the different aquifers units of the Ozark system (confined-unconfined) as well as their connections.

Bibliography

S. Adusumilli, A. A. Borsa, M. A. Fish, H. K. McMillan, and F. Silverii. A decade of water storage changes across the contiguous United States from GPS and satellite gravity. *Geophysical Research Letters*, page 2019GL085370, 2019. ISSN 0094-8276. doi: 10.1029/2019GL085370.

A. Alghamdi, M. A. Hesse, J. Chen, and O. Ghattas. Bayesian poroelastic aquifer characterization from InSAR surface deformation data. Part I: Maximum a posteriori estimate. *Water Resources Research*, 56(10):e2020WR027391, 2020. ISSN 0043-1397. doi: 10.1029/2020WR027391. URL `https://onlinelibrary.wiley.com/doi/10.1029/2020WR027391`.

Z. Altamimi, P. Rebischung, L. Métivier, and X. Collilieux. ITRF2014: A new release of the International Terrestrial Reference Frame modeling nonlinear station motions. *Journal of Geophysical Research: Solid Earth*, 121(8):6109–6131, 2016. ISSN 21699313. doi: 10.1002/2016JB013098.

F. Amelung, D. L. Galloway, J. W. Bell, H. A. Zebker, and R. J. Laczniak. Sensing the ups and downs of Las Vegas: InSAR reveals structural control of land subsidence and aquifer-system deformation. *Geology*, 27:483, 6 1999. ISSN 0091-7613. doi: 10.1130/0091-7613(1999)027<0483:STUADO>2.3.CO;2.

D. F. Argus, Y. Fu, and F. W. Landerer. Seasonal variation in total water storage in California inferred from GPS observations of vertical land motion. *Geophysical Research Letters*, 41(6):1971–1980, 2014. ISSN 00948276. doi: 10.1002/2014GL059570.

D. F. Argus, F. W. Landerer, D. N. Wiese, H. R. Martens, Y. Fu, J. S. Famiglietti, B. F. Thomas, T. G. Farr, A. W. Moore, and M. M. Watkins. Sustained water loss in California's mountain ranges during severe drought from 2012 to 2015 inferred from GPS. *Journal of Geophysical Research: Solid Earth*, 122(12): 10,559–10,585, dec 2017. ISSN 21699313. doi: 10.1002/2017JB014424.

C. Bailly, J. Fortin, M. Adelinet, and Y. Hamon. Upscaling of elastic properties in carbonates: A modeling approach based on a multiscale geophysical data set. *Journal of Geophysical Research: Solid Earth*, 124(12):13021–13038, dec 2019. ISSN 2169-9313. doi: 10.1029/2019JB018391.

S. Barbot, J. D. Moore, and V. Lambert. Displacement and stress associated with distributed anelastic deformation in a half-space. *Bulletin of the Seismological Society of America*, 107, 2017. ISSN 19433573. doi: 10.1785/0120160237.

E. R. Bayless, L. D. Arihood, H. W. Reeves, B. J. Sperl, S. L. Qi, V. E. Stipe, and A. R. Bunch. Maps and grids of hydrogeologic information created from standardized water-well drillers' records of the glaciated United States. Technical report, 2017.

J. W. Bell, F. Amelung, A. Ferretti, M. Bianchi, and F. Novali. Permanent scatterer InSAR reveals seasonal and long-term aquifer-system response to groundwater pumping and artificial recharge. *Water Resources Research*, 44, 2 2008. ISSN 00431397. doi: 10.1029/2007WR006152.

S. Bettadpur. Gravity Recovery and Climate Experiment Level-2 Gravity Field Product User Handbook. 734:1–21, 2018.

P. Bettinelli, J.-P. Avouac, M. Flouzat, L. Bollinger, G. Ramillien, S. Rajaure, and S. Sapkota. Seasonal variations of seismicity and geodetic strain in the Himalaya induced by surface hydrology. *Earth and Planetary Science Letters*, 266(3-4): 332–344, 2008. ISSN 0012-821X. doi: 10.1016/J.EPSL.2007.11.021.

M. Bevis and A. Brown. Trajectory models and reference frames for crustal motion geodesy. *Journal of Geodesy*, 88(3):283–311, 2014. ISSN 0949-7714. doi: 10.1007/s00190-013-0685-5.

G. Blewitt, D. Lavallée, P. Clarke, and K. Nurutdinov. A new global mode of Earth deformation: Seasonal cycle detected. *Science (New York, N.Y.)*, 294(5550): 2342–5, 2001. ISSN 0036-8075. doi: 10.1126/science.1065328.

G. Blewitt, W. C. Hammond, and C. Kreemer. Harnessing the GPS data explosion for interdisciplinary science. *Eos*, 99, 2018. doi: 10.1029/2018EO104623.

A. A. Borsa, D. C. Agnew, and D. R. Cayan. Ongoing drought-induced uplift in the western United States. *Science*, 345(6204):1587–1590, sep 2014. doi: 10.1126/SCIENCE.1260279.

J. Boussinesq. *Application des potentiels à l'étude de l'équilibre et du mouvement des solides élastiques*. Blanchard: Reprint Paris, 1885.

E. Calais, T. Camelbeeck, S. Stein, M. Liu, and T. J. Craig. A new paradigm for large earthquakes in stable continental plate interiors. *Geophysical Research Letters*, 43(20):10,621–10,637, 2016. ISSN 00948276. doi: 10.1002/2016GL070815.

G. Carlson, M. Shirzaei, C. Ojha, and S. Werth. Subsidence-derived volumetric strain models for mapping extensional fissures and constraining rock mechanical properties in the San Joaquin Valley, California. *Journal of Geophysical Research: Solid Earth*, 125, 9 2020. ISSN 2169-9313. doi: 10.1029/2020JB019980. URL `https://onlinelibrary.wiley.com/doi/10.1029/2020JB019980`.

K. Chanard, L. Fleitout, E. Calais, P. Rebischung, and J. Avouac. Toward a global horizontal and vertical elastic load deformation model derived from GRACE and GNSS station position time series. *Journal of Geophysical Research: Solid Earth*, 123(4):3225–3237, 2018. ISSN 2169-9313. doi: 10.1002/2017JB015245.

K. Chanard, M. Métois, P. Rebischung, and J.-P. Avouac. A warning against over-interpretation of seasonal signals measured by the Global Navigation Satellite System. *Nature Communications*, 11(1):1375, 2020. ISSN 2041-1723. doi: 10.1038/s41467-020-15100-7.

E. Chaussard, R. Bürgmann, M. Shirzaei, E. J. Fielding, and B. Baker. Predictability of hydraulic head changes and characterization of aquifer-system and fault properties from InSAR-derived ground deformation. *Journal of Geophysical Research: Solid Earth*, 119(8):6572–6590, 2014. ISSN 21699313. doi: 10.1002/2014JB011266.

E. Chaussard, P. Milillo, R. Bürgmann, D. Perissin, E. J. Fielding, and B. Baker. Remote sensing of ground deformation for monitoring groundwater management practices: Application to the Santa Clara Valley during the 2012-2015 California drought. *Journal of Geophysical Research: Solid Earth*, 122(10):8566–8582, 2017. ISSN 21699313. doi: 10.1002/2017JB014676.

R. Choudrey. Variational methods for Bayesian independent component analysis. *Robots.Ox.Ac.Uk*, page 261, 2002. URL `http://www.robots.ox.ac.uk/{~}parg/projects/ica/riz/Pubs/thesis.ps.gz`.

T. J. Craig and E. Calais. Strain accumulation in the New Madrid and Wabash Valley seismic zones from 14 years of continuous GPS observation. *Journal of Geophysical Research: Solid Earth*, 119(12):9110–9129, 2014.

T. J. Craig, K. Chanard, and E. Calais. Hydrologically-driven crustal stresses and seismicity in the New Madrid seismic zone. *Nature Communications*, 8(1):2143, 2017. ISSN 2041-1723. doi: 10.1038/s41467-017-01696-w.

P. A. Domenico and F. W. Schwartz. *Physical and Chemical Hydrogeology*. Wiley, 1998. ISBN 0471597627.

D. Dong, P. Fang, Y. Bock, M. K. Cheng, and S. Miyazaki. Anatomy of apparent seasonal variations from GPS-derived site position time series. *Journal of Geophysical Research: Solid Earth*, 107(B4):ETG 9–1–ETG 9–16, 2002. ISSN 01480227. doi: 10.1029/2001JB000573.

W. E. Farrell. Deformation of the Earth by surface loads. *Reviews of Geophysics*, 10(3):761, 1972. ISSN 8755-1209. doi: 10.1029/RG010i003p00761.

V. Ferreira, C. Ndehedehe, H. Montecino, B. Yong, P. Yuan, A. Abdalla, and A. Mohammed. Prospects for imaging terrestrial water storage in south america using daily GPS observations. *Remote Sensing*, 11(6):679, 2019. ISSN 2072-4292. doi: 10.3390/rs11060679.

M. Ferronato, N. Castelletto, and G. Gambolati. A fully coupled 3-d mixed finite element model of biot consolidation. *Journal of Computational Physics*, 229, 2010. ISSN 10902716. doi: 10.1016/j.jcp.2010.03.018.

L. Fleitout and K. Chanard. Displacements and stresses induced by temperature and poroelastic pressure variations in the surficial layers for an earth with realistic elastic properties. In *AGU Fall Meeting Abstracts*, volume 2018, pages G53B–03, Dec. 2018.

J. Fortin, Y. Guéguen, and A. Schubnel. Effects of pore collapse and grain crushing on ultrasonic velocities and Vp/Vs. *Journal of Geophysical Research: Solid Earth*, 112(8), aug 2007. ISSN 21699356. doi: 10.1029/2005JB004005.

Y. Fu, D. F. Argus, and F. W. Landerer. GPS as an independent measurement to estimate terrestrial water storage variations in Washington and Oregon. *Journal of Geophysical Research: Solid Earth*, 120(1):552–566, 2015. ISSN 21699313. doi: 10.1002/2014JB011415.

D. L. Galloway and T. J. Burbey. Review: Regional land subsidence accompanying groundwater extraction. *Hydrogeology Journal*, 19(8):1459–1486, 2011. ISSN 1431-2174. doi: 10.1007/s10040-011-0775-5.

S. Ge and G. Garven. Hydromechanical modeling of tectonically driven groundwater flow with application to the Arkoma Foreland Basin. *Journal of Geophysical Research*, 97(B6):9119, 1992. ISSN 0148-0227. doi: 10.1029/92JB00677.

T. Gleeson, T. Wagener, P. Döll, S. C. Zipper, C. West, Y. Wada, R. Taylor, B. Scanlon, R. Rosolem, S. Rahman, N. Oshinlaja, R. Maxwell, M.-H. Lo, H. Kim, M. Hill, A. Hartmann, G. Fogg, J. S. Famiglietti, A. Ducharne, I. de Graaf, M. Cuthbert, L. Condon, E. Bresciani, and M. F. P. Bierkens. GMD perspective: The quest to improve the evaluation of groundwater representation in continental to global scale models. *Geoscientific Model Development Discussions*, 2021:1–59, 2021. doi: 10.5194/gmd-2021-97. URL `https://gmd.copernicus.org/preprints/gmd-2021-97/`.

GRACE. GRACE field geopotential coefficients CSR release 6.0 ver. 6.0 PO.DAAC, CA, USA. 2018. doi: 10.5067/GRGSM-20C06.

A. Gualandi and Z. Liu. Variational Bayesian independent component analysis for InSAR displacement time-series with application to central California, USA. *Journal of Geophysical Research: Solid Earth*, 126:e2020JB020845, 2021. ISSN 2169-9313. doi: 10.1029/2020JB020845.

A. Gualandi, E. Serpelloni, and M. E. Belardinelli. Blind source separation problem in GPS time series. *Journal of Geodesy*, 90(4):323–341, 2016. ISSN 0949-7714. doi: 10.1007/s00190-015-0875-4.

R. M. Hart, B. R. Clark, and S. E. Bolyard. Digital surfaces and thicknesses of selected hydrogeologic units within the Mississippi Embayment Regional Aquifer Study (MERAS). Technical report, 2008.

P. D. Hays, K. J. Knierim, B. Breaker, D. A. Westerman, and B. R. Clark. Hydrogeology and hydrologic conditions of the Ozark Plateaus aquifer system. *U.S. Geological Survey Scientific Investigations Report*, (2016-5137):61, 2016.

D. C. Helm. Horizontal aquifer movement in a theis-thiem confined system. *Water Resources Research*, 30, 1994. ISSN 19447973. doi: 10.1029/94WR00030.

L. S. G. D. L. Hoffmann, J. and A. Wilson. Modflow-2000 ground-water model—user guide to the subsidence and aquifer-system compaction (sub) package. Technical report, 2003.

X. Hu and R. Bürgmann. Aquifer deformation and active faulting in Salt Lake Valley, Utah, USA. *Earth and Planetary Science Letters*, 547:116471, 2020. ISSN 0012-821X. doi: 10.1016/J.EPSL.2020.116471.

J. L. Imes. Analysis of the effect of pumping on groundwater flow in the Springfield Plateau and Ozark Aquifers near Springfield, Missouri. *Water Resources Investigations Report*, 89-4079, 1989.

J. L. Imes and L. F. Emmett. Geohydrology of the Ozark Plateaus aquifer system in parts of Missouri, Arkansas, Oklahoma, and Kansas. *US Geological Survey Professional Paper*, 1414 D, 1994. ISSN 10449612. doi: 10.3133/pp1414d.

C. W. Johnson, Y. Fu, and R. Bürgmann. Seasonal water storage, stress modulation, and California seismicity. *Science (New York, N.Y.)*, 356(6343):1161–1164, 2017. ISSN 1095-9203. doi: 10.1126/science.aak9547.

K. L. Johnson. *Contact Mechanics*. Cambridge University Press, 1987. ISBN 9780521347969.

N. E. King, D. Argus, J. Langbein, D. C. Agnew, G. Bawden, R. S. Dollar, Z. Liu, D. Galloway, E. Reichard, A. Yong, F. H. Webb, Y. Bock, K. Stark, and D. Barseghian. Space geodetic observation of expansion of the San Gabriel Valley, California, aquifer system, during heavy rainfall in winter 2004–2005. *Journal of Geophysical Research*, 112(B3):B03409, 2007. ISSN 0148-0227. doi: 10.1029/2006JB004448.

K. J. Knierim, A. M. Nottmeier, S. Worland, D. A. Westerman, and B. R. Clark. Challenges for creating a site-specific groundwater-use record for the Ozark Plateaus aquifer system (central USA) from 1900 to 2010. *Hydrogeology Journal*, 2017. doi: 10.1007/s10040-017-1593-1.

J. Kusche, R. Schmidt, S. Petrovic, and R. Rietbroek. Decorrelated GRACE time-variable gravity solutions by GFZ, and their validation using a hydrological model. *Journal of Geodesy*, 83(10):903–913, 2009.

S. Larochelle, A. Gualandi, K. Chanard, and J. P. Avouac. Identification and extraction of seasonal geodetic signals due to surface load variations. *Journal of Geophysical Research: Solid Earth*, 123(12):11,031–11,047, 2018. ISSN 21699356. doi: 10.1029/2018JB016607.

W. Li, T. van Dam, Z. Li, and Y. Shen. Annual variation detected by GPS, GRACE and loading models. *Studia Geophysica et Geodaetica*, 60(4):608–621, 2016.

L. Longuevergne, N. Florsch, and P. Elsass. Extracting coherent regional information from local measurements with Karhunen-Loève transform: Case study of an alluvial aquifer (Rhine valley, France and Germany). *Water Resources Research*, 43, 4 2007. ISSN 00431397. doi: 10.1029/2006WR005000. URL `http://doi.wiley.com/10.1029/2006WR005000`.

MATLAB. *9.3.0.713579 (R2017b)*. The MathWorks Inc., Natick, Massachusetts, 2017.

C. Matonti, Y. Guglielmi, S. Viseur, P. Bruna, J. Borgomano, C. Dahl, and L. Marié. Heterogeneities and diagenetic control on the spatial distribution of carbonate rocks acoustic properties at the outcrop scale. *Tectonophysics*, 638:94–111, jan 2015. ISSN 0040-1951. doi: 10.1016/J.TECTO.2014.10.020. URL `https://www.sciencedirect.com/science/article/pii/S0040195114005666`.

S. Michel, A. Gualandi, and J.-P. Avouac. Interseismic coupling and slow slip events on the cascadia megathrust. *Pure and Applied Geophysics*, 176(9):3867–3891, 2019.

M. M. Miller, M. Shirzaei, and D. Argus. Aquifer mechanical properties and decelerated compaction in Tucson, Arizona. *Journal of Geophysical Research: Solid Earth*, 122(10):8402–8416, 2017. ISSN 21699313. doi: 10.1002/2017JB014531.

T. Mura. *General Theory of Eigenstrains*. Springer Netherlands, 1982. doi: 10.1007/978-94-011-9306-1_1.

C. Ojha, M. Shirzaei, S. Werth, D. F. Argus, and T. G. Farr. Sustained groundwater loss in California's Central Valley exacerbated by intense drought periods. *Water Resources Research*, 54(7):4449–4460, 2018. ISSN 0043-1397. doi: 10.1029/2017WR022250.

K. J. Ouellette, C. de Linage, and J. S. Famiglietti. Estimating snow water equivalent from GPS vertical site-position observations in the western United States. *Water Resources Research*, 49(5):2508–2518, 2013. ISSN 00431397. doi: 10.1002/wrcr.20173.

B. Riel, M. Simons, D. Ponti, P. Agram, and R. Jolivet. Quantifying ground deformation in the Los Angeles and Santa Ana coastal basins due to groundwater withdrawal. *Water Resources Research*, 54(5):3557–3582, 2018. ISSN 0043-1397. doi: 10.1029/2017WR021978.

S. Roberts and R. Everson, editors. *Independent Component Analysis*. Cambridge University Press, mar 2001. ISBN 9780521792981. doi: 10.1017/CBO9780511624148.

E. Serpelloni, F. Pintori, A. Gualandi, E. Scoccimarro, A. Cavaliere, L. Anderlini, M. E. Belardinelli, and M. Todesco. Hydrologically induced karst deformation: Insights From GPS measurements in the Adria-Eurasia plate boundary zone. *Journal of Geophysical Research: Solid Earth*, 123(5):4413–4430, 2018. ISSN 2169-9313. doi: 10.1002/2017JB015252.

I. Shiklomanov. World fresh water resources. In P. H. Gleick, editor, *Water in Crisis: A Guide to the World's Fresh Water Resources*. Oxford University Press, 1993. ISBN 0195076281.

F. Silverii, N. D'Agostino, M. Métois, F. Fiorillo, and G. Ventafridda. Transient deformation of karst aquifers due to seasonal and multiyear groundwater variations observed by GPS in southern Apennines (Italy). *Journal of Geophysical Research: Solid Earth*, 121(11):8315–8337, nov 2016. ISSN 2169-9313. doi: 10.1002/2016JB013361.

F. Silverii, N. D'Agostino, A. A. Borsa, S. Calcaterra, P. Gambino, R. Giuliani, and M. Mattone. Transient crustal deformation from karst aquifers hydrology in the Apennines (Italy). *Earth and Planetary Science Letters*, 506:23–37, jan 2019. ISSN 0012-821X. doi: 10.1016/J.EPSL.2018.10.019.

B. D. Tapley, S. Bettadpur, J. C. Ries, P. F. Thompson, and M. M. Watkins. GRACE measurements of mass variability in the earth system. *Science*, 305(5683):503–505, 2004.

V. C. Tsai. A model for seasonal changes in GPS positions and seismic wave speeds due to thermoelastic and hydrologic variations. *Journal of Geophysical Research*, 116(B4):B04404, apr 2011. ISSN 0148-0227. doi: 10.1029/2010JB008156.

T. van Dam, J. Wahr, P. C. D. Milly, A. B. Shmakin, G. Blewitt, D. Lavallée, and K. M. Larson. Crustal displacements due to continental water loading. *Geophysical Research Letters*, 28(4):651–654, 2001. ISSN 00948276. doi: 10.1029/2000GL012120.

M. Vergnolle, A. Walpersdorf, V. Kostoglodov, P. Tregoning, J. Santiago, N. Cotte, and S. Franco. Slow slip events in mexico revised from the processing of 11 year GPS observations. *Journal of Geophysical Research: Solid Earth*, 115(B8), 2010.

A. Verruijt. Elastostatics of a Half Space. In *An Introduction to Soil Dynamics*. 2009. ISBN 9789048134410. doi: 10.1007/978-90-481-3441-0.

J. B. Walsh. The effect of cracks on the compressibility of rock. *Journal of Geophysical Research (1896-1977)*, 70(2):381–389, 1965. doi: https://doi.org/10.1029/JZ070i002p00381.

H. F. Wang. *Theory of Linear Poroelasticity with Applications to Geomechanics and Hydrogeology*. Princeton University Press, 2000. ISBN 9780691037462.

D. A. Westerman, J. A. Gillip, J. M. Richards, P. D. Hays, and B. R. Clark. Altitudes and thicknesses of hydrogeologic units of the Ozark Plateaus Aquifer System in Arkansas, Kansas, Missouri, and Oklahoma. *U.S. Geological Survey Scientific Investigations Report*, (2016-5130):32, 2016.

B. A. Wisely and D. Schmidt. Deciphering vertical deformation and poroelastic parameters in a tectonically active fault-bound aquifer using InSAR and well level data, San Bernardino basin, California. *Geophysical Journal International*, 181:1185–1200, 3 2010. ISSN 0956540X. doi: 10.1111/j.1365-246X.2010.04568.x. URL `https://academic.oup.com/gji/article-lookup/doi/10.1111/j.1365-246X.2010.04568.x`.

Chapter 3

VERTICAL AND HORIZONTAL POROELASTIC DEFORMATION DRIVEN BY GROUNDWATER EXTRACTION IN THE SACRAMENTO VALLEY, CALIFORNIA

To be submitted as:

S. Larochelle, K. Chanard, M. Dalaison, L. Fleitout, J. Fortin, R. Jolivet, L. Longuevergne, D. Argus, and J.-P. Avouac. Vertical and horizontal poroelastic deformation driven by groundwater extraction in the Sacramento Valley, California.

3.1 Introduction

Groundwater makes up approximately 99% of all liquid freshwater on Earth and supplies roughly 25% of the global demand for freshwater (United Nations, 2022). With climate change increasing the likelihood and intensity of extreme weather events like droughts (IPCC, 2022) and with groundwater being more resilient to these changes than surface water, groundwater is bound to become an even more vital resource in the near future. Characterizing and understanding the inner workings of groundwater systems is thus crucial and necessary to ensure that it is being used sustainably.

In California, decades of unsustainable extraction have already caused significant loss of groundwater storage capacity as suggested by meters of permanent land subsidence (Galloway et al., 1999). This has led California's Sustainable Groundwater Management Act to designate 21 of its 143 groundwater subbasins as *critically overdrafted* (CA-DWR, 2021) and has prompted a number of studies investigating the process of irreversible storage depletion, notably in the San Joaquin Valley which makes up the southern 2/3 of the Central Valley aquifer (Figure 3.1a) (Faunt et al., 2016; Smith et al., 2017; Ojha et al., 2018; Chaussard and Farr, 2019; Gualandi and Liu, 2021; Neely et al., 2021). The Sacramento Valley, which makes up the other 1/3, is not yet considered critically stressed but is monitored through an extensive network of observation wells (Figure 3.1b). It thus serves as an ideal case study to further our understanding of relatively healthy aquifer systems and hence prevent them from reaching overdrafted conditions.

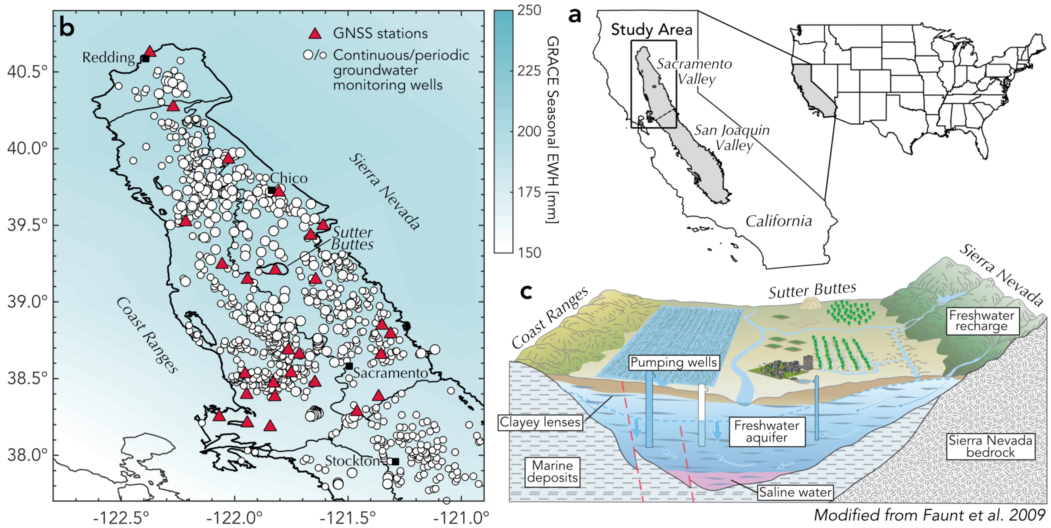

Figure 3.1: Hydrogeological setting and datasets of the Sacramento Valley. (a) Geographic location of the Sacramento Valley. (b) Position of GNSS stations (triangles) and continuous (larger circles) and periodic (smaller circles) groundwater monitoring wells used in this study. The colormap indicates the seasonal equivalent water height measured by GRACE. (c) Schematic hydrogeologic cross-section of the Sacramento Valley modified from Faunt (2009).

In this study, we use space-based geodesy to characterize the recoverable, so-called *poroelastic* response of the Sacramento Valley to seasonal and multiannual fluctuations in groundwater levels. In recent years, satellite-based techniques such as GNSS, InSAR, and GRACE have provided new ways to monitor groundwater processes by measuring the associated ground deformation (e.g., Amelung et al., 1999; Wisely and Schmidt, 2010; Chaussard et al., 2014; Riel et al., 2018; Hu and Bürgmann, 2020) and gravimetric fluctuations (e.g., Scanlon et al., 2012; Frappart and Ramillien, 2018). In particular, such measurements can provide constraints on an aquifer's elastic storage capacity. Remote sensing techniques are also promising for assessing and monitoring groundwater resources in less-instrumented regions. Indeed, the high costs and logistics associated with installation and maintenance of a groundwater monitoring well network can be a major obstacle to sustainable groundwater exploitation (United Nations, 2022). We thus hope that our work on the highly-instrumented Sacramento Valley can serve as a calibration between space-based and in situ measurements.

While the eventual goal is to combine InSAR and GNSS techniques to provide a complete spatiotemporal characterization at high spatial and temporal resolutions, here we focus on analysing GNSS time series which provide a daily record of 3D deformation in the Sacramento Valley over a 17-year period. The manuscript is organized as follows: We first describe and characterize spatiotemporal variations in groundwater levels in Section 3.2 before extracting the associated poroelastic deformation from GNSS time series in Section 3.3 and relating the two sets of observations through modeling in Section 3.4.

3.2 Characterizing Groundwater Level Variations in the Sacramento Valley

In this section, we first summarize the hydrogeologic setting and groundwater level data of the study area before applying the methodology of Larochelle et al. (2022) to extract the main sources of signals from continuous groundwater time series. We then extend the recovered spatial distribution of groundwater variations by making use of incomplete, periodic time series.

3.2.1 Hydrogeologic Setting of the Sacramento Valley

The Sacramento Valley makes up the northern one-third of the long and narrow Central Valley sedimentary basin nestled between the Sierra Nevada to the east, the Klamath Mountains to the north and the Coast Ranges to the west (Figure 3.1ab). The basin is filled with continental sediments originating from the surrounding mountain ranges and is underlain by marine deposits and a crystalline basement which crops out in nearby mountains (Figure 3.1c). The continental deposits, which average 730 meters in thickness in the Central Valley, consist of coarser sediments interlaced with discontinuous lenses of low-permeability, fine-grained clay (Page, 1986). As such, the entire layer of continental deposits can be conceptualized as a single aquifer unit with spatially heterogeneous confinement and hydraulic properties varying according to the percentage of coarse-grained materials and the density of wells, which increases the vertical conductivity of the system (Williamson et al., 1989; Faunt, 2009). The Sutter Buttes at the center of Sacramento Valley are the remnants of a volcanic plug and hence are not part of the aquifer system.

While precipitations do occur in the semi-arid valley, aquifer recharge mostly comes from the Sierra Nevada and Klamath Mountains snowpacks whose runoff is regulated through a series of dammed reservoirs at the mountains base (Faunt et al., 2016). From there, surface water is distributed in the valley through a system of canals and streams as well as through the Sacramento River which divides the valley in half. When supplies of surface water run low during drier summer months and droughts,

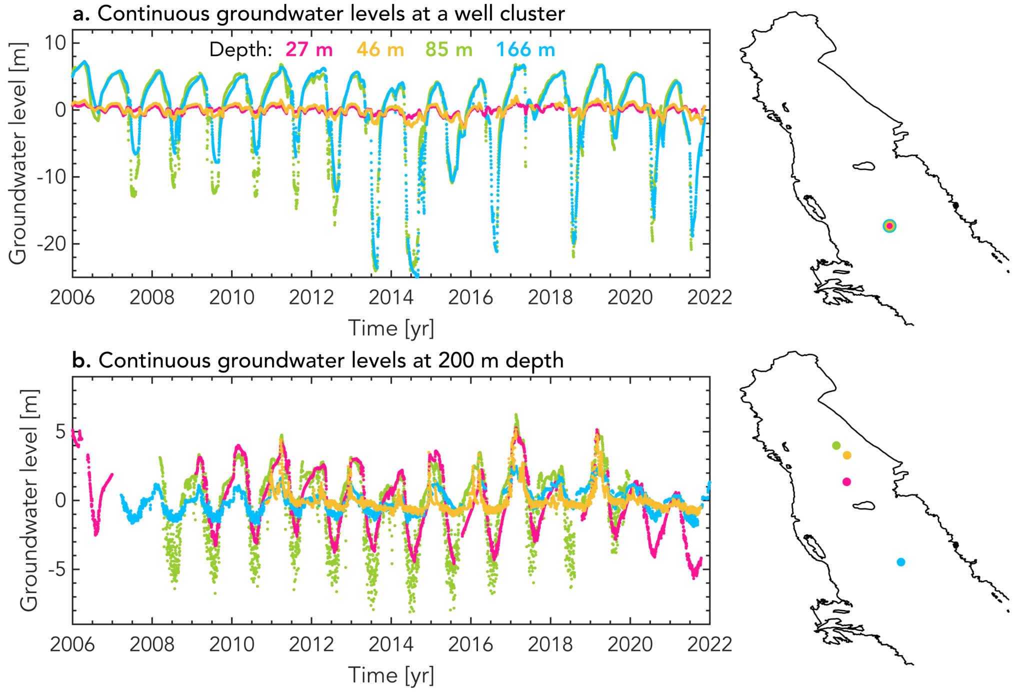

Figure 3.2: Sample continuous groundwater level time series for (a) a well cluster at different depths and (b) wells at 200 m depth. The locations of the measurements are indicated on the right. Note that the time series have been recentered at 0 for comparison purposes but they were not detrended.

groundwater extraction increases, meeting roughly one-third of the region's water needs in an average year (CA-DWR, 2021).

3.2.2 Continuous Groundwater Level Time Series

As part of its efforts to regulate groundwater usage throughout California, the Department of Water Resources (CA-DWR) operates a network of groundwater monitoring wells equipped with automated recorders that continuously track fluctuations in groundwater levels, the vast majority of which is located in the Sacramento Valley. In this work, we make use of the daily mean time series recorded at these wells (`https://data.cnra.ca.gov/dataset/continuous-groundwater-level-measurements`). Of the 481 wells located in the study area, we retain the 459 stations with at least 10 data points during the study period of 2006 to 2022. The retained stations are indicated by the larger circles in Figure 3.1b. Note that since these wells often come in closely-spaced clusters probing groundwater levels at different depths, not all 459 of them are visible in this map view.

Figure 3.2a shows examples of continuous groundwater level measurements recorded at different depths at one such cluster and Figure 3.2b shows measurements at the same depth of 200 m at different locations throughout the valley. The sample time series clearly illustrate the heterogeneous but correlated nature of spatiotemporal groundwater variations in the Sacramento Valley. In particular, the characteristic seasonal cycle of groundwater pumping (sinking levels) and recharge (recovering levels) can be observed at most monitoring stations. In light of these observations, we follow the methodology of Larochelle et al. (2022) which uses an Independent Component Analysis (ICA) to identify and characterize the most important modes of temporal variations and hence most likely to induce significant geodetic deformation.

3.2.3 Extracting the Dominant Temporal Functions from Continuous Groundwater Levels

Here we perform an ICA on all the selected continuous groundwater time series to extract the sources of signals — i.e., Independent Components (IC) — that dominate the dataset. We use the variational Bayesian form of ICA (vbICA) (Choudrey, 2002; Gualandi et al., 2016) which isolates ICs by maximizing the statistical independence of their temporal probability density functions. Each IC is expressed in the space and time domain with a temporal function V_i, a spatial distribution U_i and a weighting factor S_i as $\mathrm{IC}_i = U_i S_i V_i^T$. Since we are primarily interested in seasonal and multiannual deformation and the techniques requires a zero mean, we perform the ICA on detrended time series.

Figure 3.3 shows the temporal functions V_i (a, b) and weighted spatial distributions $S_i U_i$ (c, d) of a 2-component ICA with IC_1 and IC_2 explaining 42% and 4% of data variance, respectively. The independent components are ordered according to the data variance they explain. Note that analyses with a higher number of components result in additional components that explain an even smaller portion of data variance (i.e., 1.2% for the 3$^{\mathrm{rd}}$ component). Both recovered components present temporal functions V_1 and V_2 (Figure 3.3ab) that are dominated by seasonal and multiannual fluctuations reflecting variations in groundwater pumping rates and the regional hydroclimate. Figure 3.4 confirms that groundwater levels in the Sacramento Valley, as depicted by the dominant temporal function V_1, correlate well with drought intensity characterized with the U.S. Drought Monitor (USDM) classification system: Groundwater levels decline during intense drought conditions and recover during less dry periods.

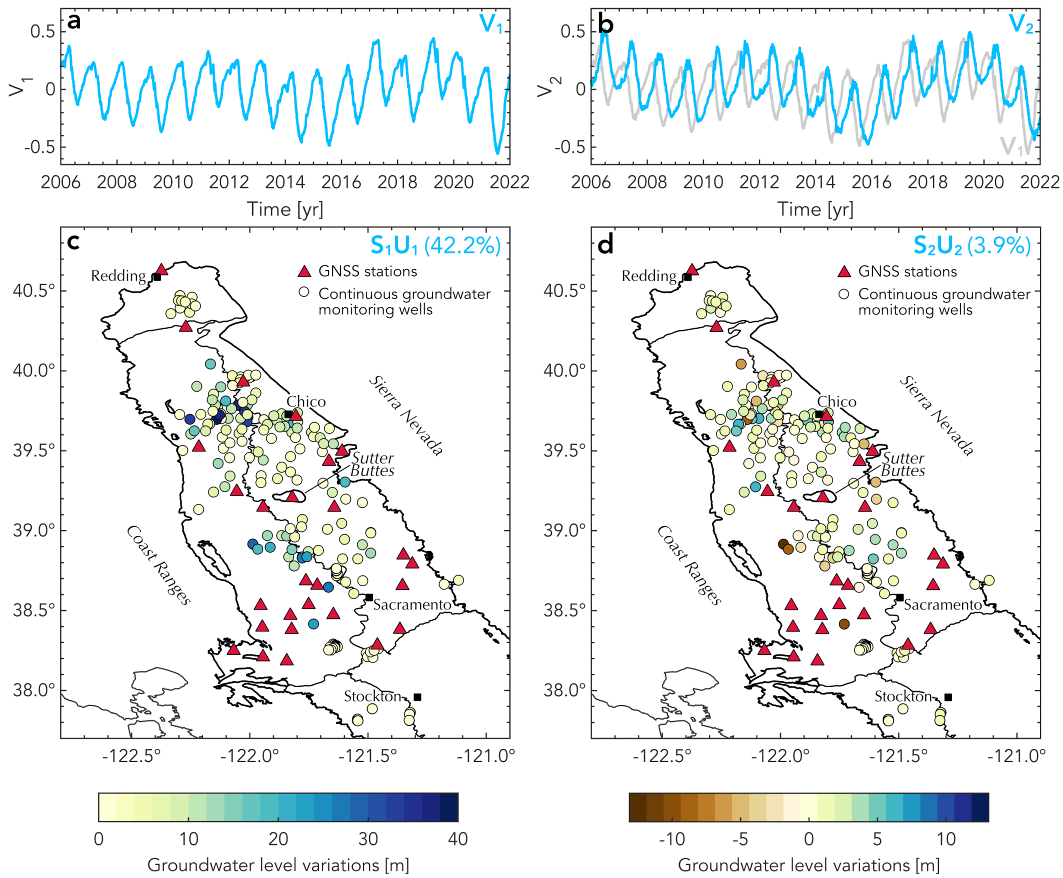

Figure 3.3: Independent Components (IC) extracted from the continuous groundwater dataset. (a,b) Temporal evolution and (c,d) spatial distribution associated with the 2 extracted ICs. Note that V_1 is reproduced in grey in panel (b) for comparison purposes. The first and second components account for 42.2% and 3.9% of the data variance, respectively.

As for the second component, Figure 3.3b shows that V_2 is essentially a time-shifted version of V_1 delayed by roughly 4 months. Hence, IC_2 accounts for temporal phase differences likely due to the different well depths and usage as well as to hydraulic heterogeneities of the aquifer system. Similar to the analysis of Larochelle et al. (2022), IC_1 displays an entirely positive spatial distribution with groundwater variations of over 40 m whereas IC_2 presents both positive and negative, more localized variations of at most 10 to 15 m. However, since IC_1 explains 10 times more data variance than IC_2 and IC_2 only incrementally improves the recovery of poroelastic displacements in Section 3.3.3, we choose to focus the remainder of the analysis on IC_1.

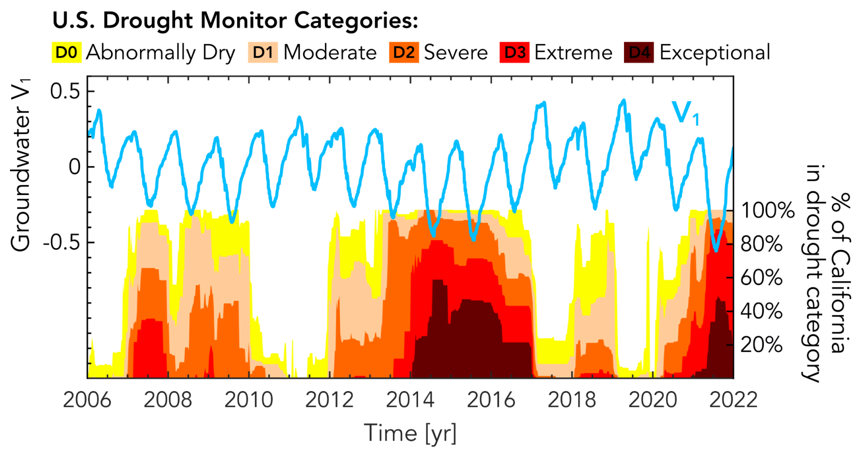

Figure 3.4: Comparison of groundwater temporal function and drought intensity. The histogram indicates the percentage of California in a given drought category, ranging from abnormally dry (yellow) to exceptional drought (dark red) as classified by the U.S. Drought Monitor (USDM) (`https://www.drought.gov/states/california#historical-conditions`)

3.2.4 Extending the Spatial Distribution with Periodic Groundwater Level Measurements

As Figure 3.3c indicates, there is unfortunately little overlap between the positions of the continuously monitoring wells and GNSS stations. Since poroelastic deformation is highly sensitive to local changes in groundwater, it is crucial to obtain an estimate of these variations as close as possible to the GNSS sites. Thankfully, in addition to the continuous network, CA-DWR also maintains an extensive database of ‘periodic’ groundwater level time series with intermittent recordings ranging from (mostly) biannual to daily frequencies (`https://data.cnra.ca.gov/dataset/periodic-groundwater-level-measurements`). We decided not to analyse the periodic data with ICA because the algorithm works best with mostly complete time series with recordings at the same epochs. Nevertheless, these intermittent time series are still highly valuable to estimate the contributions of IC_1 throughout the study area by projecting them on temporal function V_1 from the continuous dataset.

Of the 23437 periodic wells in the Central Valley, we only retain the 5831 time series with at least 10 data points during 2006-2022. Note that here we consider wells in the entire Central Valley in order to approximate the deformation induced by groundwater variations occurring in the San Joaquin Valley at GNSS stations within the Sacramento Valley (see Section 3.4). Figure 3.5 shows examples of data recorded at 4 periodic wells along with their projection onto V_1. To ensure that the

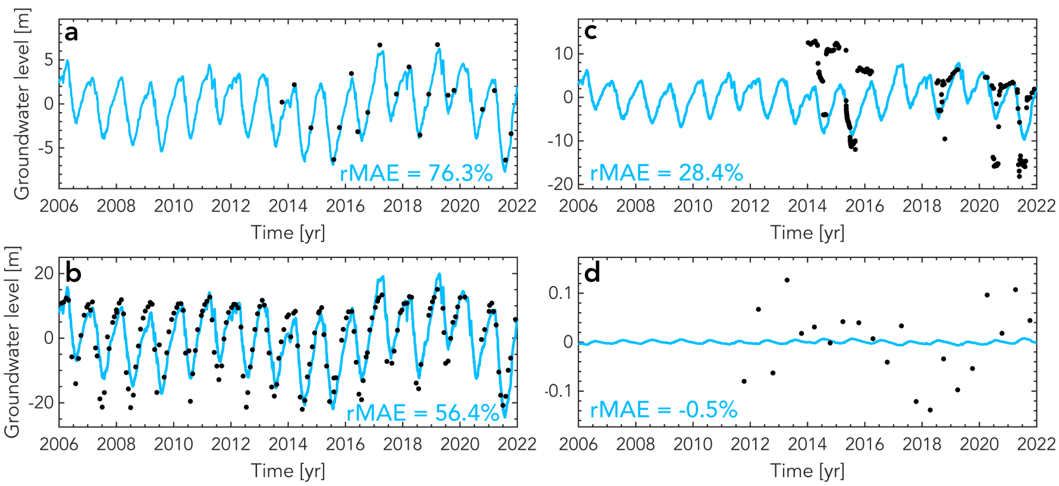

Figure 3.5: Sample periodic groundwater time series (black dots) and their projection onto temporal function V_1 from the continuous groundwater ICA analysis (blue line). The reduction in mean absolute error ($rMAE$) is indicated in each case. (a,b) Sample time series with $rMAE > 30\%$ retained for further analysis. (c,d) Sample times series with $rMAE < 30\%$ not retained for further analysis.

periodic time series are well characterized by V_1, we only keep those for which the projection results in a reduction in mean absolute error ($rMAE$) of at least 30 % where $rMAE$ is calculated as:

$$rMAE = \left(\frac{MAE_o - MAE_{proj}}{MAE_o} \right) \times 100. \tag{3.1}$$

The time series in Figure 3.5cd which have $rMAE$s of 28.3% and -0.5% are thus dismissed from the rest of the analysis. Note that we retain 5 additional wells with $25\% < rMAE < 30\%$ to be able extend the spatial distribution towards the San Francisco Bay Area where 3 GNSS stations are located. We also neglect a well with an $rMAE$ of 39.2% located in an area of relatively low well density (south of the Sutter Buttes) as it displays spurious high-amplitude fluctuations that are not well explained by V_1 and otherwise dominate the spatial interpolation at this location. Altogether, this procedure produces an additional 1110 data points with which to extend the spatial distribution of IC_1.

Figure 3.6 illustrates the resulting IC_1 distribution obtained by (1) combining the continuous S_1U_1 values and the periodic projection factors and (2) interpolating between these data points with a triangulation-based natural neighbor algorithm (MATLAB, 2017). The spatial interpolation should be quite reliable given the high density of wells in most regions of the aquifer. Variations in areas outside the aquifer boundaries (including the Sutter Buttes) are set to 0. Since we performed

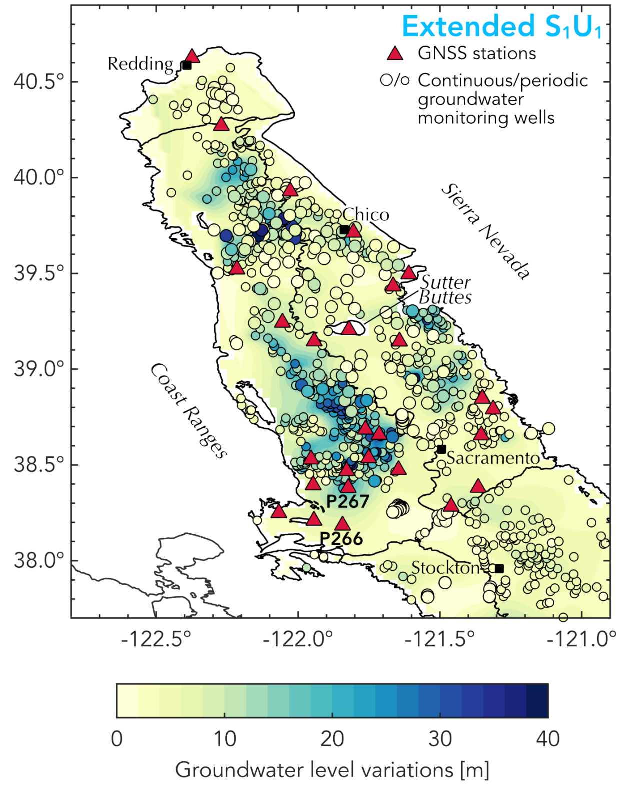

Figure 3.6: Extended distribution of groundwater level variations. The larger circles indicate the spatial distribution of IC_1 as in Figure 3.3c and the smaller circles indicate the amplitude of the projection of periodic groundwater time series onto V_1 for projections with an $rMAE > 30\%$. The background shading shows the spatial distribution of groundwater level variations interpolated from these point measurements. Note that measurements at well clusters sampling different depths are averaged as part of the interpolation.

the ICA analysis and subsequent projections on all retained time series without discriminating between the different well depths, the distribution represents average groundwater variations over the entire sampled aquifer thickness. Notice that the distribution displays a concentrated zone of high groundwater variations around the southwestern part of the valley where a number of GNSS stations are located.

3.3 Extracting Poroelastic Deformation from GNSS Time Series

Now that we have characterized seasonal and multiannual fluctuations of groundwater levels in the Sacramento Valley, we can proceed to extract the associated poroelastic deformation from geodetic time series by making use of the groundwater's temporal behavior after accounting for deformation due to hydrological loading.

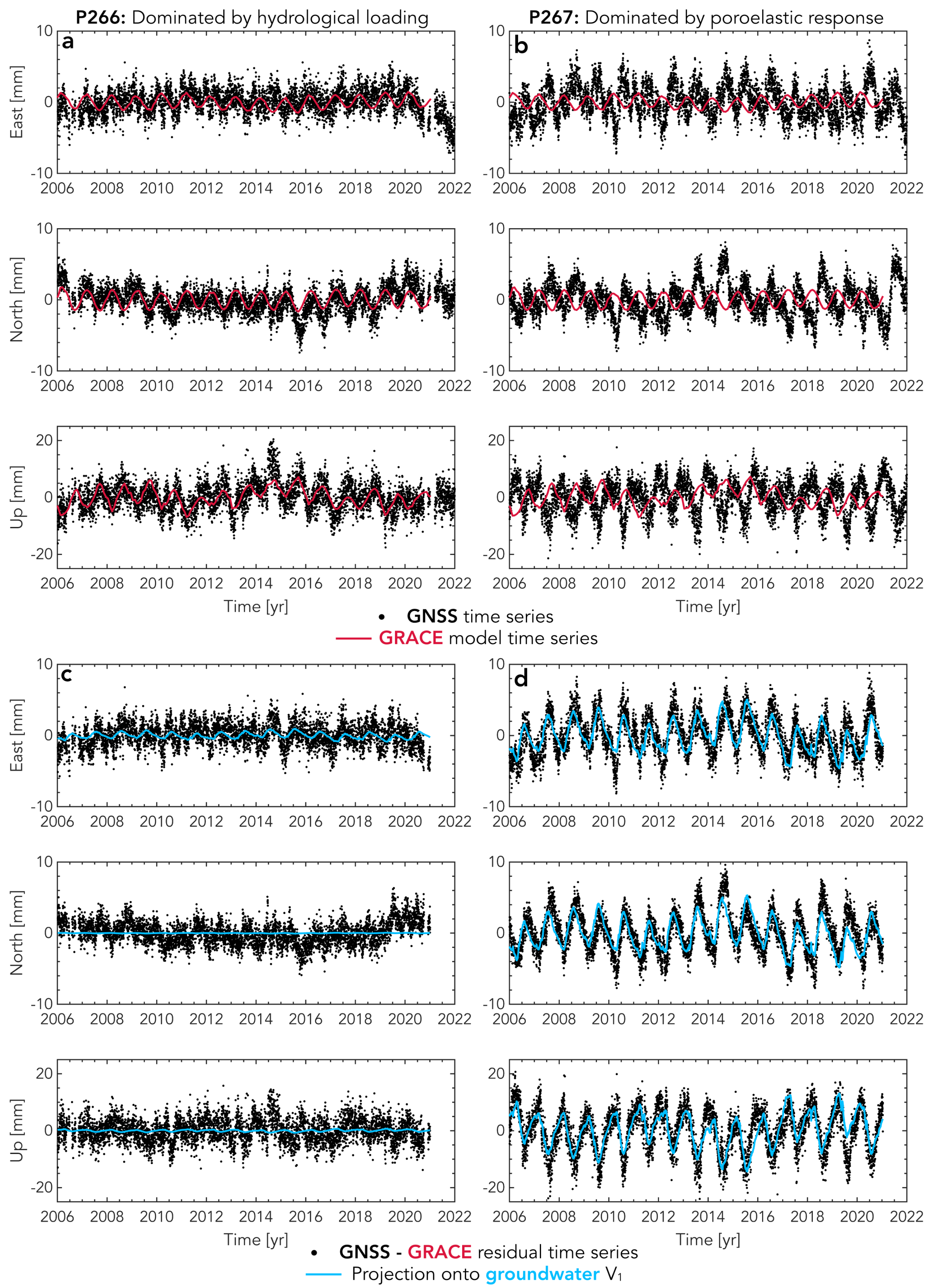

Figure 3.7: Extracting the poroelastic deformation from GNSS time series. (a,b) Detrended and corrected GNSS time series (black dots) and hydrological GRACE loading model (red line) at GNSS stations P266 and P267 (see Figure 3.6 for station locations). (c,d) Residual GNSS minus GRACE model time series (black dots) and their projections onto groundwater temporal function V_1 (blue line).

3.3.1 GNSS Time Series

We use horizontal and vertical daily GNSS position time series determined by the Nevada Geodetic Laboratory (Blewitt et al., 2018) through a Precise Point Positioning processing in ITRF2014 (Altamimi et al., 2016). The GNSS coordinates are expressed in the IGS14 reference frame (Rebischung et al., 2016) and post-processed by the Jet Propulsion Laboratory as described in Argus et al. (2021). We select the 29 stations within the boundaries of the Sacramento Valley with at least 1000 data points (~3 years of data) from 2006 to 2022. Coseismic and maintenance-related offsets as well as secular trends are estimated and removed from the time series by fitting them with a velocity term, potential offsets and a 1-yr sinusoid following the method of Argus et al. (2010). Figure 3.7ab show examples of the resulting detrended and corrected time series at stations P266 and P267 whose positions are indicated in Figure 3.6a.

3.3.2 GRACE Time Series and Global Hydrological Loading Model

We predict the long-wavelength hydrological loading deformation experienced at the GNSS stations using a spherical stratified elastic Earth model loaded with global gravimetric observations of hydrological, atmospheric and non-tidal oceanic mass redistribution derived from the GRACE/GRACE-FO satellites. More specifically, we use the monthly GRACE solution of Gauer et al. (In prep.) — based on previous work by Prevost et al. (2019) — obtained by applying a DDK7 filter to the spherical harmonics solutions of five different processing centers (CSR, GFZ, GRAZ, JPL and GRGS) and performing observational gap filling and spatial filtering by extracting the common modes of variability through a Multichannel Singular Spectrum Analysis (M-SSA) (e.g., Ghil et al., 2002). We compute the resulting deformation at the GNSS sites by using the spherical elastic continental PREM Earth model of Chanard et al. (2018) based on the Love numbers formalism (Farrell, 1972). The degree-1 coefficients of the Earth's gravity field — which are not measured by the GRACE satellites — are estimated by fitting a 1-yr sinusoid to the degree-1 deformation field inverted from residual time series of a global network of GNSS stations and the GRACE loading model from 2006 to 2017.

The combined GRACE, degree-2 to 96, and degree-1 derived displacements time series computed at stations P266 and P267 are shown in Figure 3.7ab. The GNSS displacements at station P266 located in a zone of relatively small groundwater fluctuations at the edge of the aquifer (Figure 3.6) are well explained by the GRACE model, suggesting that deformation at this site is dominated by large-scale hydrological loading. At neighboring station P267 located in the concentrated zone of high groundwater variations, on the other hand, the GRACE model clearly does not match the GNSS displacements. In the following section we show that this is because the area is undergoing important poroelastic deformation in addition to the hydrological loading response.

3.3.3 Projection of Residual GNSS Time Series onto Groundwater Temporal Function

Following the methodology of Larochelle et al. (2022), we first subtract the modeled hydrological loading displacements from the GNSS time series. Since the GRACE solution has monthly time steps, we interpolate the modeled time series at GNSS's daily time steps using a shape-preserving piecewise cubic (*pchip*) interpolation (MATLAB, 2017). The resulting residual time series are shown in Figure 3.7cd. Similar to the periodic groundwater time series in section 3.2.4, we then project these residual time series onto temporal function V_1 characterizing the time evolution of the dominant component in the groundwater dataset.

At station P266 dominated by the hydrological loading response, the noisy residuals lead to small projections (Figure 3.7c), while the larger residuals at station P267 result in a larger amplitude projected signal (Figure 3.7d). The excellent agreement between the residual geodetic time series at station P267 and the groundwater projections suggests that a large portion of the residuals can be attributed to poroelastic deformation and that this deformation occurs concurrently with the groundwater fluctuations captured by V_1 (i.e., no significant temporal phase shift).

Figure 3.8 shows the (peak-to-peak) amplitudes of these projections at all GNSS stations within the study area compared to the spatial distribution of groundwater variations. GNSS stations located in the zone of elevated groundwater fluctuations west of Sacramento exhibit the largest poroelastic displacements and form a clear radial pattern of horizontal and vertical displacements centered on the zone of large groundwater variations. The measured amplitudes of poroelastic displacements and groundwater variations outside this localized zone are also generally in good agreement. In particular, GNSS station SUTB located in the non-sedimentary Sutter Buttes displays negligibly small poroelastic displacements.

A few stations in areas of smaller groundwater variations display negative vertical projection values of at most 5 mm. We believe that these small negative projections represent the deformation induced by more localized hydrological loads not

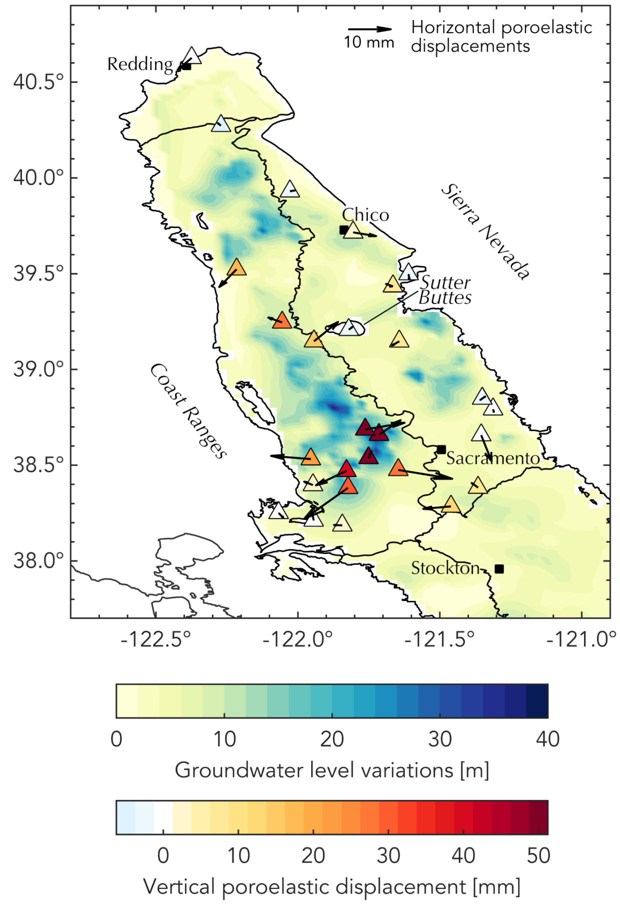

Figure 3.8: Comparison of extracted poroelastic displacements and groundwater variations. The colored triangles indicate the inferred vertical displacements and the black arrows the horizontal displacements. The background colormap shows the same interpolated spatial distribution as Figure 3.6 but without the discrete well data points.

captured by the coarse GRACE measurements. This is especially likely near the mountain ranges which undergo larger, more localized hydrological fluctuations than measured by GRACE (due to its limited 300-400 km resolution (Argus et al., 2017)). Nevertheless, our analysis clearly illustrates that seasonal and multiannual fluctuations in groundwater levels on the order of 10 to 50 m can induce important poroelastic displacements both in the vertical and horizontal directions, with amplitudes reaching 85 mm and 15 mm, respectively.

3.4 Modeling Poroelastic Deformation Due to Groundwater Variations

In this section, we seek to relate our two sets of observations through modeling. We first model surface displacements due to poroelastic perturbations in an homo-

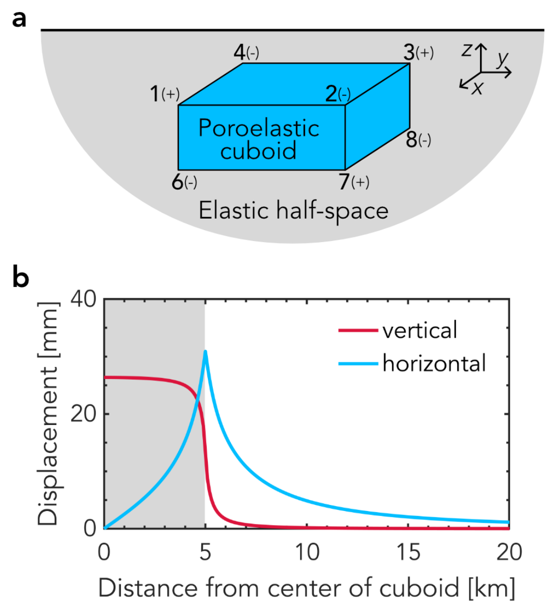

Figure 3.9: (a) Schematic diagram of the poroelastic model for a single cuboid (modified from Kuvshinov (2008)). The vertices are numbered according to the order of summation in Equations 3.2-3.4. (b) Vertical and horizontal displacements (along either x or y) for a single cuboid with a 10×10 km spatial extent, 500 m thickness, $C_m = 2.3 \times 10^{-10}$ Pa^{-1}, $\nu = 0.25$ and $\alpha = 0.8$ subjected to a 20 m increase in groundwater level.

geneous elastic half-space before discussing these results in the context of Fleitout and Chanard (2018) and Larochelle et al. (2022)'s two-layers model which accounts for higher elastic moduli at depth.

Here we make use of Kuvshinov (2008)'s analytical solutions based on Geertsma (1973)'s solution for a point nuclei of poroelastic deformation in an isotropic and homogeneous half-space. More specifically, Kuvshinov (2008) derived analytical solutions for a distributed polyhedral inclusion by integration of Geertsma's solution. The method allows to making use of Green's functions describing an arbitrarily-shaped poroelastic intrusion embedded in an homogeneous half-space.

While this specific formulation has been primarily used to model displacements and stresses associated with hydrocarbon and geothermal energy production (e.g., Smith et al., 2019, 2021; Li et al., 2021), it is equally valid for the case of groundwater pumping and recharge in an aquifer. For comparison, Hu and Bürgmann (2020) and Silverii et al. (2019) have used a finite-strain cuboid framework (Barbot et al., 2017) to model poroelastic displacements in an aquifer setting, but the approach is kinematic and does not directly relate the surface deformation to pore pressure variations. In the case of a simple cuboid intrusion like the one shown in Figure 3.9a, surface displacements ($z = 0$) are obtained by summing the contribution of each vertex labeled in Figure 3.9a as follows (Kuvshinov, 2008; Smith et al., 2021):

$$u_x = \frac{\alpha C_m \Delta p}{4\pi} \sum_{i=1}^{8} (-1)^{i-1} \left[f(\bar{y}, \zeta_-, \bar{x}, r_-) + (3-4\nu) f(\bar{y}, \zeta_+, \bar{x}, r_+) \right] \quad (3.2)$$

$$u_y = \frac{\alpha C_m \Delta p}{4\pi} \sum_{i=1}^{8} (-1)^{i-1} \left[f(\bar{x}, \zeta_-, \bar{y}, r_-) + (3-4\nu) f(\bar{x}, \zeta_+, \bar{y}, r_+) \right] \quad (3.3)$$

$$u_z = \frac{\alpha C_m \Delta p}{4\pi} \sum_{i=1}^{8} (-1)^{i-1} \left[f(\bar{x}, \bar{y}, \zeta_-, r_-) + (3-4\nu) f(\bar{x}, \bar{y}, \zeta_+, r_+) \right] \quad (3.4)$$

where function f is defined as:

$$f(x, y, z, r) = z \arctan\left(\frac{xy}{zr}\right) - x \ln|r + y| - y \ln|r + x| \quad (3.5)$$

and

$$\bar{x} = x_i - x \quad (3.6)$$

$$\bar{y} = y_i - y \quad (3.7)$$

$$\zeta^{\pm} = z_i \mp z \quad (3.8)$$

$$r_{\pm} = \sqrt{\bar{x}^2 + \bar{y}^2 + (\zeta^{\pm})^2} \quad (3.9)$$

describe the distances between the coordinates of each vertex i (x_i, y_i, z_i) and that of an observation point (x, y, z). Δp is the change in pore pressure associated with a change in groundwater level Δh ($\Delta p = \rho g \Delta h$), α is Biot's coefficient, ν the Poisson's ratio and C_m is Geertsma's uniaxial poroelastic expansion coefficient — also known as uniaxial compressibility — related to Young's modulus E and Poisson's ratio ν as (Geertsma, 1973; Wang, 2017):

$$C_m = \frac{\alpha}{E} \frac{(1+\nu)(1-2\nu)}{(1-\nu)}. \quad (3.10)$$

Note that the compressibility C_m reflects the elastic storage capacity of the aquifer system.

Figure 3.9b illustrates the vertical and horizontal displacements resulting from a single 10×10 km, 500 m-thick cuboid subjected to a 20 m increase in groundwater level. Vertical displacement is relatively uniform within the pressurized cuboid and rapidly decays to zero outside the cuboid. Horizontal displacements, on the other hand, peak at the edge of the cuboid and decay much more slowly to zero outside the pressurized zone. The horizontal displacements shown here results from the sharp transition from $\Delta h = 20$ m to $\Delta h = 0$ m.

Here we model the deforming aquifer unit as a series of 2.5×2.5 km cuboids of variable thickness. Since the exact distribution of aquifer thickness over which poroelastic deformation occurs is unknown, we use the thickness of the continental deposits layer shown in Figure 3.10a as a proxy, keeping in mind that it represents an upper bound estimate of the deforming aquifer thickness. The thickness distribution was interpolated from Figure 8 of Williamson et al. (1989) by the USGS (`https://water.usgs.gov/lookup/getspatial?ds10cnrlvl_a10`). Given that we use the entire continental deposits layer for the aquifer thickness and that the model is virtually insensitive to the depth of aquifer unit for the given set of parameters, we set the depth equal to zero for simplicity. Each cuboid is then assigned an average pore pressure value according to the groundwater level distribution of Figure 3.6. Using these aquifer thickness and pore pressure distributions as inputs and assuming standard values of $\alpha = 0.8$ and $\nu = 0.25$, we can invert the horizontal and poroelastic displacements for the best-fit compressibility C_m of 2.3×10^{-10} Pa^{-1} using the exact linear least-square solution. Note that uniformly smaller aquifer thicknesses would simply result in a larger inverted C_m as deformation is proportional to bC_m where b is the aquifer thickness.

The displacements associated with this best-fitting model are shown in Figure 3.10b. Overall, we find that the measured vertical poroelastic displacements (triangles) coincide quite well with the modeled vertical displacements (background colormap) owing to the previously noted correlation between deformation and groundwater variations (Figure 3.8). The model also roughly predicts the amplitude and direction of horizontal displacements at a number of stations undergoing important (i.e., $\sim>$ 15 mm) vertical deformation. However, towards the edges of the valley where groundwater variations, aquifer thickness and vertical displacements are generally smaller, the model consistently overpredicts the observed amplitude of horizontal displacements.

As discussed in Larochelle et al. (2022), horizontal poroelastic deformation is inherently more difficult to track and model than vertical deformation. Notably, as can been seen in Figures 3.9b and 3.10b, while vertical displacements primarily depend on the local amplitudes of pore pressure variations, horizontal displacements reflect the local spatial gradient of the pore pressure field. Horizontal displacements are thus much more sensitive to spatial variations of the pore pressure distribution.

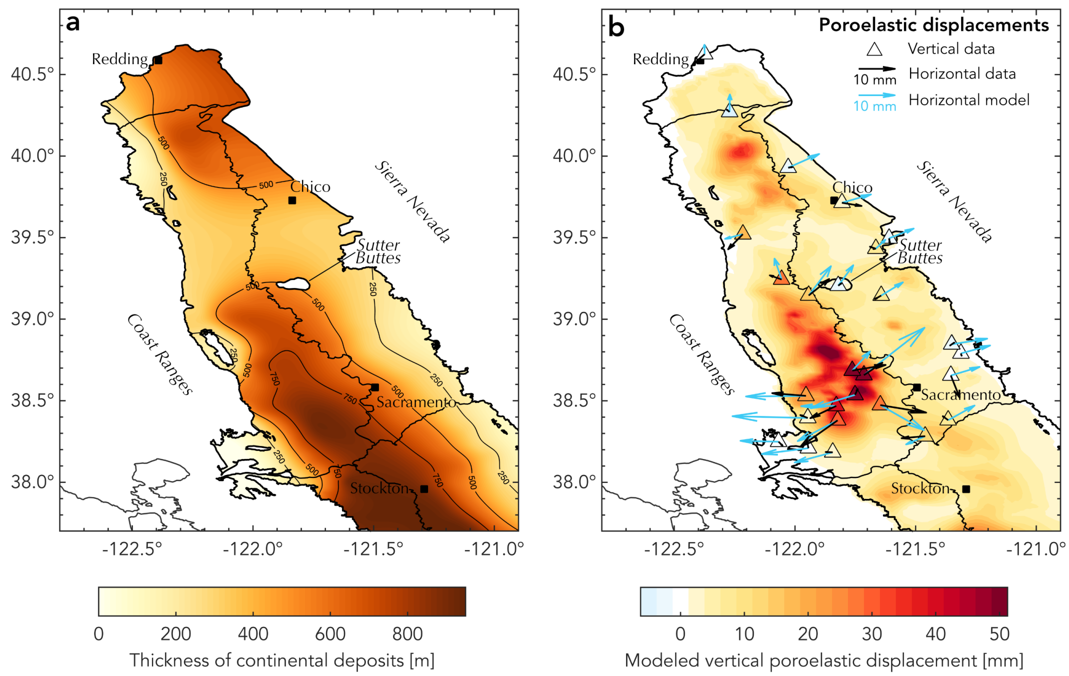

Figure 3.10: Aquifer thickness and modeled poroelastic displacements. (a) Thickness of continental deposit layer taken as a proxy for the thickness of the aquifer unit. (b) Comparison of modeled and measured poroelastic displacements. The arrows indicate the measured (black) and modeled (blue) horizontal displacements while the colored spatial distribution and triangles indicate the modeled and measured vertical displacements, respectively.

Groundwater variations which are not perfectly represented in our model — due in part to the discrete nature of monitoring wells — therefore explains at least part of the observed discrepancies. The overpredicted horizontal displacements at the two GNSS stations at the center of the concentrated zone of elevated groundwater variations, for example, may partially result from inaccurately sharp spatial gradients in the interpolated pore pressure field. The same argument can be made about potential inaccuracies in the aquifer thickness distribution. In particular, groundwater variations may not in fact occur over the entire thickness of the continental deposits, as is assumed in the current model.

Moreover, the present model assumes that the pore pressure perturbations occur in a half-space with homogeneous elastic moduli, here embodied by the constant compressibility coefficient $C_m = 2.3 \times 10^{-10}$ Pa^{-1} equivalent to a Young's modulus E of 2.9 GPa ($\nu = 0.25$ and $\alpha = 0.8$). Yet, elastic properties are known to vary both laterally and with depth. Given the good agreement between the observed vertical displacements and those predicted by the homogeneous half-space model

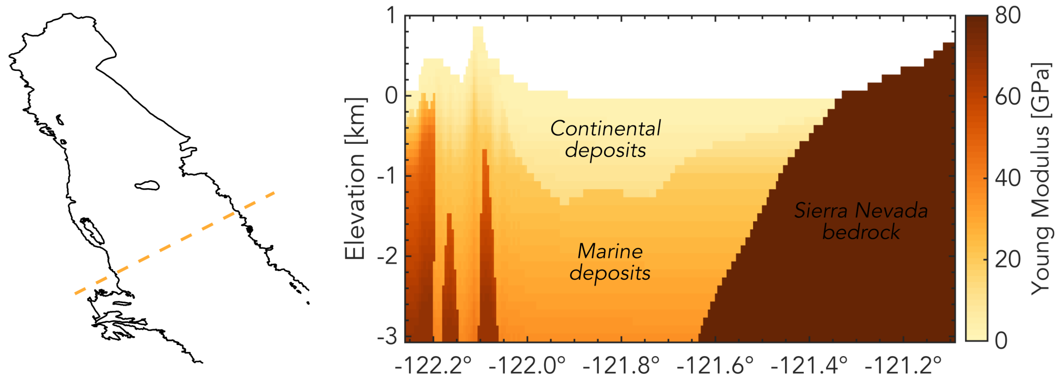

Figure 3.11: Typical cross-section of Young's modulus inferred from the USGS San Francisco Bay Region seismic velocity model.

(Figure 3.10b) as well as the relatively uniform bulk composition of the Sacramento Valley (Figure 3.1c), lateral heterogeneities in the elastic properties of the deforming aquifer unit do not appear to be a dominant effect.

In contrast, elastic properties certainly vary with depth as illustrated by Figure 3.11 which shows a typical cross section of Young's moduli in the Sacramento Valley inferred from the USGS San Francisco Bay Region seismic velocity model (Version 08.3.0, `https://baagaard-usgs.github.io/sfcvm-website/models/seismic.html`). In particular, the layer of relatively weak continental deposits making up the aquifer unit (~ 1 - 10 GPa) sits on top of stiffer marine sediments (~ 20 - 50 GPa) and on the much stronger crystalline bedrock of the Sierra Nevada (~ 80 GPa). It is clear from this picture that the aquifer unit does not exist in a homogeneous half-space and that the stronger basement might restrict the horizontal poroelastic displacements.

Fleitout and Chanard (2018) and Larochelle et al. (2022) developed semi-analytical solutions that describe horizontal displacements arising from poroelastic eigenstrains in a weak aquifer layer with a Young's modulus of E_{aq} overlaying a stronger basement with modulus E_{base}. The solution is based on a *shallow water* approximation, meaning that it remains valid as long as the horizontal extent of the aquifer is large compared to the aquifer depth. According to this approximation, shear stresses at the base of the aquifer, induced by poroelastic eigenstrains within the aquifer, do not depend on E_{base}. The horizontal displacements at the surface correspond to the deformation of the subtratum with modulus E_{base} due to these shear stresses. The horizontal displacements are then simply proportional to $1/E_{base}$ and converge to

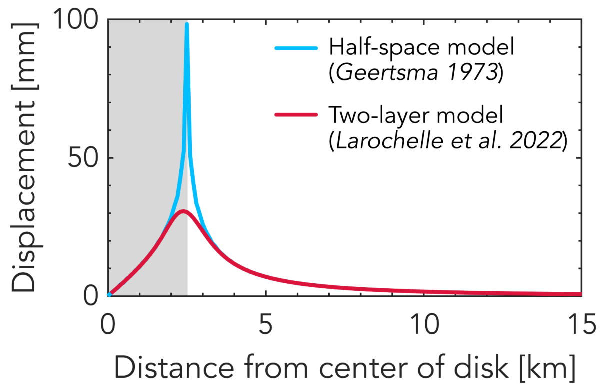

Figure 3.12: Comparison of analytical poroelastic solutions for a disk aquifer with $E_{aq} = E_{base}$.

the homogeneous half-space solution when E_{base} is set equal to E_{aq}, as illustrated for the simple case of a disk-shaped poroelastic perturbation in Figure 3.12.

Figure 3.13 shows the displacements predicted by this two-layer model for an average basement Young's modulus of 35 GPa. As expected, the resulting displacements are much smaller than those predicted by the homogeneous half-space solution. Restrained poroelastic deformation due to the strong basement is thus a potential candidate to explain the smaller-than-predicted poroelastic displacements observed near aquifer boundaries. This is especially true for GNSS stations in close proximity to the Sierra Nevada mountains.

This model alone, however, cannot explain the large horizontal displacements observed towards the center of the aquifer. We hypothesize that these large displacements might be accommodated by readily-deformable materials at the base of the aquifer. The clay lenses that make up a significant part of the continental deposits (Figure 3.1c) are a likely candidate. Considering a typical cross-section from Faunt (2009)'s texture model which shows the percentage of coarse-grain materials (Figure 3.14), fine-grained materials such as clays do appear to be present close to the base of the aquifer.

3.5 Conclusions

To summarize, in this study, we were able to reconcile independent measurements from in situ groundwater monitoring wells and space-based GNSS and GRACE techniques by accounting for both hydrological loading and poroelastic deformation in the Sacramento Valley, California. In particular, we recovered point estimates of

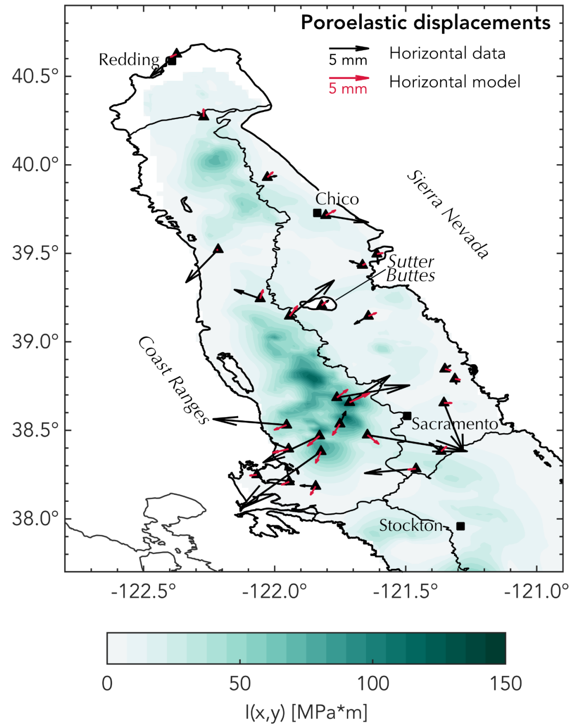

Figure 3.13: Horizontal poroelastic displacements predicted for a two-layer model with a basement Young's modulus of 35 GPa.

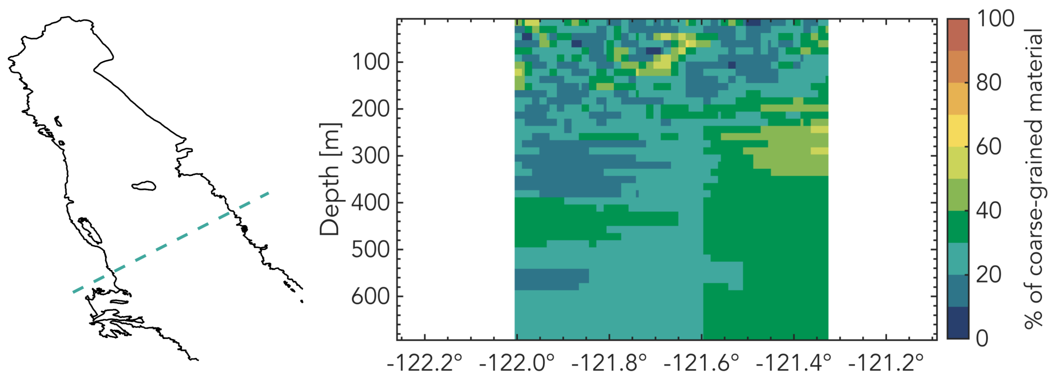

Figure 3.14: Typical cross-section through the texture model of Faunt (2009) showing the percentage of coarse-grained materials within the layer of continental deposits.

3D poroelastic displacements by projecting GNSS residual time series, corrected for GRACE-estimated hydrological loading, onto the dominant temporal function characterizing groundwater variations in the region. The resulting displacements can be reasonably well explained by analytical poroelastic solutions, suggesting that the deformation remains in the (poro)elastic regime. The modeling also led to an estimate of average compressibility associated to seasonal and multiannual variations, reflecting the aquifer basin's elastic storage capacity.

Further work is necessary to assess whether this seasonal/multiannual compressibility is consistent with longer-term deformation, which is important to predict the aquifer's response to prolonged declines in groundwater levels (assuming that it remains in the elastic regime). Future work will also focus on incorporating InSAR measurements into this framework to improve spatial resolution. This study illustrates that, given proper calibration, space-based GNSS, InSAR and GRACE techniques can be used to monitor basin-scale groundwater variations in areas where monitoring wells are sparse or nonexistent.

Bibliography

Z. Altamimi, P. Rebischung, L. Métivier, and X. Collilieux. ITRF2014: A new release of the International Terrestrial Reference Frame modeling nonlinear station motions. *Journal of Geophysical Research: Solid Earth*, 121(8):6109–6131, 2016. ISSN 21699313. doi: 10.1002/2016JB013098.

F. Amelung, D. L. Galloway, J. W. Bell, H. A. Zebker, and R. J. Laczniak. Sensing the ups and downs of Las Vegas: InSAR reveals structural control of land subsidence and aquifer-system deformation. *Geology*, 27:483, 6 1999. ISSN 0091-7613. doi: 10.1130/0091-7613(1999)027<0483:STUADO>2.3.CO;2.

D. F. Argus, R. G. Gordon, M. B. Heflin, C. Ma, R. J. Eanes, P. Willis, W. R. Peltier, and S. E. Owen. The angular velocities of the plates and the velocity of Earth's centre from space geodesy. *Geophysical Journal International*, 180(3):913–960, 2010.

D. F. Argus, F. W. Landerer, D. N. Wiese, H. R. Martens, Y. Fu, J. S. Famiglietti, B. F. Thomas, T. G. Farr, A. W. Moore, and M. M. Watkins. Sustained water loss in California's mountain ranges during severe drought from 2012 to 2015 inferred from GPS. *Journal of Geophysical Research: Solid Earth*, 122(12): 10,559–10,585, dec 2017. ISSN 21699313. doi: 10.1002/2017JB014424.

D. F. Argus, W. R. Peltier, G. Blewitt, and C. Kreemer. The viscosity of the top third of the lower mantle estimated using GPS, GRACE, and relative sea level measurements of glacial isostatic adjustment. *Journal of Geophysical Research: Solid Earth*, 126, 2021. ISSN 21699356. doi: 10.1029/2020JB021537.

S. Barbot, J. D. Moore, and V. Lambert. Displacement and stress associated with distributed anelastic deformation in a half-space. *Bulletin of the Seismological Society of America*, 107, 2017. ISSN 19433573. doi: 10.1785/0120160237.

G. Blewitt, W. C. Hammond, and C. Kreemer. Harnessing the GPS data explosion for interdisciplinary science. *Eos*, 99, 2018. doi: 10.1029/2018EO104623.

CA-DWR. California's groundwater update 2020 (bulletin 118). Technical report, The California Department of Water Resources, 2021.

K. Chanard, L. Fleitout, E. Calais, P. Rebischung, and J. Avouac. Toward a global horizontal and vertical elastic load deformation model derived from GRACE and GNSS station position time series. *Journal of Geophysical Research: Solid Earth*, 123(4):3225–3237, 2018. ISSN 2169-9313. doi: 10.1002/2017JB015245.

E. Chaussard and T. G. Farr. A new method for isolating elastic from inelastic deformation in aquifer systems: Application to the San Joaquin Valley, CA. *Geophysical Research Letters*, 46(19):10800–10809, 2019. ISSN 0094-8276. doi: 10.1029/2019GL084418.

E. Chaussard, R. Bürgmann, M. Shirzaei, E. J. Fielding, and B. Baker. Predictability of hydraulic head changes and characterization of aquifer-system and fault properties from InSAR-derived ground deformation. *Journal of Geophysical Research: Solid Earth*, 119(8):6572–6590, 2014. ISSN 21699313. doi: 10.1002/2014JB011266.

R. Choudrey. Variational methods for Bayesian independent component analysis. *Robots.Ox.Ac.Uk*, page 261, 2002. URL `http://www.robots.ox.ac.uk/{~}parg/projects/ica/riz/Pubs/thesis.ps.gz`.

W. E. Farrell. Deformation of the Earth by surface loads. *Reviews of Geophysics*, 10(3):761, 1972. ISSN 8755-1209. doi: 10.1029/RG010i003p00761.

C. C. Faunt. Groundwater availability of the Central Valley aquifer, California. Technical report, U.S. Geological Survey Professional Paper 1766, 2009.

C. C. Faunt, M. Sneed, J. Traum, and J. T. Brandt. Water availability and land subsidence in the Central Valley, California, USA. *Hydrogeology Journal*, 24, 2016. ISSN 14350157. doi: 10.1007/s10040-015-1339-x.

L. Fleitout and K. Chanard. Displacements and stresses induced by temperature and poroelastic pressure variations in the surficial layers for an Earth with realistic elastic properties. In *AGU Fall Meeting Abstracts*, volume 2018, Dec. 2018.

F. Frappart and G. Ramillien. Monitoring groundwater storage changes using the Gravity Recovery and Climate Experiment (GRACE) satellite mission: A review. *Remote Sensing*, 10(6):829, 2018.

D. L. Galloway, D. R. Jones, and S. E. Ingebritsen. *Land subsidence in the United States*, volume 1182. US Geological Survey, 1999.

L.-M. Gauer, K. Chanard, and L. Fleitout. Data-driven gap filling and spatio-temporal filtering of the GRACE-GRACE-FO records. In prep.

J. Geertsma. Land subsidence above compacting oil and gas reservoirs. *Journal of Petroleum Technology*, 25(06):734–744, 1973.

M. Ghil, M. Allen, M. Dettinger, K. Ide, D. Kondrashov, M. Mann, A. W. Robertson, A. Saunders, Y. Tian, F. Varadi, et al. Advanced spectral methods for climatic time series. *Reviews of Geophysics*, 40(1):3–1, 2002.

A. Gualandi and Z. Liu. Variational Bayesian independent component analysis for InSAR displacement time-series with application to Central California, USA. *Journal of Geophysical Research: Solid Earth*, 126:e2020JB020845, 2021. ISSN 2169-9313. doi: 10.1029/2020JB020845.

A. Gualandi, E. Serpelloni, and M. E. Belardinelli. Blind source separation problem in GPS time series. *Journal of Geodesy*, 90(4):323–341, 2016. ISSN 0949-7714. doi: 10.1007/s00190-015-0875-4.

X. Hu and R. Bürgmann. Aquifer deformation and active faulting in Salt Lake Valley, Utah, USA. *Earth and Planetary Science Letters*, 547:116471, 2020. ISSN 0012-821X. doi: 10.1016/J.EPSL.2020.116471.

IPCC. *Climate Change 2022: Impacts, Adaptation, and Vulnerability. Contribution of Working Group II to the Sixth Assessment Report of the Intergovernmental Panel on Climate Change*. Cambridge University Press, 2022.

B. N. Kuvshinov. Elastic and piezoelectric fields due to polyhedral inclusions. *International Journal of Solids and Structures*, 45(5):1352–1384, 2008.

S. Larochelle, K. Chanard, L. Fleitout, J. Fortin, A. Gualandi, L. Longuevergne, P. Rebischung, S. Violette, and J.-P. Avouac. Understanding the geodetic signature of large aquifer systems: Example of the Ozark Plateaus in central United States. *Journal of Geophysical Research: Solid Earth*, 127(3), mar 2022. doi: 10.1029/2021jb023097.

B. Q. Li, M. Khoshmanesh, and J.-P. Avouac. Surface deformation and seismicity induced by poroelastic stress at the Raft River geothermal field, Idaho, USA. *Geophysical Research Letters*, 48(18):e2021GL095108, 2021.

MATLAB. *9.3.0.713579 (R2017b)*. The MathWorks Inc., Natick, Massachusetts, 2017.

W. R. Neely, A. A. Borsa, J. A. Burney, M. C. Levy, F. Silverii, and M. Sneed. Characterization of groundwater recharge and flow in California's San Joaquin Valley from InSAR-observed surface deformation. *Water resources research*, 57 (4), 2021.

C. Ojha, M. Shirzaei, S. Werth, D. F. Argus, and T. G. Farr. Sustained groundwater loss in California's Central Valley exacerbated by intense drought periods. *Water Resources Research*, 54(7):4449–4460, 2018. ISSN 0043-1397. doi: 10.1029/2017WR022250.

R. W. Page. Geology of the fresh ground-water basin of the Central Valley, California, with texture maps and sections. Technical report, U.S. Geological Survey Professional Paper 1401-C, 1986.

P. Prevost, K. Chanard, L. Fleitout, E. Calais, D. Walwer, T. van Dam, and M. Ghil. Data-adaptive spatio-temporal filtering of GRACE data. *Geophysical Journal International*, 219(3):2034–2055, 2019.

P. Rebischung, Z. Altamimi, J. Ray, and B. Garayt. The igs contribution to itrf2014. *Journal of Geodesy*, 90(7):611–630, 2016.

B. Riel, M. Simons, D. Ponti, P. Agram, and R. Jolivet. Quantifying ground deformation in the Los Angeles and Santa Ana coastal basins due to groundwater withdrawal. *Water Resources Research*, 54(5):3557–3582, 2018. ISSN 0043-1397. doi: 10.1029/2017WR021978.

B. R. Scanlon, L. Longuevergne, and D. Long. Ground referencing GRACE satellite estimates of groundwater storage changes in the California Central Valley, USA. *Water Resources Research*, 48(4), 2012.

F. Silverii, N. D'Agostino, A. A. Borsa, S. Calcaterra, P. Gambino, R. Giuliani, and M. Mattone. Transient crustal deformation from karst aquifers hydrology in the Apennines (Italy). *Earth and Planetary Science Letters*, 506:23–37, jan 2019. ISSN 0012-821X. doi: 10.1016/J.EPSL.2018.10.019.

J. D. Smith, J.-P. Avouac, R. S. White, A. Copley, A. Gualandi, and S. Bourne. Reconciling the long-term relationship between reservoir pore pressure depletion and compaction in the Groningen region. *Journal of Geophysical Research: Solid Earth*, 124(6):6165–6178, 2019.

J. D. Smith, E. R. Heimisson, S. Bourne, and J.-P. Avouac. Stress-based forecasting of induced seismicity with instantaneous earthquake failure functions: Applications to the Groningen gas reservoir. 2021.

R. G. Smith, R. Knight, J. Chen, J. Reeves, H. Zebker, T. Farr, and Z. Liu. Estimating the permanent loss of groundwater storage in the southern San Joaquin Valley, California. *Water Resources Research*, 53(3):2133–2148, 2017.

United Nations. *The United Nations World Water Development Report 2022: Groundwater: Making the invisible visible*. UNESCO, Paris, 2022.

H. F. Wang. Theory of linear poroelasticity with applications to geomechanics and hydrogeology. In *Theory of Linear Poroelasticity with Applications to Geomechanics and Hydrogeology*. Princeton University Press, 2017.

A. K. Williamson, D. E. Prudic, and L. A. Swain. Ground-water flow in the Central Valley, California. Technical report, U.S. Geological Survey Professional Paper 1401-D, 1989.

B. A. Wisely and D. Schmidt. Deciphering vertical deformation and poroelastic parameters in a tectonically active fault-bound aquifer using InSAR and well level data, San Bernardino basin, California. *Geophysical Journal International*, 181:1185–1200, 3 2010. ISSN 0956540X. doi: 10.1111/j.1365-246X.2010.04568.x. URL https://academic.oup.com/gji/article-lookup/doi/10.1111/j.1365-246X.2010.04568.x.

Chapter 4

CONSTRAINING FAULT FRICTION AND STABILITY WITH FLUID-INJECTION FIELD EXPERIMENTS

Published as:

S. Larochelle, N. Lapusta, J.-P. Ampuero, and F. Cappa. Constraining fault friction and stability with fluid-injection field experiments. *Geophysical Research Letters*, 48, 2021. doi: 10.1029/2020GL091188.

4.1 Introduction

Earthquakes induced by fluid injection into the subsurface pose a major challenge for the geoenergy industry and society in general (Ellsworth, 2013; Grigoli et al., 2017). Tectonically-quiescent regions where dormant faults could be reactivated are particularly challenging, as their infrastructure is often not designed for large-magnitude induced earthquakes (McGarr et al., 2015). At the same time, some faults have been observed to slip stably at aseismic speeds of 10^{-7} – 10^{-2} m/s in response to fluid injection (Cornet et al., 1997; Duboeuf et al., 2017; Guglielmi et al., 2015; Scotti and Cornet, 1994; Wei et al., 2015). While induced earthquakes have been located anywhere from a few meters to tens of kilometers from injection wells (Goebel and Brodsky, 2018), the spatial extent of fluid-induced aseismic slip is not as well characterized due to the paucity of direct observations. Understanding what conditions lead to seismic versus aseismic and localized versus widespread fault reactivation is central to physics-based hazard forecasting.

An outstanding opportunity to investigate these questions is offered by a decametric-scale fluid injection experiment recently conducted in an underground tunnel intercepting a dormant fault in a carbonate formation (Guglielmi et al., 2015) (Figure 4.1A). During the experiment, the fluid pressure and fault slip were recorded at the injection site. Although the observed slip was mostly aseismic, it is important to understand if the observations contained sufficient information to determine whether slip would have accelerated into an earthquake rupture if injection had continued. Previous efforts to model the field experiment with a slip-weakening friction law concluded that aseismic slip outgrew the pressurized zone, potentially leading to a runaway earthquake with continued injection (Bhattacharya and Viesca, 2019).

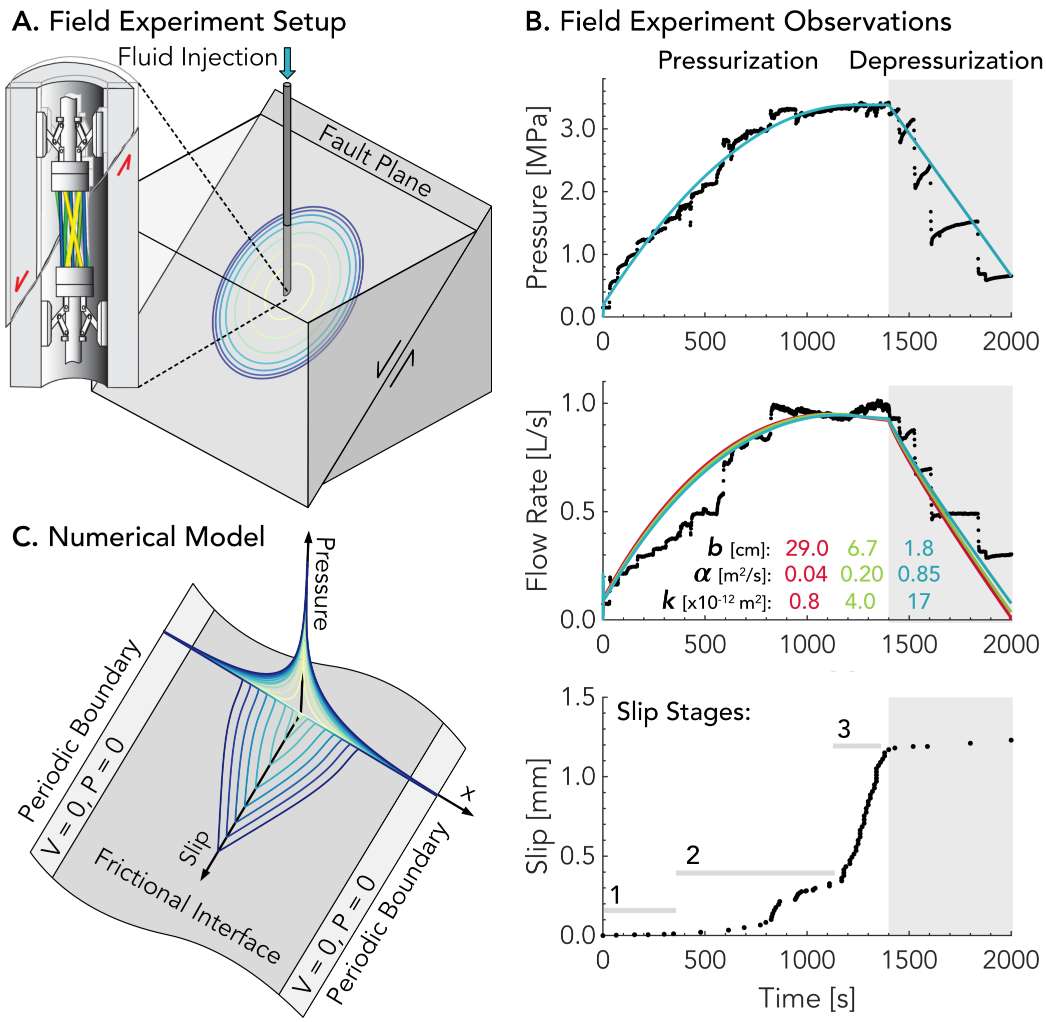

Figure 4.1: In situ measurement and modeling of fault slip induced by fluid injection. (A) Schematic of the field experiment presented in Guglielmi et al. (2015) in which fluid injected into a borehole crossing a natural but inactive fault caused its reactivation. A special borehole probe (SIMFIP) was used to measure the fault displacements directly at the injection site. (B) Pressure, flow rate, and fault slip measured during the field experiment. The colored lines and associated parameters correspond to the three different hydrological models considered in this study. The grey area indicates the depressurization stage that has not been shown nor modeled in prior studies. (C) Schematic of the model used to simulate slip on a fault plane embedded in an elastic bulk medium. Snapshots of a sample fluid pressure diffusion scenario and its resulting fault slip are shown for illustration (the darker colors indicate later times). Schematics (A) and (C) are not to scale.

Here, we use the data from the field experiment to examine the issue of slow and confined vs. fast and runaway slip in models with more realistic, laboratory-derived rate-and-state friction laws (Dieterich, 1979, 2007; Ruina, 1983) consistent with laboratory results on materials from this specific fault zone (Cappa et al., 2019). Furthermore, we use the modeling to identify promising avenues to quantify the fault properties and control injection-induced seismicity hazard. We adopt a fully-dynamic computational framework that resolves both aseismic and seismic slip on faults. We keep other model ingredients relatively simple to better understand frictional effects in the presence of a diffusing fluid. For example, we do not explicitly model the change in fault permeability induced by slip as in previous studies (Bhattacharya and Viesca, 2019; Cappa et al., 2019; Guglielmi et al., 2015). Nonetheless, we find that multiple frictional scenarios of varying spatial behavior and proneness to large earthquakes match the slip observations of the field experiment equally well during fault pressurization. We also find that depressurization provides further constraints that could help identify potentially hazardous faults.

4.2 Data and Methods

4.2.1 A Unique Fluid-Injection Experiment on a Natural Fault

The unprecedented field experiment involved injecting water directly into the fault zone and measuring the resulting fault slip at a depth of 280 m with a specially designed borehole probe (Guglielmi et al., 2015) (Figure 4.1A). Prior to the experiment, the shear and normal stress acting on the fault were estimated at 1.65 ± 0.5 and 4.25 ± 0.5 MPa, and the permeability and bulk modulus of the initially dry fault at 7 x 10^{-12} m^2 and 13.5 ± 3.5 GPa, respectively. Figure 4.1B summarizes the main observations of the experiment, including the deceleration of slip associated with depressurization not discussed in previous works. The slip measured during the pressurization phase displays three distinct slip stages. At first, the fault is inactive and no significant slip is recorded. The second stage initiates between 300 and 400 s when slip rates attain $\sim 10^{-7}$ m/s and the accumulated slip becomes measurable within the timeframe of the experiment. Stage 3 corresponds to the sharp acceleration to slip velocities of $\sim 10^{-6}$ m/s without any significant increase in injection pressure at ~1200 s. Hydromechanical modeling suggests that 70% of the 20-fold increase in permeability during the experiment occurred prior to this acceleration (Guglielmi et al., 2015). Laboratory experiments were also performed on grinded materials from the fault zone to further constrain the rate-and-state frictional properties (Cappa et al., 2019).

4.2.2 Diffusion of Pore Fluid Pressure into the Fault Zone

We model the field experiment as a fluid injection into a planar fault embedded in an elastic medium (Figure 4.1AC). We simulate the fluid injection by prescribing an evolution of pore pressure at the center of the fault that approximates the pressure history of the field experiment (Figure 4.1B, top). Simulations with a smooth pressure evolution result in similar but easier to interpret simulation results than those with the exact pressure history (Figures C.1-C.2).

The imposed pressure diffuses axisymmetrically into the fault plane as follows:

$$\frac{\partial p(r,t)}{\partial t} = \alpha \left(\frac{\partial^2 p(r,t)}{\partial r^2} + \frac{1}{r} \frac{\partial p(r,t)}{\partial r} \right) \tag{4.1}$$

where p is the pore pressure, r is radial distance, t is time, and α is the hydraulic diffusivity. The diffusion is numerically implemented using a forward finite difference scheme. Injection pressure is prescribed at a distance of r_{inj} = 0.05 m from the center of the fault to mimic the experimental procedure. Although we prescribe zero pressure boundary conditions far from the injection point to emulate the initially dry fault, the choice of boundary condition is not essential here because the size of the simulated fault (250 m) is larger than that of the pressure diffusion. Models with larger fault domains produce nearly identical results (Figure C.3).

Although both pressure and flow rate are reported as part of the field experiment, the exact value of the hydraulic diffusivity α is still uncertain because the spatial extent of the pressurized zone and the fault thickness over which the diffusion occurs, b, are poorly constrained. The volumetric flow rate, Q, depends on α and b as:

$$Q(t) = -\frac{\alpha S_s b(2\pi r_{inj})}{\rho g} \frac{\partial p}{\partial r}(r_{inj}, t) \tag{4.2}$$

where S_S is the specific storage and ρ the density of water. Hence, for a given flow rate, there is a trade-off between the fault thickness b over which the fluid diffusion occurs, the hydraulic diffusivity α and the specific storage S_S of the fault zone (and hence permeability $k = \alpha S_S \eta / \rho g$ where η is the dynamic viscosity of water). Note that α affects $Q(t)$ via both the pre-factor and the $\partial p / \partial r(r_{inj}, t)$ term in (4.2). In Section 4.3, we use hydraulic diffusivities of 0.04, 0.20, and 0.85 m^2/s to match field experimental measurements of slip for different friction regimes. Assuming a specific storage of $S_S = 2 \times 10^{-4}$ m^{-1} as in Bhattacharya and Viesca (2019), for example, these hydraulic diffusivities correspond to permeability values of 0.8, 4, and 17×10^{-12} m^2 that are within the ranges presented in previous studies that considered permeability enhancement: 0.8 to 1.3×10^{-12} m^2 (Bhattacharya and Viesca, 2019) and 7 to 100×10^{-12} m^2 (Guglielmi et al., 2015). These permeability values are also consistent with the flow rates measured in the field experiment, for reasonable values of the fault thickness b of 29, 6.7, and 1.8 cm, respectively (Figure 4.1B). While considering permeability enhancement may be necessary to match the finer features of the pressure and flow rate histories (unless the fault thickness b affected by fluid flow varies with time or with space), all three combinations of the parameters we use reproduce the hydrologic observations to the first order. We therefore consider a range of constant hydraulic diffusivity (and hence permeability) values in our search for models that reproduce the main features of the experimental observations.

4.2.3 Numerical Modeling of Fluid-Induced Fault Slip

As fluid pressure increases and diffuses into the fault plane, fault friction eventually decreases and measurable slip ensues (Figure 4.1C). We model this induced fault slip using a fully-dynamic 2D antiplane boundary integral method capable of simulating the complete seismic cycle including both aseismic and seismic deformation (Lapusta et al., 2000; Noda and Lapusta, 2013). Fault slip is governed by the following elastodynamic equation:

$$\tau(x,t) = f(\sigma - p(x,t)) = \tau_{ini} + F[\delta(x,t)] - \frac{\mu}{c_s} V(x,t) \tag{4.3}$$

where τ is the shear stress, f the friction coefficient, σ the normal stress, τ_{ini} the initial (i.e., background) shear stress, F a linear functional which depends on the slip history δ, μ the shear modulus of the elastic medium, c_s the shear wave speed and V the slip rate. The friction coefficient in (4.3) follows an empirical rate-and-state formulation derived from laboratory experiments which describes the dependence of f on the slip rate and a state variable θ (Dieterich, 1979, 2007; Ruina, 1983):

$$f(V,\theta) = f^* + a \ln \frac{V}{V^*} + b \ln \frac{V^* \theta}{D_{RS}} \tag{4.4}$$

where a and b are the direct and evolutionary rate-and-state parameters, D_{RS} is the critical slip distance and f^* is a reference coefficient of friction at reference slip rate V^*. The state variable is assumed to evolve according to the aging law (Marone, 1998; Ruina, 1983).

As the fault in the experiment is inactive prior to the fluid stimulation, the modeled fault is not loaded tectonically. Fault slip is thus purely fluid-induced, i.e., no significant slip would occur without the injection within the time scales considered in the simulations. To initialize the models, we impose shear and normal stresses in agreement with the values reported at the field site prior to the experiment (Guglielmi et al., 2015) and initial state variable values consistent with a dormant, highly healed fault (Section C.1, Figures C.4-C.7). The corresponding initial slip rate is then computed from Eq. (4.4).

4.3 Results

4.3.1 Models in Agreement with the Slip Observations during Pressurization

By first limiting our analysis to the pressurization stage of the experiment (up to 1400 s), we find that the observations are equally well reproduced by a family of models. Three representative cases, which we denote lower-, intermediate- and higher-friction models, are shown in Figures 4.2A-C and C.8 to C.11 and Table C.1. Below we explain how we constrained these models by examining how the various parameters govern the transitions between the different slip stages and considering the trade-off between friction and fluid pressure.

At the beginning of all simulations, slip rates are low and both inertial effects and elastic stress transfers are negligible. Eq. (4.3) then reduces to:

$$f(V,\theta)(\sigma - p(x,t)) = \tau_{ini}. \tag{4.5}$$

As p increases and τ_{ini} remains constant over time, f must increase via growing slip rates in order for (4.5) to remain true, resulting in a balance between the direct frictional effect and changes in pore pressure (Dublanchet, 2019). Slip rate and friction continue increasing until slip becomes significant at $V \sim 10^{-7}$ m/s. The onset of significant slip thus approximately coincides with the maximum friction reached during the simulations (Figures 4.2AB, C.8). The peak friction, f^p, can be approximated as:

$$f^p \sim f^* + a \ln \frac{V_s}{V^*} + b \ln \frac{V^* \theta_{ini}}{D_{RS}} \tag{4.6}$$

where $V_s = 10^{-7}$ m/s. The state variable remains at its initial value, θ_{ini}, as it has not evolved significantly yet due to negligible slip and short healing time compared to its large initial value. Moreover, because the fluid pressure at the injection site is known at all times, we can relate f^p to the timing of slip initiation, t_s:

$$f^p = \frac{\tau_{ini}}{\sigma - p(0,t_s)}. \tag{4.7}$$

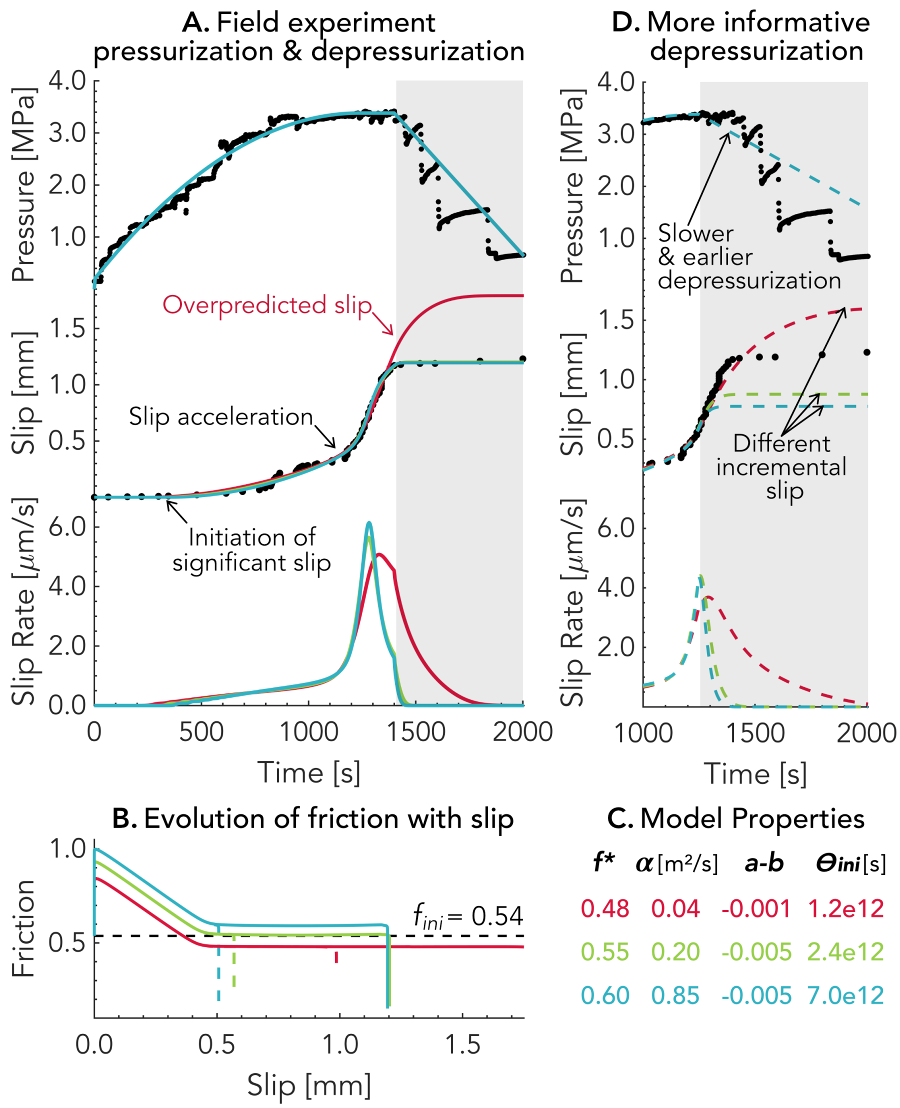

Figure 4.2: Multiple simulated scenarios match the pressurization stage of the experiment but respond differently to depressurization. (A) Temporal evolution of pore fluid pressure, slip and slip rate for three model scenarios (solid curves) that reproduce the observations (black dots) during the field-experiment pressurization. (B) Simulated evolution of friction with slip at the injection site; the three scenarios correspond to lower (red), intermediate (green), and higher (blue) residual friction in comparison to the fault prestress (black dashed line). Note that only the intermediate and higher-friction faults result in slip consistent with the depressurization part. (C) Key frictional and hydraulic properties of the three scenarios. (D) Similar to (A) but for an improved depressurization: Reducing injection pressure once slip starts to accelerate would allow to distinguish between all three cases, helping to constrain the fault friction properties.

It is thus possible to control t_s by computing the corresponding f^p with Eq. (4.7) and selecting f^*, a, b, θ_{ini} and D_{RS} such that Eq. (4.6) is satisfied. The three example models have t_s between 300 and 400s and f^p between 0.84 and 0.99 (Figures 4.2B, C.8).

Once significant slip starts accumulating, the fault begins weakening until it reaches steady state and friction reaches its quasi-static residual value of $f^r = f^* + (a - b)\ln V/V^*$ at the latest stage of the fault pressurization experiment (Figure 4.2B, C.8). As in Dublanchet (2019)'s rate-strengthening models, we find that this transition to steady state is accompanied with a marked acceleration in slip rate (Phase II in Dublanchet (2019)) which we assume to explain the acceleration observed at 1200s.

The critical slip distance, δ_c, over which friction weakens from f^p to f^r can be approximated as:

$$\delta_c \sim \frac{f^p - f^r}{b/D_{RS}} \tag{4.8}$$

since $\partial f/\partial\delta \sim b/D_{RS}$. Furthermore, from elasticity, slip is related to stress drop by:

$$\Delta\delta \propto \frac{\Delta\tau h}{\mu} \tag{4.9}$$

where h is the length of the slipping zone. By equating Eq. (4.8) and (4.9) at the center of the fault, we can estimate the slipping zone size, h_{ac}, at which steady state is reached and Stage 3 initiates:

$$h_{ac} \propto \frac{\mu D_{RS}}{b}\frac{f^p - f^r}{\Delta\tau}. \tag{4.10}$$

Moreover, by choosing V^* to be on the same order of magnitude as the fastest slip rate measured during the field experiment ($V^* = 10^{-6}$ m/s), we can approximate f^r with f^* since the contribution of $(a - b)\ln V/V^*$ becomes small compared to that of f^*. Eq. (4.10) can then be rewritten in terms of known parameters as:

$$h_{ac} \propto \frac{\mu D_{RS}}{b}\frac{a\ln\frac{V_s}{V} + b\ln\frac{V^*\theta_{ini}}{D_{RS}}}{\tau_{ini} - f^*(\sigma - p(0, t_{ac}))} \tag{4.11}$$

where t_{ac} denotes the onset of Stage 3. For all the simulations presented in this work, we find that adding a pre-factor of 3 to Eq. (4.11) provides a good estimate of the slipping zone size at t_{ac} (Section C.2). Remarkably, h_{ac} only depends on quantities

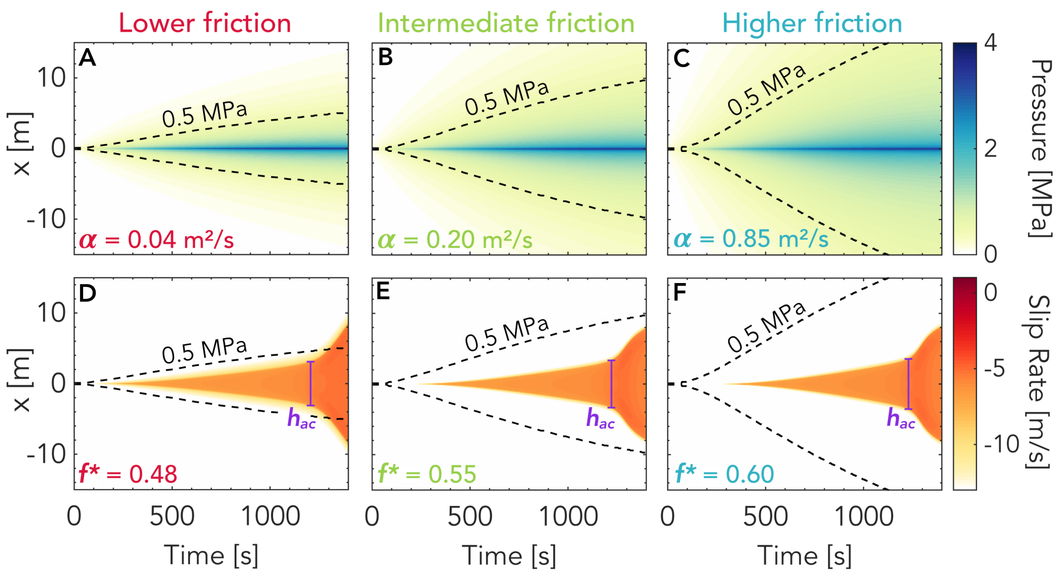

Figure 4.3: Whether the slipping zone is contained within or outruns the pressurized zone depends on fault friction. Spatial and temporal evolution of (A-C) pore fluid pressure and (D-F) slip rate for the three scenarios of Figure 4.2 during pressurization. The purple line shows the estimate h_{ac} of the slipping zone for the acceleration stage. Black dashed lines indicate the extent of the pressurized zone defined by 0.5 MPa fluid pressure contours. During the pressurization stage, the slipping zone of the lower-friction case outruns the pressurized zone while the intermediate- and higher-friction cases remain confined to the pressurized zone.

at the injection site. We can thus control the initiation of Stage 3 in our simulations by tuning the model parameters such that the slipping zone reaches length h_{ac} at $\sim$1200 s as is the case for our three representative models in Figure 4.3.

Another critical aspect in these simulations is the balance between friction and the pore pressure forcing. Figures C.20-C.23 illustrate how the aseismic slip zone grows with decreasing f^* and increasing α, respectively. In particular, during Stage 3, the spatial extent of the slipping zone with respect to the pressurized zone and the slip rate at the injection site depend on the difference between the residual and initial friction, $f^r - f_{ini}$, which controls the elastic energy available to drive fault rupture once initiated (Bhattacharya and Viesca, 2019; Dublanchet, 2019; Galis et al., 2017; Garagash and Germanovich, 2012) (Figure C.19A-C). Note that this is distinct from the difference between peak and initial friction, $f^p - f_{ini}$ (e.g., Gischig, 2015), which controls the timing of fault reactivation as discussed above.

Given all these consideration, for each diffusion scenario presented in Figure 4.1B, we find a corresponding frictional model by adjusting f^* such that the simulated slip matches the observations during the first 2 slip stages and produces a sufficiently large slip transient during Stage 3. To be able to use f^r (and hence f^*) values in agreement with the range 0.55 - 0.65 inferred from laboratory experiments on the grinded fault zone material (Cappa et al., 2019), we set f_{ini} to 0.54 (τ_{ini} = 2.15 MPa, σ = 4.00 MPa), which is within the uncertainty range of the initial stress measurements. A smaller f_{ini} would require smaller values of f^* outside of this range to obtain the same slip at the injection site. Moreover, the selected values of f^* restrict the range of possible values for the term $b \ln V\theta_{ini}/D_{RS}$ in Eq. (4.6) in order for slip to initiate between 300 and 400 s, which in turn restricts factor $\mu D_{RS}/b$ in Eq. (4.11) in order for Stage 3 to initiate at 1200s. The factor μD_{RS} which appears in estimates of critical nucleation lengths also needs to be large enough to avoid nucleation of dynamic events within the experimental time (e.g., Rice and Ruina, 1983; Rubin and Ampuero, 2005). Finally, we fine tune parameters a and θ_{ini} to adjust the slope and timing of the acceleration, respectively. Note that decreasing a while keeping b constant increases the slope of the slip acceleration — due to the (weak) dependence of f^r on $(a - b)$ – and eventually leads to the nucleation of a dynamic event right at t_{ac} (Figure C.16 and C.19D-F). This procedure results in a family of models with f^*= 0.48 to 0.60, $a - b = -0.001$ to -0.005 ($b = 0.016$), $\theta_{ini} = 1.2 \times 10^{12}$ to 7.0×10^{12} s and $\alpha = 0.04$ to 0.85 m^2/s that match the slip observations equally well during pressurization.

Although the three models exhibit comparable slip histories at the injection site, they differ in features that were not directly accessible to field observation. In particular, their spatial behaviors differ qualitatively (Figure 4.3, C.9-C.11). Defining the pressurized zone with 0.5 MPa pressure contours as in previous works, the lower-friction scenario produces an aseismic front that outruns the pressurized region, within 1400 s, as in slip-weakening models (Bhattacharya and Viesca, 2019) (Figure 4.3D). By contrast, in the higher-friction model, which reproduces the observations equally well, aseismic slip remains confined well within the pressurized area (Figure 4.3F). Our models demonstrate that slip did not necessarily extend beyond the pressure perturbation during the experiment; that explaining a slip history at a single point in space is a non-unique problem; and that further hydro-mechanical complexity is not required to explain the observed slip to first order. Monitoring fault slip and fluid pressure along the length of the fault, directly with additional probes or remotely with geophysical methods, would help distinguish between these different scenarios and would allow to study additional fault processes such as permeability evolution and inelastic dilatancy (Segall and Rice, 1995).

4.3.2 Distinguishing between Models with Depressurization

We find that the depressurization stage of the field experiment, which was not discussed or modeled in previous studies (Bhattacharya and Viesca, 2019; Cappa et al., 2019; Derode et al., 2015; Guglielmi et al., 2015), contains valuable information on fault properties. In this pressure-reduction stage, the lower-friction model features a pronounced delayed slip response that is not observed in the experiment or in the other two cases (Figure 4.2A). The intermediate- and higher-friction models, which also have higher hydraulic diffusivities, thus explain the entire set of observations better than the lower-friction model. Further discriminating between these two models is not possible with the current dataset because, by the time depressurization is initiated, the slip rates in these simulations are too low to produce a detectable difference in incremental slip. However, if the injection pressure is decreased more gradually and earlier in the acceleration phase – at which point the intermediate- and higher-friction scenarios have approximately the same (and higher) slip rate – the three scenarios lead to diverging levels of incremental slip (Figure 4.2D). As we only investigate a limited portion of the rate-and-state parameter space in this study, we cannot conclude that timely depressurization can uniquely discriminate between all possible frictional scenarios. However, it is clear that timely depressurization can provide additional constraints on the frictional and hydromechanical properties of fault zones.

In addition to fitting the entire set of slip observations better, models with f^* of 0.55 and 0.60 are also more consistent with the range of residual friction values of 0.55 to 0.65 derived from laboratory experiments on grinded fault gouge (Cappa et al., 2019). Moreover, the initial fault conditions implied by these higher-friction cases are fully consistent with those of a dormant fault whereas the low-friction case is not (Text C.1). Our preferred model for the site of the injection experiment is thus a rate-weakening fault with $0.55 < f^* < 0.60$, $0.20 < \alpha < 0.85$ m^2/s, $a = 0.011$ and $b = 0.016$. This is in contrast to the original Guglielmi et al. (2015) study in which the authors inferred a rate-strengthening fault from a spring-slider model with permeability enhancement. Within the limited parameter space that we explored through the procedure outlined in Section 4.3.1, we could only find rate-strengthening models with relatively low f^* and hence ones that only match the pressurization stage of the experiment (Figure C.24). It is possible that there are rate-strengthening models that match the entire slip history that we have not considered here but that would not change our conclusions that the field measurements can be matched with multiple friction scenarios and that the depressurization stage provides further constraints than pressurization alone.

4.3.3 Diverging Fault Stability with Sustained Injection

Modeling what would have happened if the fluid injection had continued for longer highlights why distinguishing between the three qualitatively different scenarios identified in this study is crucial. In response to an extended constant-pressure injection (Figure 4.4, Figures C.3, C.25-C.27), the low-friction fault nucleates an earthquake almost immediately, while the intermediate and higher-friction faults decelerate and continue slipping aseismically before eventually transitioning to seismic slip rates. Once a seismic rupture initiates, whether it is self-arrested or run-away depends on the dynamic residual friction, f^d, which is generally slightly lower than f^r (Galis et al., 2017; Garagash and Germanovich, 2012). If $f^d < f_{ini}$, as in the low- and intermediate-friction cases (Figure 4.4B), the rupture may release enough elastic energy to propagate beyond the fluid-affected regions and would only be stopped by less favorably stressed fault patches, geometrical barriers, or more stable materials not present in the current model (Figures 4.4C,D). Such runaway ruptures may be preceded by smaller ruptures or aseismic slip transients (Figures C.15 and C.19A); indeed, in fracture mechanics models (Galis et al., 2017), the transition to runaway rupture requires a certain balance between fluid pressurization and background stress to be reached. If $f^d > f_{ini}$, as in the high-friction case, the rupture self-arrests once out of the pressurized zone (Figure 4.4E). For low- to intermediate-friction faults, the maximum expected earthquake magnitude, M_{max}, is thus controlled by hydro-mechanical and geometrical fault properties as opposed to injection attributes (e.g., cumulative volume injected) (van der Elst et al., 2016; Galis et al., 2017; Gischig, 2015; McGarr, 2014). For example, varying the injection rate in our simulations does not alter the event size (Figure C.28). In the intermediate-friction case, the fault ultimately undergoes a runaway earthquake despite having stably released energy for over an hour, thus demonstrating that aseismic slip does not signify an absence of earthquake hazard. Fortunately, comparing the depressurization and prolonged injection scenarios reveals that reducing the injection pressure might be sufficient to suppress earthquake nucleation at the injection site. The lower the friction on the fault, the faster the rate of this depressurization needs to be (Figure C.29). Note, however, that earthquakes could still be triggered by aseismic slip itself on more unstable heterogeneities away from the injection site (Eyre et al., 2019; Guglielmi et al., 2015).

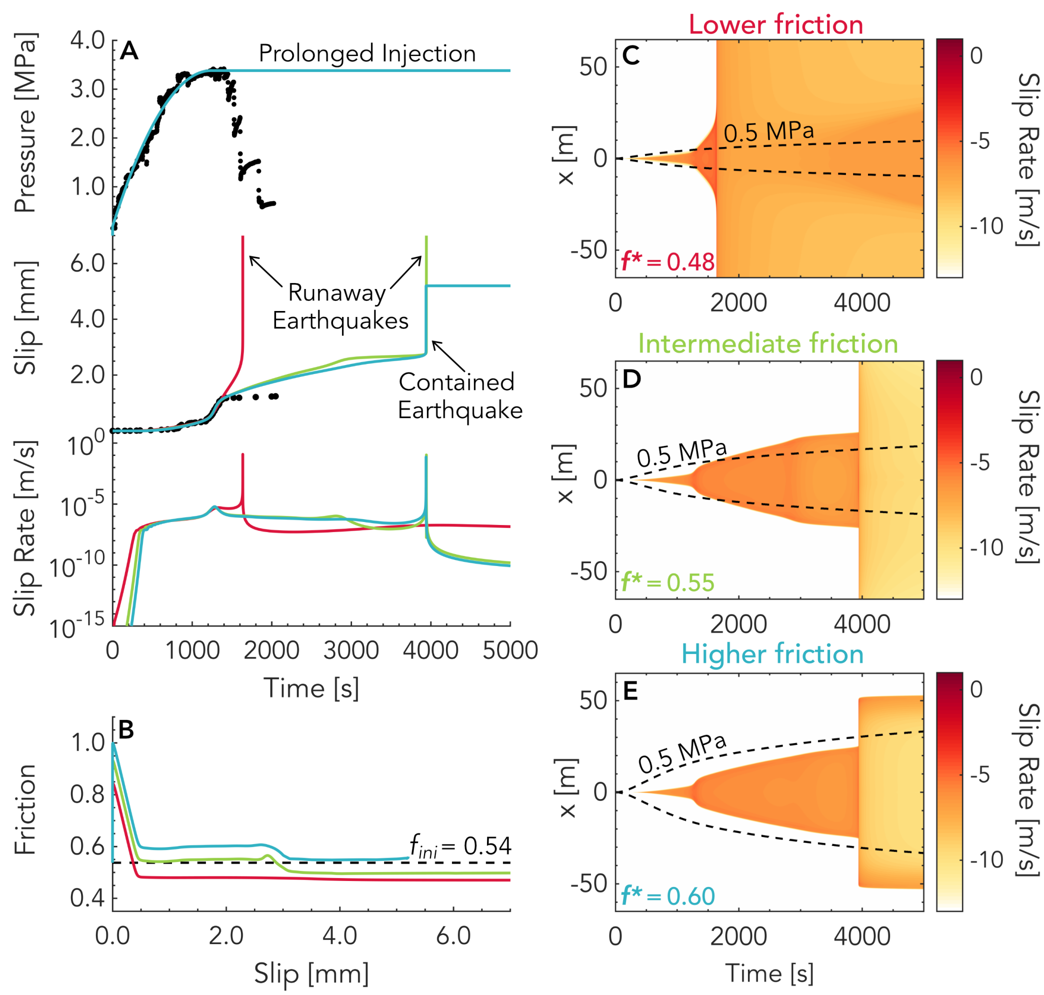

Figure 4.4: Prolonged injection reveals the diverging stability of the different fault models. Same as Figure 4.2(A-B) and Figure 4.3(C-E) but for a longer injection scenario, keeping the pressure at the center of the fault constant past 1400 s instead of decreasing it. The low-friction case (red in A, C) produces a runaway earthquake rupture much sooner than the intermediate-friction case (green in A, D), while the higher-friction case (blue in A, E) — which is consistent with most known information about the fault — results in a self-arresting earthquake confined to the pressurized zone (blue).

4.4 Discussion and Conclusions

To summarize, our modeling of a fluid-injection experiment into a fault zone reveals that the difference between fault prestress and quasi-static or dynamic fault friction controls whether slip is confined to the fluid-affected zone or outruns it. We find that: (i) multiple scenarios with different hydrologic assumptions and friction levels are consistent with the measured slip at the injection site during the pressurization phase, (ii) the low-friction scenario in which slow slip outruns the pressurized region is inconsistent with slip during the depressurization phase, and (iii) the high-friction scenario, in which the slipping zone is well confined within the pressurized region, is most consistent with the full range of information from the experiment, including the fault behavior during fault depressurization and laboratory friction measurements on the materials from the fault zone. Key hydro-mechanical parameters such as the difference between quasi-static friction and initial normalized prestress, $f^r - f_{ini}$, the rate dependence of friction, $a - b$, and the hydraulic diffusivity, α, exercise a first-order control on the stability and spatial extent of a fault response to fluid injections. Further constraining these parameters is thus critical for seismic hazard management. In the geoenergy industry, test injections with timely depressurization and spatiotemporal monitoring of fluid pressure and aseismic slip could be performed prior to exploitation to ensure that there are no low-friction faults nearby. Our findings show that augmenting fault-pressurization experiments with suitably designed depressurization phases and multiple monitoring locations along the fault could provide invaluable insight into the physics of both induced and natural earthquakes Savage et al. (2017) and friction properties of dormant faults. Such more advanced injection experiments and corresponding modeling work will potentially be able to assess the effects and relative importance of additional mechanisms such as poroelastic stresses (Deng et al., 2016; Goebel et al., 2017; Segall and Lu, 2015), slip-induced dilatancy (Cappa et al., 2019; Segall and Rice, 1995), bulk fluid diffusion, enhanced dynamic weakening and material heterogeneities (e.g., Eyre et al., 2019).

Bibliography

P. Bhattacharya and R. Viesca. Fluid-induced aseismic fault slip outpaces pore-fluid migration. *Science*, 364(6439):464–468, 2019. doi: 10.1126/science.aaw7354. URL `https://doi.org/10.1126/science.aaw7354`.

F. Cappa, M. Scuderi, C. Collettini, Y. Guglielmi, and J.-P. Avouac. Stabilization of fault slip by fluid injection in the laboratory and in situ. *Science Advances*, 5(3):

4065, 2019. doi: 10.1126/sciadv.aau4065. URL https://doi.org/10.1126/sciadv.aau4065.

F. Cornet, J. Helm, H. Poitrenaud, and A. Etchecopar. Seismic and aseismic slips induced by large-scale fluid injections. In *Seismicity Associated with Mines, Reservoirs and Fluid Injections*, page 563–583. Birkhäuser Basel, Basel, 1997. doi: 10.1007/978-3-0348-8814-1_12. URL https://doi.org/10.1007/978-3-0348-8814-1_12.

K. Deng, Y. Liu, and R. Harrington. Poroelastic stress triggering of the December 2013 Crooked Lake, Alberta, induced seismicity sequence. *Geophysical Research Letters*, 43(16):8482–8491, 2016. doi: 10.1002/2016GL070421. URL https://doi.org/10.1002/2016GL070421.

B. Derode, Y. Guglielmi, L. Barros, and F. Cappa. Seismic responses to fluid pressure perturbations in a slipping fault. *Geophysical Research Letters*, 42(9): 3197–3203, 2015. doi: 10.1002/2015GL063671. URL https://doi.org/10.1002/2015GL063671.

J. Dieterich. Modeling of rock friction: 1. Experimental results and constitutive equations. *Journal of Geophysical Research*, 84(B5):2161, 1979. doi: 10.1029/JB084iB05p02161. URL https://doi.org/10.1029/JB084iB05p02161.

J. Dieterich. Applications of rate- and state-dependent friction to models of fault slip and earthquake occurrence. *Treatise on Geophysics*, page 107–129, 2007. doi: 10.1016/B978-044452748-6.00065-1. URL https://doi.org/10.1016/B978-044452748-6.00065-1.

P. Dublanchet. Fluid driven shear cracks on a strengthening rate-and-state frictional fault. *Journal of the Mechanics and Physics of Solids*, 132:103672, 2019. doi: 10.1016/j.jmps.2019.07.015. URL https://doi.org/10.1016/j.jmps.2019.07.015.

L. Duboeuf, L. Barros, F. Cappa, Y. Guglielmi, A. Deschamps, and S. Seguy. Aseismic motions drive a sparse seismicity during fluid injections into a fractured zone in a carbonate reservoir. *Journal of Geophysical Research: Solid Earth*, 122(10):8285–8304, 2017. doi: 10.1002/2017JB014535. URL https://doi.org/10.1002/2017JB014535.

W. Ellsworth. Injection-induced earthquakes. *Science*, 341(6142):1225942, 2013. doi: 10.1126/science.1225942. URL https://doi.org/10.1126/science.1225942.

T. Eyre, D. Eaton, D. Garagash, M. Zecevic, M. Venieri, R. Weir, and D. Lawton. The role of aseismic slip in hydraulic fracturing–induced seismicity. *Science Advances*, 5(8):7172, 2019. doi: 10.1126/sciadv.aav7172. URL https://doi.org/10.1126/sciadv.aav7172.

M. Galis, J. Ampuero, P. Mai, and F. Cappa. Induced seismicity provides insight into why earthquake ruptures stop. *Science Advances*, 3(12):7528, 2017. doi: 10.1126/sciadv.aap7528. URL `https://doi.org/10.1126/sciadv.aap7528`.

D. Garagash and L. Germanovich. Nucleation and arrest of dynamic slip on a pressurized fault. *Journal of Geophysical Research: Solid Earth*, 117(B10), 2012. doi: 10.1029/2012JB009209. URL `https://doi.org/10.1029/2012JB009209`.

V. Gischig. Rupture propagation behavior and the largest possible earthquake induced by fluid injection into deep reservoirs. *Geophysical Research Letters*, 42(18):7420–7428, 2015. doi: 10.1002/2015GL065072. URL `https://doi.org/10.1002/2015GL065072`.

T. Goebel, M. Weingarten, X. Chen, J. Haffener, and E. Brodsky. The 2016 mw5.1 fairview, oklahoma earthquakes: Evidence for long-range poroelastic triggering at gt;40 km from fluid disposal wells. *Earth and Planetary Science Letters*, 472: 50–61, 2017. doi: 10.1016/J.EPSL.2017.05.011. URL `https://doi.org/10.1016/J.EPSL.2017.05.011`.

T. H. Goebel and E. Brodsky. The spatial footprint of injection wells in a global compilation of induced earthquake sequences. *Science*, 361(6405):899–904, 2018. doi: 10.1126/science.aat5449. URL `https://doi.org/10.1126/science.aat5449`.

F. Grigoli, S. Cesca, E. Priolo, A. Rinaldi, J. Clinton, and T. Stabile. Current challenges in monitoring, discrimination, and management of induced seismicity related to underground industrial activities: A European perspective. *Reviews of Geophysics*, 55(2):310–340, 2017. doi: 10.1002/2016RG000542. URL `https://doi.org/10.1002/2016RG000542`.

Y. Guglielmi, F. Cappa, J. Avouac, P. Henry, and D. Elsworth. Seismicity triggered by fluid injection-induced aseismic slip. *Science*, 348(6240), 2015. doi: 10.1126/science.aab0476. URL `https://doi.org/10.1126/science.aab0476`.

N. Lapusta, J. Rice, Y. Ben-Zion, and G. Zheng. Elastodynamic analysis for slow tectonic loading with spontaneous rupture episodes on faults with rate- and state-dependent friction. *Journal of Geophysical Research*, 105(B10): 765–788, 2000. doi: 10.1029/2000JB900250. URL `https://doi.org/10.1029/2000JB900250`.

C. Marone. Laboratory-derived friction laws and their application to seismic faulting. *Annual Review of Earth and Planetary Sciences*, 26, 1998. Retrieved from www.annualreviews.org.

A. McGarr. Maximum magnitude earthquakes induced by fluid injection. *Journal of Geophysical Research: Solid Earth*, 119(2):1008–1019, 2014. doi: 10.1002/2013JB010597. URL `https://doi.org/10.1002/2013JB010597`.

A. McGarr, B. Bekins, N. Burkardt, J. Dewey, P. Earle, and W. Ellsworth. Coping with earthquakes induced by fluid injection. *Science*, 347(6224):830 – 831, 2015. doi: 10.1126/science.aaa0494. URL `https://doi.org/10.1126/science.aaa0494`.

H. Noda and N. Lapusta. Stable creeping fault segments can become destructive as a result of dynamic weakening. *Nature*, 493(7433):518–521, 2013. doi: 10.1038/nature11703. URL `https://doi.org/10.1038/nature11703`.

J. Rice and A. Ruina. Stability of steady frictional slipping. *Journal of Applied Mechanics*, 50(2):343, 1983. doi: 10.1115/1.3167042. URL `https://doi.org/10.1115/1.3167042`.

A. Rubin and J.-P. Ampuero. Earthquake nucleation on (aging) rate and state faults. *Journal of Geophysical Research: Solid Earth*, 110(B11), 2005. doi: 10.1029/2005JB003686. URL `https://doi.org/10.1029/2005JB003686`.

A. Ruina. Slip instability and state variable friction laws. *Journal of Geophysical Research: Solid Earth*, 88(B12):10359–10370, 1983. doi: 10.1029/JB088iB12p10359. URL `https://doi.org/10.1029/JB088iB12p10359`.

H. Savage, J. Kirkpatrick, J. Mori, E. Brodsky, W. Ellsworth, and B. Carpenter. Scientific exploration of induced seismicity and stress (seisms. *Scientific Drilling*, 23:57–63, 2017. doi: 10.5194/sd-23-57-2017. URL `https://doi.org/10.5194/sd-23-57-2017`.

O. Scotti and F. Cornet. In situ evidence for fluid-induced aseismic slip events along fault zones. *International Journal of Rock Mechanics and Mining Sciences Geomechanics Abstracts*, 31(4):347–358, 1994. doi: 10.1016/0148-9062(94)90902-4. URL `https://doi.org/10.1016/0148-9062(94)90902-4`.

P. Segall and S. Lu. Injection-induced seismicity: Poroelastic and earthquake nucleation effects. *Journal of Geophysical Research: Solid Earth*, 120(7):5082–5103, 2015. doi: 10.1002/2015JB012060. URL `https://doi.org/10.1002/2015JB012060`.

P. Segall and J. Rice. Dilatancy, compaction, and slip instability of a fluid-infiltrated fault. *Journal of Geophysical Research: Solid Earth*, 100(B11):22155–22171, 1995. doi: 10.1029/95JB02403. URL `https://doi.org/10.1029/95JB02403`.

N. van der Elst, M. Page, D. Weiser, T. Goebel, and S. Hosseini. Induced earthquake magnitudes are as large as (statistically) expected. *Journal of Geophysical Research: Solid Earth*, 121(6):4575–4590, 2016. doi: 10.1002/2016JB012818. URL `https://doi.org/10.1002/2016JB012818`.

S. Wei, J.-P. Avouac, K. Hudnut, A. Donnellan, J. Parker, and R. Graves. The 2012 brawley swarm triggered by injection-induced aseismic slip. *Earth and*

Planetary Science Letters, 422:115–125, 2015. doi: 10.1016/j.epsl.2015.03.054. URL https://doi.org/10.1016/j.epsl.2015.03.054.

Chapter 5

FAULT REACTIVATION AND EARTHQUAKE NUCLEATION DUE TO FLUID INJECTION

To be submitted as:

S. Larochelle, J.-P. Ampuero, V. Lambert, and N. Lapusta. Fault reactivation and earthquake nucleation due to fluid injection.

5.1 Introduction

In the previous chapter, we presented a number of simulations highlighting the wide range of possible slip behaviors when faults are subjected to fluid injections, from steady aseismic slip to runaway earthquakes. The conditions that give rise to these distinct responses and, in particular, what controls whether the induced slip is seismic or aseismic are still poorly understood. Of special interest is the so-called *nucleation length* which describes the size of the slipping zone as it approaches dynamic speeds and produces an earthquake. A number of lengthscales (e.g., see Table 5.1) have been proposed to explain the process of earthquake nucleation observed in different tectonically-loaded fault models and analog laboratory experiments. However, whether and how these various lengthscales apply in the context of fluid-induced slip is still an open question, notably because fluid injections lead to spatially- and temporally-variable effective normal stress. At the same time, the effective normal stress — a key parameter in nucleation lengthscales — was assumed to be constant in space and time in their derivations.

In this chapter, we investigate these questions by considering simulations similar to those of Chapter 4 but for the simpler case of a fixed-length pressurized zone with changing pore fluid pressure. The manuscript is organized as follows: We first establish the close similarity of the slip behavior in diffusive and fixed-length pressurization models before focusing on the latter. We then proceed to identify key lengthscales and derive additional closed-form solutions to explain the slip behaviors observed throughout the different stages of the simulations.

5.2 Study Scope

Let us first consider the evolution of slip induced by two different fluid injection scenarios in fault slip models similar to those presented in Chapter 4. In the

Table 5.1: Definition of important (half-)lengthscales and their values for the reference parameters listed in Table 5.2

Description	Symbol	Formula	$t = 0$	Stage 2
Fixed-length pressurized zone	L_p	-	1.25 m	1.25 m
Crack expansion lengthscale	L_{ss}	Eqs. (5.24), (5.25)	0 m	1.43 m
Nucleation lengthscales				
Dieterich (1992) and Rubin and Ampuero (2005) above steady state lengthscale	L_b	$1.377\dfrac{\mu D_{rs}}{b(\sigma - p)}$	0.69 m	0.98 m
Uenishi and Rice (2003) universal slip weakening lengthscale	L_{UR}	$0.579\dfrac{\mu D_{rs}}{b(\sigma - p)}$	0.29 m	0.41 m
Rice and Ruina (1983) linear stability lengthscale	L_{RR}	$\dfrac{\pi}{8}\dfrac{\mu D_{rs}}{(b-a)(\sigma - p)}$	0.98 m	1.38 m
Rubin and Ampuero (2005) steady-state crack lengthscale	L_{RA}	$\dfrac{1}{\pi}\dfrac{b\mu D_{rs}}{(b-a)^2(\sigma - p)}$	3.98 m	5.59 m

first one, the fault is subjected to pore pressure increasing as $p(t) = rt = 5000t$, where r is a pressurization rate, over a fixed zone of half-length $L_p = 1.25$ m (Figure 5.1a). In the second one, the same pressure increase is applied over a (much smaller) injection interval $L_{inj} = 0.1$ m but pore pressure is allowed to diffuse along the fault plane (as in Chapter 4) with hydraulic diffusivity $\alpha = 0.01$ m^2/s (Figure 5.1b). We simulate fault slip resulting from these two pressurization scenarios for different values of a while keeping b constant at 0.01 and the parameter values listed in Table 5.2 (Figure 5.1, panels b-j). Despite clear differences at early times, the two sets of simulations show qualitatively similar overall behaviors: Faults with $a = 0.004$ undergo a spontaneous runaway seismic event that propagate through the entire modeled domain; faults with $a = 0.007$ produce a series of smaller, contained earthquake ruptures that approximately track the steady crack expansion half-length estimate L_{ss} (see Section 5.3.3); faults with $a = 0.008$ first slip aseismically following L_{ss} before nucleating a contained earthquake rupture and, finally, faults with $a = 0.01$ slip aseismically throughout the simulated time.

The similarities between the two sets of simulations result from the following parameter choices. First, we focus on faults which are relatively well-stressed in comparison to the reference friction (0.575 vs. 0.6), allowing for the slipping zone to extend beyond the pressurized zone. Second, we consider low enough hydraulic

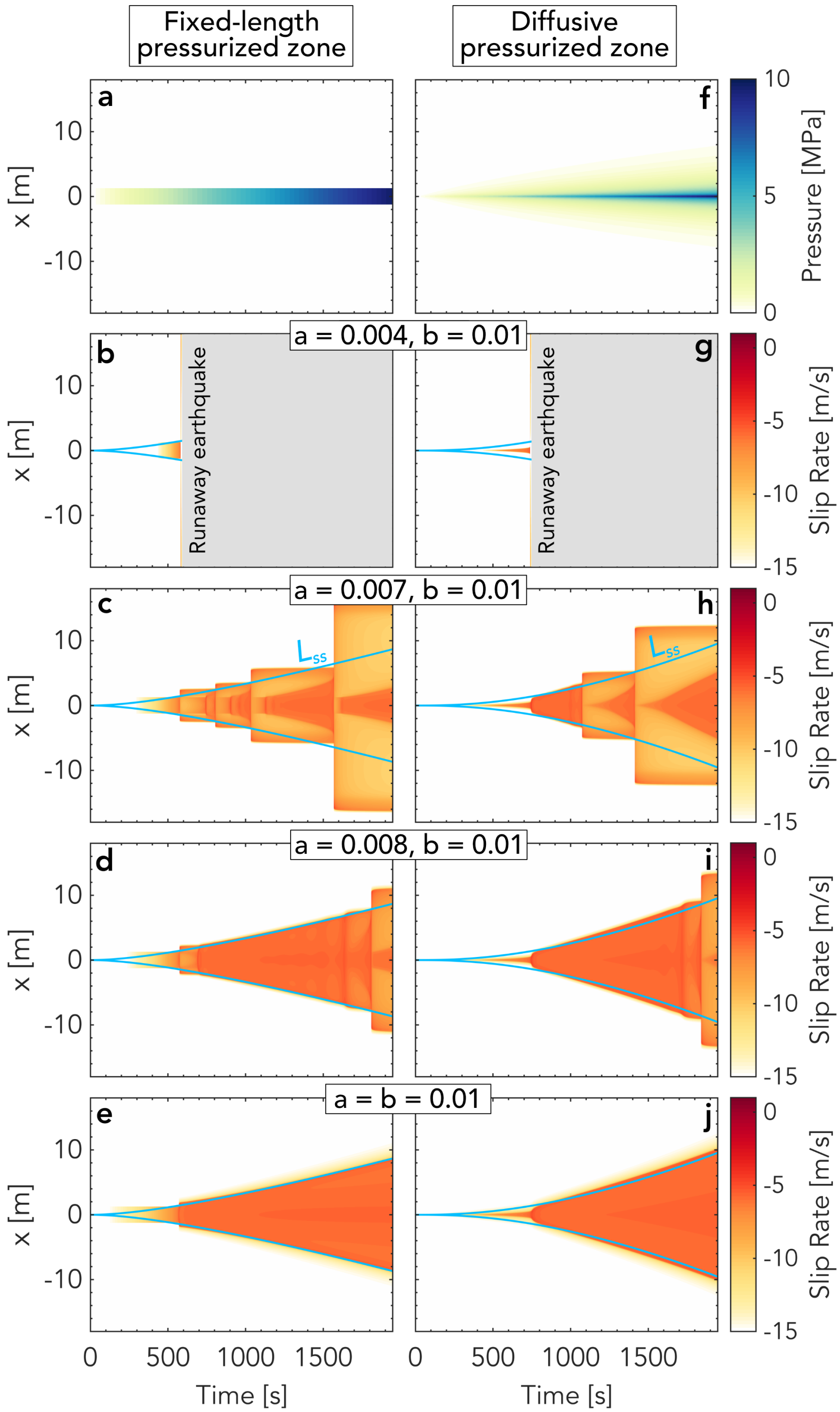

Figure 5.1: Spatiotemporal evolution of pore pressure (a,f) and slip rates (b-j) for simulations with a fixed-length pressurized zone (a-e) and a diffusive pressurized zone (f-j), and different values of a. Note that since simulations with $a = 0.004$ generate runaway earthquakes that hit the model boundaries, we do not show these simulations for timesteps after the seismic event. The blue lines indicate the steady-state crack expansion lengthscale derived in section 5.3.3.1.

Table 5.2: Reference parameter values. Unless otherwise indicated, the parameters in the simulations shown throughout this manuscript are set to these values.

Parameter	Symbol	Value	Units
Pressurization rate	r	5000	Pa/s
Initial shear stress	τ_{ini}	5.75	MPa
Initial normal stress	σ_{ini}	10.00	MPa
Initial friction coefficient	f_{ini}	0.575	
Reference friction coefficient	f^*	0.600	
Reference slip rate	V^*	10^{-6}	m/s
Dynamic slip rate	V_{dyn}	10^{-1}	m/s
Rate frictional parameter	a	0.008	
State frictional parameter	b	0.010	
Critical slip distance	D_{rs}	5	μm
Initial state variable	θ_{ini}	10^{10}	s
Shear modulus	μ	10	GPa

diffusivity in the cases with the expanding pressurized zone such that the (varying) width of the pressurized zone remains comparable to the selected width of the fixed pressurized zone for the duration of our simulations. The two factors taken together ensure that the slipping zone is larger than the pressurized zone in both types of simulations for most of the simulated time, allowing for similar fault response. Third, the evolving integrated pore pressure $P(t)$ over the pressurized zone is similar in the two cases.

Given these similarities, here we focus on understanding the simpler, fixed-pressurized zone simulations to develop an intuition for these models. In order to isolate the effects of fluid injections and examine earthquake nucleation, we focus on velocity-weakening (VW) faults without tectonic loading (i.e., $V_{pl} = 0$). As discussed in Chapter 4 and Larochelle et al. (2021), long-term VW fault models with the aging law and without tectonic or fluid loading indicate that the state variable θ should be approximately equal to time ($\theta \sim t$), the slip rate V should decay with time as $V \propto t^{-b/a}$, and hence $\Omega = V\theta/D_{rs} \propto t^{1-b/a}$. Velocity-weakening faults should thus tend towards below steady-state conditions ($\Omega < 1$) for long periods of time without loading since $1 - b/a < 0$. In light of these expected initial conditions, this work mostly focuses on VW faults that are initially well healed and below steady state.

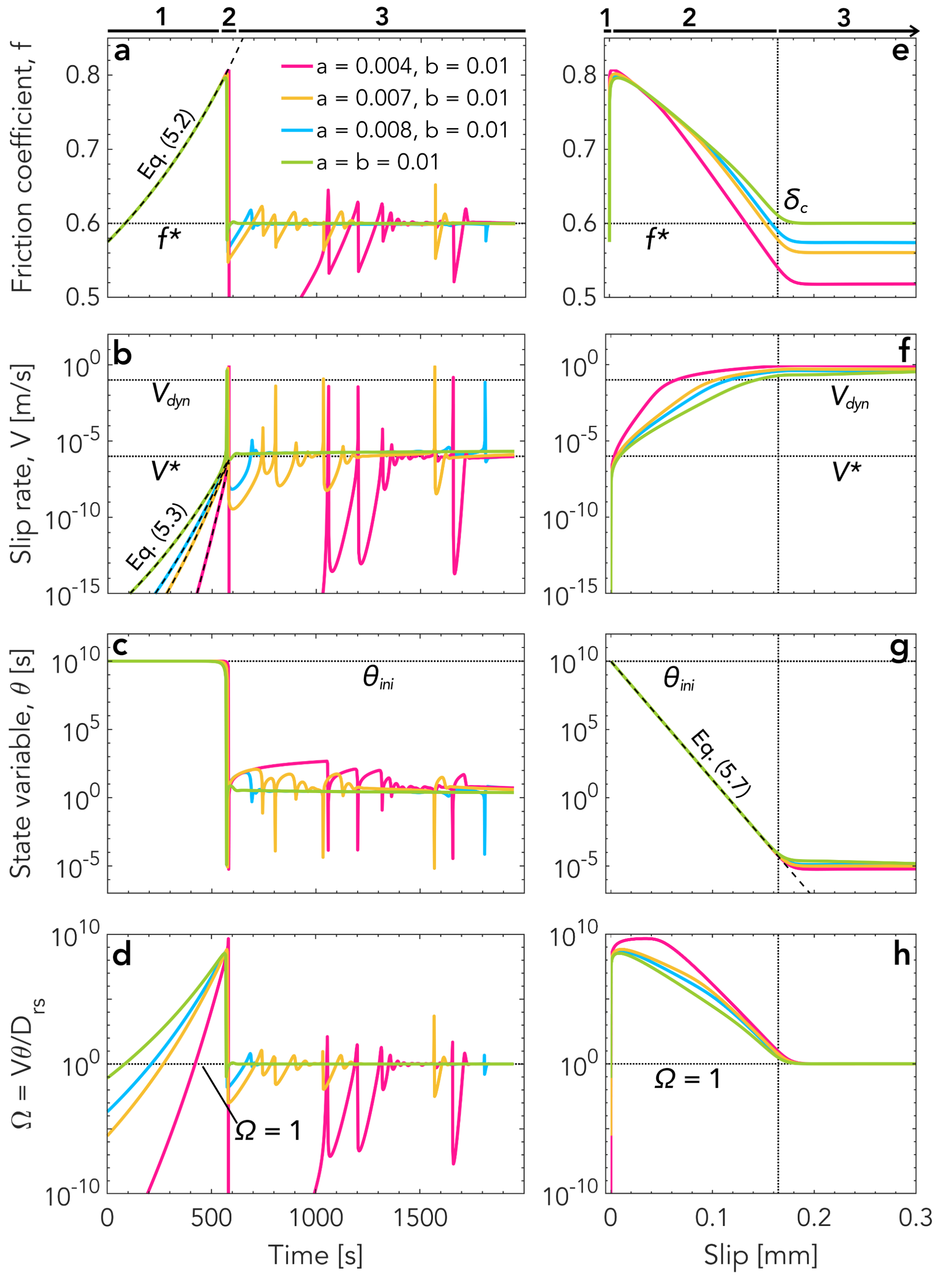

Figure 5.2: Evolution of the friction coefficient (a,e), slip rate (b,f), state variable (c,g) and Ω (d,h) with time (a-d) and slip (e-h) at the center of the fault for the simulations with a fixed-length pressurized zone shown in Figure 5.1(a-e). The different stages of the simulations are indicated at the top of panels (a) and (e). The left column shows the evolution of the quantities with time and the tight column shows the beginning of their evolution with slip.

5.3 Understanding Fault Slip due to Fixed-length Pressurization

Figure 5.2(a-d) shows the temporal evolution of key variables at the center of the fault for the same fixed-zone simulations as in Figure 5.1. As indicated on top of panels (a), all four simulations undergo three distinct stages. Stage 1 is characterized by an increase in friction coefficient f to its relatively high peak value appropriate for a well-healed fault and with negligible slip and increasing but relatively small slip rates, Stage 2 by pronounced frictional weakening to steady-state values, and Stage 3 by initially steady-state friction that subsequently oscillates around the steady-state value, increasingly so for simulations with lower values of a, as the slipping zone extends. We examine each stage in more details in the following sections.

5.3.1 Stage 1: Increasing Friction and Slip Rate

As described in Larochelle et al. (2021) (also see Dublanchet (2019)), since initial slip rates are very small ($V_{ini} < 10^{-15}$ m/s) (Figure 5.2b), slip and inertial effects are negligible during Stage 1. The shear stress thus remains constant at $\tau = \tau_{ini}$ and:

$$\tau_{ini} = f(\sigma_{ini} - p). \tag{5.1}$$

This implies that the increase in pore pressure p must be entirely accommodated by an increase in friction coefficient f such that

$$f = \frac{\tau_{ini}}{(\sigma_{ini} - p)}. \tag{5.2}$$

Figure 5.2a reveals that Eq. 5.2 (dashed line) remains true throughout Stage 1. Moreover, since the state variable θ does not significantly evolve (Figure 5.2c) — due to the negligible slip and relatively small simulated time ($\sim$ 500 s) compared to its initial value of 10^{10} s — the increase in f has to come entirely from an increase in slip rate V. Specifically,

$$V = V^* \exp\left(\frac{\frac{\tau_{ini}}{(\sigma_{ini}-p)} - f^* - b \ln \frac{V^*\theta_{ini}}{D_{rs}}}{a}\right) \tag{5.3}$$

as indicated by the dashed lines in Figure 5.2b. Moreover since θ remains constant at θ_{ini}, Ω directly tracks the increase in V, bringing all four cases very much above steady state by the end of Stage 1 (Figure 5.2d).

For a fault to overcome this regime, V has to increase up to a value, V_s, at which slip becomes significant, either (i) in comparison to the characteristic slip distance D_{rs} to allow for the evolution of the state variable, which would start to decrease towards steady-state values, or (ii) to decrease the shear stress in the middle of the fault due to sufficiently larger slip there in comparison to the surrounding fault areas. In Larochelle et al. (2021), we evaluated V_s for (i) to be around 10^{-7} m/s. We see (panel g) that condition (i) is reached at the same slip of several microns (comparable to $D_{rs} = 5\ \mu$m) for all cases. The friction coefficient stays about constant over these slips of the order of D_{rs} (panel e), resulting in further increase of slip rate and even more slip, leading shortly to condition (ii) and decrease in shear stress and hence friction coefficient. Hence the friction is maximum at approximately $V = V_s$ and:

$$f^p \approx f^* + a \ln \frac{V_s}{V^*} + b \ln \frac{V^* \theta_o}{D_{rs}}. \tag{5.4}$$

For the parameter values listed in Table 5.2, Eq. (5.4) evaluates to $f^p = 0.80$. Replacing this value in Eq. (5.1) yields an estimate of the critical pore pressure p^p necessary for fault reactivation by this mechanism:

$$p^p = \sigma_{ini} - \frac{\tau_{ini}}{f^p} \tag{5.5}$$

equal to 2.77 MPa for the parameters listed in Table 5.2.

The spatio-temporal evolution of slip rate and friction up to the end of Stage 2 (Figure 5.3) shows that this increase of slip rate and friction coefficient during stage 1 occurs uniformly throughout the (uniformly) pressurized region. This is one difference from simulations with a diffusive pressurized zone, in which the slip zone is expanding with the pressurized zone.

5.3.2 Stage 2: No-healing Frictional Weakening

Since the fault segment is far above steady state when the state variable starts to evolve in stage 2, $\Omega \gg 1$, the evolution of the state variable occurs in the no-healing limit (Dieterich, 1992; Bizzarri and Cocco, 2003; Rubin and Ampuero, 2005; Ampuero and Rubin, 2008) as:

$$\frac{\partial \theta}{\partial t} = 1 - \frac{V\theta}{D_{rs}} \approx \frac{V\theta}{D_{rs}} \tag{5.6}$$

implying that θ decays with slip δ as:

$$\theta = \theta_{ini} \exp(-\delta / D_{rs}) \tag{5.7}$$

as illustrated by the dashed line in Figure 5.2(g). Hence, friction evolves with slip rate and slip as:

$$f = f^* + a \ln \frac{V}{V^*} + b \ln \frac{V^* \theta_{ini}}{D_{rs}} - \frac{b\delta}{D_{rs}}. \tag{5.8}$$

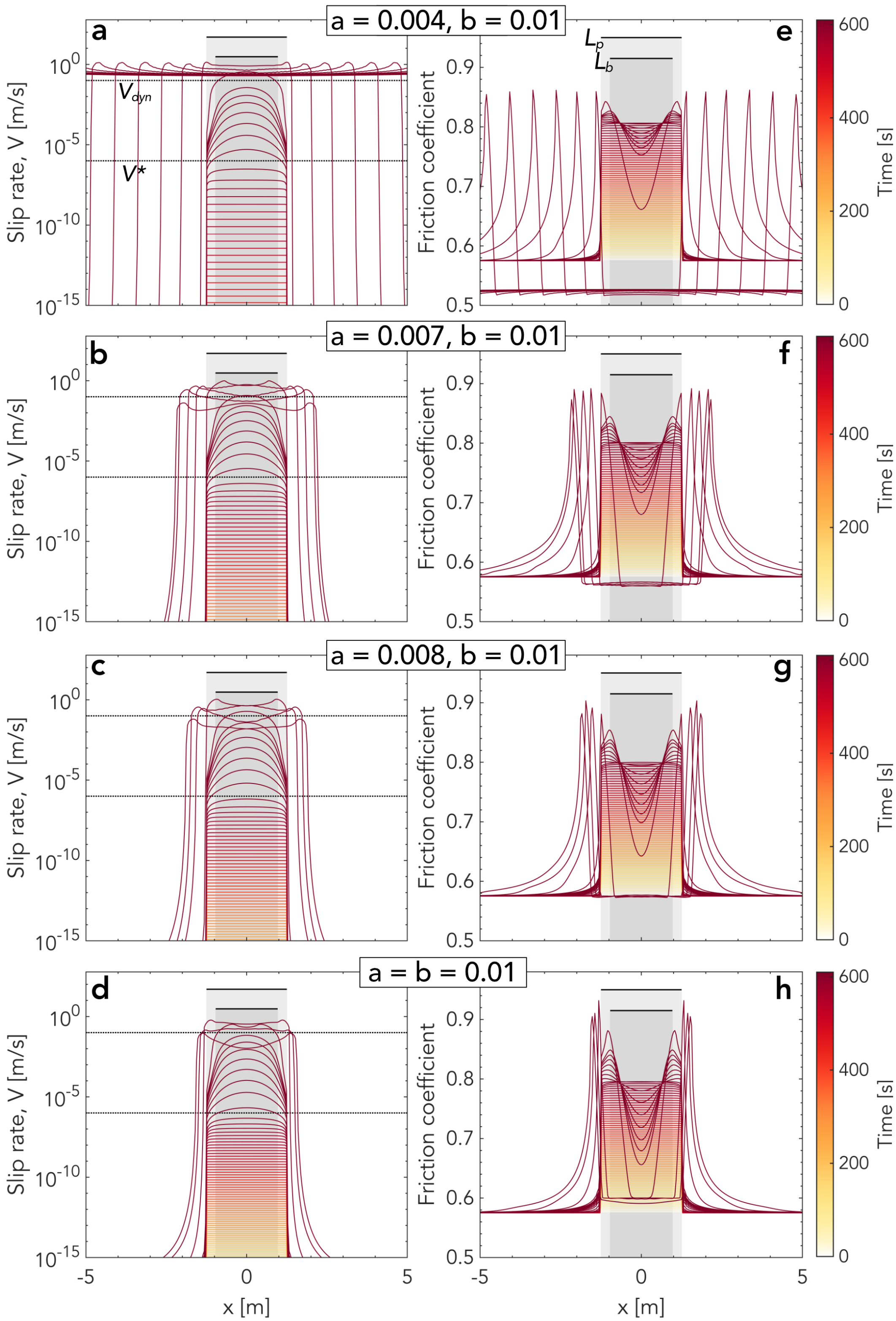

Figure 5.3: Alternative view of the spatiotemporal evolution of slip rate (a-d) and friction coefficient (e-h) to emphasize the nucleation process of the simulations shown in Figure 5.1(a-e). Note that the colorbar now indicates time. The fixed-length pressurized zone L_p and lengthscale L_b (evaluated with the pore pressure during Stage 2) are indicated with the lighter and darker gray boxes, respectively. The simulations are plotted from $t = 0$ until they either produce a seismic runaway event ($a = 0.004$) or start decelerating ($a = 0.007, 0.008, 0.01$).

For tectonically-loaded faults above steady state in the no-healing limit, Dieterich (1992) and Rubin and Ampuero (2005) found that the nucleating zone localizes to a lengthscale proportional to $\mu D_{rs}/b(\sigma - p)$. Here we use the definition of Rubin and Ampuero (2005) derived by considering a fixed-length accelerating patch with finite stresses:

$$L_b \approx 1.377 \frac{\mu D_{rs}}{b(\sigma - p)}. \tag{5.9}$$

Note that all lengthscales defined in this work refer to half-lengths. The spatio-temporal evolution of slip rate and friction up to the end of Stage 2 (Figure 5.3) reveals that this is also the case for these fluid-loaded faults. Indeed, all four simulations show a slipping zone that localizes to L_b (evaluated with p at the onset of Stage 2) as slip rates approach dynamic values, here defined as $V > V_{dyn} = 0.1$ m/s. Additional simulations in which we vary parameter b while keeping $a - b$ constant (Figure 5.4) confirm that the localization scales with $1/b$. Note that, contrary to the cases studied by Rubin and Ampuero (2005), there does not appear to be an upper limit on the value of a/b for which this lengthscale applies. This is likely because the increase in pore pressure brings the perturbed zone far above steady-state for all values of a/b considered here (e.g., Figure 5.2(d,h)).

When $L_p < L_b$ as in Figure 5.5, the slipping zone instead remains confined to the pressurized zone. The size of the slipping zone as it approaches dynamic slip rates during Stage 2 is thus equal to the smaller of L_p and L_b. As pointed out by Rubin and Ampuero (2005), L_b is not the shortest slipping zone capable of reaching instability, which implies that reaching dynamic speeds is possible even when $L_p < L_b$, as is the case in Figure 5.5. We thus consider different L_p scenarios with respect to lengthscale L_b to investigate the factors that control whether or not slip reaches dynamic speeds during Stage 2.

5.3.2.1 The Case of $L_p = L_b$

Figure 5.6 shows the evolution of key variables with slip for simulations with $L_p = L_b$ (achieved by $b = 0.01$) and different values of a. Note that, for some of these cases, the fault is velocity-neutral (VN) (a = 0.01) or velocity-strengthening (VS) (a = 0.012) in steady state, with $a \geq b$. As discussed in Rubin and Ampuero (2005), a fault slipping with fixed size L_b is equivalent to a spring-block slider system with an effective stiffness of $k_b = 0.622\mu/L_b$. Frictional weakening from the peak friction f^p while the slipping zone L is equal to L_b can then be described

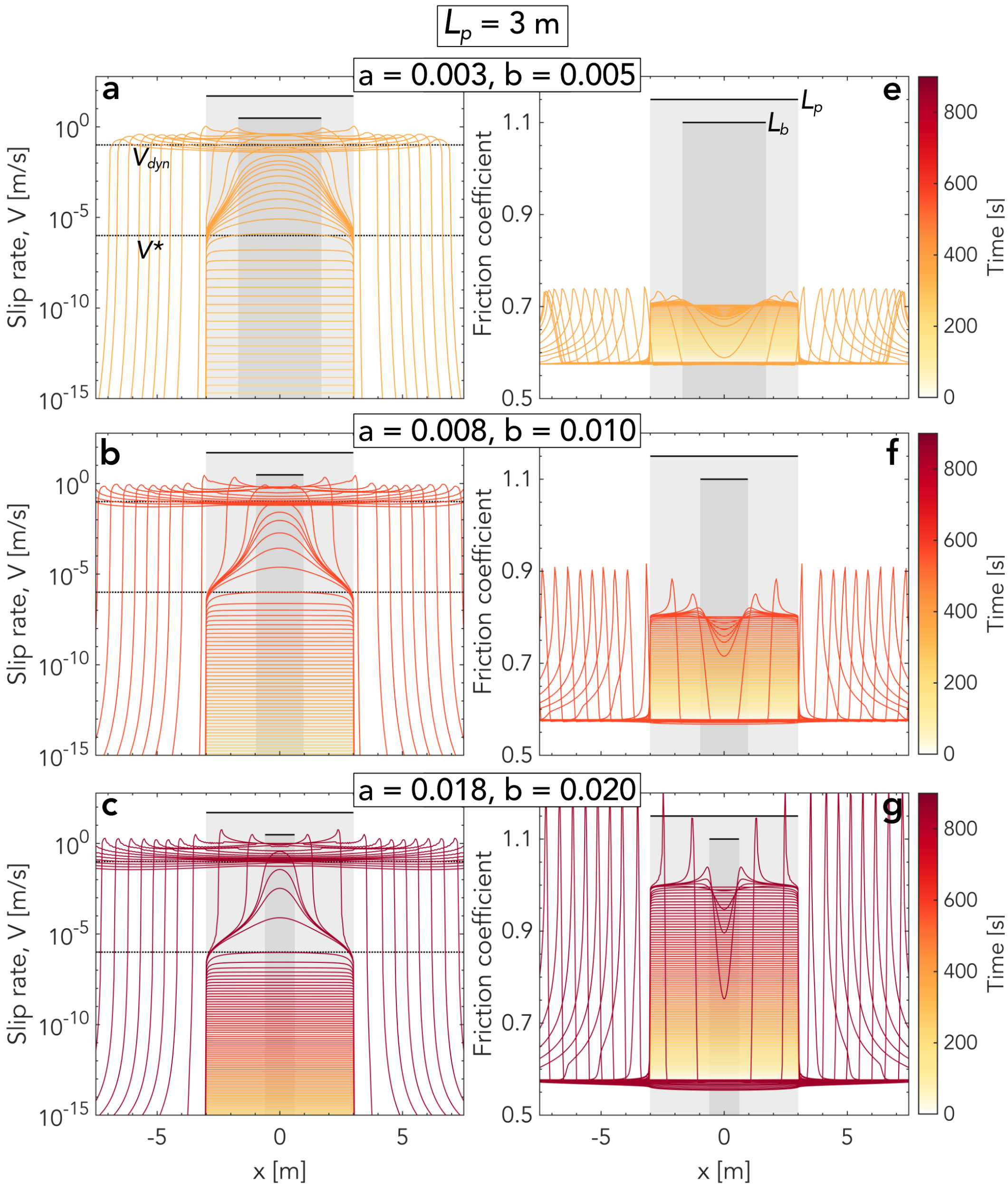

Figure 5.4: Similar to Figure 5.3 but for cases with b = 0.005, 0.010 and 0.020, keeping $a - b$ constant at -0.002 and L_p = 3 m.

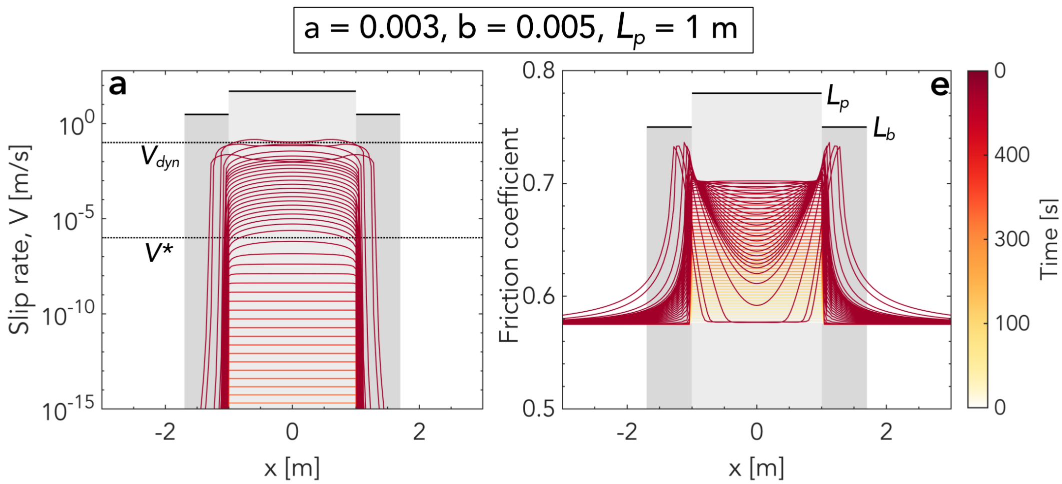

Figure 5.5: Similar to Figure 5.3 but for a case with $a = 0.003$, $b = 0.005$ and $L_p = 1$ m $< L_b$.

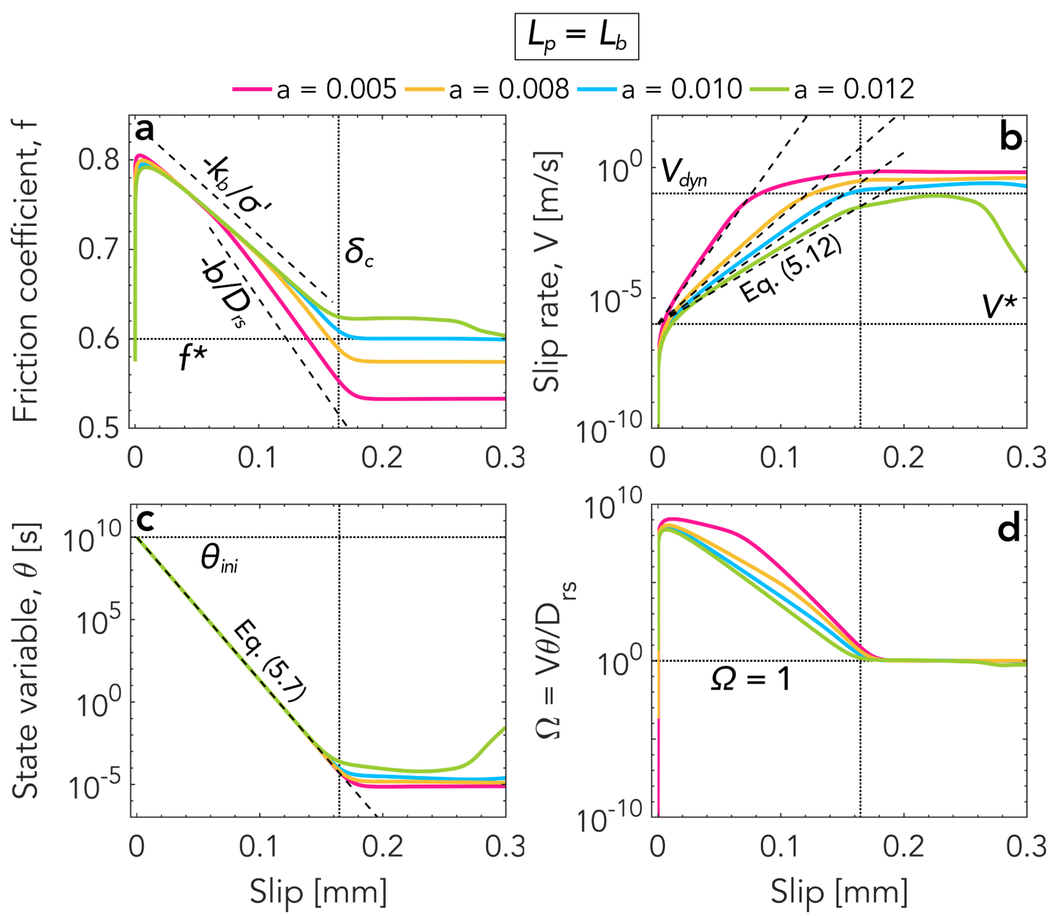

Figure 5.6: Similar to Figure 5.2(e-h) but for simulations with L_p set to L_b and $a = 0.005, 0.008, 0.010$ and 0.012 with $b = 0.010$. The different frictional weakening slopes and the slip rate prediction of Eq. 5.12 are indicated in panels (a) and (b).

with:

$$f = f^p - \frac{k_b}{(\sigma - p)}\delta. \tag{5.10}$$

Panels a and b show that friction indeed initially weakens with slip with a slope of $-k_b/(\sigma - p)$. Once dynamic speeds are reached, however, frictional weakening occurs with slope $-b/D_{rs}$ since the direct effect's contribution to weakening, $(a(\sigma - p)\dot{V}/V^2$, see Rubin and Ampuero (2005)), becomes negligible for the lower acceleration and higher slip rates associated with $V > V_{dyn}$.

Equating (5.10) to a rate-and-state friction coefficient in the no-healing limit (Eq. 5.8) and substituting for f^p (Eq. 5.4) yields:

$$f^* + a\ln\frac{V_s}{V^*} + b\ln\frac{V^*\theta_{ini}}{D_{rs}} - 0.622\frac{b\delta}{D_{rs}} = f^* + a\ln\frac{V}{V^*} + b\ln\frac{V^*\theta_{ini}}{D_{rs}} - \frac{b\delta}{D_{rs}} \tag{5.11}$$

from which we can obtain an estimate of slip rate evolution by solving for V:

$$V = V_s \exp\left(0.378\frac{b}{a}\frac{\delta}{D_{rs}}\right). \tag{5.12}$$

Eq. (5.12) adequately describes the evolution of slip rate with slip as it approaches the dynamic threshold (Figure 5.6b). Note that, here, V_s had to be set to 10^{-6} m/s instead of the $V_s = 10^{-7}$ m/s used to evaluate f^p in Eq. (5.4) to provide a better match to the observed slip rates. Further work is required to estimate this best-fitting V_s a priori.

Eq. (5.12) can be used to infer whether a fault would reach V_{dyn} during stage 2. Specifically, for an earthquake to nucleate during Stage 2, V must reach V_{dyn} before δ reaches δ_c — the effective characteristic slip distance — at which point the fault reaches steady state and thus enters Stage 3. In this regime, δ_c can be estimated as (Bizzarri and Cocco, 2003; Rubin and Ampuero, 2005):

$$\delta_c = D_{rs}\ln\frac{V\theta_{ini}}{D_{rs}}. \tag{5.13}$$

Setting $\delta = \delta_c$ and $V = V_{dyn}$ in Eq. (5.12) and solving for a/b yields a critical value of a/b below which seismic slip occurs during Stage 2:

$$\frac{a}{b} = 0.378\frac{\ln V_{dyn}\theta_{ini}/D_{rs}}{\ln V_{dyn}/V_s}. \tag{5.14}$$

For the parameters listed in Table 5.2, except for L_p which is set to L_b and V_s to 10^{-6} m/s, we find that seismic slip rates are reached during Stage 2 for $a/b \leq 1.1$ (i.e.,

$a \leq 0.011$). This is in agreement with the simulations in Figure 5.6b which shows that a fault with $a = 0.010$ reaches seismic speeds while a fault with $a = 0.012$ does not.

Hence Eq. (5.14) suggests that (i) fault friction does not necessarily have to be velocity weakening for the fault to host seismic slip during Stage 2 and (ii) the critical a/b value depends on θ_{ini}: the longer a fault heals (higher θ_{ini}), the less velocity-weakening and (more velocity-strengthening) the fault friction can be and still generate seismic slip in the presence of fluid injection. Note that fault shear resistance still experiences significant weakening overall, due to increasing pore fluid pressure, and that, for less velocity-weakening faults, the seismic slip would be more self-limiting once the slip exits the pressurized patch. Furthermore, the basic assumption of the modeling in this study — that the fault is healing before the fluid injection — is theoretically inconsistent with velocity-strengthening (VS) faults. A VS fault would be expected, theoretically speaking, to respond to shear loading with steady-state slip (often called creep) and not be progressively healing, resulting in qualitatively different initial conditions than considered in this study. So Eq. (5.14), theoretically speaking, is not applicable to VS faults. Practically speaking, friction properties of a fault can change, with a VW fault experiencing an earthquake and getting into a healing regime as considered here, and then exhibiting VS upon fluid stimulation, in which case Eq. (5.14) would still apply. Another caveat of Eq. (5.14) is that V_s may not be the same for different friction properties.

To verify the dependence on the initial state variable (and hence on fault healing), we reduce θ_{ini} to 10^6 s instead of 10^{10} s (Figure 5.7) and find that this indeed lowers the critical a/b to ~ 0.8 and thus results in some VW faults (e.g., $a = 0.009$) not reaching V_{dyn}. Nevertheless, Eq. (5.14) suggests that all velocity-weakening to velocity-neutral faults that have healed for at least a few years ($\sim$ 5 years) for relatively small D_{rs} ($\sim 1\ \mu$m) and at least a few hundred years ($\sim$ 500 years) for relatively large D_{rs} ($\sim 100\ \mu$m), should reach V_{dyn} during Stage 2 for $L_p = L_b$.

5.3.2.2 The case of $L_p > L_b$

Increasing the size of the pressurized zone further promotes nucleation of seismic slip during Stage 2. Indeed, Figure 5.8 shows that increasing L_p brings the VS, $a = 0.012$ fault above the dynamic threshold. For $L_p > L_b$, the evolution of friction with slip (Figure 5.8a) "curves out" from the constant k_b stiffness line because the slipping zone first has to localize to L_b. This causes the slip rate to increase more

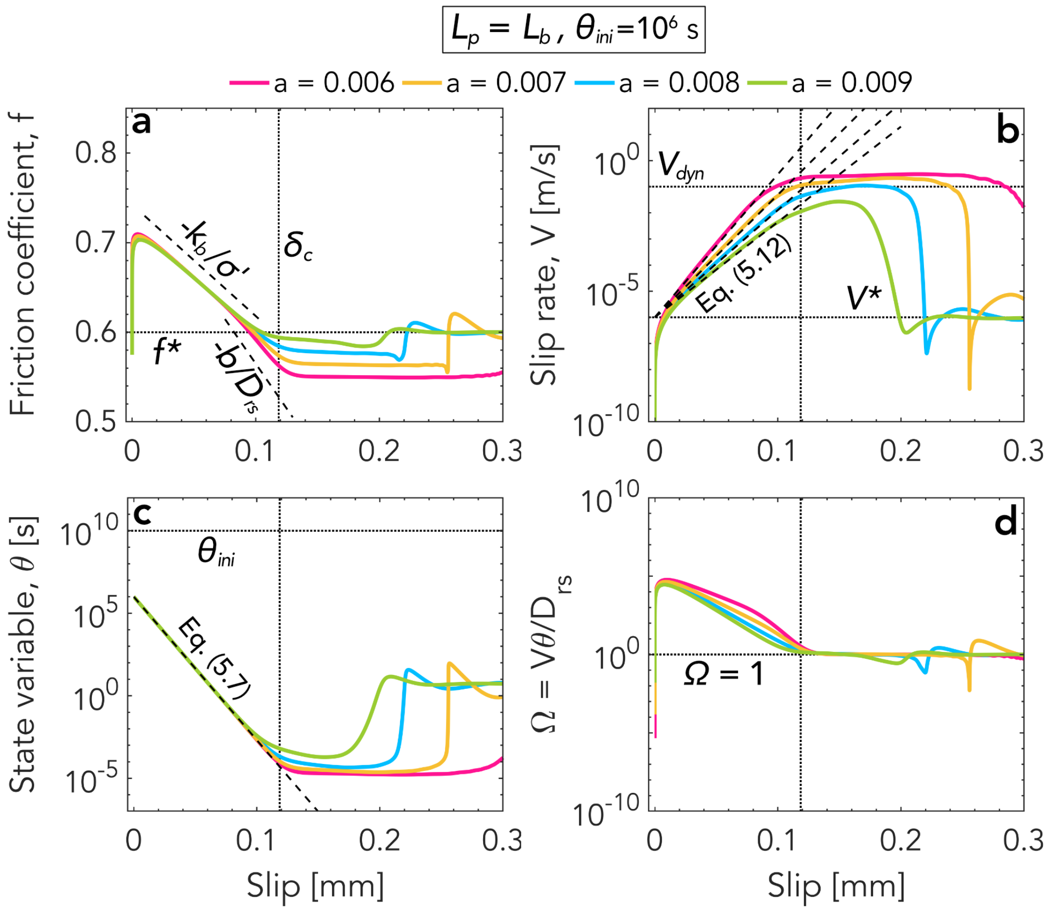

Figure 5.7: Similar to Figure 5.6 but for simulations with a lower θ_{ini} of 10^6 s and $a = 0.006, 0.007, 0.008$ and 0.009 with $b = 0.010$.

rapidly than the Eq. (5.12) prediction and enables it to reach V_{dyn} before δ reaches δ_c.

5.3.2.3 The case of $L_p < L_b$

As noted earlier and as evidenced by Figure 5.9 showing cases with $L_p \leq L_b$, dynamic slip rates can still be reached even when $L_p < L_b$ (e.g., see $L_p = 0.75$ m case). Reducing L_p and hence the size of the slipping zone L increases the effective stiffness of the system (increasing slope in f vs δ plot) and hence slows down the acceleration of slip to dynamic speeds. Notice, however, that cases with $L_p = 0.20$ m and $L_p = 0.35$ m display very similar stiffnesses of $k \approx b(\sigma - p)/D_{rs}$. The pressurized zone size L_p at which this maximum stiffness occurs approximately

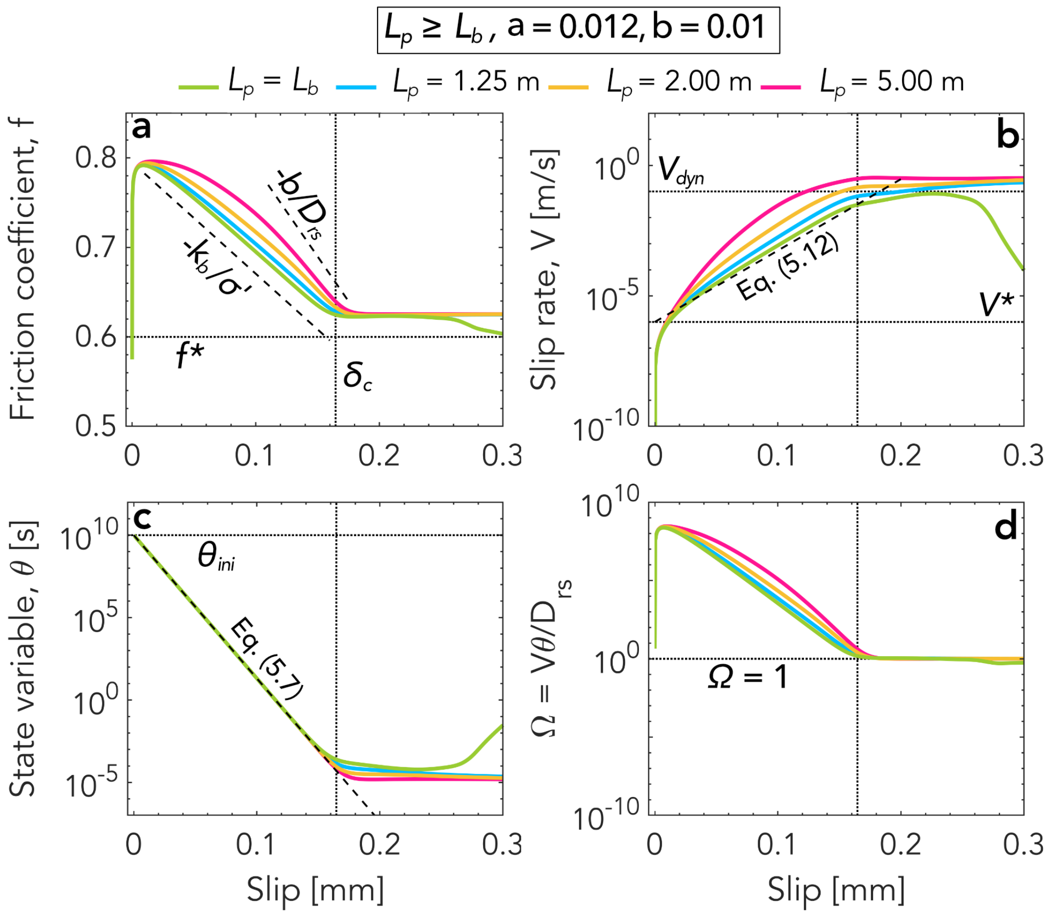

Figure 5.8: Similar to Figure 5.6 but for simulations with a = 0.012, b = 0.01 and $L_p = L_b$, 1.25 m, 2.00 m and 5.00 m.

corresponds to the lengthscale L_{UR} (= 0.41 m in this case):

$$L_{UR} = 0.579 \frac{\mu D_{rs}}{b(\sigma - p)} \tag{5.15}$$

derived by Uenishi and Rice (2003) for slip-weakening faults and recovered by Rubin and Ampuero (2005) for a rate-and-state fault with $a = 0$. The slip-weakening lengthscale applies in this case because friction weakens solely with slip, i.e., with slope $-b/D_{rs}$. Indeed, rewriting Eq. (5.16) with a stiffness k of $b(\sigma - p)/D_{rs}$ yields:

$$f^* + a \ln \frac{V_s}{V^*} + b \ln \frac{V^* \theta_{ini}}{D_{rs}} - \frac{b\delta}{D_{rs}} = f^* + a \ln \frac{V}{V^*} + b \ln \frac{V^* \theta_{ini}}{D_{rs}} - \frac{b\delta}{D_{rs}} \tag{5.16}$$

and hence $V_s = V$, meaning that there is no acceleration during frictional weakening (as can be seen in Figure 5.9b for L_p = 0.20 m and L_p = 0.35 m). The minimum possible L_p that can induce seismic slip during Stage 2 is thus L_{UR}.

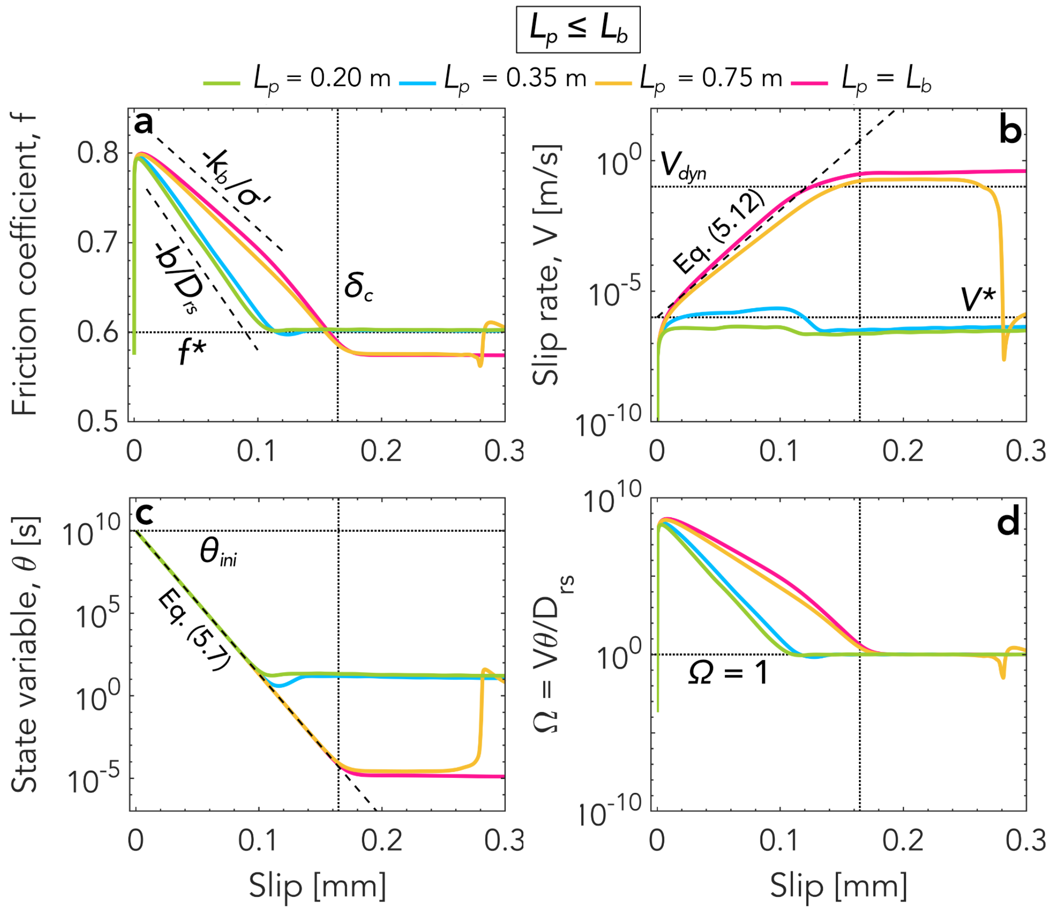

Figure 5.9: Similar to Figure 5.6 but for simulations with a = 0.008, b = 0.01, L_p = 0.20 m, 0.35 m, 0.75 m and L_b.

5.3.2.4 Summary of nucleation of seismic slip during Stage 2

To summarize, for a well-healed VW fault, seismic slip rates occur for $L_p \geq L_b$ and may occur for $L_{UR} \leq L_p < L_b$ for small enough a/b. Nucleation on VS faults is also possible at this stage — with the caveat that the starting point of a well-healed fault may not be applicable to VS faults — for faults with relatively high θ_{ini}/D_{rs} and subjected to relatively large L_p's.

5.3.3 Stage 3: Expansion of the Slipping Zone

5.3.3.1 Crack expansion lengthscale, L_{ss}

At the end of Stage 2, steady state ($\Omega = 1$) is reached at the center of the fault, with the subsequent expansion of the slipping zone marked by smaller to no variations in the fault friction compared to stages 1 and 2, depending on the friction properties.

For cases with smaller a, the expansion proceeds through a series of increasingly larger seismic events, with more variations in fault friction. For cases with larger a, the expansion proceeds as a steady quasi-static crack, with near-constant slipping rates inside the slipping zone.

To get some insight into the extent of the slip-zone expansion, let us consider a quasi-static stress intensity balance for a quasi-static expanding crack adapted for fluid-driven cracks. This consideration should be directly applicable to the cases with larger a that result in such behavior. Note that Dublanchet (2019) found a similar regime for velocity-strengthening faults. As in previous work with slip-weakening (Garagash and Germanovich, 2012; Galis et al., 2017) and rate-and-state friction (Garagash, 2021), we approximate the fluid perturbation as a hypocentral point load P. For the fixed-length pressurized zone considered here, P is simply equal to the injection pressure p multiplied by twice the fixed half-length L_p:

$$P(t) = 2p(t)L_p. \tag{5.17}$$

We can then approximate the resulting stress intensity factor, K, by superimposing the contributions of a uniform background stress drop, K_s, and that of a hypocentral pressure point load, K_P (Garagash and Germanovich, 2012; Galis et al., 2017):

$$K = K_s + K_P = (f_{ini} - f_{ss})\sigma'_{ini}\sqrt{\pi L} + \frac{f_{ss}P}{\sqrt{\pi L}} \tag{5.18}$$

where f_{ini} is the initial friction coefficient equal to the ratio of initial shear to normal stresses, σ'_{ini} is the initial effective normal stress, L is the half-length of the slipping zone, and f_{ss} is the residual, steady-state friction coefficient in the interior of the slipping zone:

$$f_{ss} = f^* + (a - b)\ln\frac{V_{ss}}{V^*}. \tag{5.19}$$

This stress intensity factor balances the fracture toughness, K^*, computed from the estimate of energy release rate, G^*, derived in Rubin and Ampuero (2005):

$$G^* = \frac{\sigma'_{ini} b D_{rs}}{2}\left(\ln\frac{V\theta_{ini}}{D_{rs}\Omega}\right)^2 \tag{5.20}$$

for the aging evolution law, assuming that the slipping region is much larger than the pressurized zone so that σ'_{ini} is the relevant effective normal stress. The fracture toughness can then be estimated as:

$$K^* = \sqrt{2\mu G^*} = \sqrt{\sigma'_{ini} b D_{rs}\mu}\left(\ln\frac{V\theta_{ini}}{D_{rs}}\right) \tag{5.21}$$

assuming that $\Omega = 1$. The resulting stress intensity balance is then:

$$\sqrt{\sigma'_{ini} b D_{rs} \mu} \left(\ln \frac{V^* \theta_{ini}}{D_{rs}} + \ln \frac{V}{V^*} \right) = \left(f_{ini} - f^* + (b - a) \ln \frac{V}{V^*} \right) \sigma'_{ini} \sqrt{\pi L} + \left(f^* + (a - b) \ln \frac{V}{V^*} \right) \frac{P}{\sqrt{\pi L}} \tag{5.22}$$

If we set the reference slip rate V^* as the approximate quasi-static slip rate V_{ss} reached at the interior of the crack, then f^* becomes a proxy for the quasi-static residual friction and $\ln(V_{ss}/V^*) \approx 0$. In the limit $\ln(V_{ss}/V^*) \to 0$, Eq. (5.22) simplifies to:

$$\sqrt{\sigma'_{ini} b D_{rs} \mu} \left(\ln \frac{V^* \theta_{ini}}{D_{rs}} \right) = \left(f_{ini} - f^* \right) \sigma'_{ini} \sqrt{\pi L} + \frac{f^* P}{\sqrt{\pi L}}. \tag{5.23}$$

Solving for the quadratic equation in L, we get solutions:

$$L_{ss} = \frac{1}{2} \left(A^2 - 2B \pm A \sqrt{A^2 - 4B} \right) \tag{5.24}$$

where

$$A = \sqrt{\sigma'_{ini} b D_{rs} \mu} \left(\ln \frac{V^* \theta_{ini}}{D_{rs}} \right) \frac{1}{(f_{ini} - f^*) \sigma'_{ini} \sqrt{\pi}} \quad \text{and} \quad B = \frac{f^* P}{(f_{ini} - f^*) \sigma'_{ini} \pi}. \tag{5.25}$$

Equations 5.24 and 5.25 thus provide an expression for the crack expansion as a function of frictional properties, initial fault healing, prestress and the integrated pore pressure force P. Moreover, in the special case where the reference coefficient f^* corresponds to the initial friction f_{ini}, Equation (5.23) simplifies to:

$$\sqrt{\sigma'_{ini} b D_{rs} \mu} \left(\ln \frac{V^* \theta_{ini}}{D_{rs}} \right) = \frac{f^* P}{\sqrt{\pi L}} \tag{5.26}$$

and L_{ss} to:

$$L^*_{ss} = \frac{1}{\pi \sigma'_{ini} b D_{rs} \mu} \left(\frac{f^* P}{\ln \left(V^* \theta_{ini} / D_{rs} \right)} \right)^2. \tag{5.27}$$

The L_{ss} estimate indeed tracks very well the expansion of the slipping zone during Stage 3 in cases with larger a that result in such behavior, for both the fixed-length and diffusive injection scenarios (Figure 5.1). L_{ss} works not only for aseismically slipping zones (e.g., $a = 0.010$) but also for those slipping via small, contained earthquakes (e.g., $a = 0.007$). Note that dynamic events consistently overrun the extent predicted by L_{ss}, as would be expected due to inertial effects and larger stress changes within the (faster) slipping zone not accounted for by the current derivation, both of which would tend to concentrate stress more efficiently at the slipping zone front. Since Stage 2 nucleation on the $a = 0.004$ fault results in a runaway earthquake event that ruptures the entire modeled domain, L_{ss} does not apply in this case. For the simulations shown in Figure 5.1, we use the full quadratic equation from Eqs. 5.24 and 5.25 since the initial friction coefficient $f_{ini} = 0.575$ is not equal to the reference friction $f^* = 0.6$. Figure 5.10 shows that L_{ss} holds for different cases with $f_{ini} <= f^*$, including a case where $f_{ini} = f^*$ for which the L_{ss}^* simplification from Eq. 5.27 is used. Notice that, for $f_{ini} = 0.625$, L_{ss} only has real solutions up to ~ 300 s because the radicand $A^2 - 4B$ in Eq. 5.24 becomes negative. However, like the $a = 0.004$ case from Figure 5.1, L_{ss} does not apply here because the fault undergoes a runaway event during stage 2.

As discussed in previous studies (e.g., Garagash and Germanovich, 2012; Galis et al., 2017; Dublanchet, 2019; Bhattacharya and Viesca, 2019; Larochelle et al., 2021), runaway earthquake events occur when there is sufficient stress drop available outside the pressurized zone to drive the seismic rupture, which happens when f_{dyn}, the dynamic residual friction coefficient, remains sufficiently lower than f_{ini} to enable a sufficiently high stress drop. Hence the necessary (but not sufficient) condition for ruptures to run away outside the pressurized region is given by:

$$f_{ini} > f_{dyn} \approx f^* + (a - b) \ln \frac{V_{dyn}}{V^*}. \tag{5.28}$$

This explains why lower values of a (e.g., Figure 5.1bg) and higher values of f_{ini} (e.g., Figure 5.10dh) promote runaway behavior. Note that f_{ini} needs to be sufficiently higher than f_{dyn} to enable sufficient seismic stress drop. However, if $f_{ini} \leq f_{dyn}$, the dynamic rupture would be definitely arresting, as there is no stress drop, making L_{ss} clearly relevant.

5.3.3.2 Earthquake nucleation during Stage 3

While the overall expansion of the slipping region can be characterized by L_{ss} for a range of cases, we find that whether this expansion occurs aseismically or seismically is related to the critical lengthscale L_{RR} (Rice and Ruina, 1983) which describes the critical half-length of a perturbation such that larger perturbations would be growing on a steadily slipping fault:

$$L_{RR} = \frac{\pi}{8} \frac{\mu D_{rs}}{(b - a)(\sigma - p)}. \tag{5.29}$$

Figure 5.11 compares the temporal evolution of L_{ss} and L_{RR} (evaluated with the prescribed pressure p) to the spatiotemporal evolution of slip rate for an $a = 0.008$ fault subjected to injections with different sized L_p of the pressurized zone.

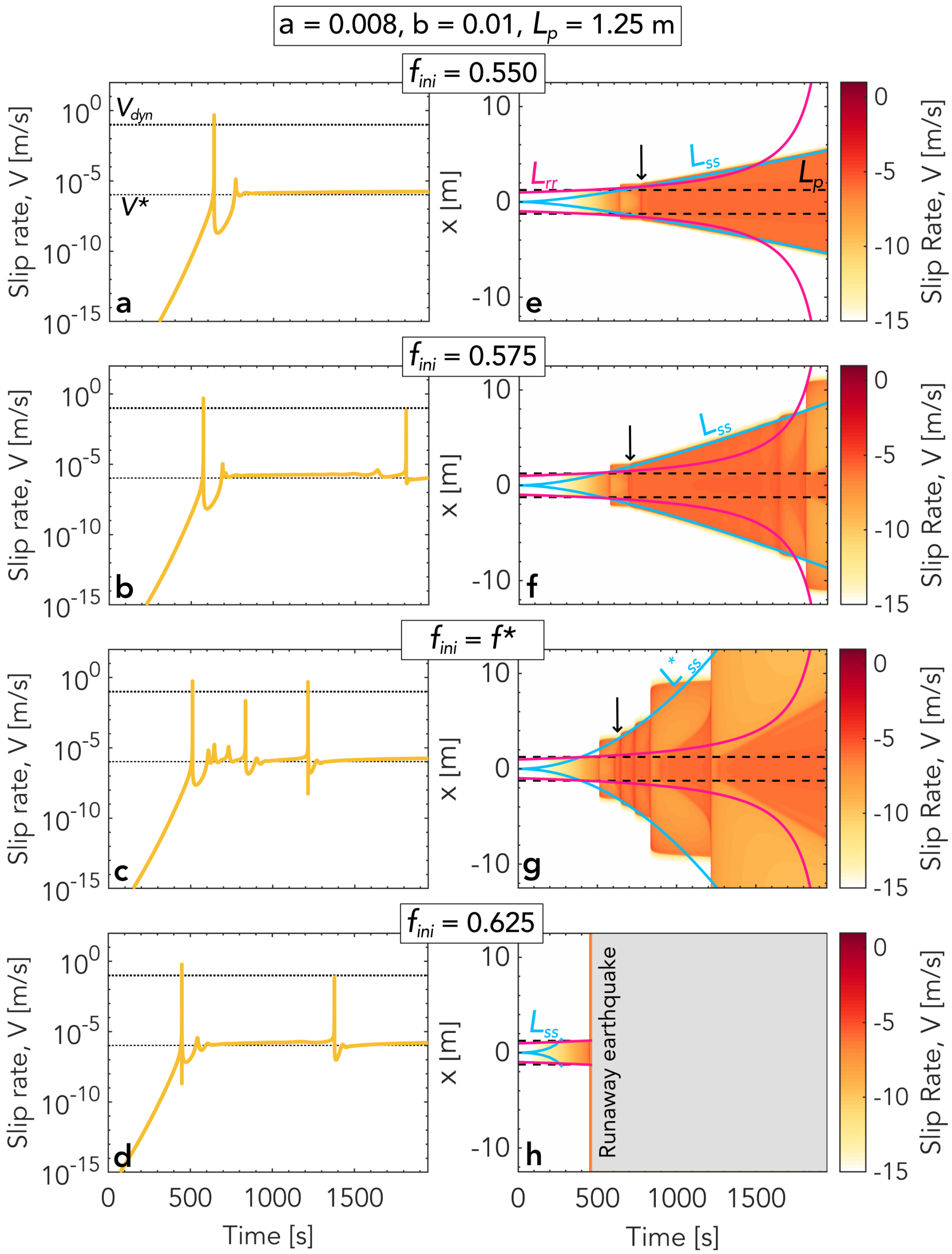

Figure 5.10: Temporal evolution at the center of the fault (a-d) and spatiotemporal evolution (e-h) of slip rate for simulations with different f_{ini} ($f^* = 0.60$). The fixed-length pressurized zone L_p, crack expansion lengthscales L_{ss} and L^*_{ss} as well as the linear stability lengthscale L_{RR} are indicated in panels (e-h). The arrows indicates the transition from a stationary to expanding crack described in Section 5.3.3.2.

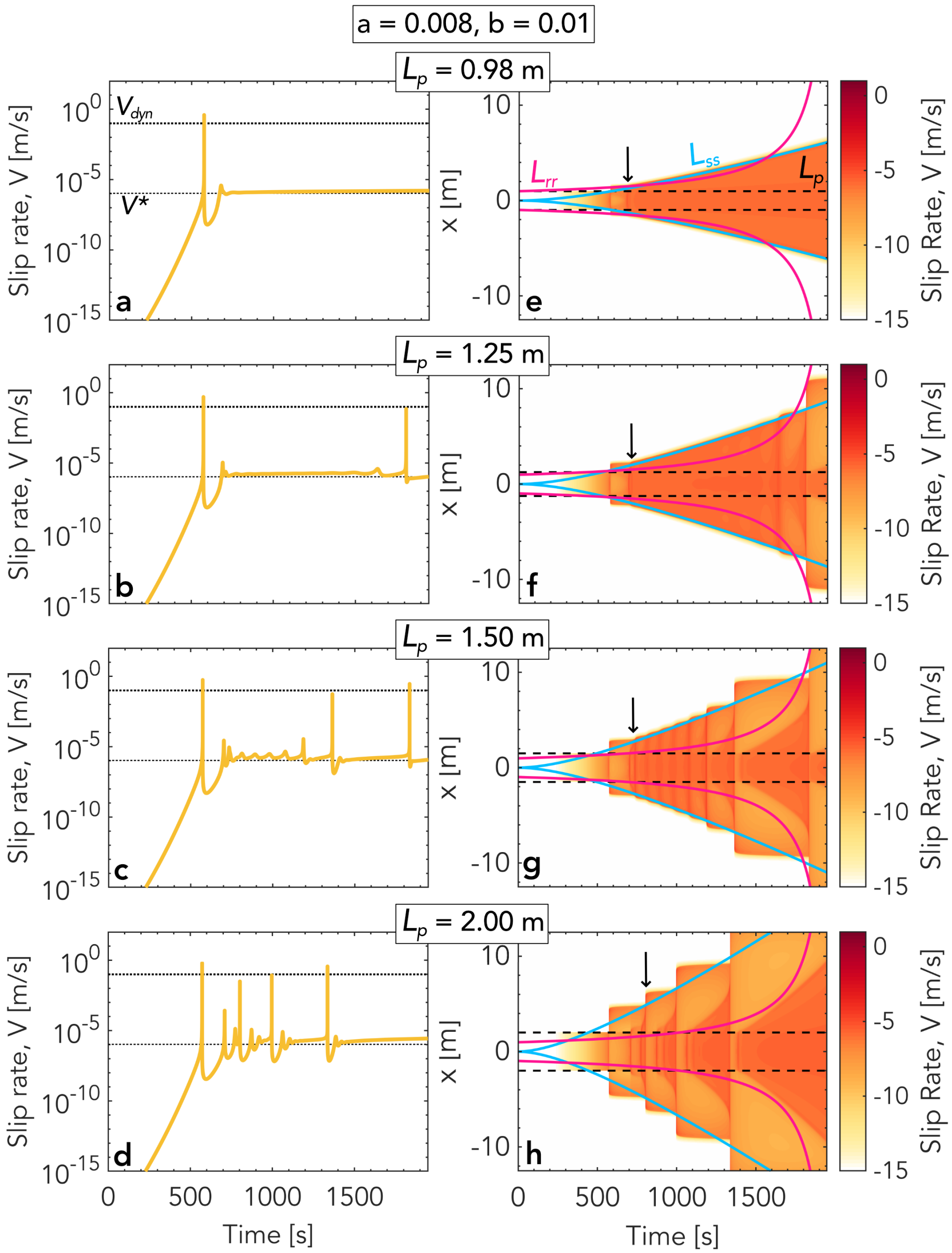

Figure 5.11: Similar to Figure 5.10 but for the reference case with L_p of 0.98 m, 1.25m, 1.50 m and 2.00 m.

We observe two features relevant to slip instability, which we intend to study more in the future. First, the relation between L_{ss} and L_{RR} overall seems to predict how unstable the slip would be during the expansion. When L_{RR} is tracing L_{ss}, the slip remains aseismic and steady (Figures 5.10e, 5.11e, 5.12e). This is consistent with the findings of Dal Zilio et al. (2020) that the VW slipping zone needs to be larger than L_{RR} for slip to spontaneously accelerate. The larger the slipping zone in comparison to L_{RR}, the larger the unstable wavelengths involved with the higher growth rates, and the more unsteady or unstable the slip. Consistently, we see that as L_{ss} becomes increasingly larger than L_{RR} for different cases, they become more unsteady, all the way to accumulating slip through sequences of unstable events (Figures 5.10-5.12). Note that L_{RR} evaluated at the evolving pore fluid pressure in the presurized zone, as plotted in Figures 5.10-5.12, is actually an upper bound for the critical wavelength which becomes increasingly inaccurate as L_{RR} becomes larger than the pressurized region and involves more and more fault locations with the lower background pore fluid pressure. That is why this upper bound becomes larger than the slipping zone at the end of all simulations; the more precise L_{RR} would account for the distribution of the pore fluid pressure in the slipping zone.

This merits a closer look at the relation between L_{RR} and the size of L_p early in the simulation and leads us to the second observation. When seismic slip occurs during Stage 2, the beginning of Stage 3 is characterized by a stationary slipping zone which only starts expanding once L_{ss} catches up with it. The time at which this happens is indicated by the black arrows in Figure 5.11(e-h). Panels (e-h) suggest that if $L_p > L_{RR}$ at that point in time, then the crack expands through seismic events (e.g., $L_p = 2.00$ m case). If $L_p < L_{RR}$ as is the case for the $L_p = 0.98$ m and $L_p = 1.25$ m cases, on the other hand, the crack expands aseismically. The $L_p = 1.50$ m $\approx L_{RR}$ case is clearly at the boundary between these two regimes with small transient acceleration events modulating the aseismic expansion. Figure 5.12 illustrates the same transition from purely aseismic expansion ($L_p = 0.55$ m) and transient-modulated aseismic expansion ($L_p = 0.75$ m) to seismic expansion ($L_p = 0.98$ m and $L_p = 1.25$ m) for a fault with $a = 0.006$. Figure 5.13 with $a = 0.01$ and $L_p = 5$ m confirms that seismic expansion during Stage 3 does not occur for $a \geq b$ even for a relatively large L_p. This is consistent with Stage 3 expansion being controlled by $1/(b-a)$ as opposed to $1/b$ in Stage 2. Moreover, whenever $L_p > L_{RR}$ (e.g., Figure 5.12(d,h)), transient acceleration events can also occur within the confines of the main stationary crack. In fact, these transient acceleration events can even grow into small seismic events in models with large

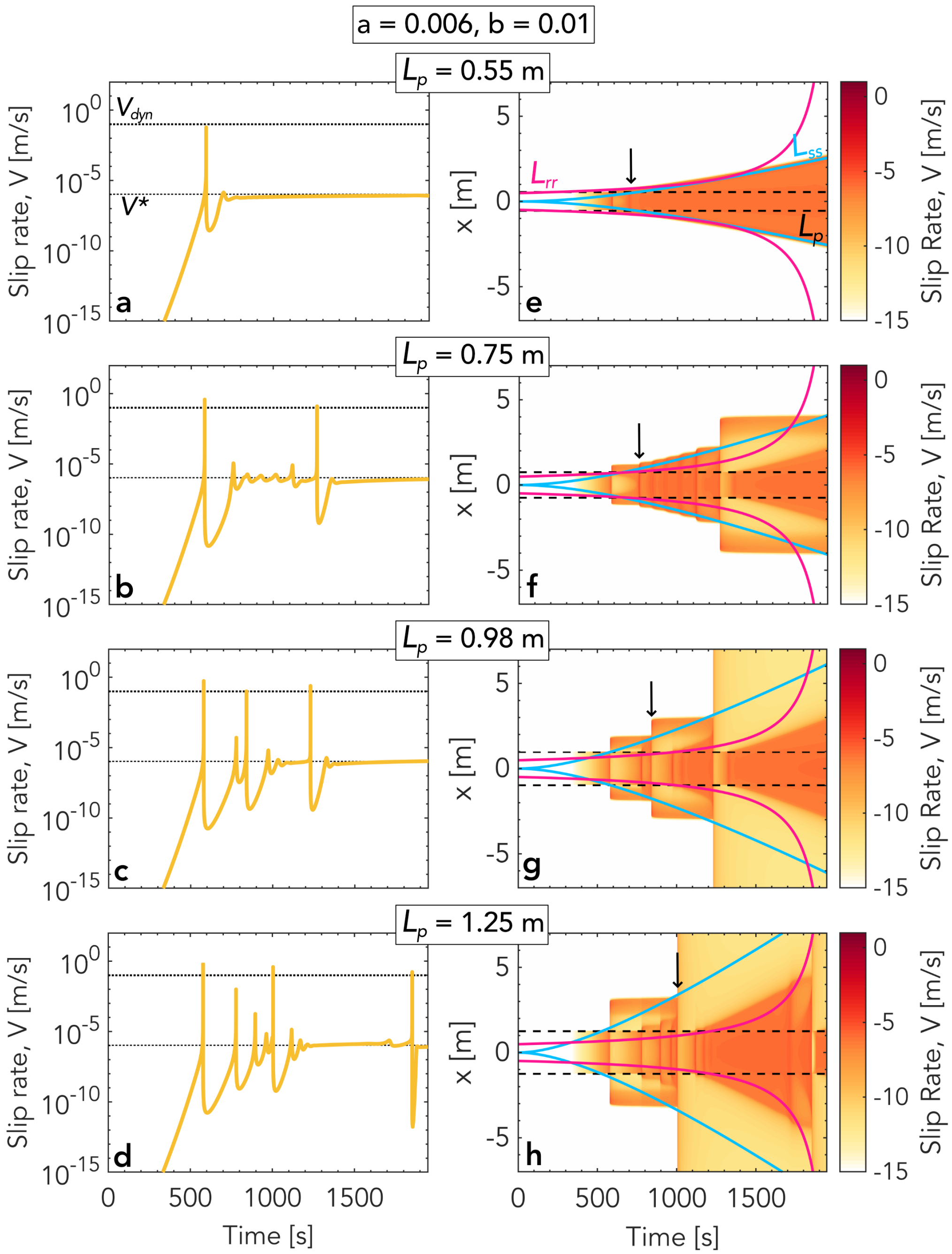

Figure 5.12: Similar to Figure 5.11 but for simulations with $a = 0.006$ and $b = 0.01$ with L_p of 0.55 m, 0.75m, 0.98 m and 1.25 m.

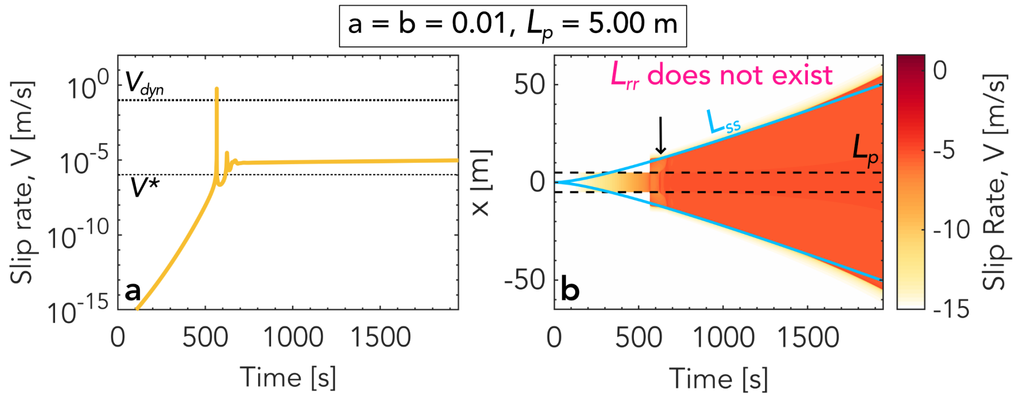

Figure 5.13: Similar to Figure 5.11 but for a simulation with $a = b = 0.01$ and $L_p = 5.00$ m.

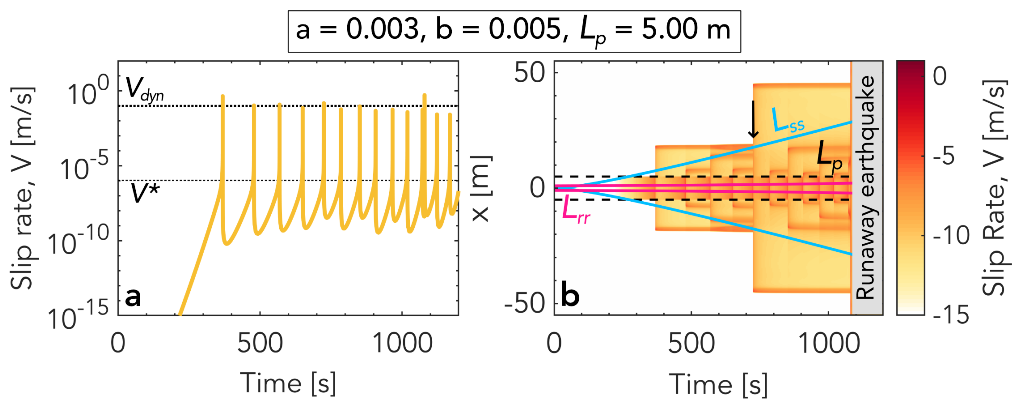

Figure 5.14: Similar to Figure 5.11 but for a simulation with $a = 0.003$, $b = 0.005$ and $L_p = 5.00$ m.

enough L_p and small enough a as can be seen for the case with $L_p = 5$ m, $a = 0.003$ and $b = 0.005$ in Figure 5.14.

5.3.3.3 Nucleation in non-pressurized zones

Finally, notice that some simulations which expand aseismically for some time during Stage 3 do eventually end up producing an earthquake even if $L_p \ll L_{RR}$ (e.g., Figure 5.11(b,f)). We hypothesize that, in this case, seismic slip nucleation involves significant non-pressurized portions of the expanding crack and hence would be more closely governed by instability scales evaluated at the background pore fluid pressure. Indeed, while the low effective normal stress within the pressurized zone precludes nucleation, the rest of the crack has much higher effective normal stress and hence might be able to host seismic events if it grows sufficiently large. Given that, in these cases, the expansion initially proceeds as an expanding steady-state crack, we would expect nucleation to be controlled by Rubin and Ampuero (2005)'s lengthscale:

$$L_{RA} = \frac{1}{\pi} \frac{b\mu D_{rs}}{(b-a)^2(\sigma - p)}. \tag{5.30}$$

Indeed, Figure 5.15 showing similar simulations with different a and L_p reveals that the slipping zone half-length at the time of nucleation approximately corresponds to $2L_{RA}$ evaluated with $p = 0$, suggesting that each side of the crack must be able to accommodate a full crack of length $2L_{RA}$ to be able to slip seismically. In this regime, it thus appears that the pressurized zone acts as a nucleation barrier between the two halves of the crack. Further investigation into this nucleation regime is warranted.

5.4 Discussion and Conclusions

Our analysis illustrates that even relatively simple fluid injection scenarios such as a linearly increasing pressure over a fixed zone can give rise to a wide variety of fault slip behaviors. Fortunately, all simulations shown here go through the same 3 stages that can each be understood in terms of key lengthscales and parameters. During Stage 1, friction balances out the increase in pore pressure through increasing slip rates, bringing the fault above steady state in the process. Stage 2 corresponds to a no-healing frictional weakening regime from above steady-state conditions down to steady state. Seismic slip may be reached during this stage depending on parameters a/b and θ_{ini}/D_{rs} and on the size of the pressurized zone, L_p, with respect to lengthscales L_b and L_{UR}. Stage 3 is characterized by an expanding slipping zone which can be approximated by a steady-state quasi-statically expanding crack driven by the integrated pore pressure force P, unless the fault prestress is high enough to result in a run-away fault rupture. Whether the expansion is aseismic or seismically-modulated is controlled by the linear stability analysis lengthscale L_{RR}. Earthquake nucleation during Stage 3 may also occur as a result of the slipping zone over the non-pressurized portions of the fault reaching the nucleation lengthscale $2L_{RA}$. Hence, our work clearly shows that fault slip induced via fixed-length pressurization is not governed by a single nucleation length, but rather by a combination of several stability lengthscales that reflect different fault conditions.

In terms of injection parameters, our modeling reveals that the increase of pore pressure p, the size of the pressurized zone L_p and the integrated pore pressure P —

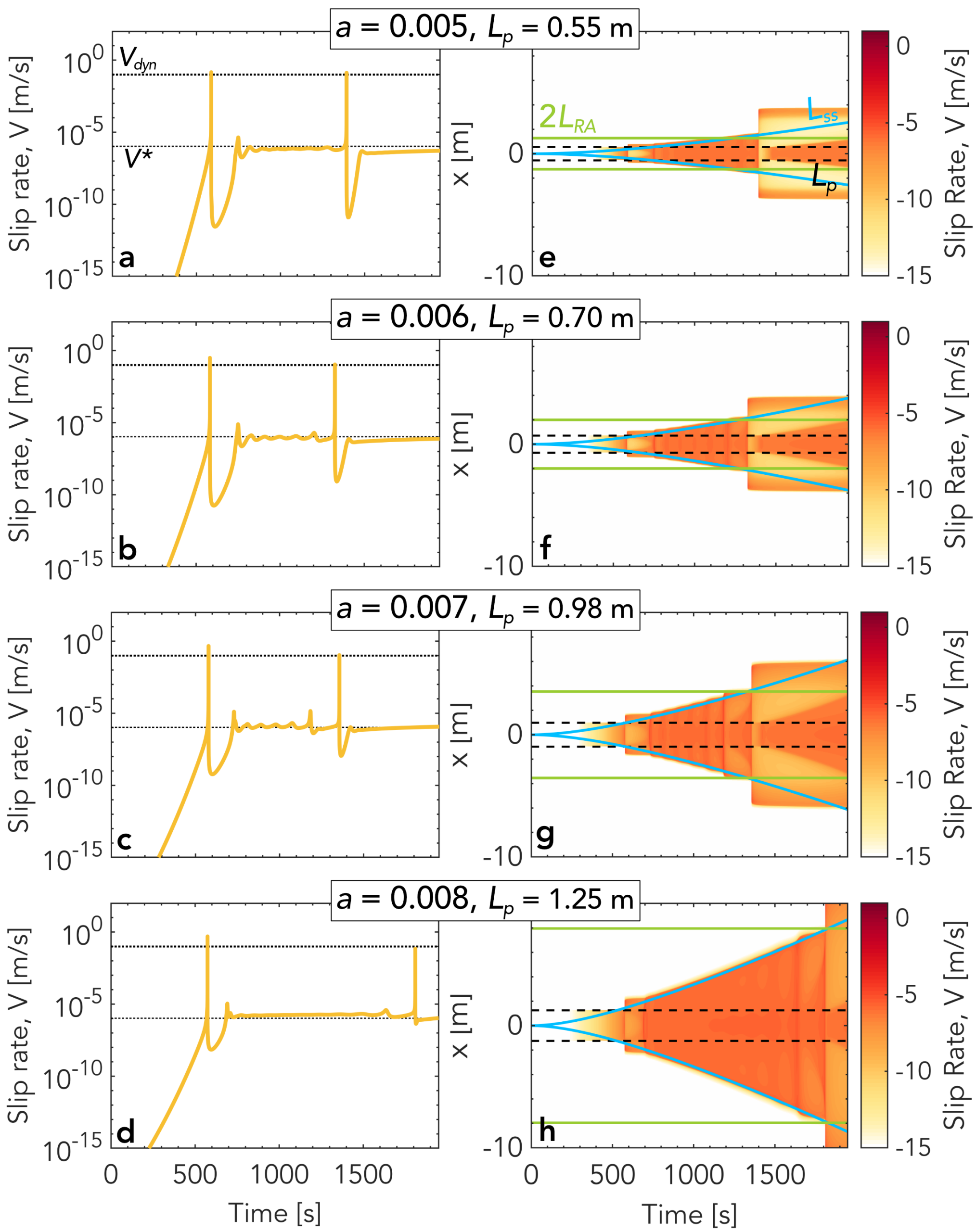

Figure 5.15: Similar to Figure 5.11 but for simulations with different a and L_p that undergo a seismic event after slipping aseismically for a while during Stage 3. The green lines indicate the lengthscale $2L_{RA}$ discussed in Section 5.3.3.3.

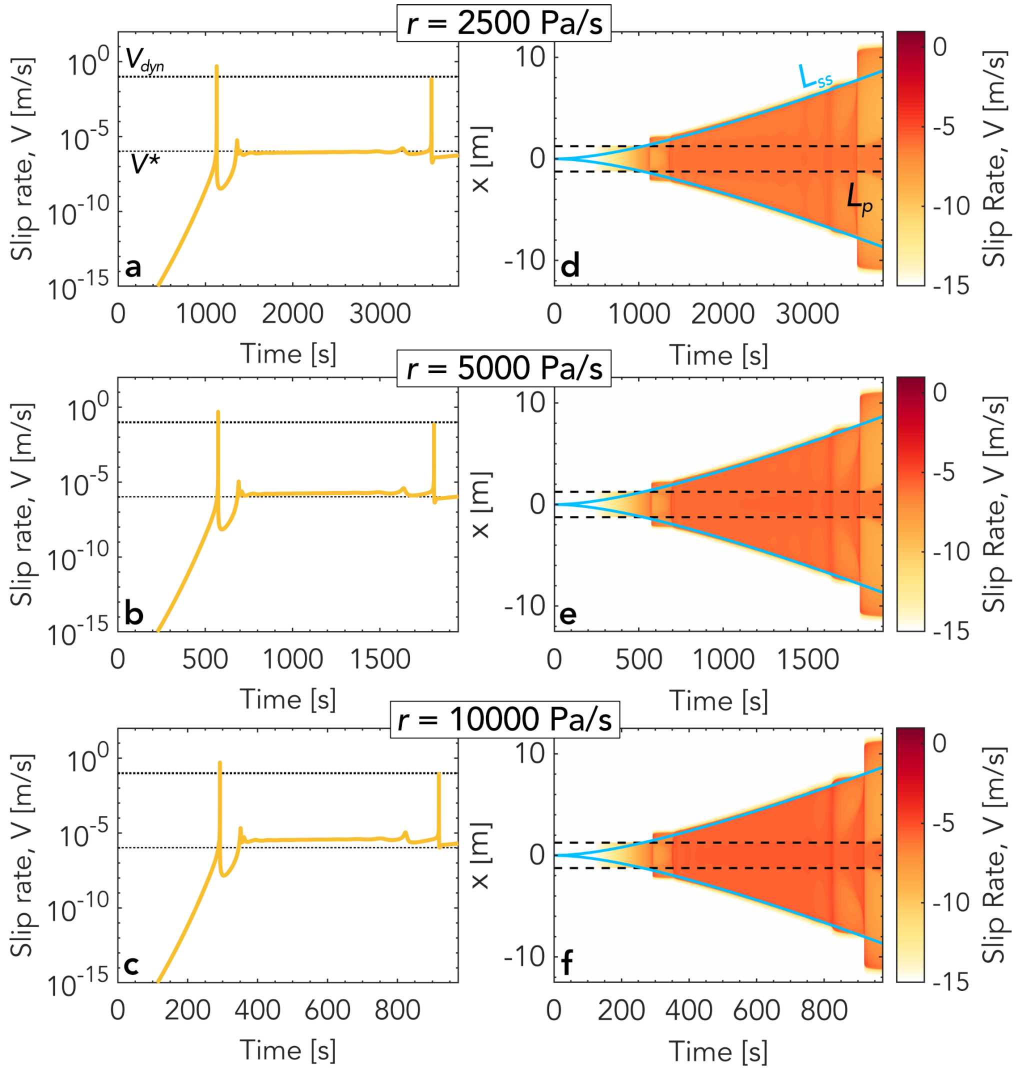

Figure 5.16: Similar to Figure 5.11 but for simulations with the reference parameters listed in Table 5.2, varying the pressurization rate r. Note the different timescale for each simulation.

proportional to fluid volume (Galis et al., 2017) — affect the slip behavior in Stages 1-3, 2-3 and 3, respectively. The rate of pressurization r, on the other hand, does not appear to be a controlling parameter as far as these simplified pressurization models with quasi-static pressurization rates go. In fact, changing the rate to $r = 2500$ and $r = 10000$ Pa/s in Figure 5.16 reveals nearly identical simulation results as the reference case with $r = 5000$ Pa/s. Injection rates would be more important in diffusive scenarios since it affects the size of the pressurized zone.

While the analysis presented here focuses on the simpler case of fixed-length injection, it provides significant insights into diffusive pressurization scenarios. In particular, given the similarities of the simulations shown in Figure 5.1 during Stage 3, lengthscales L_{RR} and L_{RA} — or some variant of these lengthscales — would be relevant to understanding the behavior observed in the diffusive cases as well. Stage 2 frictional weakening also occurs for the diffusive scenario but the effective pressurized zone in the case of $a = 0.007$, 0.008 and 0.01 might not be large enough in comparison to L_b and L_{UR} to reach seismic speeds. Increasing hydraulic diffusivity α may promote earthquake nucleation during this stage. Finally, since in practice fluids are usually not injected directly into a fault zone but rather at some distance from it, by the time the fluids reach the fault, the pressurized zone may be closer to the uniform L_p scenario investigated here than to the sharply-peaked pore pressure distribution associated with in-fault injection scenarios.

Overall, this study provides additional insight with which to interpret and design fluid-injection experiments, both in the field (Guglielmi et al., 2015) and in the laboratory (e.g., Gori et al., 2021). For the field experiment described in Chapter 4, for example, our analysis suggests that the pressurized and slipping zones were large enough to induce significant slip acceleration at 1200 s, but smaller than the different stability lengthscales such that no seismic slip events nucleated at the injection site. More generally, our study has important implications for understanding how fluids and fault friction interact to give rise to seismic and aseismic slip. Such interactions are central to understanding both fluid-induced and tectonic fault processes.

Bibliography

J. P. Ampuero and A. M. Rubin. Earthquake nucleation on rate and state faults - aging and slip laws. *Journal of Geophysical Research: Solid Earth*, 113, 2008. ISSN 21699356. doi: 10.1029/2007JB005082.

P. Bhattacharya and R. C. Viesca. Fluid-induced aseismic fault slip outpaces pore-fluid migration. *Science*, 364(6439):464–468, 2019.

A. Bizzarri and M. Cocco. Slip-weakening behavior during the propagation of dynamic ruptures obeying rate-and state-dependent friction laws. *Journal of Geophysical Research: Solid Earth*, 108(B8), 2003.

L. Dal Zilio, N. Lapusta, and J.-P. Avouac. Unraveling scaling properties of slow-slip events. *Geophysical Research Letters*, 47(10):e2020GL087477, 2020.

J. H. Dieterich. Earthquake nucleation on faults with rate-and state-dependent strength. *Tectonophysics*, 211(1-4):115–134, 1992.

P. Dublanchet. Fluid driven shear cracks on a strengthening rate-and-state frictional fault. *Journal of the Mechanics and Physics of Solids*, 132:103672, 11 2019. ISSN 00225096. doi: 10.1016/j.jmps.2019.07.015. URL https://www.sciencedirect.com/science/article/pii/S0022509619305393?via3Dihub.

M. Galis, J.-P. Ampuero, P. M. Mai, and F. Cappa. Induced seismicity provides insight into why earthquake ruptures stop. *Science Advances*, 3:eaap7528, 2017. ISSN 2375-2548. doi: 10.1126/sciadv.aap7528.

D. I. Garagash. Fracture mechanics of rate-and-state faults and fluid injection induced slip. *Philosophical Transactions of the Royal Society A: Mathematical, Physical and Engineering Sciences*, 379:20200129, 2021. ISSN 1364-503X. doi: 10.1098/rsta.2020.0129.

D. I. Garagash and L. N. Germanovich. Nucleation and arrest of dynamic slip on a pressurized fault. *Journal of Geophysical Research: Solid Earth*, 117, 2012. ISSN 01480227. doi: 10.1029/2012JB009209. URL http://doi.wiley.com/10.1029/2012JB009209.

M. Gori, V. Rubino, A. J. Rosakis, and N. Lapusta. Dynamic rupture initiation and propagation in a fluid-injection laboratory setup with diagnostics across multiple temporal scales. *Proceedings of the National Academy of Sciences*, 118(51), 2021.

Y. Guglielmi, F. Cappa, J. Avouac, P. Henry, and D. Elsworth. Seismicity triggered by fluid injection-induced aseismic slip. *Science*, 348(6240), 2015. doi: 10.1126/science.aab0476. URL https://doi.org/10.1126/science.aab0476.

S. Larochelle, N. Lapusta, J.-P. Ampuero, and F. Cappa. Constraining fault friction and stability with fluid-injection field experiments. *Geophysical Research Letters*, n/a(n/a):e2020GL091188, 2021. doi: https://doi.org/10.1029/2020GL091188. e2020GL091188 2020GL091188.

J. R. Rice and A. L. Ruina. Stability of steady frictional slipping. *Journal of Applied Mechanics*, 50:343, 6 1983. ISSN 00218936. doi: 10.1115/1.3167042. URL http://AppliedMechanics.asmedigitalcollection.asme.org/article.aspx?articleid=1406945.

A. M. Rubin and J.-P. Ampuero. Earthquake nucleation on (aging) rate and state faults. *Journal of Geophysical Research: Solid Earth*, 110, 2005. ISSN 01480227. doi: 10.1029/2005JB003686.

K. Uenishi and J. R. Rice. Universal nucleation length for slip-weakening rupture instability under nonuniform fault loading. *Journal of Geophysical Research: Solid Earth*, 108, 1 2003. ISSN 01480227. doi: 10.1029/2001JB001681. URL http://doi.wiley.com/10.1029/2001JB001681.

CONCLUSIONS AND PERSPECTIVES

In this thesis, we developed methodologies and models to probe water-solid Earth interactions in the context of hydrological loading, aquifer poroelasticity and fluid-induced fault slip. Here we highlight directions of ongoing and future work in each of these areas.

In Chapter 1, we used Independent Component Analysis (ICA) and a global GRACE-based deformation model to extract seasonal signals due to redistribution of continental water mass in GNSS time series. The resulting vertical and horizontal deformation field could be used to refine the temporal and spatial resolution of continental water storage estimates in regions equipped with GNSS networks denser than GRACE's limited spatial resolution of 300-400 km. For example, Figure 6.1 shows the dominant vertical hydrological loading signal extracted from California's high-density GNSS network. We note, however, that care should be taken to isolate the contribution of loads hydrological loads from that of loads outside the study area by inverting the spatial discrepancies between the extracted GNSS and GRACE-model independent components. This inversion would also require accounting for poroelastic effects, which is the point addressed in Chapters 2 and 3.

In Chapters 2 and 3, we presented a methodology to extract poroelastic deformation associated with aquifer groundwater level variations from GNSS datasets. While GNSS can provide a high-precision, high-frequency record of poroelastic deformation, GNSS lacks the high spatial resolution of Synthetic Aperture Radar interferometry (InSAR). Indeed, although InSAR measurements come with their own set of technical challenges and systematic errors, they provide the continuous spatial coverage necessary to capture poroelastic deformation directly at the monitoring wells locations. Combining GNSS and InSAR measurements (e.g., Riel et al., 2018; Hu and Bürgmann, 2020; Gualandi and Liu, 2021) is beneficial to minimize the effect of systematic errors as well as to better separate the vertical and horizontal deformation fields which, as discussed in Chapters 2 and 3, are affected by variations in groundwater levels and elastic properties in different ways. The preliminary analysis shown in Figure 6.2, for example, reveals a generally good agreement between GNSS and InSAR-inferred seasonal displacements in and around the Sacramento Valley in California. We thus believe that the future of aquifer monitoring lies in combining GNSS, InSAR and GRACE techniques to track groundwater variations primarily from space.

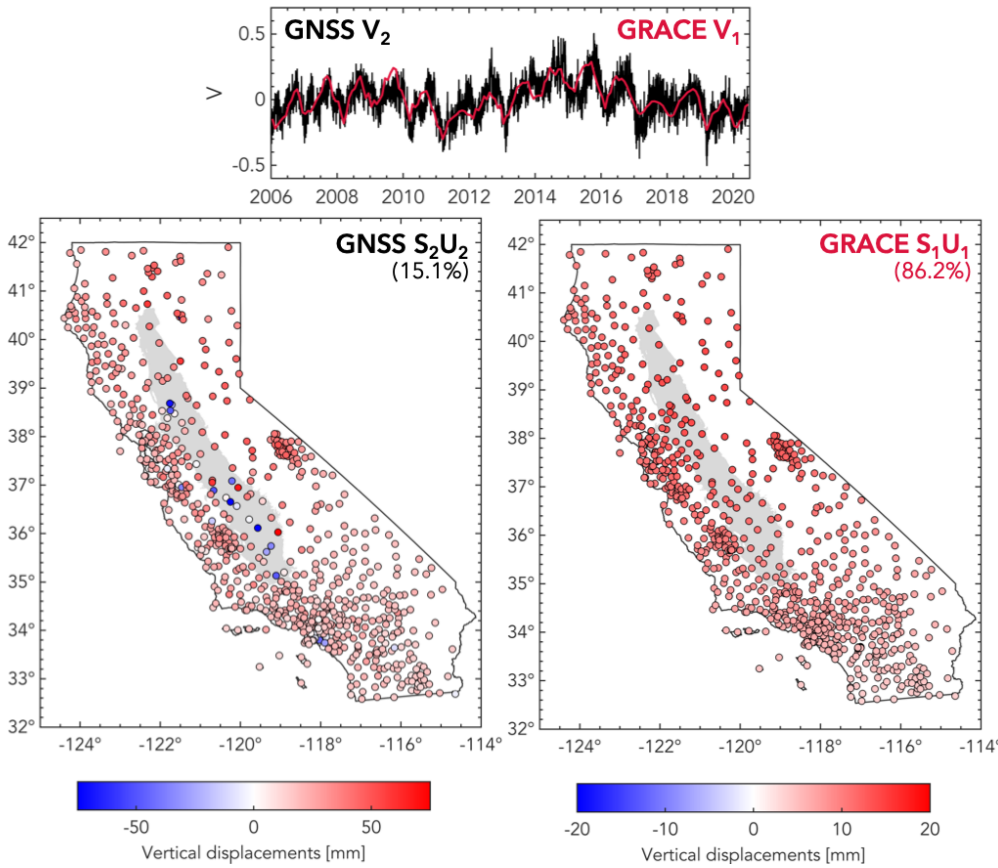

Figure 6.1: Comparison of the dominant seasonal and multiannual hydrological loading signals extracted from vertical GNSS and GRACE-model time series in California with ICA.

More generally, the methodologies we developed here for seasonal and multiannual hydrogeodetic signals could be extended to secular deformation fields in order to monitor long-term changes in water resources. Beyond hydrogeodesy, our refined hydrogeodetic signals could also be helpful in improving the recovery of other important geodetic signals related to tectonic (Vergnolle et al., 2010; Michel et al., 2019), volcanic (Montgomery-Brown et al., 2015) and thermoelastic (Ben-Zion and Leary, 1986; Tsai, 2011) processes, for example. Our hydrological loading and poroelastic deformation fields could also be used to evaluate the relative importance of these mechanisms in modulating background seismicity (Bettinelli et al., 2008; Craig et al., 2017; Johnson et al., 2017; Hu and Bürgmann, 2020).

Then, in Chapter 4, we developed a numerical model for simulating fault slip due to crustal water injections. Calibration of the model against a field experiment on a natural fault revealed that frictional scenarios with different inherent stability

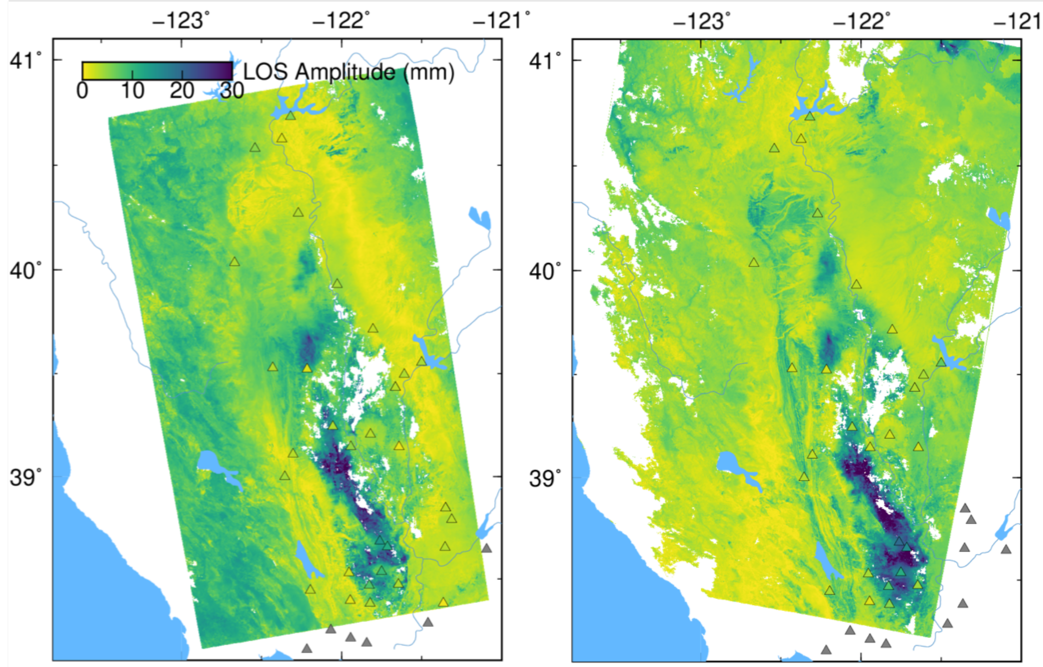

Figure 6.2: Seasonal oscillation of ground displacement measured by InSAR (color map) and GPS (colored triangles) along ascending (left) and descending (right) InSAR tracks in the Sacramento Valley, California. InSAR amplitudes with standard deviations larger than 3 mm are excluded. (*Preliminary InSAR data processed by Manon Dalaison and Romain Jolivet at École normale supérieure (ENS) Paris.*)

could equally well explain the slip observations during pressurization, highlighting the importance of constraining fault frictional properties for forecasting seismic hazard associated with fluid injections. In that regard, we have been developing a new procedure to constrain the frictional properties of sliding interfaces through frictional healing experiments in the laboratory (*In preparation*Sirorattanakul et al.*In preparation*). Indeed, as illustrated in Figure 6.3, fitting the temporal evolution of micrometric slip during interface healing with rate-and-state friction relationships restricts the set of possible parameter values. Such constraints can then inform the modeling of fluid-injection experiments performed on these interfaces (Gori et al., 2021).

Finally, in Chapter 5, we presented a theoretical analysis of fluid-induced fault slip simulations for the case of a fixed-length pressurized zone. Further work in this direction is certainly needed to better understand the behavior of diffusive pressurization scenarios and, eventually, of models with additional fluid effects such as thermal pressurization (Sibson, 1973; Noda and Lapusta, 2010), slip-induced

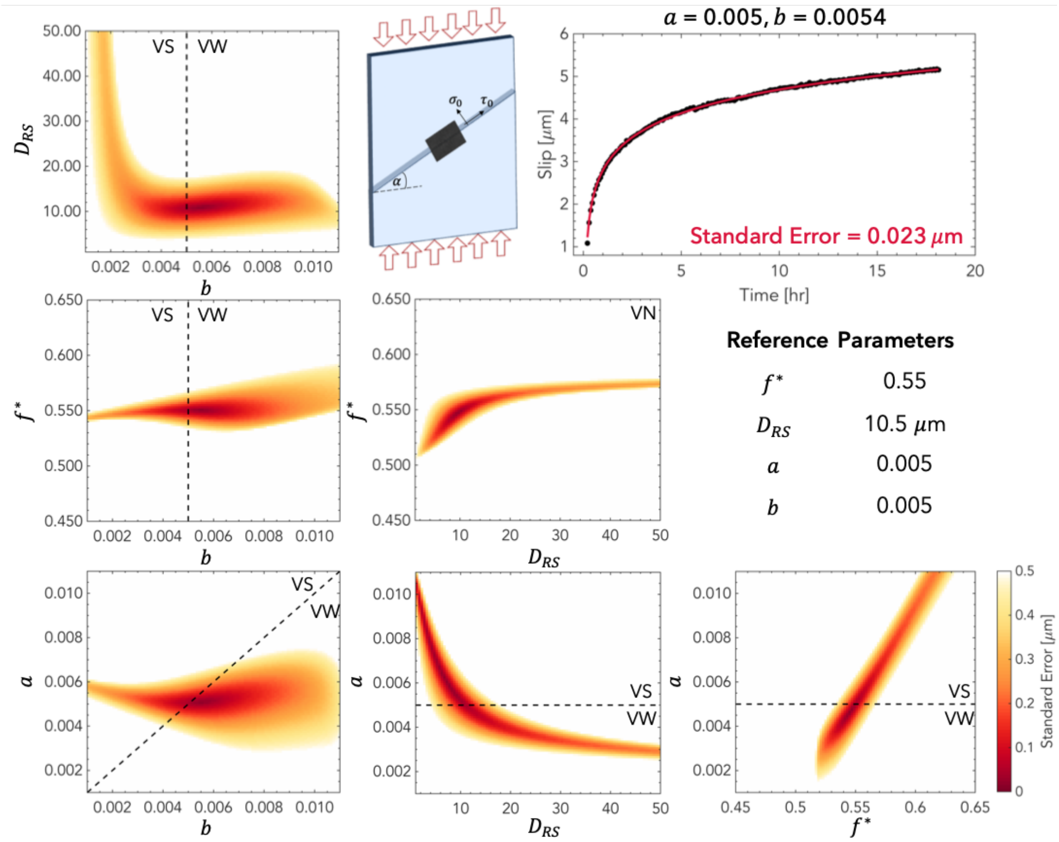

Figure 6.3: Exploration of the rate-and-state parameter space for the slip evolution (black dots) shown on the top right, measured during an interface healing laboratory experiment. The lower the standard error (white to red colormap), the better the fit to the data. The red line shows the slip associated with the set of parameter that minimizes the standard error. (*Slip data from laboratory experiment performed by Pond Sirorattanakul, Vito Rubino and Ares Rosakis at Caltech.*)

dilatancy (Segall and Rice, 1995; Liu and Rubin, 2010; Yang and Dunham, 2021; Heimisson et al., 2022) and poroelastic stresses (Segall and Lu, 2015; Heimisson et al., 2019). Such theoretical insight could help guide the design of future fluid-injection fault slip experiments, in both the field and the laboratory, as well as help interpret seismic and geodetic observations associated with geoenergy activities.

To conclude, understanding mechanical interactions between water and the solid Earth will no doubt become even more important in years to come given our changing climate and increasing reliance on groundwater and geoenergy resources. Similar interactions between water, ice and the solid Earth are also occurring in the cryosphere (Figure 6.4): Meltwater-driven fractures are thought to promote ice-shelf collapse (Lai et al., 2020); sub-glacial hydrology is thought to control frictional sliding at the

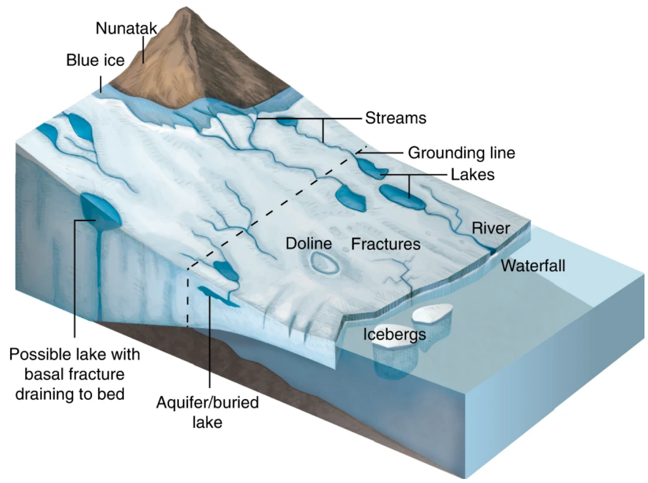

Figure 6.4: Schematic diagram illustrating various mechanical interactions between water, ice and solid Earth at play on the Antarctic Ice Sheet (from Bell et al. (2018)).

base of fast-flowing glaciers (Bartholomew et al., 2010; Stevens et al., 2022; Tsai et al., 2022); and so-called *firn aquifers* are being discovered on ice sheets (Miller et al., 2020; Montgomery et al., 2020). My hope is that some of the methodologies and insight we have derived in this thesis can also help address pressing questions in glaciology.

Bibliography

I. Bartholomew, P. Nienow, D. Mair, A. Hubbard, M. A. King, and A. Sole. Seasonal evolution of subglacial drainage and acceleration in a greenland outlet glacier. *Nature Geoscience*, 3(6):408–411, 2010.

R. E. Bell, A. F. Banwell, L. D. Trusel, and J. Kingslake. Antarctic surface hydrology and impacts on ice-sheet mass balance. *Nature Climate Change*, 8(12):1044–1052, 2018.

Y. Ben-Zion and P. Leary. Thermoelastic strain in a half-space covered by unconsolidated material. *Bulletin of the Seismological Society of America*, 76, 1986. ISSN 0037-1106. doi: 10.1785/bssa0760051447.

P. Bettinelli, J.-P. Avouac, M. Flouzat, L. Bollinger, G. Ramillien, S. Rajaure, and S. Sapkota. Seasonal variations of seismicity and geodetic strain in the Himalaya induced by surface hydrology. *Earth and Planetary Science Letters*, 266(3-4): 332–344, 2008. ISSN 0012-821X. doi: 10.1016/J.EPSL.2007.11.021.

T. J. Craig, K. Chanard, and E. Calais. Hydrologically-driven crustal stresses and seismicity in the New Madrid Seismic Zone. *Nature Communications*, 8(1):2143, 2017. ISSN 2041-1723. doi: 10.1038/s41467-017-01696-w.

M. Gori, V. Rubino, A. J. Rosakis, and N. Lapusta. Dynamic rupture initiation and propagation in a fluid-injection laboratory setup with diagnostics across multiple temporal scales. *Proceedings of the National Academy of Sciences*, 118(51), 2021.

A. Gualandi and Z. Liu. Variational bayesian independent component analysis for InSAR displacement time-series with application to Central California, USA. *Journal of Geophysical Research: Solid Earth*, 126:e2020JB020845, 2021. ISSN 2169-9313. doi: 10.1029/2020JB020845.

E. R. Heimisson, E. M. Dunham, and M. Almquist. Poroelastic effects destabilize mildly rate-strengthening friction to generate stable slow slip pulses. *Journal of the Mechanics and Physics of Solids*, 130:262–279, 2019.

E. R. Heimisson, S. Liu, N. Lapusta, and J. Rudnicki. A spectral boundary-integral method for faults and fractures in a poroelastic solid: Simulations of a rate-and-state fault with dilatancy, compaction, and fluid injection. *In revision*, 2022.

X. Hu and R. Bürgmann. Aquifer deformation and active faulting in Salt Lake Valley, Utah, USA. *Earth and Planetary Science Letters*, 547:116471, 2020. ISSN 0012-821X. doi: 10.1016/J.EPSL.2020.116471.

C. W. Johnson, Y. Fu, and R. Bürgmann. Seasonal water storage, stress modulation, and California seismicity. *Science (New York, N.Y.)*, 356(6343):1161–1164, 2017. ISSN 1095-9203. doi: 10.1126/science.aak9547.

C.-Y. Lai, J. Kingslake, M. G. Wearing, P.-H. C. Chen, P. Gentine, H. Li, J. J. Spergel, and J. M. van Wessem. Vulnerability of antarctica's ice shelves to meltwater-driven fracture. *Nature*, 584(7822):574–578, 2020.

Y. Liu and A. M. Rubin. Role of fault gouge dilatancy on aseismic deformation transients. *Journal of Geophysical Research: Solid Earth*, 115(B10), 2010.

S. Michel, A. Gualandi, and J.-P. Avouac. Similar scaling laws for earthquakes and cascadia slow-slip events. *Nature*, 574(7779):522–526, 2019.

O. Miller, D. Solomon, C. Miège, L. Koenig, R. Forster, N. Schmerr, S. Ligtenberg, A. Legchenko, C. Voss, L. Montgomery, and J. McConnell. Hydrology of a perennial firn aquifer in southeast Greenland: An overview driven by field data. *Water Resources Research*, 56(8), 2020. doi: 10.1029/2019WR026348. URL `https://doi.org/10.1029/2019WR026348`.

L. Montgomery, C. Miège, J. Miller, T. Scambos, B. Wallin, O. Miller, D. Solomon, R. Forster, and L. Koenig. Hydrologic properties of a highly permeable firn aquifer in the Wilkins ice shelf, Antarctica. *Geophysical Research Letters*, 47 (22), 2020. doi: 10.1029/2020GL089552. URL `https://doi.org/10.1029/2020GL089552`.

E. Montgomery-Brown, C. Wicks, P. F. Cervelli, J. O. Langbein, J. L. Svarc, D. R. Shelly, D. P. Hill, and M. Lisowski. Renewed inflation of Long Valley caldera, California (2011 to 2014). *Geophysical Research Letters*, 42(13):5250–5257, 2015.

H. Noda and N. Lapusta. Three-dimensional earthquake sequence simulations with evolving temperature and pore pressure due to shear heating: Effect of heterogeneous hydraulic diffusivity. *Journal of Geophysical Research: Solid Earth*, 115(B12), 2010.

B. Riel, M. Simons, D. Ponti, P. Agram, and R. Jolivet. Quantifying ground deformation in the Los Angeles and Santa Ana coastal basins due to groundwater withdrawal. *Water Resources Research*, 54(5):3557–3582, 2018. ISSN 0043-1397. doi: 10.1029/2017WR021978.

P. Segall and S. Lu. Injection-induced seismicity: Poroelastic and earthquake nucleation effects. *Journal of Geophysical Research: Solid Earth*, 120(7): 5082–5103, 2015. doi: 10.1002/2015JB012060. URL `https://doi.org/10.1002/2015JB012060`.

P. Segall and J. R. Rice. Dilatancy, compaction, and slip instability of a fluid-infiltrated fault. *Journal of Geophysical Research: Solid Earth*, 100(B11): 22155–22171, 1995. doi: 10.1029/95JB02403. URL `https://doi.org/10.1029/95JB02403`.

R. Sibson. Interactions between temperature and pore-fluid pressure during earthquake faulting and a mechanism for partial or total stress relief. *Nature Physical Science*, 243(126):66–68, 1973.

K. P. Sirorattanakul, S. Larochelle, V. Rubino, A. J. Rosakis, and N. Lapusta. Frictional interfaces are always evolving. *In preparation*.

L. A. Stevens, M. Nettles, J. L. Davis, T. T. Creyts, J. Kingslake, A. P. Ahlstrøm, and T. B. Larsen. Helheim glacier diurnal velocity fluctuations driven by surface melt forcing. *Journal of Glaciology*, 68(267):77–89, 2022.

V. C. Tsai. A model for seasonal changes in GPS positions and seismic wave speeds due to thermoelastic and hydrologic variations. *Journal of Geophysical Research*, 116(B4):B04404, apr 2011. ISSN 0148-0227. doi: 10.1029/2010JB008156.

V. C. Tsai, L. C. Smith, A. S. Gardner, and H. Seroussi. A unified model for transient subglacial water pressure and basal sliding. *Journal of Glaciology*, 68 (268):390–400, 2022.

M. Vergnolle, A. Walpersdorf, V. Kostoglodov, P. Tregoning, J. Santiago, N. Cotte, and S. Franco. Slow slip events in mexico revised from the processing of 11 year GPS observations. *Journal of Geophysical Research: Solid Earth*, 115(B8), 2010.

Y. Yang and E. M. Dunham. Effect of porosity and permeability evolution on injection-induced aseismic slip. *Journal of Geophysical Research: Solid Earth*, 126(7):e2020JB021258, 2021.

Appendix A

SUPPLEMENTARY MATERIALS FOR CHAPTER I

A.1 Moving load derivation

We show through an analytical proof that a deformation field induced by a single load moving at constant velocity can be well explained by only 2 ICs.

The vbICA algorithm assumes that the ICA reconstruction matrix $\boldsymbol{X}(\boldsymbol{x}, t)$ is a linear mix of sources:

$$\boldsymbol{X}(\boldsymbol{x}, t) = \sum_{i=1}^{R} a_i(\boldsymbol{x}) s_i(t) \tag{A.1}$$

where $\boldsymbol{x}$ is the position vector of recording stations, t is time, R is the number of components, a_i and s_i are the mixing factor and temporal function of source i, respectively. In the case of a two-component ICA decomposition,

$$\boldsymbol{X}(\boldsymbol{x}, t) = a_1(\boldsymbol{x}) s_1(t) + a_2(\boldsymbol{x}) s_2(t). \tag{A.2}$$

We can express an arbitrary deformation field $\boldsymbol{F}$ as a Fourier series:

$$\boldsymbol{F}(u) = \frac{\alpha_0}{2} + \sum_{n=1}^{\infty} \left(\alpha_n \cos \frac{n\pi u}{\lambda} + \beta_n \sin \frac{n\pi u}{\lambda} \right) \tag{A.3}$$

where u is an arbitrary variable, α_n and β_n are the Fourier series coefficients and λ is the load wavelength. Note that $\alpha_0 = 0$ here since the time series are detrended and oscillate around 0. In general the deformation field recorded by the stations depends on the relative distance between the stations and the source, that is, $\boldsymbol{F} = \boldsymbol{F}(\boldsymbol{x} - \boldsymbol{\xi}, t)$ where $\boldsymbol{\xi}$ is the position vector of the source. However, if we assume that the source velocity $\boldsymbol{v}$ is constant, then $\boldsymbol{\xi}$ and t are related by $\boldsymbol{\xi} = \boldsymbol{v}t$ and thus $\boldsymbol{F}(\boldsymbol{x} - \boldsymbol{\xi}, t) = \boldsymbol{F}(\boldsymbol{x} - \boldsymbol{v}t)$. We can then set the dummy variable u in equation (A.3) to be $\boldsymbol{x} - \boldsymbol{v}t$:

$$\mathbf{F}(\boldsymbol{x} - \boldsymbol{v}t) = \sum_{n=1}^{\infty} \alpha_n \cos \frac{n\pi(\boldsymbol{x} - \boldsymbol{v}t)}{\lambda} + \sum_{n=1}^{\infty} \beta_n \sin \frac{n\pi(\boldsymbol{x} - \boldsymbol{v}t)}{\lambda}. \tag{A.4}$$

Then, by Ptolemy's trigonometric identities:

$$\mathbf{F}(\boldsymbol{x}-\boldsymbol{v}t) = \sum_{n=1}^{\infty} \alpha_n \left(\cos\frac{n\pi\boldsymbol{x}}{\lambda}\cos\frac{n\pi\boldsymbol{v}t}{\lambda} + \sin\frac{n\pi\boldsymbol{x}}{\lambda}\sin\frac{n\pi\boldsymbol{v}t}{\lambda}\right) + \sum_{n=1}^{\infty} \beta_n \left(\sin\frac{n\pi\boldsymbol{x}}{\lambda}\cos\frac{n\pi\boldsymbol{v}t}{\lambda} - \cos\frac{n\pi\boldsymbol{x}}{\lambda}\sin\frac{n\pi\boldsymbol{v}t}{\lambda}\right). \quad \text{(A.5)}$$

Reorganizing Equation (5), we obtain:

$$\mathbf{F}(\boldsymbol{x}-\boldsymbol{v}t) = \sum_{n=1}^{\infty} \left(\alpha_n \cos\frac{n\pi\boldsymbol{x}}{\lambda} + b_n \sin\frac{n\pi\boldsymbol{x}}{\lambda}\right)\cos\frac{n\pi\boldsymbol{v}t}{\lambda} + \sum_{n=1}^{\infty} \left(\beta_n \sin\frac{n\pi\boldsymbol{x}}{\lambda} - b_n \cos\frac{n\pi\boldsymbol{x}}{\lambda}\right)\sin\frac{n\pi\boldsymbol{v}t}{\lambda}. \quad \text{(A.6)}$$

Equating the ICA reconstruction (equation (A.2)) to the deformation field (equation (A.6)), we obtain:

$$a_1(\boldsymbol{x})s_1(t) + a_2(\boldsymbol{x})s_2(t) = \sum_{n=1}^{\infty} \left(\alpha_n \sin\frac{n\pi\boldsymbol{x}}{\lambda} - \beta_n \cos\frac{n\pi\boldsymbol{x}}{\lambda}\right)\sin\frac{n\pi\boldsymbol{v}t}{\lambda} + \sum_{n=1}^{\infty} \left(\alpha_n \cos\frac{n\pi\boldsymbol{x}}{\lambda} + \beta_n \sin\frac{n\pi\boldsymbol{x}}{\lambda}\right)\cos\frac{n\pi\boldsymbol{v}t}{\lambda}. \quad \text{(A.7)}$$

Implying that:

$$a_1(\boldsymbol{x})s_1(t) = \sum_{n=1}^{\infty} \left(\alpha_n \sin\frac{n\pi\boldsymbol{x}}{\lambda} - \beta_n \cos\frac{n\pi\boldsymbol{x}}{\lambda}\right)\sin\frac{n\pi\boldsymbol{v}t}{\lambda} \quad \text{(A.8)}$$

$$a_2(\boldsymbol{x})s_2(t) = \sum_{n=1}^{\infty} \left(\alpha_n \cos\frac{n\pi\boldsymbol{x}}{\lambda} + \beta_n \sin\frac{n\pi\boldsymbol{x}}{\lambda}\right)\cos\frac{n\pi\boldsymbol{v}t}{\lambda}. \quad \text{(A.9)}$$

If we further assume that the $n = 1$ terms explain most of the deformation, then:

$$a_1(\boldsymbol{x})s_1(t) \cong \left(\alpha_1 \sin\frac{\pi\boldsymbol{x}}{\lambda} - \beta_1 \cos\frac{\pi\boldsymbol{x}}{\lambda}\right)\sin\frac{\pi\boldsymbol{v}t}{\lambda} \quad \text{(A.10)}$$

$$a_2(\boldsymbol{x})s_2(t) \cong \left(\alpha_1 \cos\frac{\pi\boldsymbol{x}}{\lambda} + \beta_1 \sin\frac{\pi\boldsymbol{x}}{\lambda}\right)\cos\frac{\pi\boldsymbol{v}t}{\lambda} \quad \text{(A.11)}$$

and thus,

$$a_1(\boldsymbol{x}) = \left(\alpha_1 \sin\frac{\pi\boldsymbol{x}}{\lambda} - \beta_1 \cos\frac{\pi\boldsymbol{x}}{\lambda}\right) \quad \text{(A.12)}$$

$$s_1(t) = \sin\frac{\pi\boldsymbol{v}t}{\lambda} \quad \text{(A.13)}$$

$$a_2(\boldsymbol{x}) = \left(\alpha_1 \cos\frac{\pi\boldsymbol{x}}{\lambda} + \beta_1 \sin\frac{\pi\boldsymbol{x}}{\lambda}\right) \tag{A.14}$$

$$s_2(t) = \cos\frac{\pi\boldsymbol{v}t}{\lambda}. \tag{A.15}$$

The fact that the deformation field can be expressed in terms of $a_1(\boldsymbol{x})s_1(t)$ and $a_2(\boldsymbol{x})s_2(t)$ implies that two ICs suffice to fully explain it. We also note that the temporal source $s_2(t)$ is proportional to the derivative of $s_1(t)$ and vice-versa. If the temporal sources are normalized (as is the case with the Vs presented in this study), then they should be derivatives of one another.

A.2 Supplementary Tables and Figures

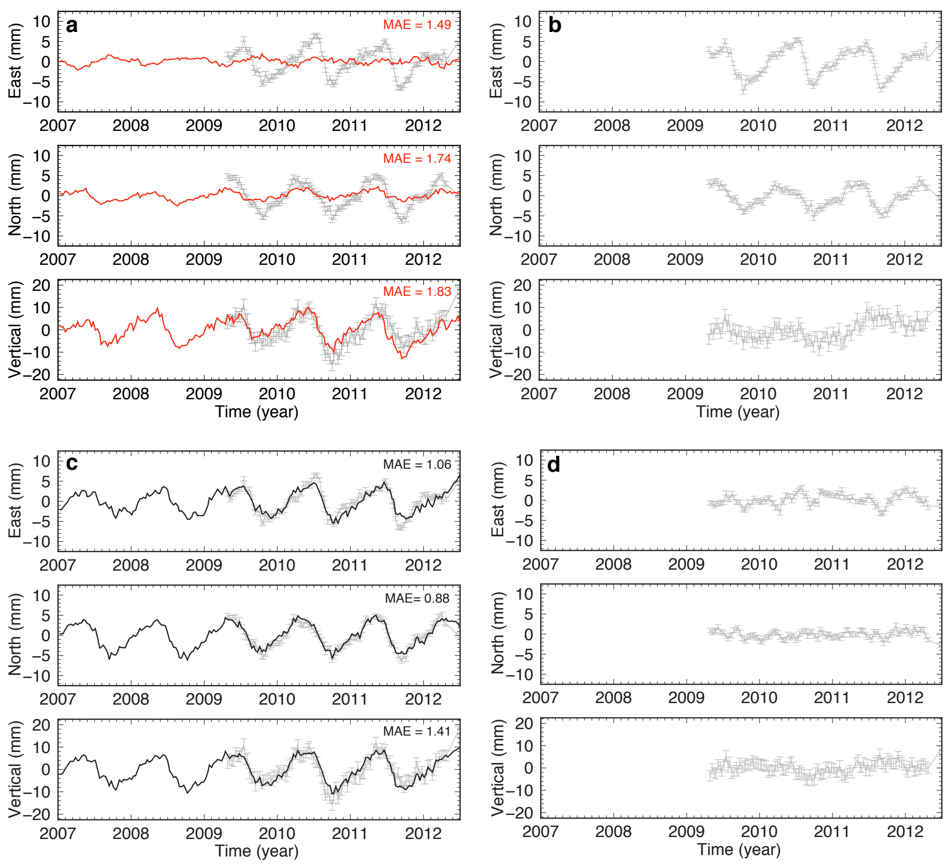

Figure A.1(i): Same as Figure 1.2 in the main text but for station BYNA in Nepal.

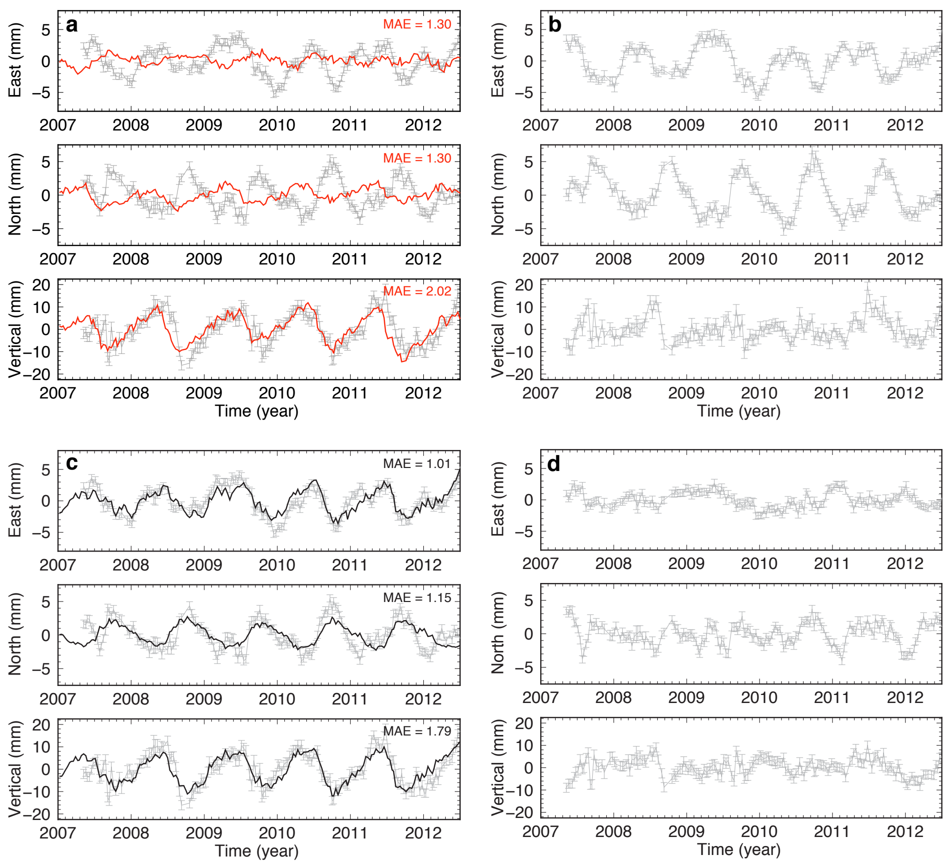

Figure A.1(ii): Same as Figure 1.2 in the main text but for station GRHI in Nepal.

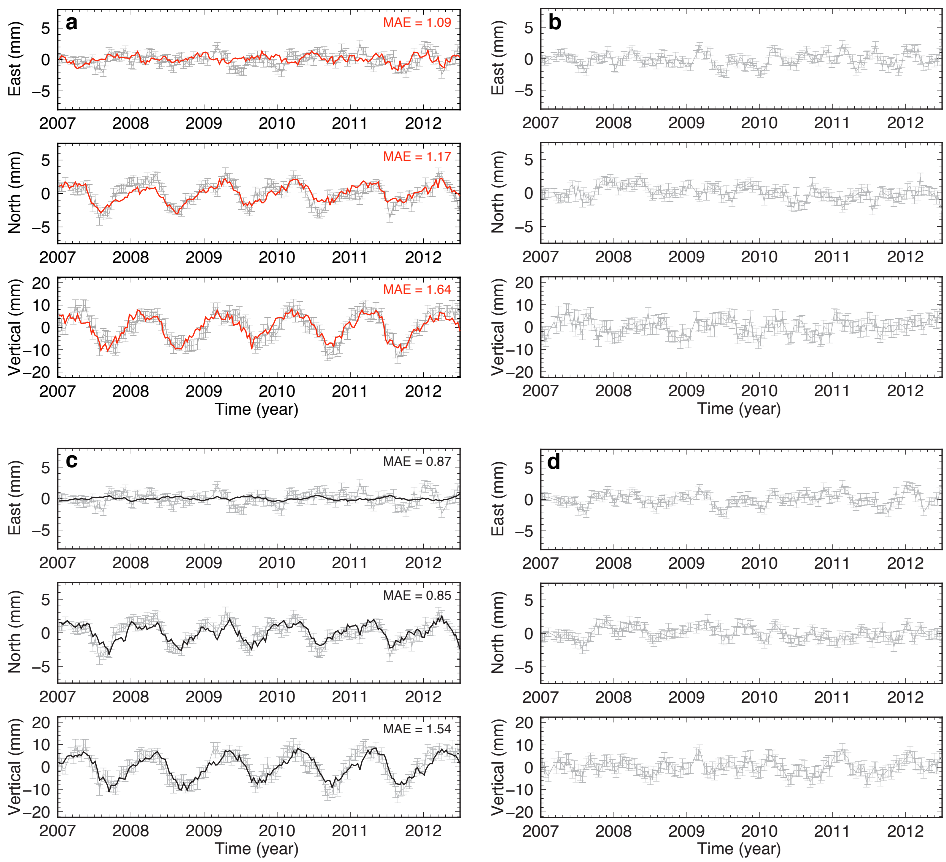

Figure A.1(iii): Same as Figure 1.2 in the main text but for station LHAZ in Tibet.

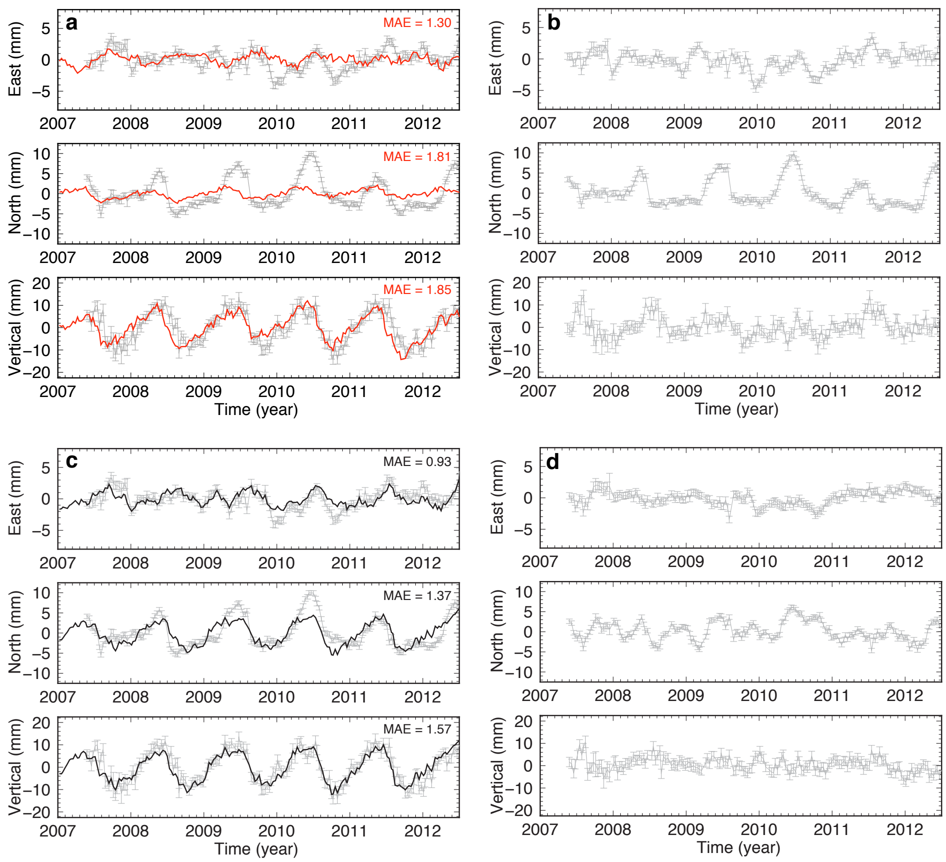

Figure A.1(iv): Same as Figure 1.2 in the main text but for station NPGJ in Nepal.

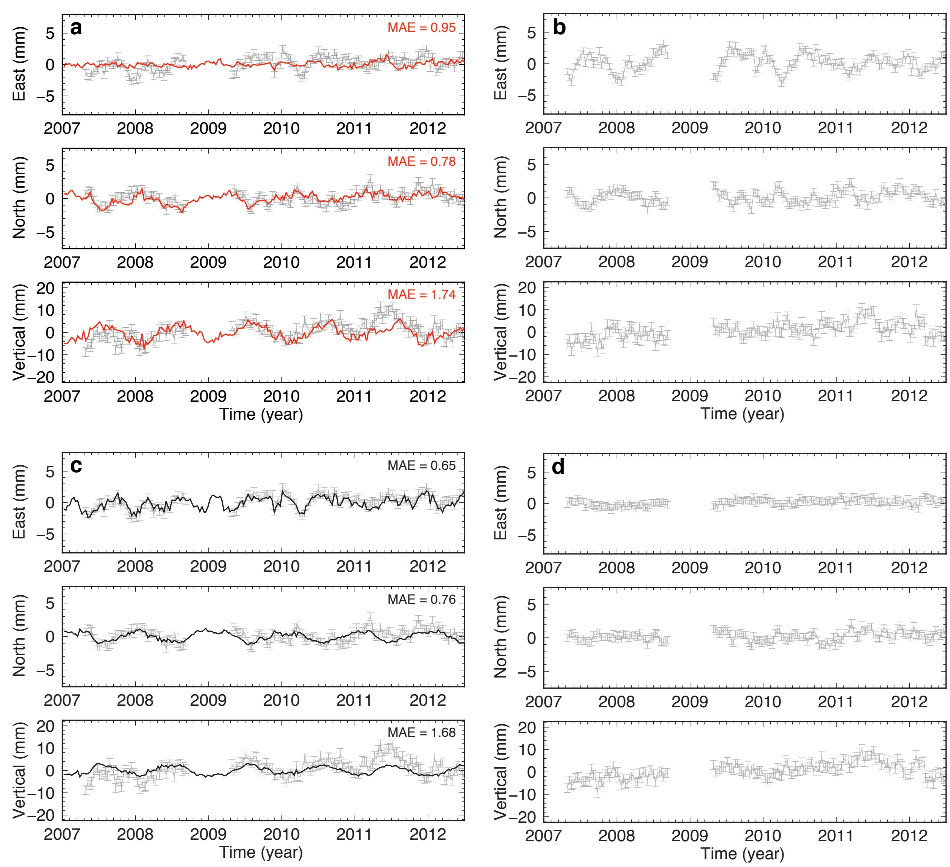

Figure A.1(v): Same as Figure 1.2 in the main text but for station ALWJ in Saudi Arabia.

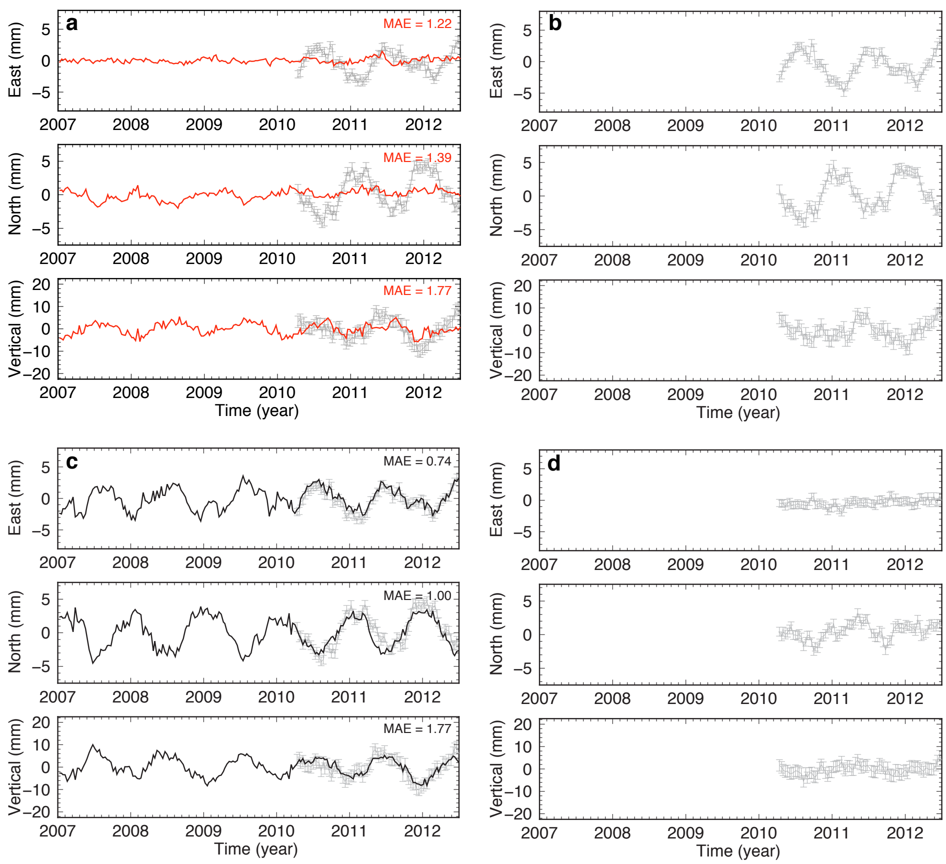

Figure A.1(vi): Same as Figure 1.2 in the main text but for station HALY in Saudi Arabia.

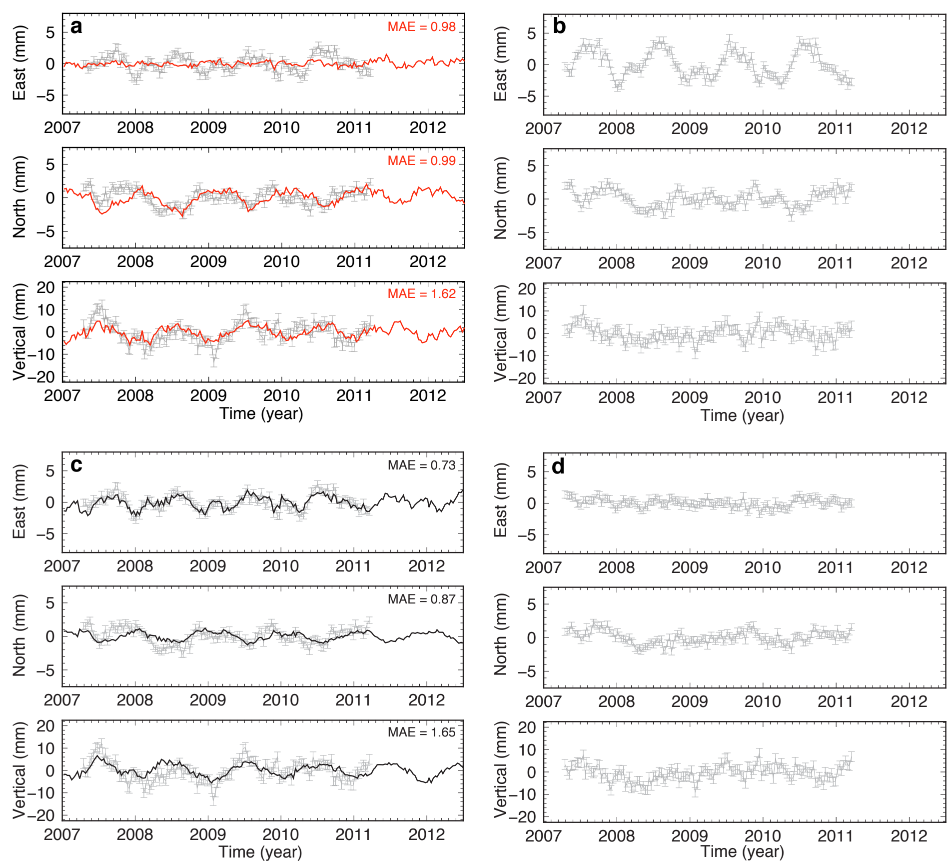

Figure A.1(vii): Same as Figure 1.2 in the main text but for station JIZN in the Red Sea.

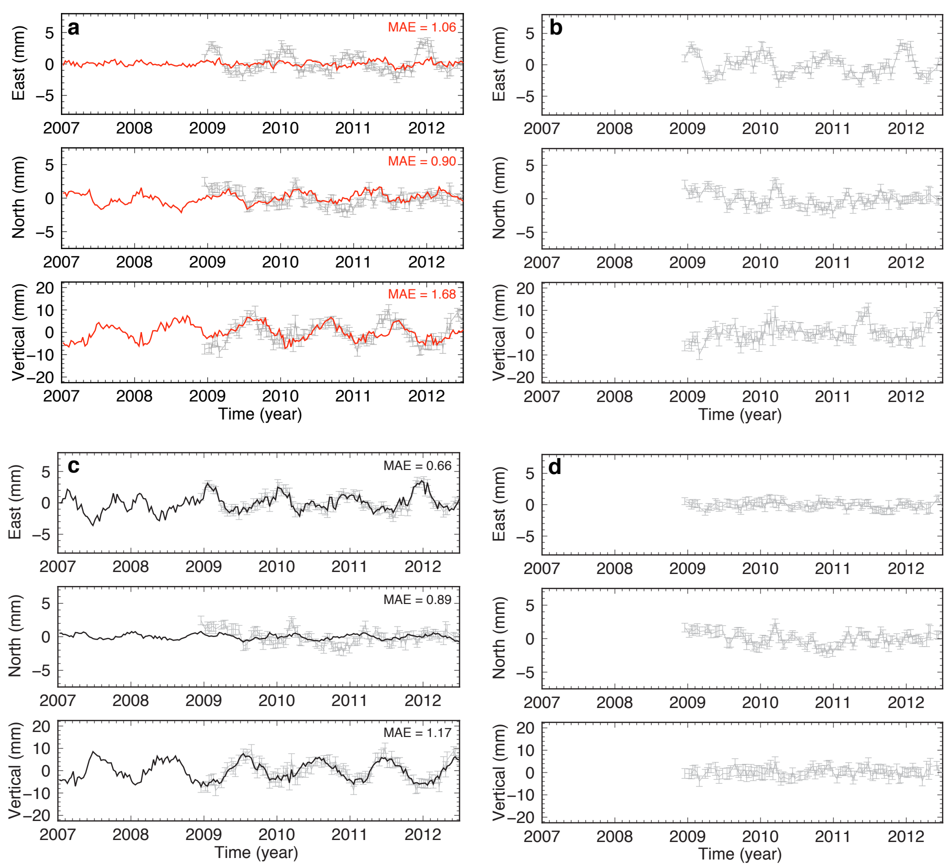

Figure A.1(viii): Same as Figure 1.2 in the main text but for station ISNA in Iraq.

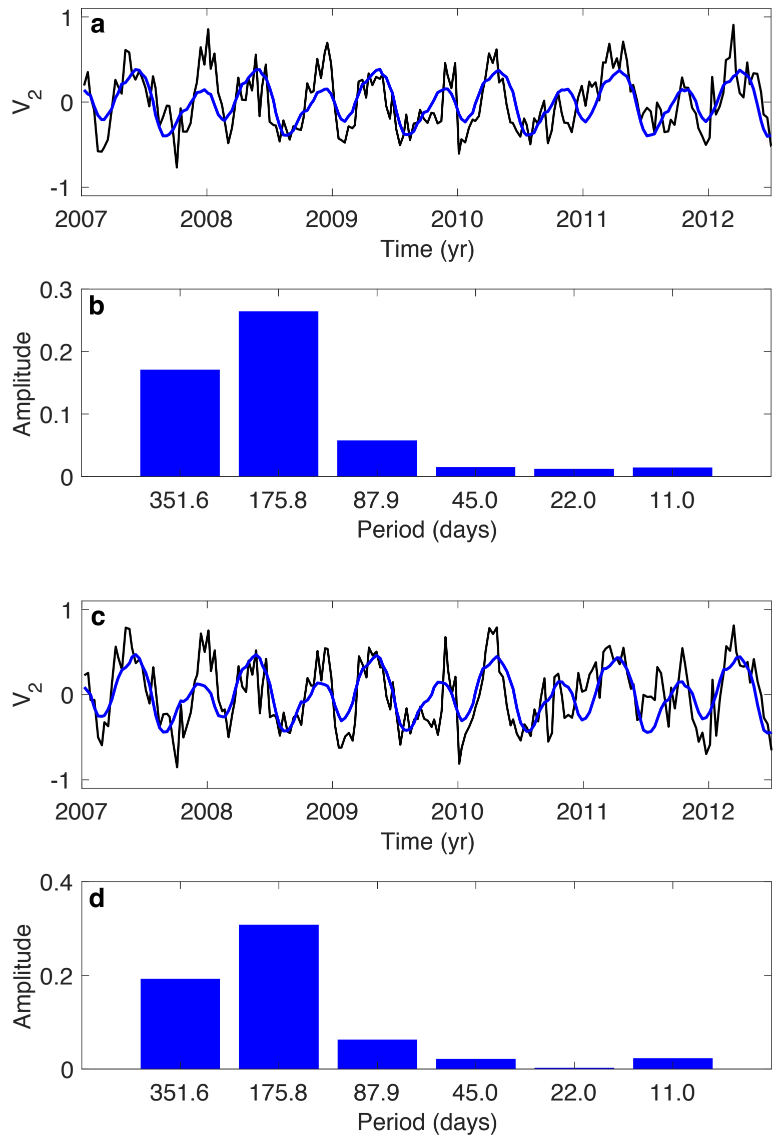

Figure A.2: Sum of sinusoidal fit for V_2^{GNSS} in the Arabian Peninsula for the (a,b) degrees > 1 and (c,d) all degrees cases. (a) Detrended V_2^{GNSS} (black) and least-square best-fit function (blue) made of sinusoidals with frequencies corresponding to the first 6 draconitic harmonics. (b) Amplitude of each sinusoidal in the best-fit function. The best-fit function explains 46.5% of V_2^{GNSS} variance for the degrees > 1 case and 48.0% for the all degrees case.

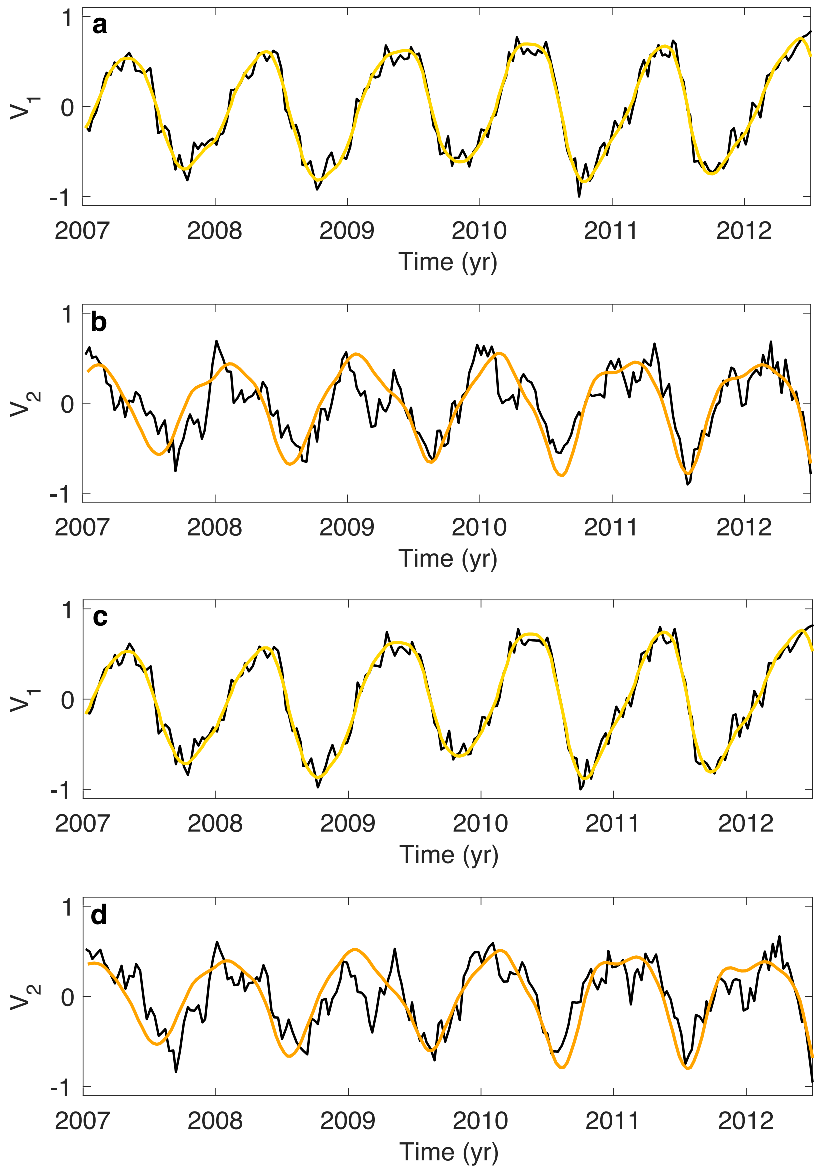

Figure A.3: V_2^{GNSS} is approximately the derivative of V_1^{GNSS} in the Nepal Himalaya case. (a) V_1^{GNSS} as in Figure 1.5a in the main text (black) and lowpass-filtered V_1^{GNSS} (yellow). (b) V_2^{GNSS} as in Figure 1.5d in the main text (black) and derivative (orange) of the lowpass-filtered V_1^{GNSS} in (a). (c) and (d) Same as (a) and (b) but for the all-degrees case.

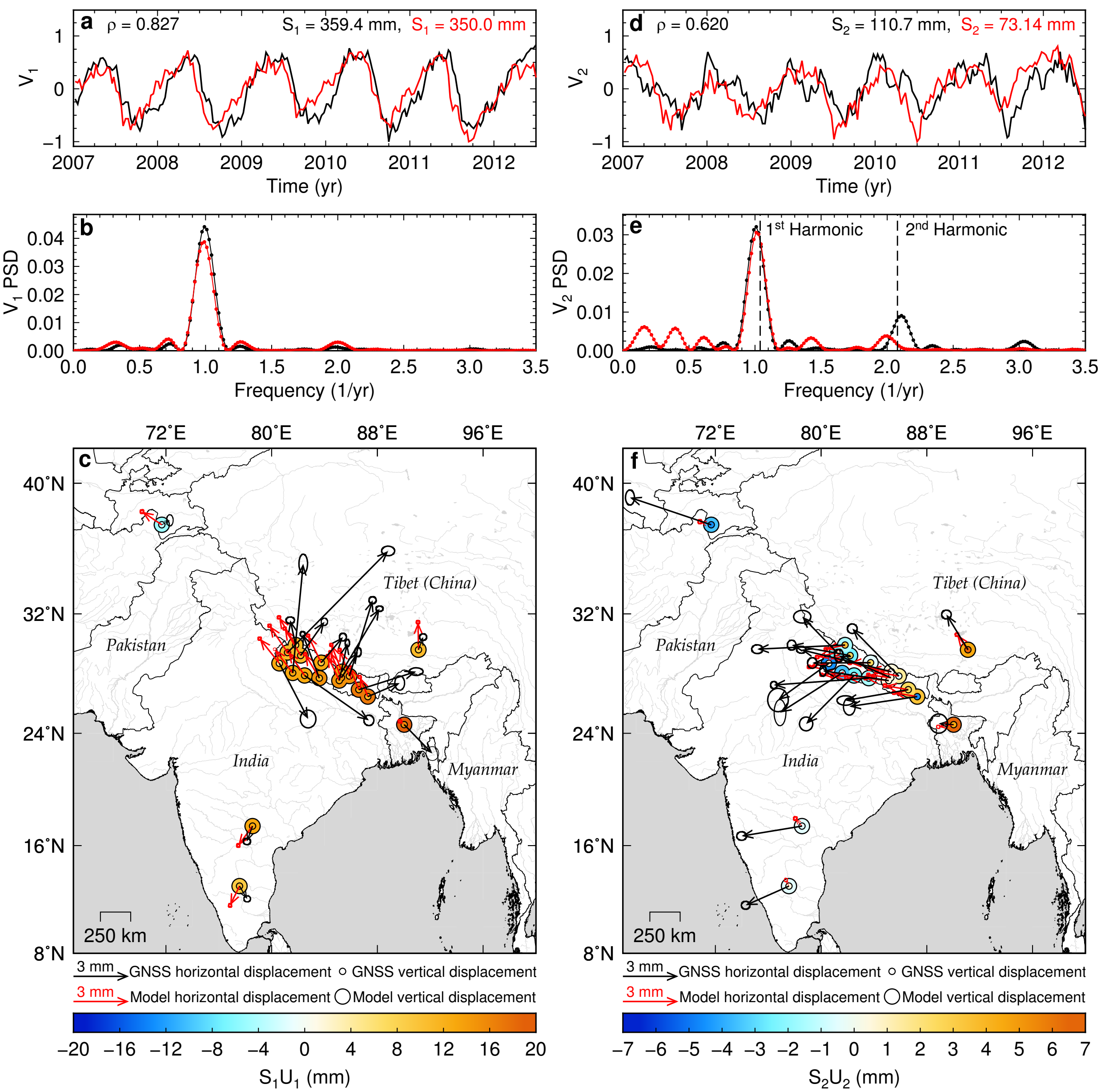
a
ρ = 0.827
S_1 = 359.4 mm, S_1 = 350.0 mm
V_1
Time (yr)
b
V_1 PSD
Frequency (1/yr)
c
Pakistan
Tibet (China)
India
Myanmar
250 km
72˚E
80˚E
88˚E
96˚E
40˚N
32˚N
24˚N
16˚N
8˚N
3 mm GNSS horizontal displacement
GNSS vertical displacement
3 mm Model horizontal displacement
Model vertical displacement
S_1U_1 (mm)
d
ρ = 0.620
S_2 = 110.7 mm, S_2 = 73.14 mm
V_2
Time (yr)
e
1st Harmonic
2nd Harmonic
V_2 PSD
Frequency (1/yr)
f
Pakistan
Tibet (China)
India
Myanmar
250 km
3 mm GNSS horizontal displacement
GNSS vertical displacement
3 mm Model horizontal displacement
Model vertical displacement
S_2U_2 (mm)

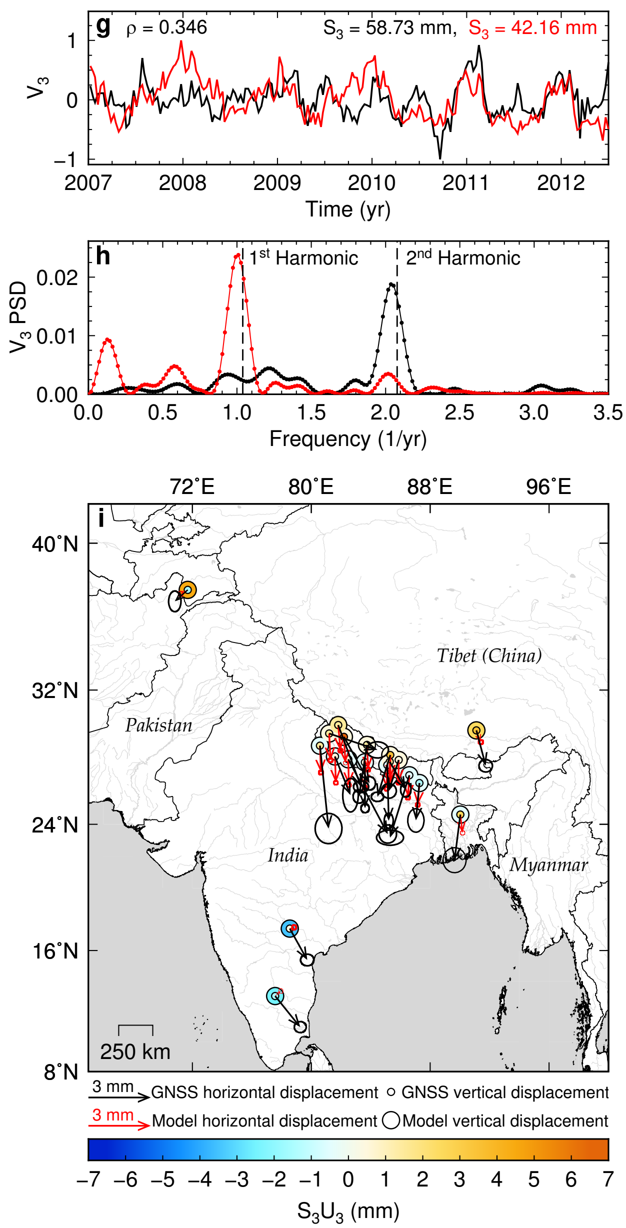

Figure A.4: Same as Figure 1.5 in main text but for a 3-component ICA.

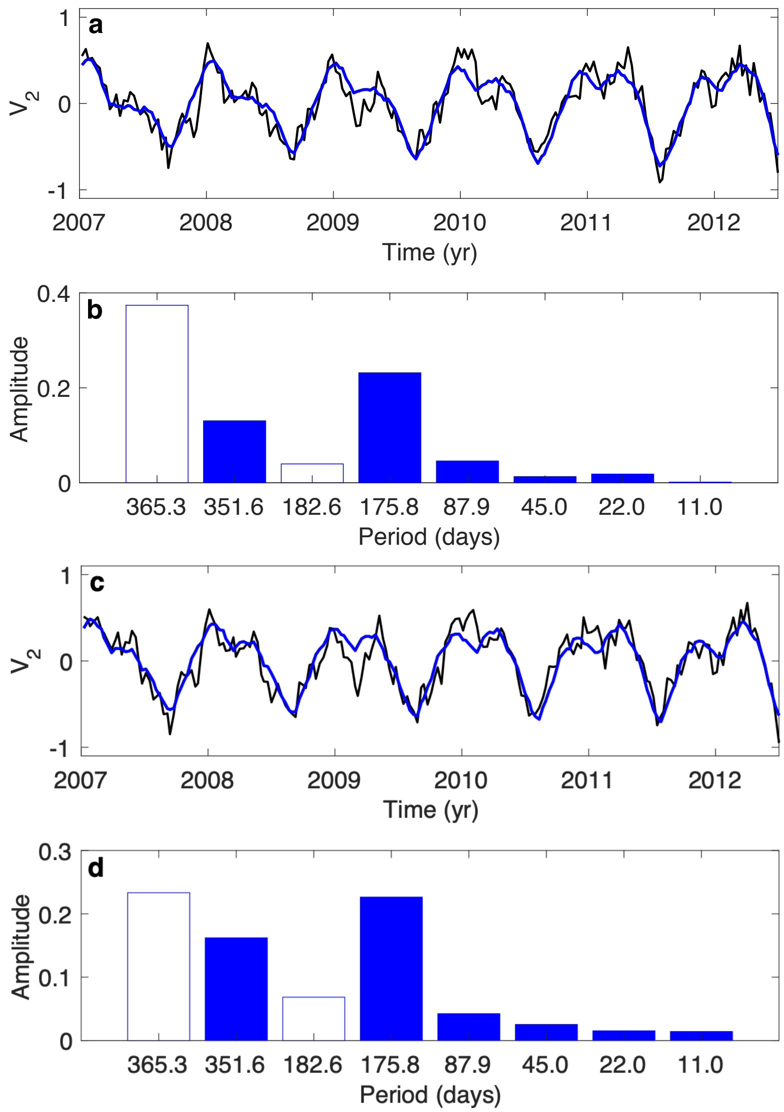

Figure A.5: Same as Figure A.2 but for V_2^{GNSS} for the Nepal Himalaya for the (a,b) degrees > 1 and (c,d) all degrees cases. Annual and bi-annual sinusoidal signals are now included in the best-fit function as indicated by the white-filled vertical bars in (b). The best-fit function explains 81.4% of the variance of V_2^{GNSS} for the degrees > 1 case and 79.5% for the all degrees case.

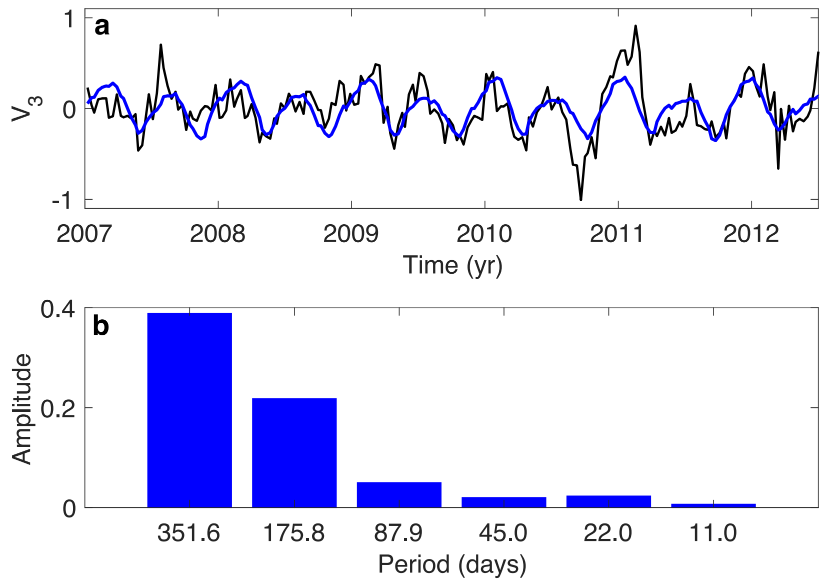

Figure A.6: Same as Figure A.5 but for V_3^{GNSS} for a 3 components decomposition of the Nepal Himalaya case (degrees > 1). The best-fit function explains 40.0% of the variance of V_3^{GNSS}.

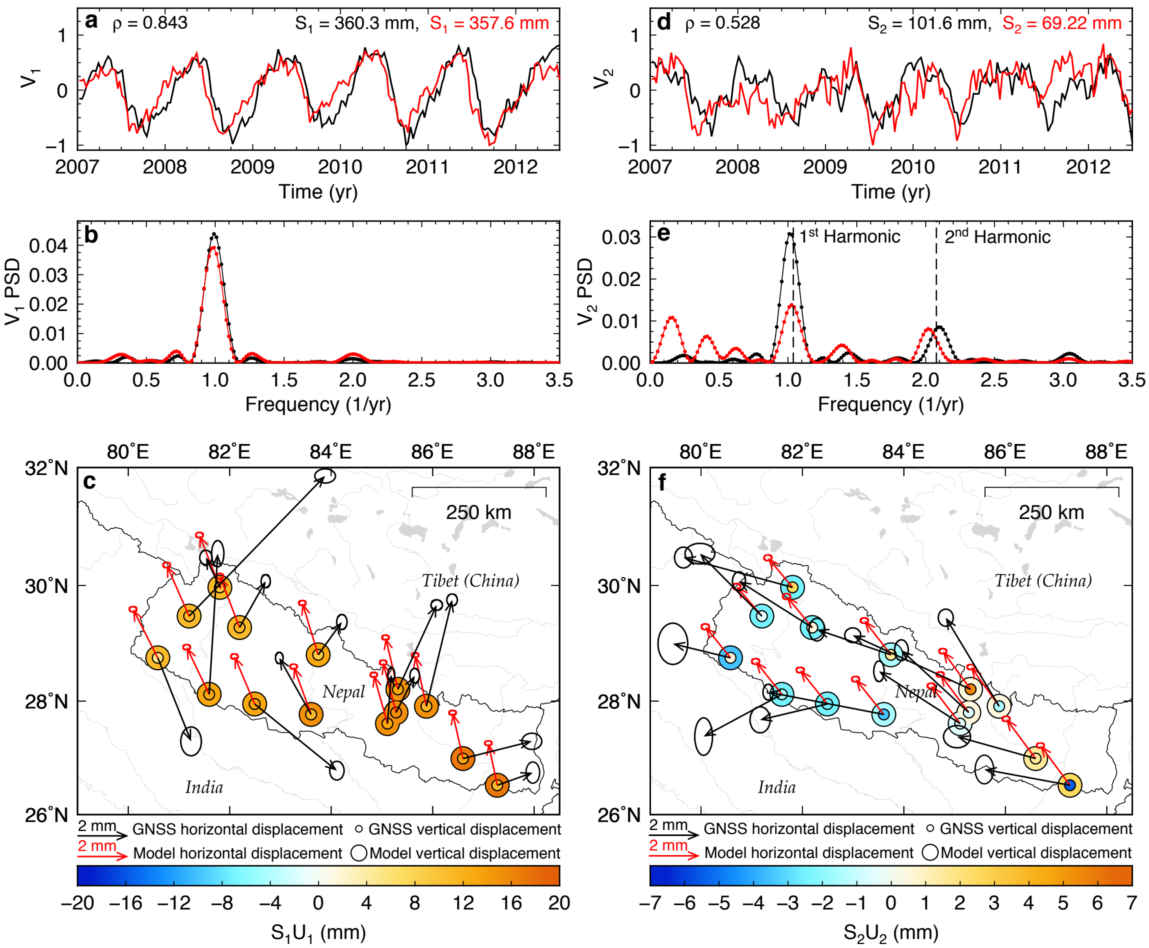

Figure A.7: Close-up on Nepal for combined case with all degrees.

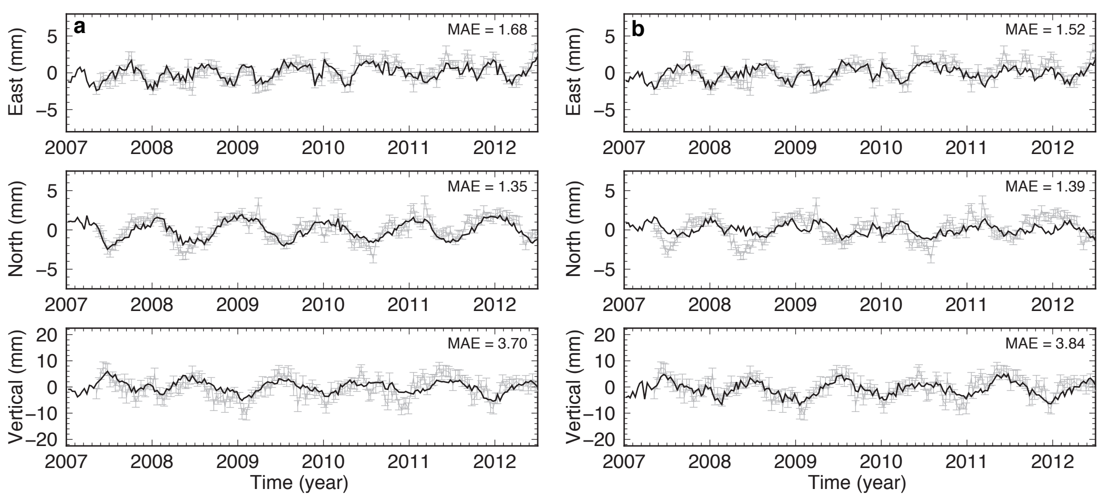

Figure A.8: Example of ICA reconstruction using (a) the combined analysis versus (b) the horizontal/vertical analysis (with degree 1) at station NAMA in the Arabian Peninsula.

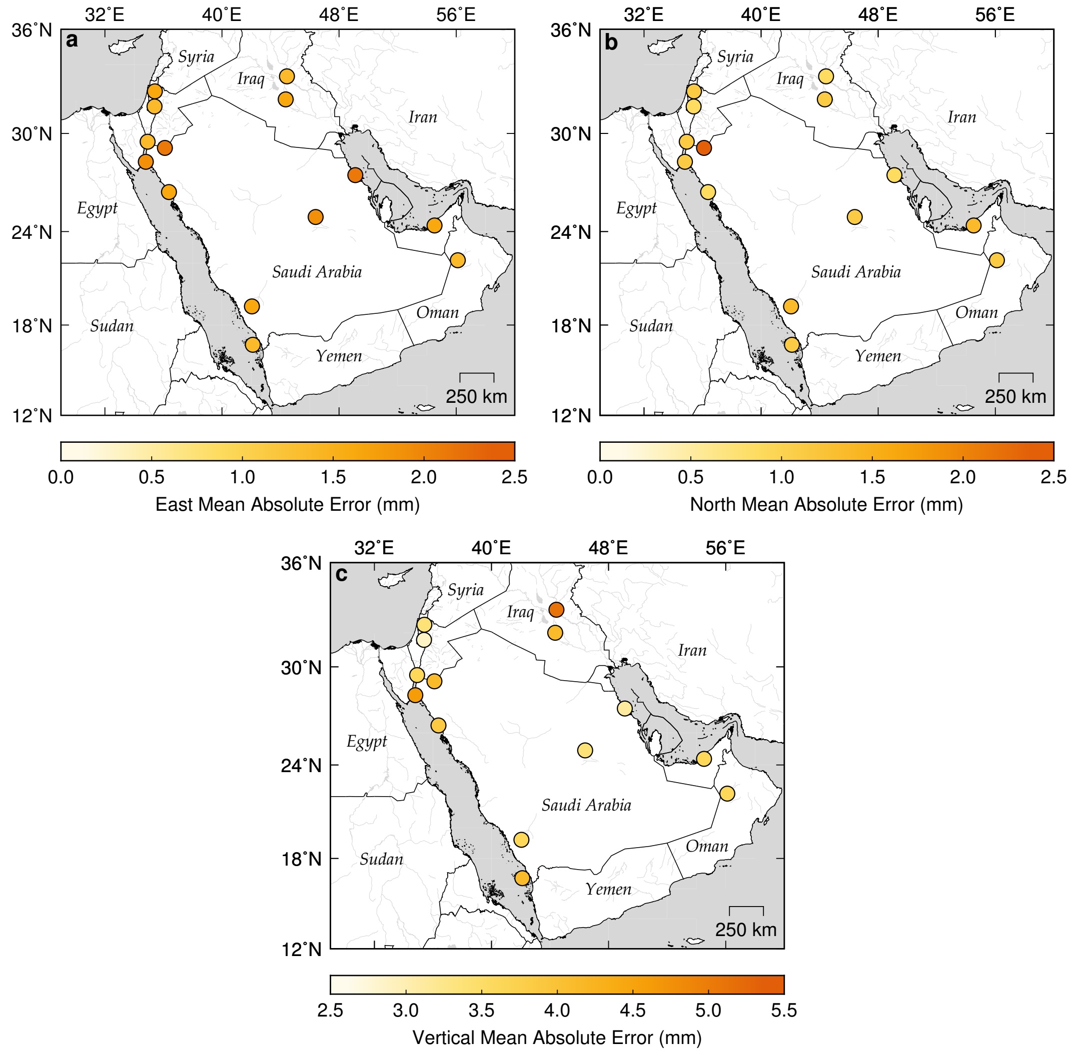

Figure A.9: Mean absolute error values between the GNSS data and the combined ICA reconstruction with all degrees in the Arabian Peninsula for (a) east, (b) north, and (c) vertical components.

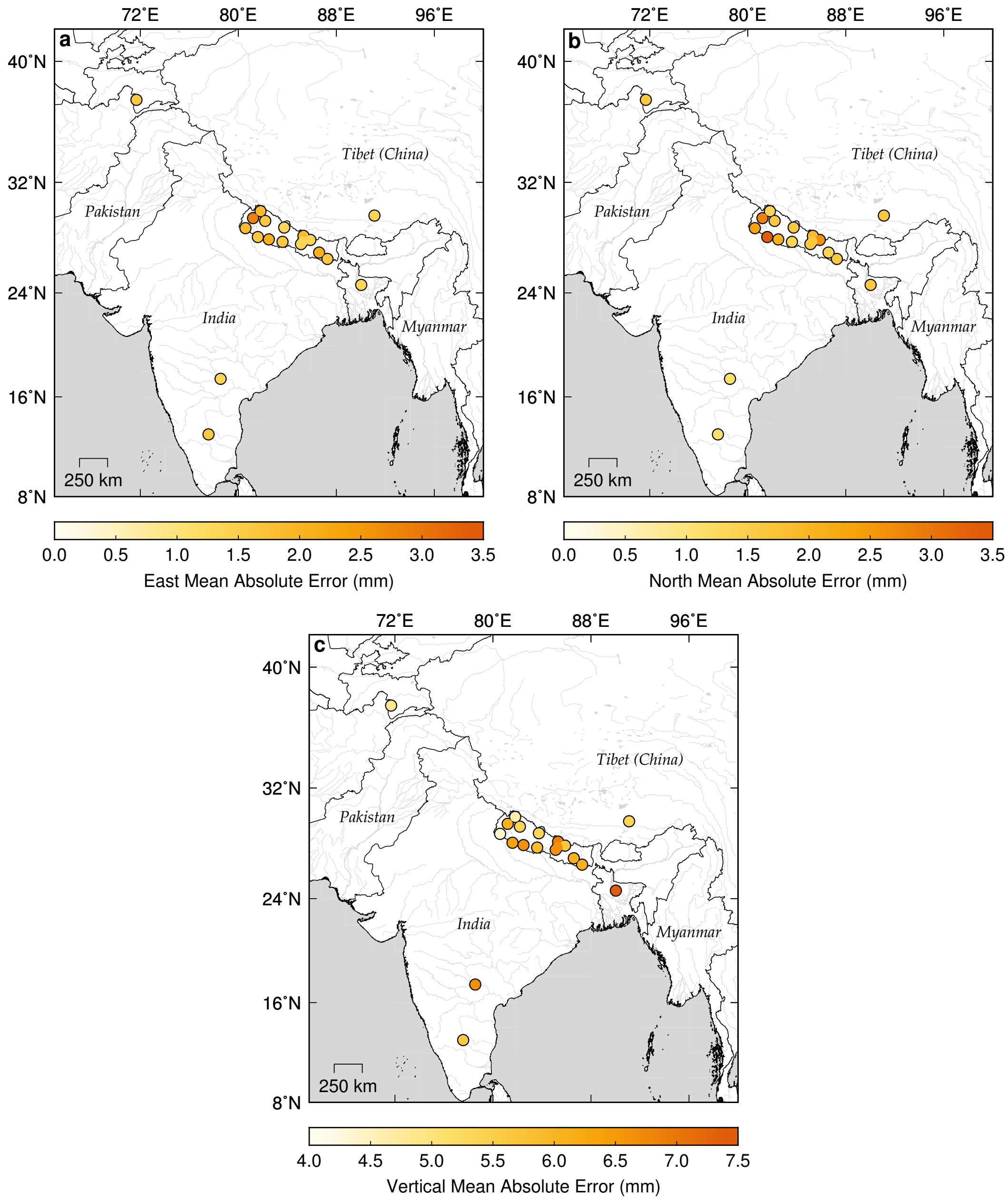

Figure A.10: Same as Figure A.9 but for the Nepal Himalaya.

Table A.1: List of extra offsets prescribed in the GNSS time series (in addition to those prescribed by NGL).

Station	Epoch(s)	
Arabian Peninsula		
FG31	2010.00	
YIBL	2008.00	
Nepal Himalaya		
IISC	2009.02	
JMLA	2012.49	
JMSM	2011.28	
KKN4	2011.00	
LHAZ	2007.16	
MANM	2009.81, 2011.07	2010.71,

Table A.2: Values of hyper-parameters used for the vbICA.

Hyper-Parameter	**Data (GNSS) Values**	**Model (GRACE) Values**
$b_{\alpha 0}$	10^3	10^3
$c_{\alpha 0}$	10^{-3}	10^{-3}
$b_{\lambda 0}$	10^3	10^{-1}
$c_{\lambda 0}$	10^{-3}	10^1
b_0	10^3	10^3
c_0	10^{-3}	10^{-3}

Note: The hyper-parameters reported in Table A.2 control the strength of the a priori assumption on the precision (i.e., the inverse of the variance) of the normal distributions relative to the Gaussians in the MoG which describe the sources ($\boldsymbol{b_0}$, $\boldsymbol{c_0}$), the noise ($\boldsymbol{b_{\lambda 0}}$, $\boldsymbol{c_{\lambda 0}}$), and the mixing matrix ($\boldsymbol{b_{\alpha 0}}$, $\boldsymbol{c_{\alpha 0}}$). In practice, each random variable from the set of parameters W which describes the precision of a normal distribution is described by a Gamma distribution, for which two parameters are needed: the scale $\boldsymbol{b}$ and the shape $\boldsymbol{c}$. The Gamma distribution is selected because it is the conjugate prior distribution associated with a normal distribution with known mean (https://en.wikipedia.org/wiki/Conjugate_prior, see table "Continuous distributions"). By selecting $\boldsymbol{b} = \mathbf{10^3}$ and $\boldsymbol{c} = \mathbf{10^{-3}}$, we are forcing the distribution of the precision to be highly peaked around 0, meaning that we think our a priori precision is likely to be around 0. As a consequence, we allow for a large variance which gives the data the power to change the decomposition result.

Table A.3: Correlation coefficients between $\boldsymbol{V}^{\mathrm{GNSS}}$ and $\boldsymbol{V}^{\mathrm{GRACE}}$ in the Arabian Peninsula.

Degrees > 1		**All Degrees**	
Combined Analysis			
1) V_1^{GNSS} - V_1^{GRACE}:	0.692	1) V_1^{GNSS} - V_1^{GRACE}:	0.747
2) V_1^{GNSS} - V_2^{GRACE}:	0.347	2) V_1^{GNSS} - V_2^{GRACE}:	-0.141
3) V_2^{GNSS} - V_2^{GRACE}:	0.164	3) V_2^{GNSS} - V_2^{GRACE}:	0.115
Horizontal Analysis			
1) V_1^{GNSS} - V_1^{GRACE}:	-0.012	1) V_1^{GNSS} - V_1^{GRACE}:	0.523
2) V_1^{GNSS} - V_2^{GRACE}:	-0.378	2) V_1^{GNSS} - V_2^{GRACE}:	-0.261
3) V_2^{GNSS} - V_1^{GRACE}:	0.109	3) V_2^{GNSS} - V_2^{GRACE}:	-0.013
4) V_2^{GNSS} - V_2^{GRACE}:	-0.030		
Vertical Analysis			
1) V_1^{GNSS} - V_1^{GRACE}:	0.623	1) V_1^{GNSS} - V_1^{GRACE}:	0.581
2) V_1^{GNSS} - V_2^{GRACE}:	0.268	2) V_1^{GNSS} - V_2^{GRACE}:	0.287
3) V_2^{GNSS} - V_2^{GRACE}:	0.039	3) V_2^{GNSS} - V_2^{GRACE}:	-0.013

Note: V^{GNSS}- V^{GRACE} pairs that are selected as good matches are highlighted in yellow.

Table A.4: Same as Table A.3 but for the Nepal Himalaya.

Degrees > 1		**All Degrees**	
Combined Analysis			
1) V_1^{GNSS} - V_1^{GRACE}:	0.825	1) V_1^{GNSS} - V_1^{GRACE}:	0.843
2) V_1^{GNSS} - V_2^{GRACE}:	-0.171	2) V_1^{GNSS} - V_2^{GRACE}:	-0.047
3) V_2^{GNSS} - V_2^{GRACE}:	0.648	3) V_2^{GNSS} - V_2^{GRACE}:	0.528
Horizontal Analysis			
1) V_1^{GNSS} - V_1^{GRACE}:	0.837	1) V_1^{GNSS} - V_1^{GRACE}:	0.699
2) V_1^{GNSS} - V_2^{GRACE}:	-0.114	2) V_1^{GNSS} - V_2^{GRACE}:	-0.209
3) V_2^{GNSS} - V_1^{GRACE}:	0.667	3) V_2^{GNSS} - V_2^{GRACE}:	0.019
Vertical Analysis			
1) V_1^{GNSS} - V_1^{GRACE}:	0.841	1) V_1^{GNSS} - V_1^{GRACE}:	0.845
2) V_1^{GNSS} - V_2^{GRACE}:	-0.102	2) V_1^{GNSS} - V_2^{GRACE}:	-0.079
3) V_2^{GNSS} - V_2^{GRACE}:	0.745	3) V_2^{GNSS} - V_2^{GRACE}:	0.747

Appendix B

SUPPLEMENTARY MATERIALS FOR CHAPTER II

B.1 Arbitrary 2D Poroelastic Eigenstrains in an Elastic Half-space

When the 2D spatial distribution is arbitrary, quantity I defined in Equation (2.14) can be rewritten in Cartesian coordinates as:

$$I(x,y) = \int_0^b \frac{E_{aq}(x,y)\varepsilon_{eig}(x,y) - \nu(x,y)\sigma_{zz}(x,y)}{1-\nu(x,y)}\partial z. \tag{B.1}$$

We can decompose $I(x,y)$ into its Fourier components as:

$$\begin{aligned} I(x,y) \quad = \quad & \sum_{k_x,k_y} A_1(k_x,k_y)\cos(k_x x)\cos(k_y y) + A_2(k_x,k_y)\cos(k_x x)\sin(k_y y) \\ & + A_3(k_x,k_y)\sin(k_x x)\cos(k_y y) + A_4(k_x,k_y)\sin(k_x x)\sin(k_y y) \end{aligned} \tag{B.2}$$

where k_x and k_y are the wavenumbers in the x and y directions. Similar to Equation (2.22), the horizontal displacement field can then be computed as:

$$\begin{aligned} u_x \quad = \quad & \frac{2(1-\nu^2)}{E_{deep}} \sum_{k_x,k_y} -A_1(k_x,k_y)\sin(k_x x)\cos(k_y y) - A_2(k_x,k_y)\sin(k_x x)\sin(k_y y) \\ & + A_3(k_x,k_y)\cos(k_x x)\cos(k_y y) + A_4(k_x,k_y)\cos(k_x x)\sin(k_y y) \end{aligned} \tag{B.3}$$

$$\begin{aligned} u_y \quad = \quad & \frac{2(1-\nu^2)}{E_{deep}} \sum_{k_x,k_y} -A_1(k_x,k_y)\cos(k_x x)\sin(k_y y) + A_2(k_x,k_y)\cos(k_x x)\cos(k_y y) \\ & - A_3(k_x,k_y)\sin(k_x x)\sin(k_y y) + A_4(k_x,k_y)\sin(k_x x)\cos(k_y y). \end{aligned} \tag{B.4}$$

B.2 Analytical Elastic Loading Solution for $r \to a$

Since $\mathcal{K}(k)$ in Equation (2.22) diverges when $r = a$, the solution diverges at $r = a$. However, we can express and evaluate the $\mathcal{K}(k)$ and $\mathcal{E}(k)$ terms with infinite series truncated for an arbitrary n to numerically approach the solution at $r = a$:

$$\left(\frac{2}{k^2} - 1\right)\mathcal{K}(k) - \frac{2}{k^2}\mathcal{E}(k) = \frac{\pi}{2}\sum_{n=0}^{\infty}\frac{n}{n+1}\left(\frac{(2n)!}{2^{2n}(n!)^2}\right)^2 k^{2n}. \tag{B.5}$$

B.3 Supplementary Table and Figures

Table B.1: Elastic properties from Ge and Garven (1992). Note that the Young moduli were computed from the reported values of Poisson ratio and bulk modulus.

Rock Type	Confining stress [MPa]	Poisson's ratio	Matrix bulk modulus [MPa]	Young modulus [MPa]
Blair Dolomite	0	0.25	83	125
Maxville Limestone	0	0.23	42	68
Berea Sandstone	10	0.25	6	9
Chattanooga Shale	0	0.16	5	11

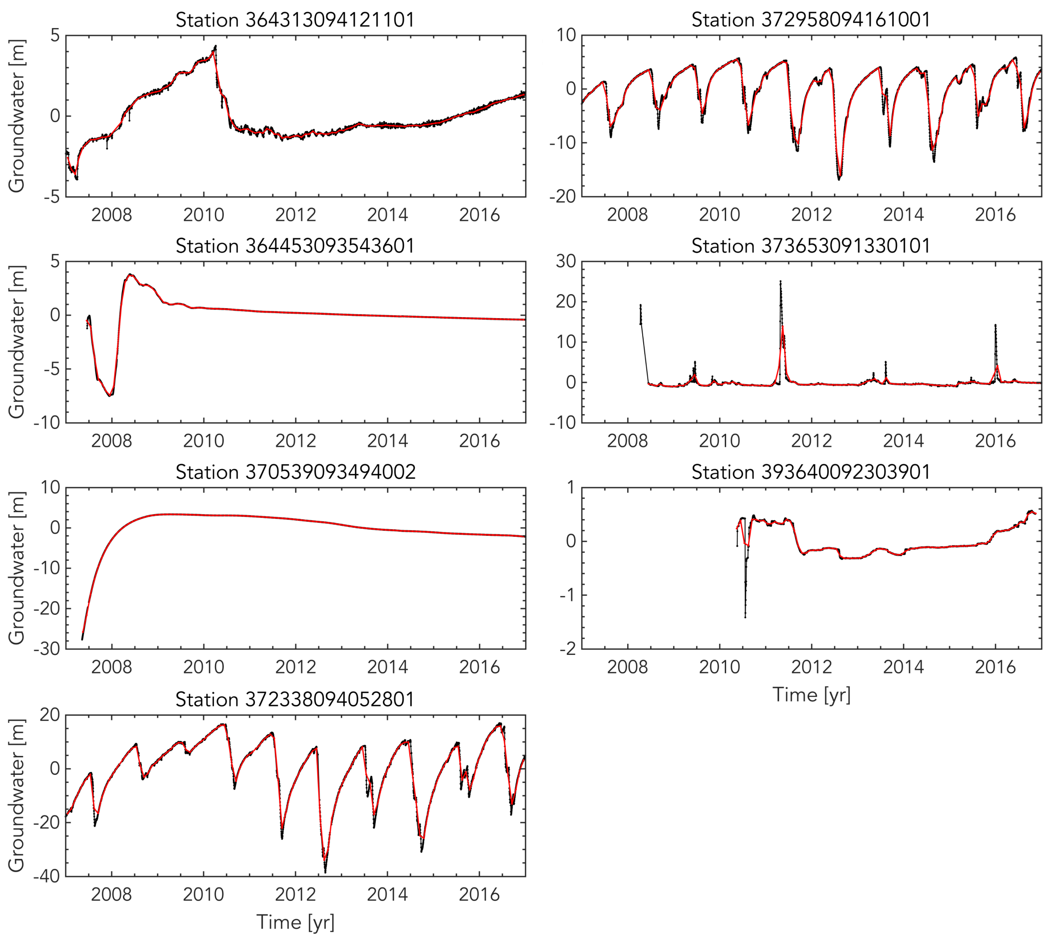

Figure B.1: Groundwater time series excluded from the analysis. Black dots are the raw daily data and the red lines are the monthly averages. Stations 372958094161001 and 372338095042801 likely reflect local pumping effects.

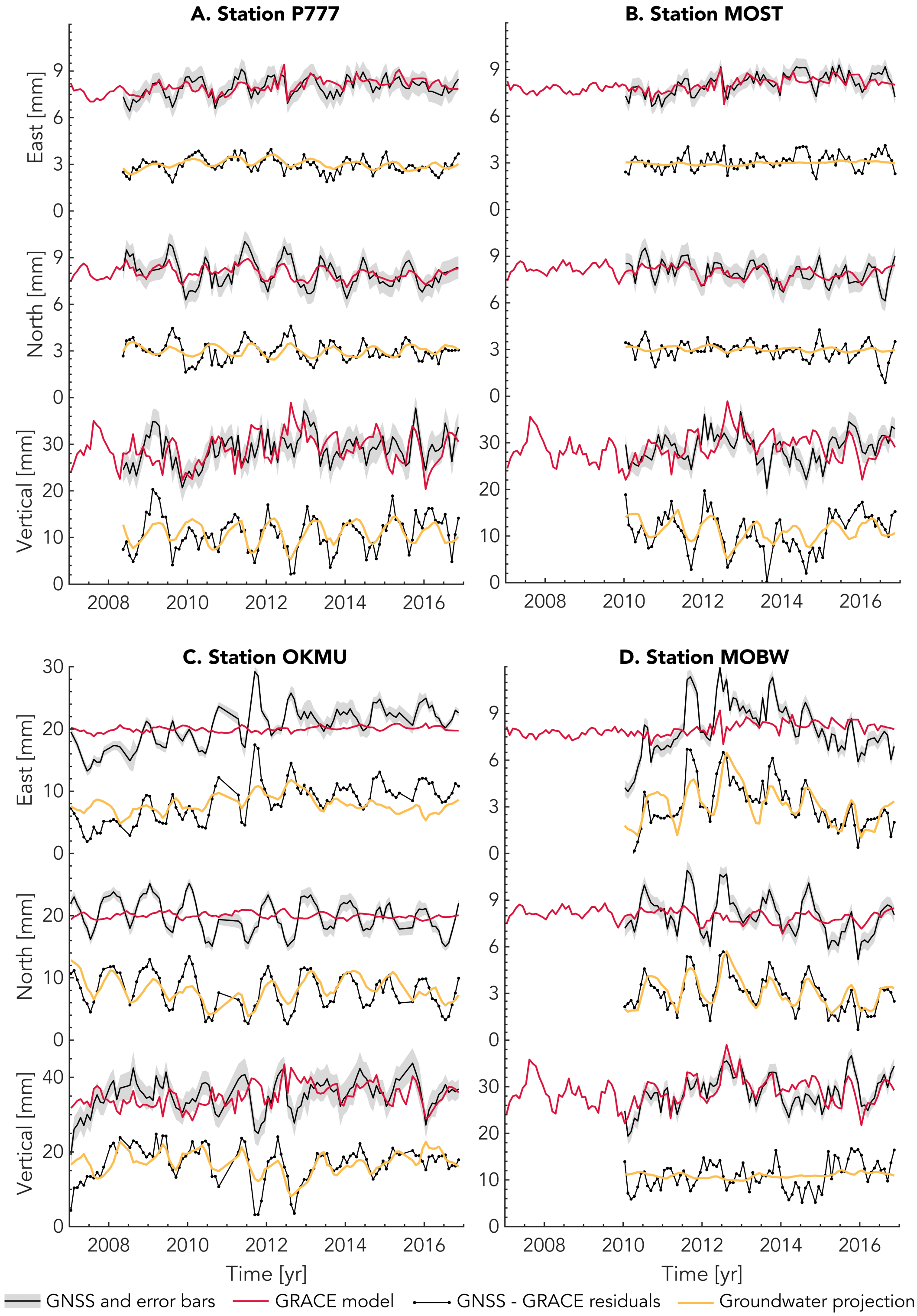

A. Station P777
B. Station MOST
C. Station OKMU
D. Station MOBW
East [mm]
North [mm]
Vertical [mm]
Time [yr]
GNSS and error bars
GRACE model
GNSS - GRACE residuals
Groundwater projection

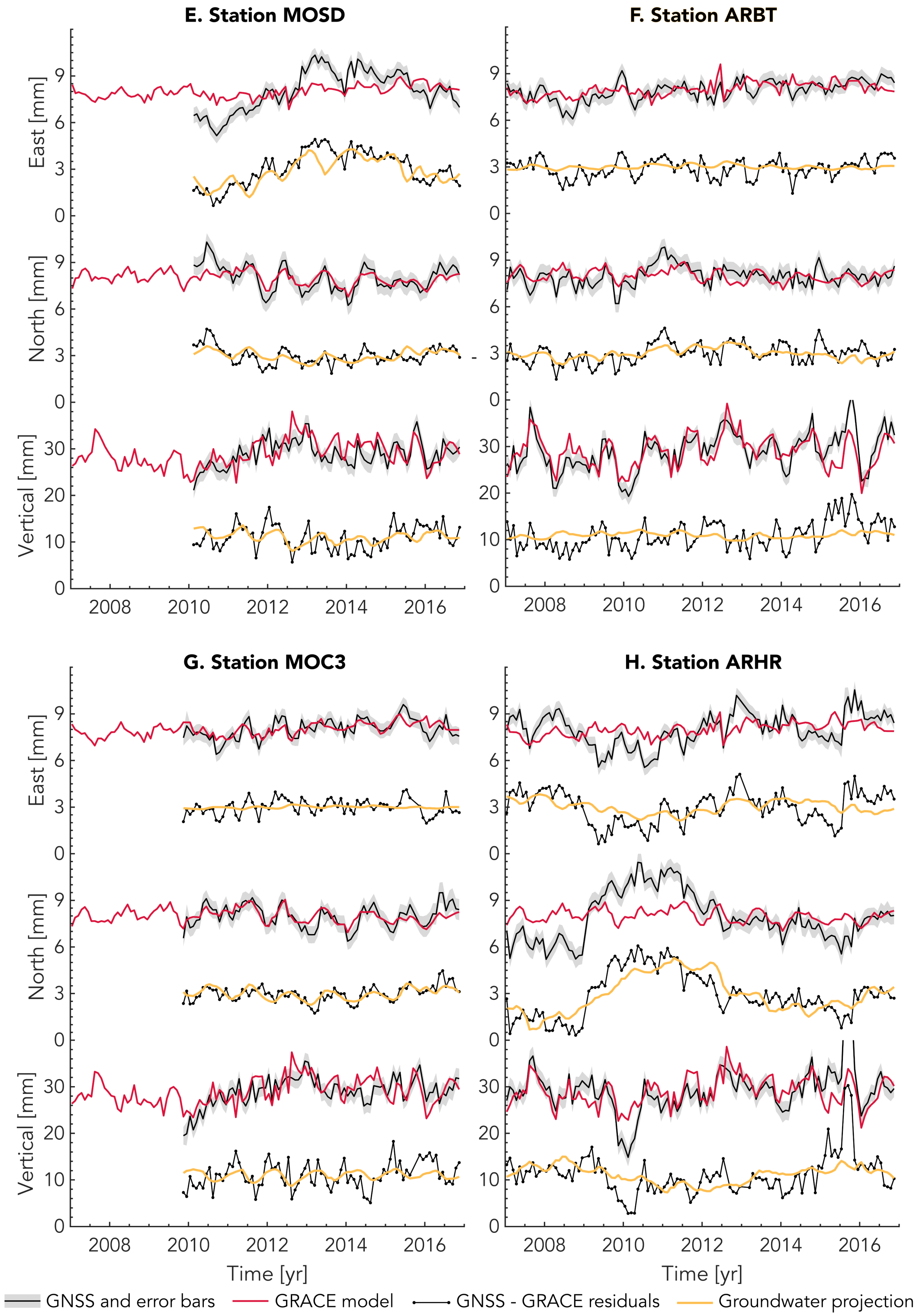

Figure B.2: Additional examples of extracted poroelastic signals at different GNSS stations as in Figure 2.7. Note the different scales for station OKMU.

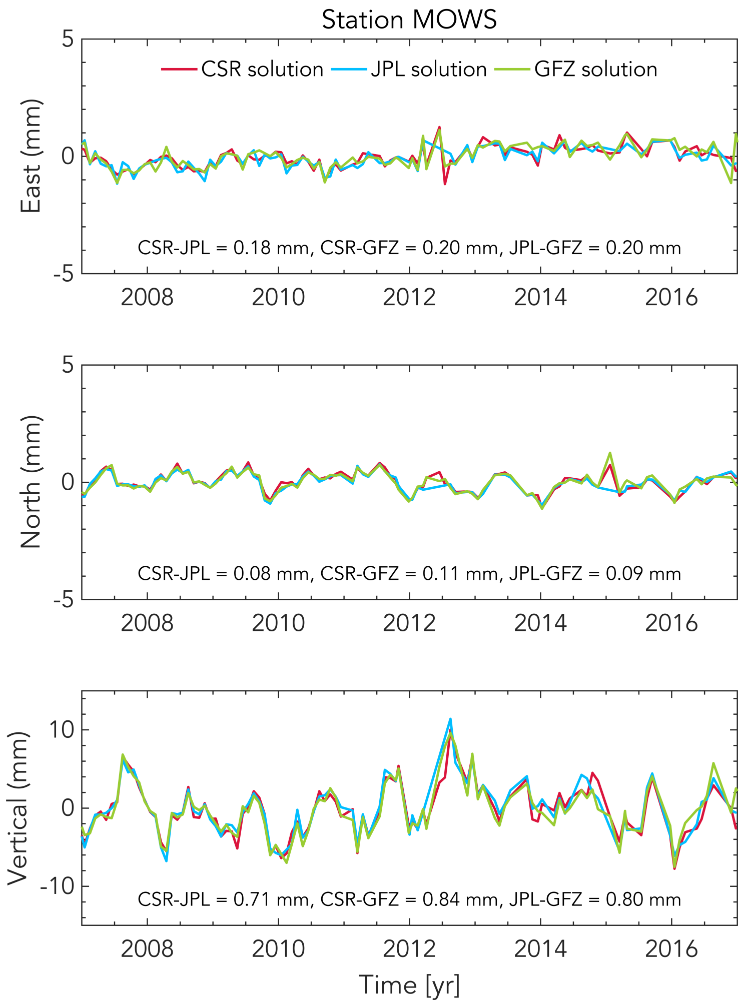

Figure B.3: Modeled hydrological elastic loading displacements with different GRACE solutions. The mean absolute deviation between the different solutions are indicated in each subplot.

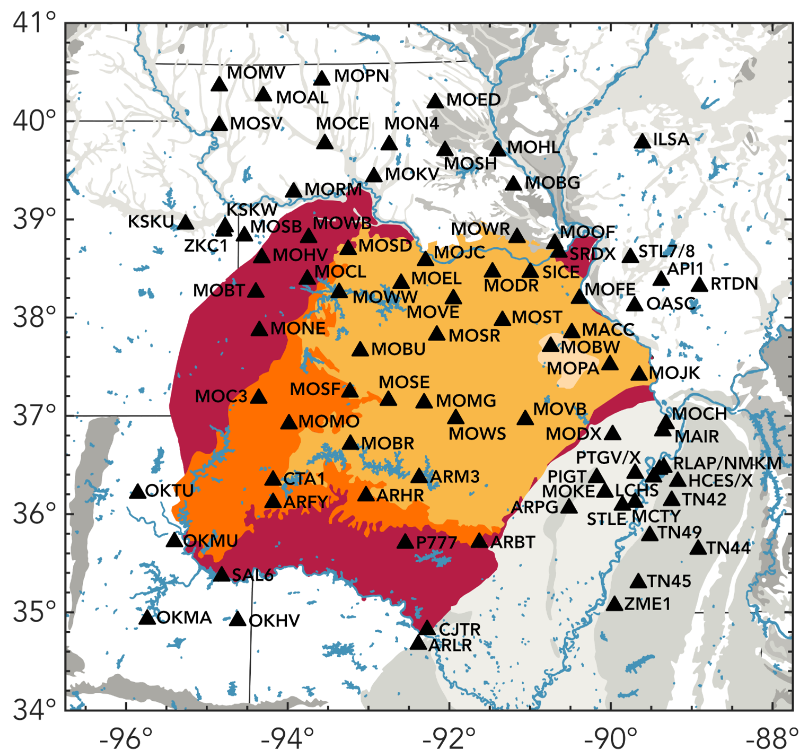

Figure B.4: Names of the 86 GNSS stations retained for the analysis.

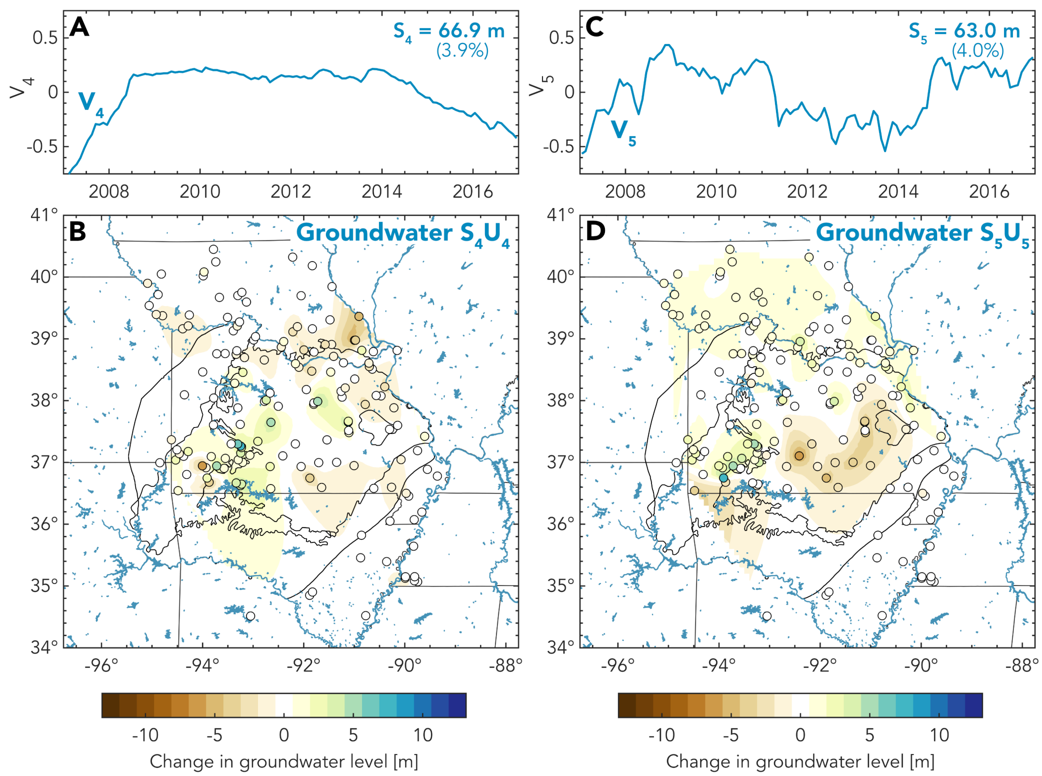

Figure B.5: IC4 and IC5 of a 5-component groundwater ICA. IC1, IC2, and IC3 are similar to the 3-component ICA in Figure 2.5.

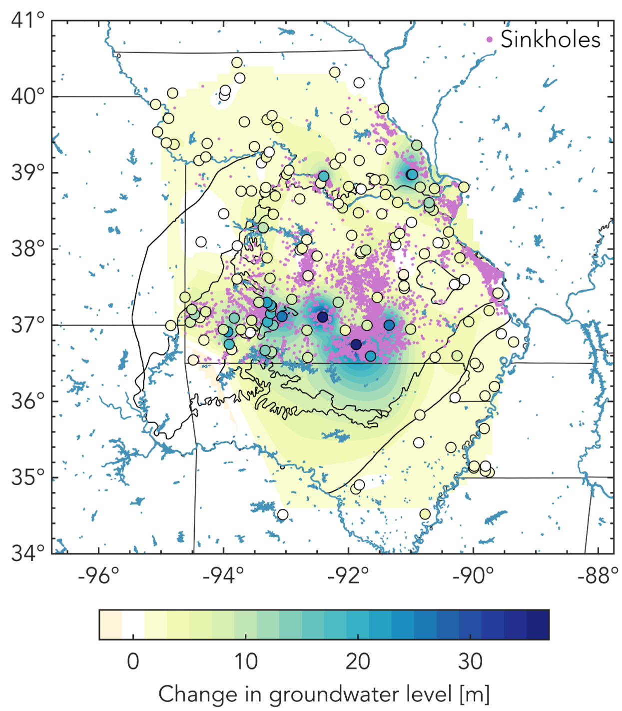

Figure B.6: Comparison between the spatial distributions of sinkholes (proxy for karstification) and groundwater IC1. Purple dots indicate the location of known sinkholes in Missouri as reported by the Missouri Geological Survey (https://dnr.mo.gov/geology/geosrv/envgeo/sinkholes.htm). The spatial distribution of IC1 groundwater (same as Figure 2.4B) is shown for comparison.

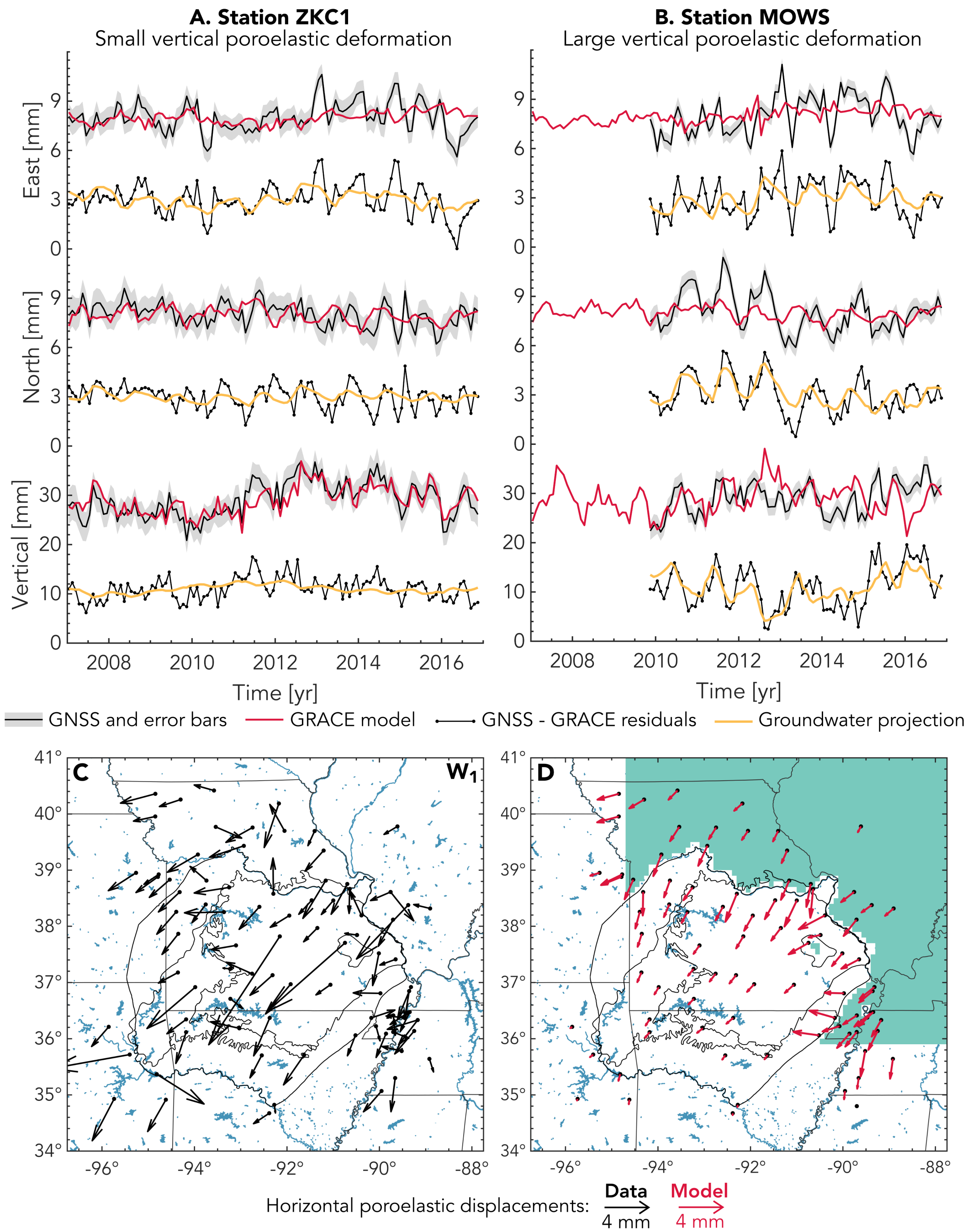

Figure B.7: Common mode poroelastic signal from neighbouring aquifers. (A,B) Similar to Figure 2.7 but without removing horizontal common mode. (C) Horizontal poroelastic displacements inferred by projecting onto W_1 without removing common mode. (D) Modeled horizontal displacements due to poroelastic eigenstrains outside OPAS in turquoise (Δh = 10m, b = 1000m).

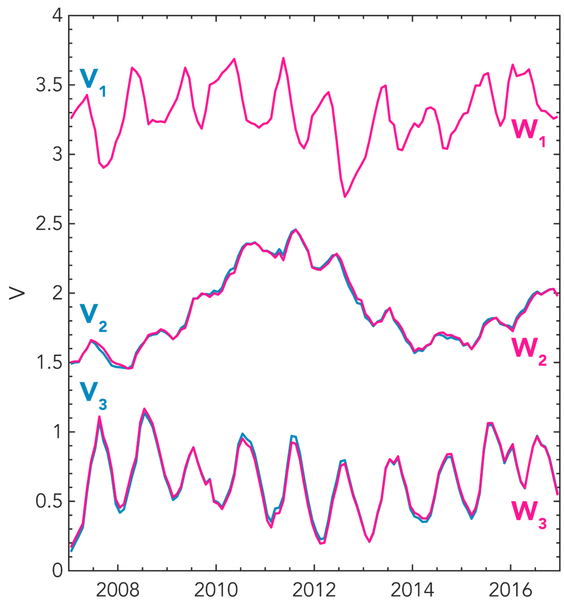

Figure B.8: Original groundwater V's vs orthogonalized W's.

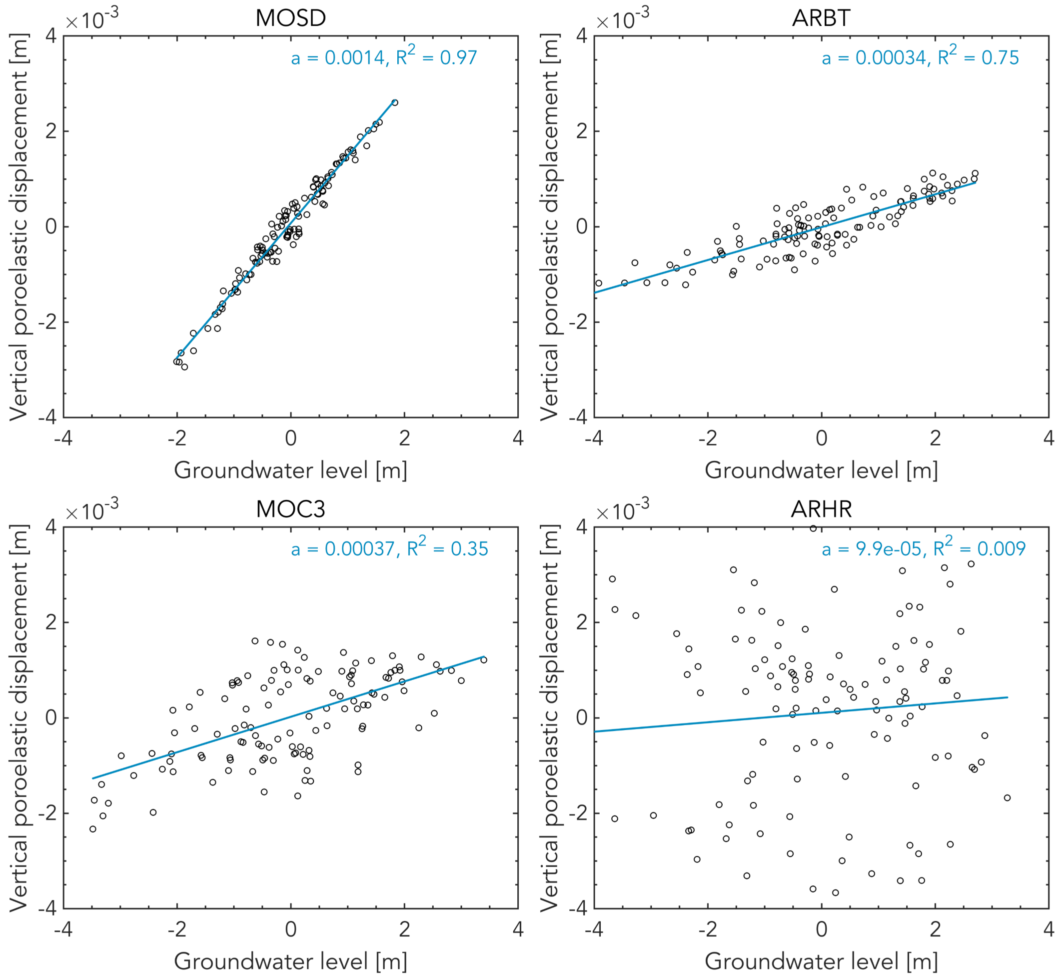

Figure B.9: Coefficient of determination for stations shown in Figure 2.10. Parameter a is the slope of the best-fit line.

Appendix C

SUPPLEMENTARY MATERIALS FOR CHAPTER IV

C.1 Long-term Simulations without Tectonic or Fluid Pressure Loading

In the models presented in this study, we prescribe initial conditions that are consistent with a dormant fault by starting with a highly healed fault (i.e., high initial value of the state variable θ_{ini}). This choice of initial conditions is justified by the long-term simulations without tectonic or fluid pressure loading shown in Figures C.4-C.7. The initial values affect some initial behavior/slip of the fault but, long-term, the fault heals under the near-constant values of shear stress, with a power-law decrease in slip rate as well as an increase in state variable over time; at long times, the value of the state variable is approximately equal to the healing time of the fault. This behavior can be predicted analytically: When the fault is well below steady-state ($V\theta/D_{RS} \ll 1$), $\dot{\theta} \sim 1$ and thus $\theta \sim t$. Moreover, with shear stress being almost constant, the rate-and-state friction coefficient is fixed and $\dot{f} = a\dot{V}/V + b/t = 0$, implying that $V \propto t^{-b/a}$. The initial conditions in the intermediate- and high-friction cases in this study are consistent with this behavior. In the low-friction case, although we do prescribe a high initial state variable and a low initial slip rate, the fault needs to be initially above steady state to match the measured slip behavior at the injection size and therefore not consistent with the behavior described above.

C.2 h_{ac}: Estimate of Slipping Zone Length at Slip Acceleration

In the main text, we derived an estimate of the slipping zone length at the time of slip acceleration (beginning of Stage 3). If $(\sigma - p)$ remained constant throughout the simulation, Eq. (4.11) would reduce to $h_{ac} \propto \mu D_{RS}/b$ which is similar to the condition for acceleration $k < k_b$ (where k is stiffness) in the spring-block slider model (Dieterich, 1992; Helmstetter and Shaw, 2009) and to the condition $h > L_b$ for acceleration on continuum fault segments that are far above steady-state (Rubin and Ampuero, 2005). Eq. (4.11) is also similar to the findings for seismic slip nucleation in slip-weakening friction models (Uenishi and Rice, 2003; Viesca and Rice, 2012) except that h_{ac} depends on pressure; specifically on the maximum value of pressure (at the injection site). The fact that this lengthscale does not depend — at least to first order — on the extent or shape of the pore pressure distribution is also consistent with prior findings (Uenishi and Rice, 2003; Viesca and Rice, 2012). At the same time, h_{ac} is different from some of the discussed critical lengthscales, since it does not signify the transition to dynamic, inertially-controlled earthquake slip, but rather corresponds to the beginning of the different quasi-static slip stage in this particular experiment. The existence of h_{ac} is linked to the two-stage quasi-static slip process in the field experiment which the simulations are trying to emulate. The associated evolution of the friction coefficient — with sharp increase to a peak value, then near-linear decrease vs. slip with the slope of b, and then near-constant value — is likely related to the relatively rapid increase of the pore pressure at the injection site compared to the timescale of state variable evolution considered in this work.

To demonstrate that Eq. (4.11) holds, in Figures C.12 and C.14(A-C) we show 3 simulations in which $h_a c$ is increased compared to the intermediate-friction case by increasing μ (pink), increasing D_{RS} (yellow) or decreasing b (turquoise) while keeping t_s constant. Figures C.13 and C.14(D-E) show simulations in which both t_s and h_{ac} are increased by increasing f^* (pink) or θ_{ini} (yellow). Figures C.13 and C.14(F) also show a case (turquoise) in which both t_s and h_{ac} are kept the same as in the intermediate-friction reference case but t_{ac} is delayed due to the decreased hydraulic diffusivity α which controls how fast the slipping zone expands during Stage 2. In all cases, the onset of Stage 3 is delayed compared to the intermediate-friction reference case. Thus, parameters μ, D_{RS}, b, t_s and α have a primary control on the onset of Stage 3 observed in all simulations shown in this work.

As for the amplitude and slope of the slip acceleration, four parameters — f^*, $a - b$, μ and α — have been identified to play a key role in controlling them as shown in Figures C.15 to C.19.

Bibliography

J. Dieterich. Earthquake nucleation on faults with rate-and state-dependent strength. *Tectonophysics*, 211(1–4):115–134, 1992. doi: 10.1016/0040-1951(92)90055-B. URL https://doi.org/10.1016/0040-1951(92)90055-B.

A. Helmstetter and B. Shaw. Afterslip and aftershocks in the rate-and-state friction law. *Journal of Geophysical Research: Solid Earth*, 114(B1), 2009. doi: 10.1029/2007JB005077. URL https://doi.org/10.1029/2007JB005077.

A. Rubin and J.-P. Ampuero. Earthquake nucleation on (aging) rate and state faults. *Journal of Geophysical Research: Solid Earth*, 110(B11), 2005. doi: 10.1029/2005JB003686. URL https://doi.org/10.1029/2005JB003686.

K. Uenishi and J. Rice. Universal nucleation length for slip-weakening rupture instability under nonuniform fault loading. *Journal of Geophysical Research: Solid Earth*, 108(B1), 2003. doi: 10.1029/2001JB001681. URL `https://doi.org/10.1029/2001JB001681`.

R. Viesca and J. Rice. Nucleation of slip-weakening rupture instability in landslides by localized increase of pore pressure. *Journal of Geophysical Research: Solid Earth*, 117(B3), 2012. doi: 10.1029/2011JB008866. URL `https://doi.org/10.1029/2011JB008866`.

C.3 Supplementary Tables and Figures

Table C.1: Model parameters for the three cases presented in Figures 4.2-4.4 in the main text.

Properties	**Symbol**	**Low Friction**	**Intermediate Friction**	**High Friction**
Total fault length [m]	x_{tot}	250	250	250
Frictional interface length [m]	x_{fr}	200	200	200
Initial shear stress [MPa]	τ_{ini}	2.15	2.15	2.15
Initial normal stress [MPa]	σ_{ini}	4.00	4.00	4.00
Initial coefficient of friction	f_{ini}	0.5375	0.5375	0.5375
Reference coefficient of friction	f^*	0.4815	0.5500	0.6000
Reference slip rate [m/s]	V^*	10^{-6}	10^{-6}	10^{-6}
Direct effect frictional parameter	a	0.01500	0.01125	0.01125
Evolutionary friction parameter	b	0.01600	0.01600	0.01600
Critical slip distance [μm]	D_{RS}	16.75	16.75	16.75
Hydraulic diffusivity [m^2/s]	α	0.04	0.20	0.85
Initial state variable [s]	θ_{ini}	1.21e12	2.38e12	7.00e12
Shear modulus [GPa]	μ	10	10	10

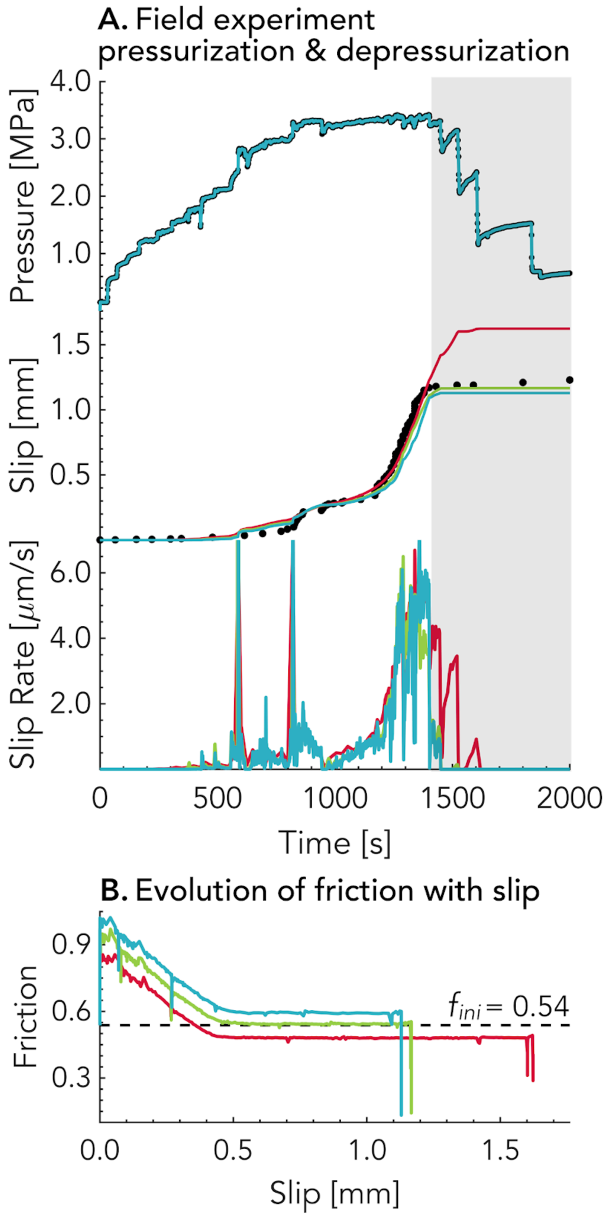

Figure C.1: Temporal evolution of pore pressure, slip and slip rate and evolution of friction as a function of slip as in Figure 4.2AB in the main text but for the exact pressure history. The simulated slip rate is similar but noisier and harder to interpret.

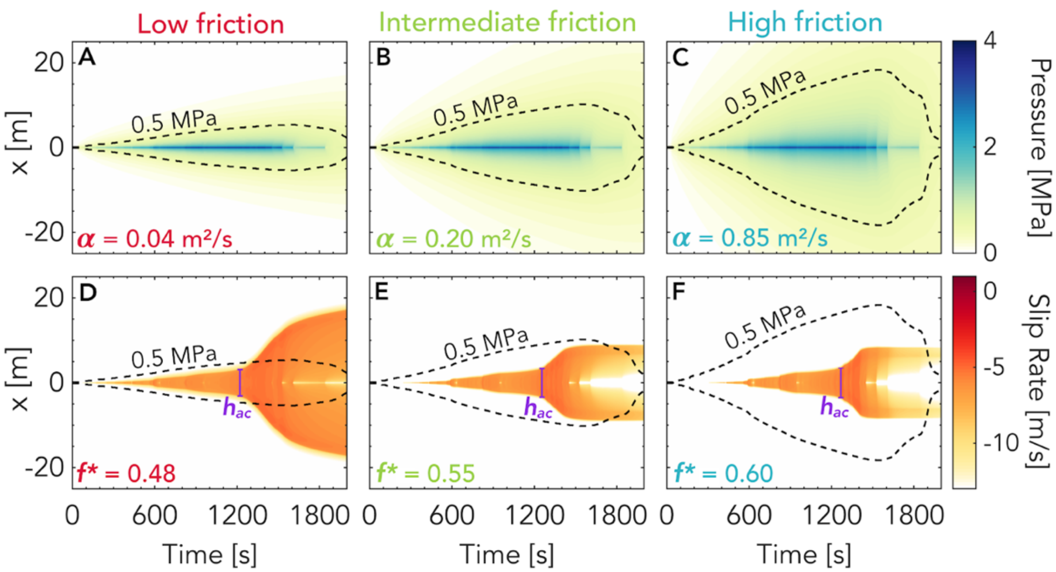

Figure C.2: Spatial and temporal evolution of pore pressure and slip as Figure 4.3 in the main text but for the exact pressure history as in Figure C.1 and including the depressurization stage.

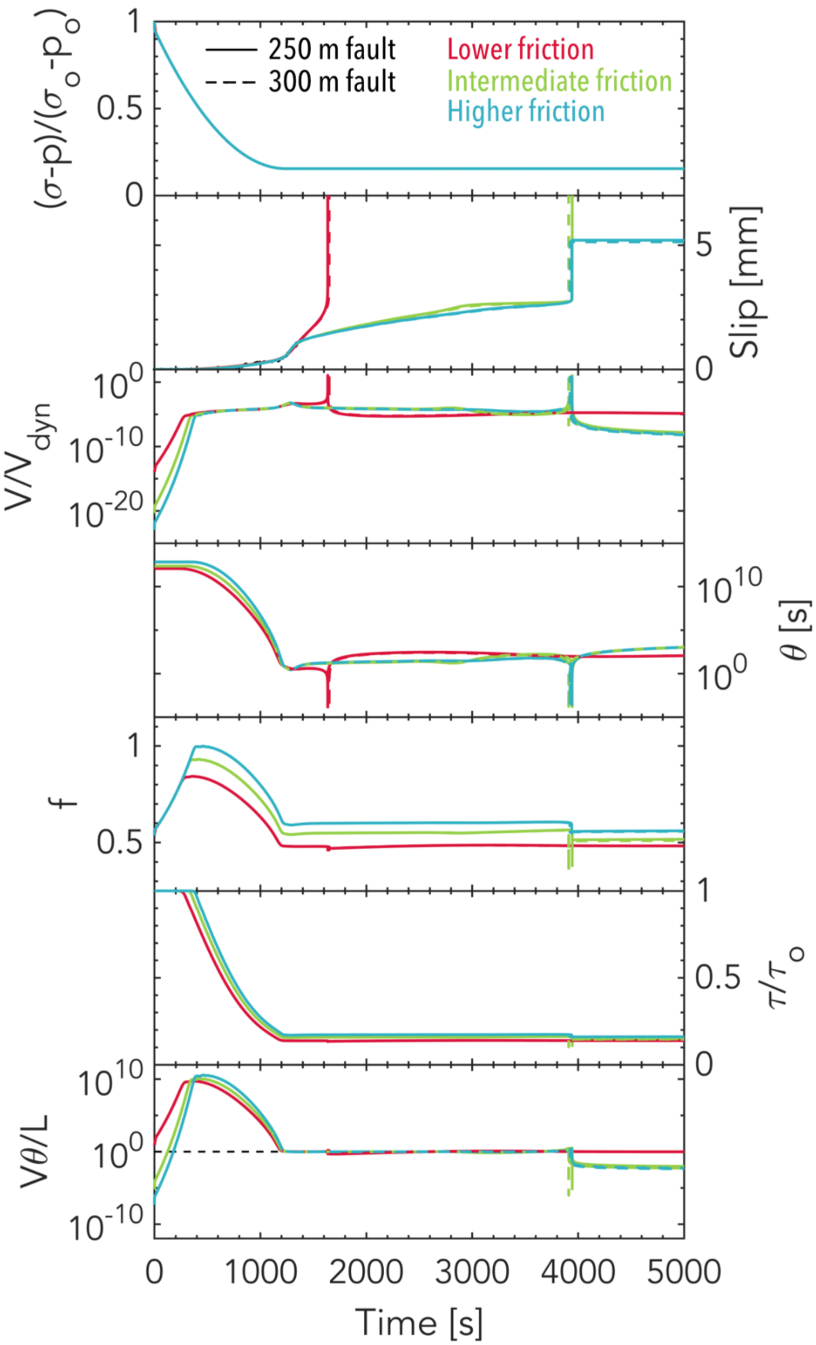

Figure C.3: Temporal evolution of several quantities at the injection site for the prolonged injection simulations (Figure 4.4) with domain sizes of 250 m (solid lines) and 300 m (dashed lines). From top to bottom: the normalized effective normal stress, slip, normalized slip rate (V_{dyn} = 10^{-2} m/s), state variable, friction coefficient, normalized shear stress and closeness to steady state at the injection site. Changing the domain size slightly changes the timing of the dynamic events but not the overall behavior.

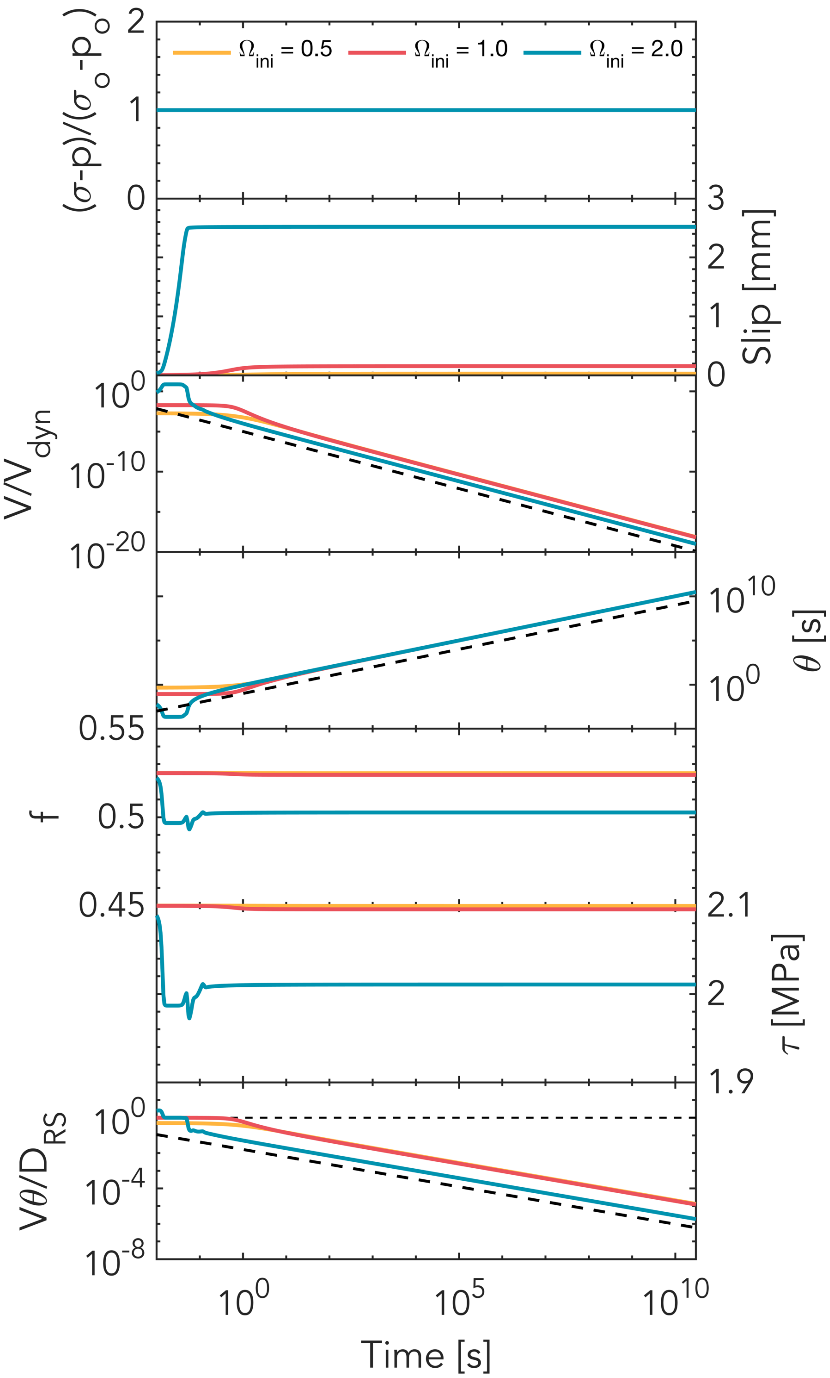

Figure C.4: Simulations that illustrate long-term fault healing in the absence of slip, with $f^* = 0.550$, $f_{ini} = 0.525$, $a = 0.011$, and $b = 0.016$, varying the initial closeness to steady state ($\Omega_{ini} = V_{ini}\theta_{ini}/D_{RS}$). No matter what the initial values are, all cases eventually undergo a logarithmic decrease in slip rate and an increase in state variable with time. Note that the time axis is logarithmic. The thick dashed lines indicate the slopes discussed in Section C.1.

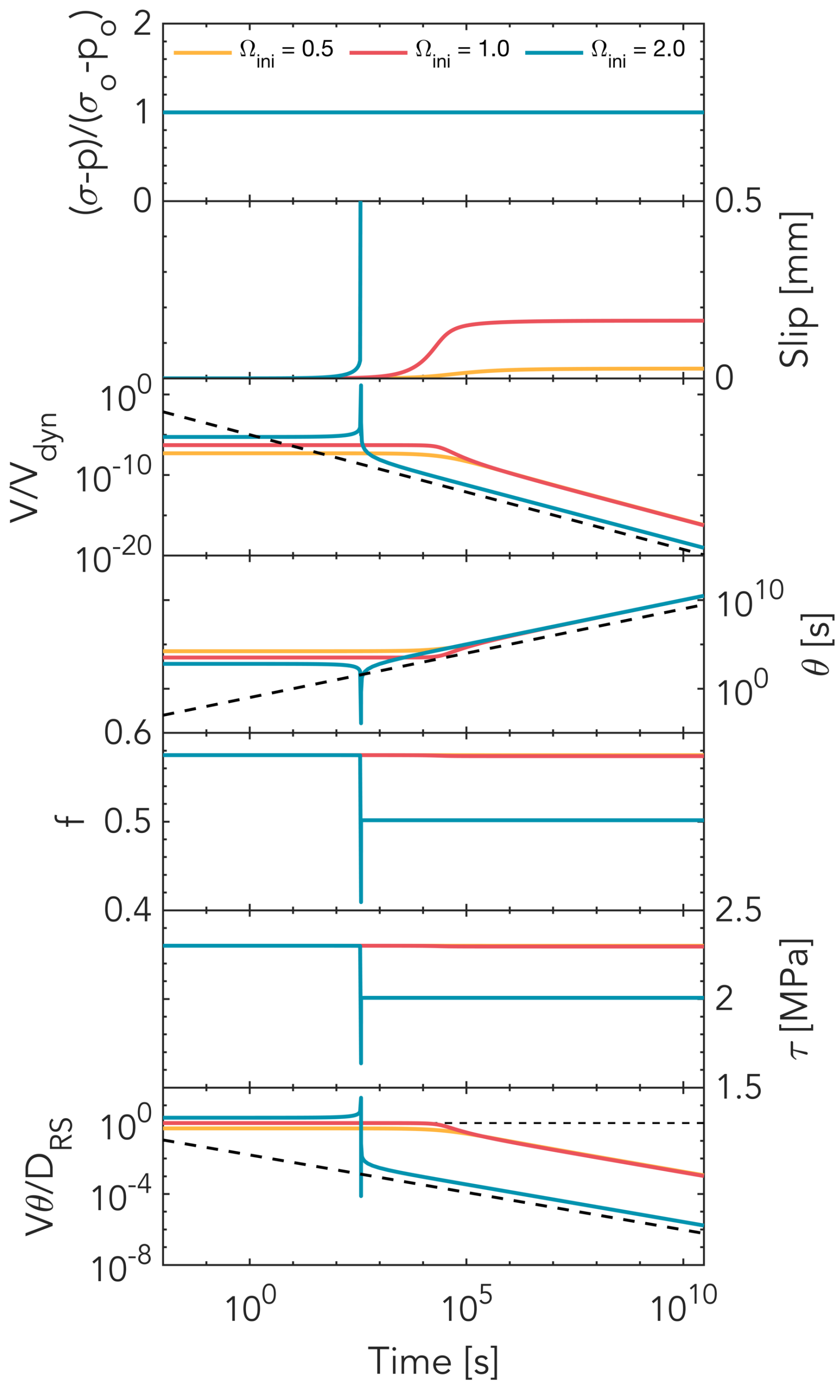

Figure C.5: Simulations that illustrate long-term fault healing in the absence of slip, with $f^* = 0.550$, $f_{ini} = 0.575$, $a = 0.011$, and $b = 0.016$, varying the initial closeness to steady state ($\Omega_{ini} = V_{ini}\theta_{ini}/D_{RS}$). No matter what the initial values are, all cases eventually undergo a logarithmic decrease in slip rate and an increase in state variable with time, even the initially above steady-state case which experiences a run-away earthquake a few minutes into the simulation. Note that the time axis is logarithmic. The thick dashed lines indicate the slopes discussed in Section C.1.

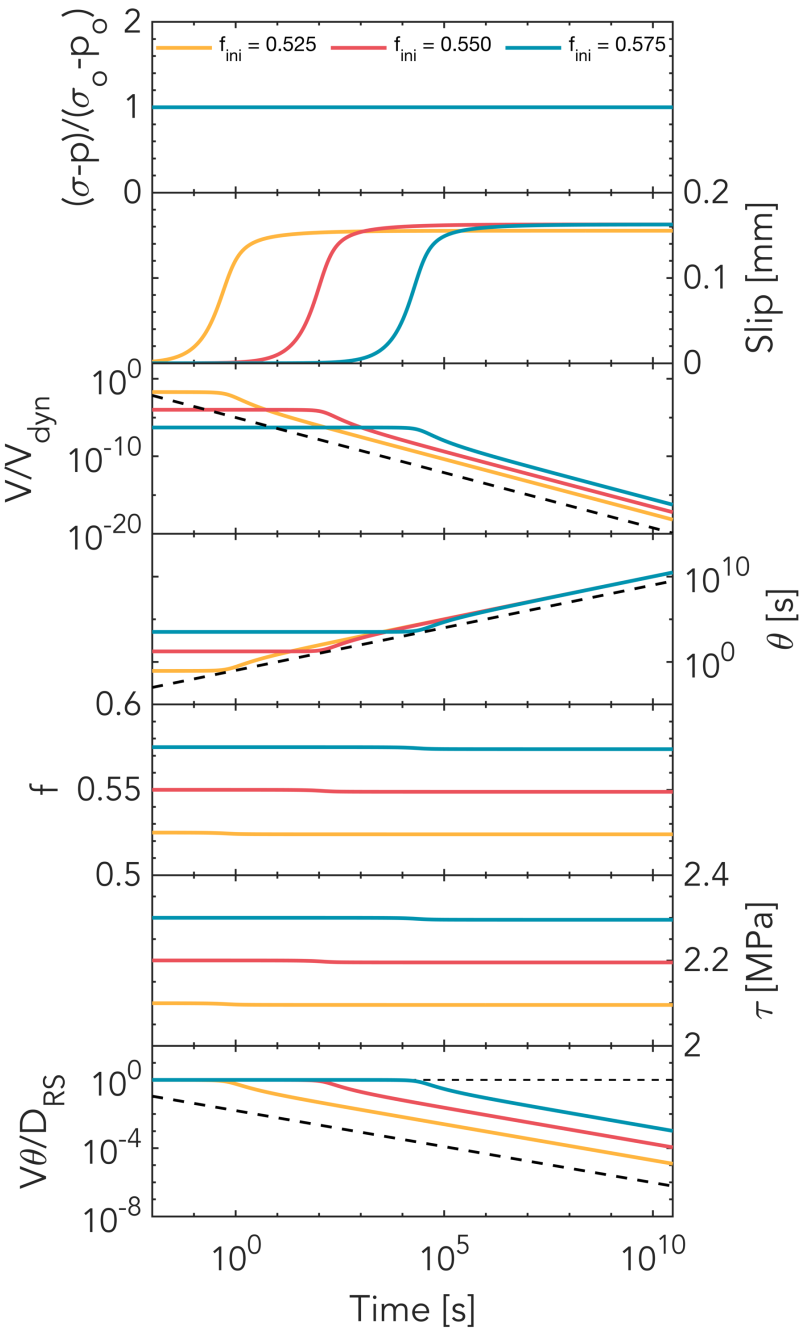

Figure C.6: Simulations that illustrate long-term fault healing in the absence of slip, with $f^* = 0.550$, $\Omega_{ini} = 1$, $a = 0.011$, and $b = 0.016$, varying the initial friction coefficient, f_{ini}. No matter what the initial values are, all cases eventually undergo a logarithmic decrease in slip rate and an increase in state variable with time. Note that the time axis is logarithmic. The thick dashed lines indicate the slopes discussed in Section C.1.

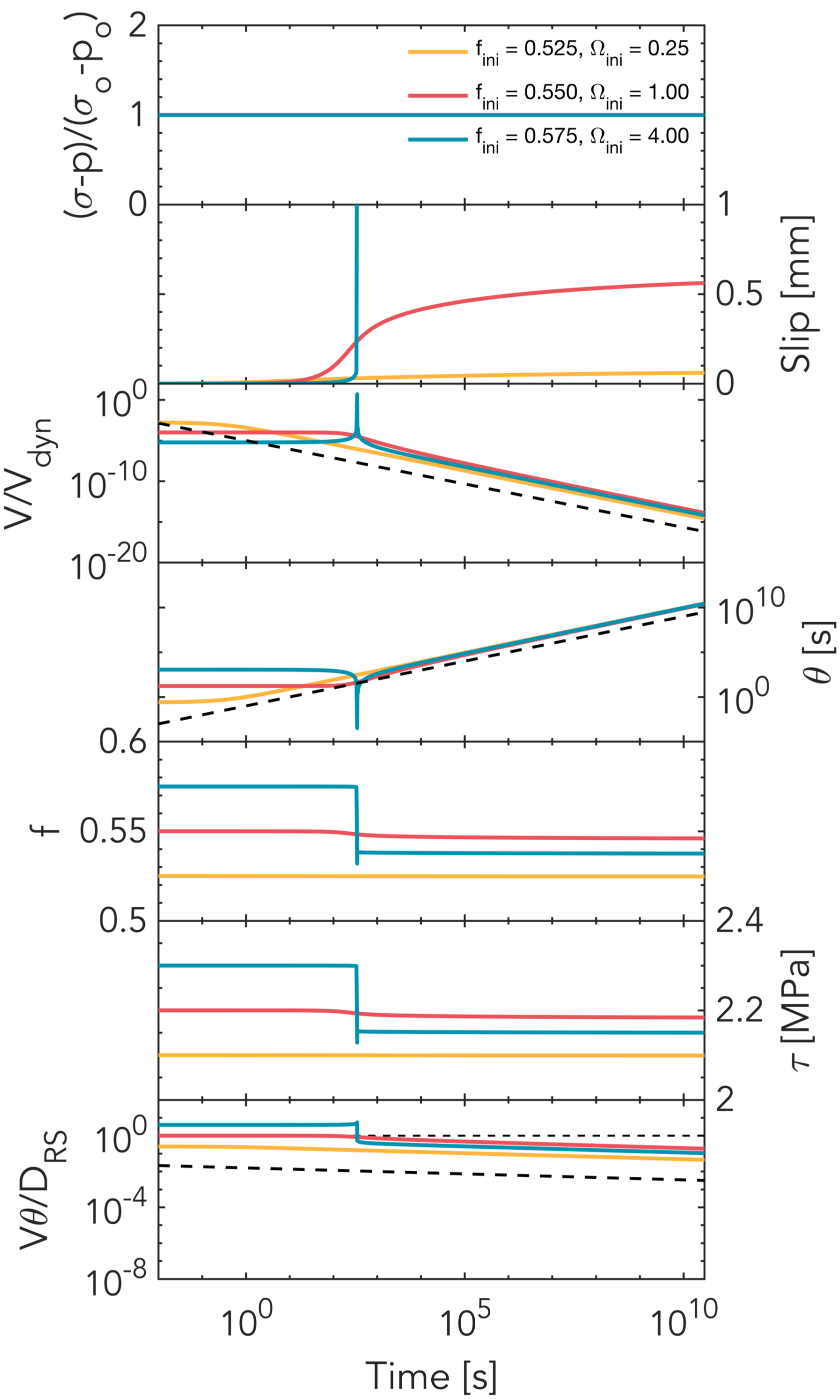

Figure C.7: Simulations that illustrate long-term fault healing in the absence of slip, with $f^* = 0.550$, $a = 0.015$, and $b = 0.016$, varying the initial closeness to steady state ($\Omega_{ini} = V_{ini}\theta_{ini}/D_{RS}$) and initial friction coefficient f_{ini}. No matter what the initial values are, all cases eventually undergo a logarithmic decrease in slip rate and an increase in state variable with time, even the initially above steady-state case which experiences a run-away earthquake a few minutes into the simulation. Note that the time axis is logarithmic. The thick dashed lines indicate the slopes discussed in Section C.1.

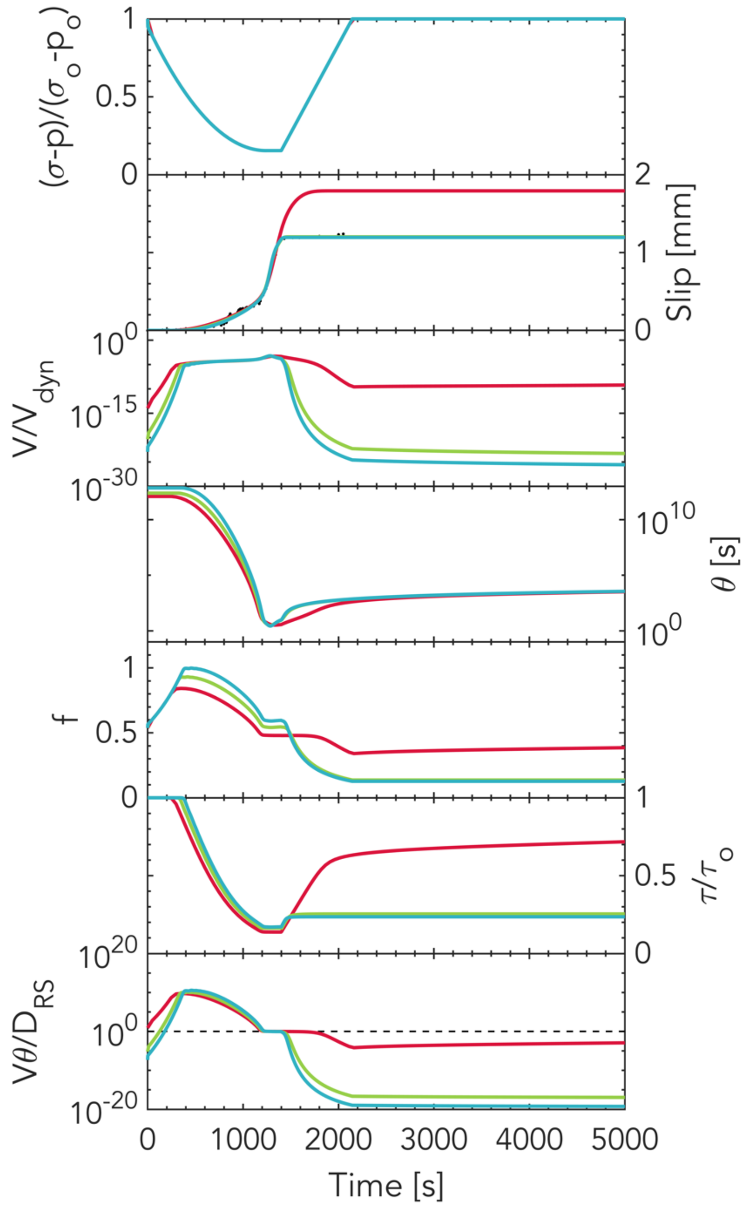

Figure C.8: Simulated temporal evolution of several quantities at the injection site for the cases of Figure 4.2A in the main text. From top to bottom: the normalized effective normal stress, slip, normalized slip rate (V_{dyn} = 10^{-2} m/s), state variable, friction coefficient, normalized shear stress and closeness to steady state at the injection site. Note that no earthquakes occur in these simulations as opposed to cases in which the pressure is kept constant at the injection site (Figure 4.4 in the main text).

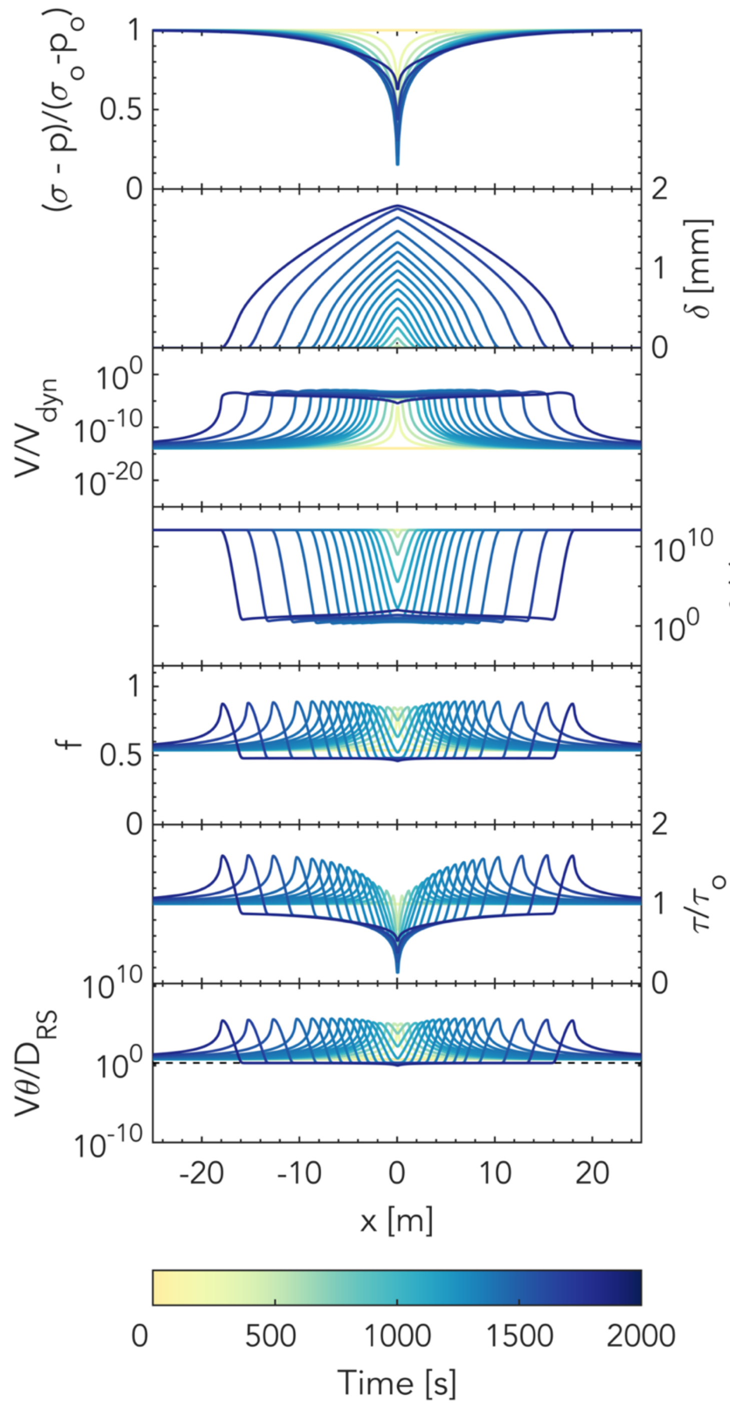

Figure C.9: Spatial and temporal evolution of the same quantities as in Figure C.8 for the low-friction case (plotted every 2000 time steps).

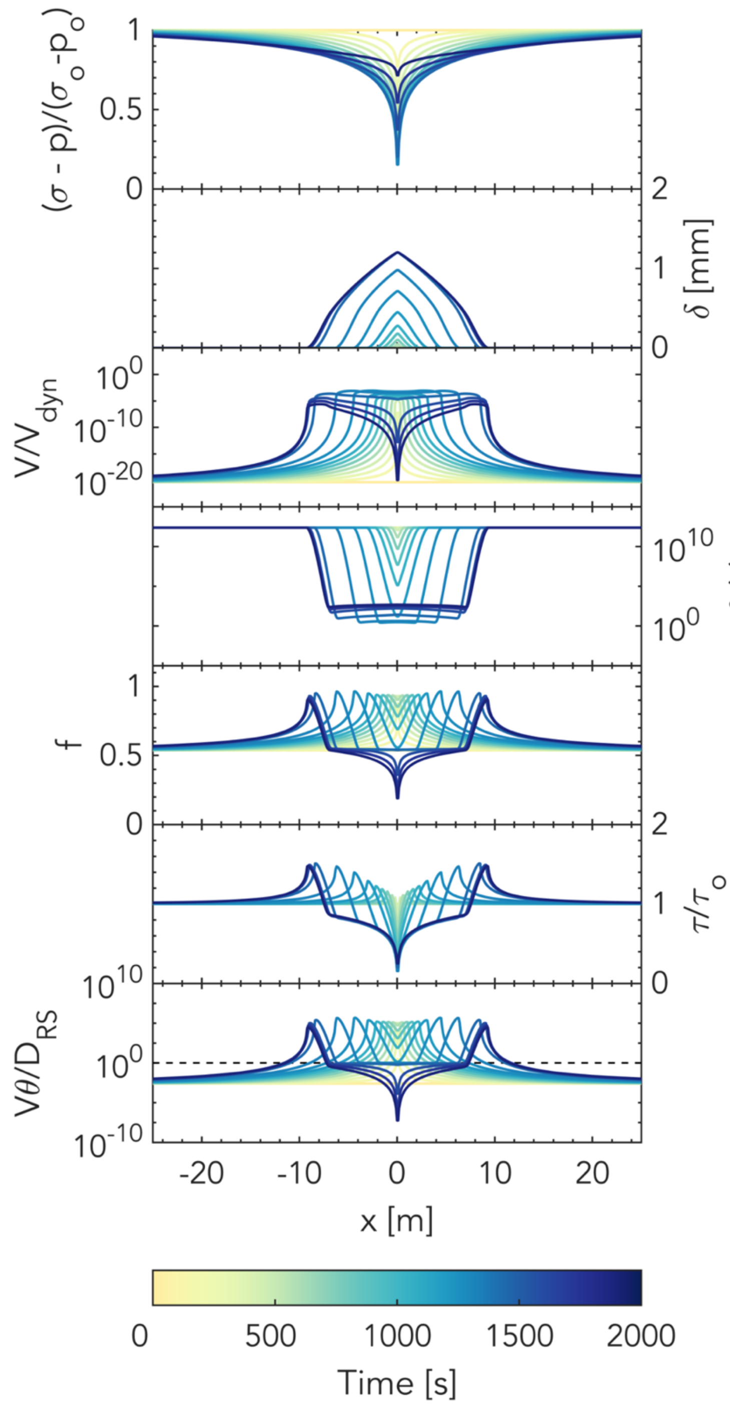

Figure C.10: Spatial and temporal evolution of the same quantities as in Figure C.8 for the intermediate-friction case (plotted every 6000 time steps).

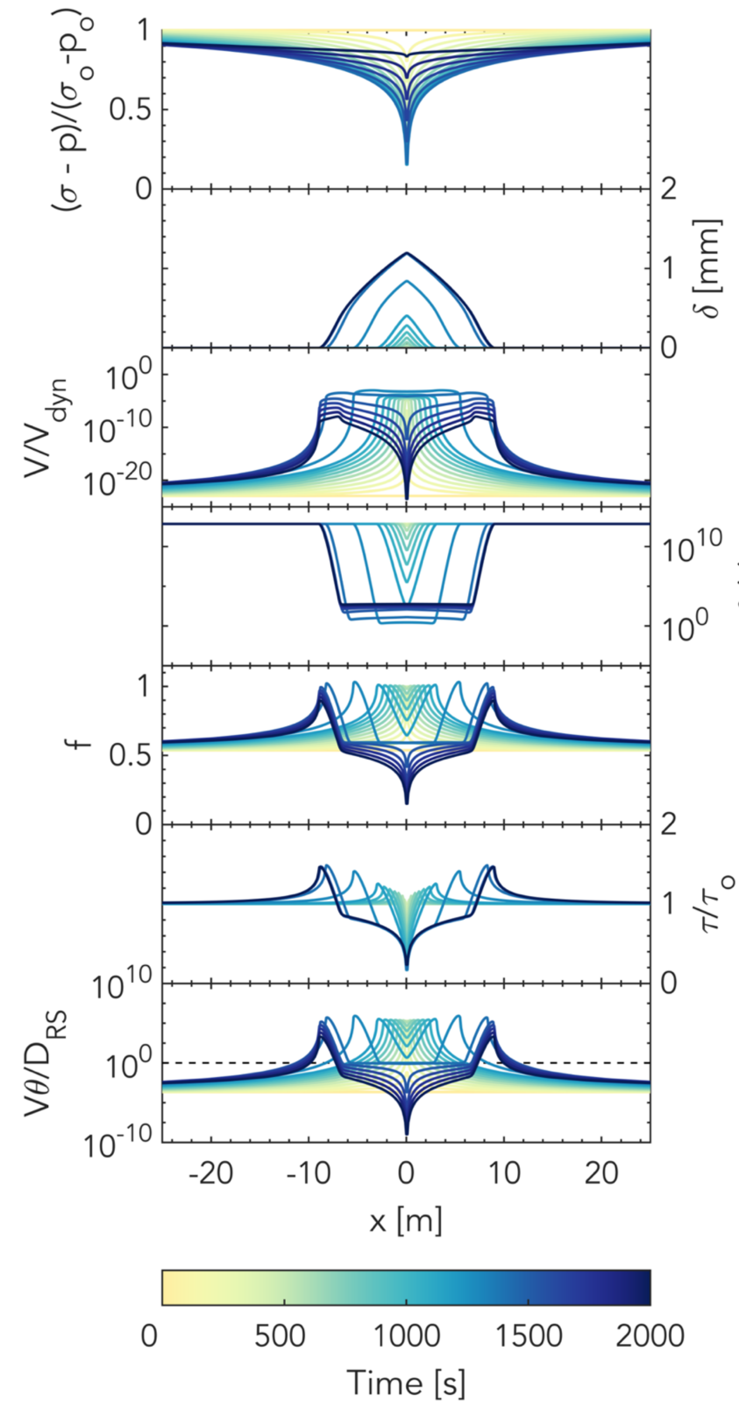

Figure C.11: Spatial and temporal evolution of the same quantities as in Figure C.8 for the high-friction case (plotted every 20000 time steps).

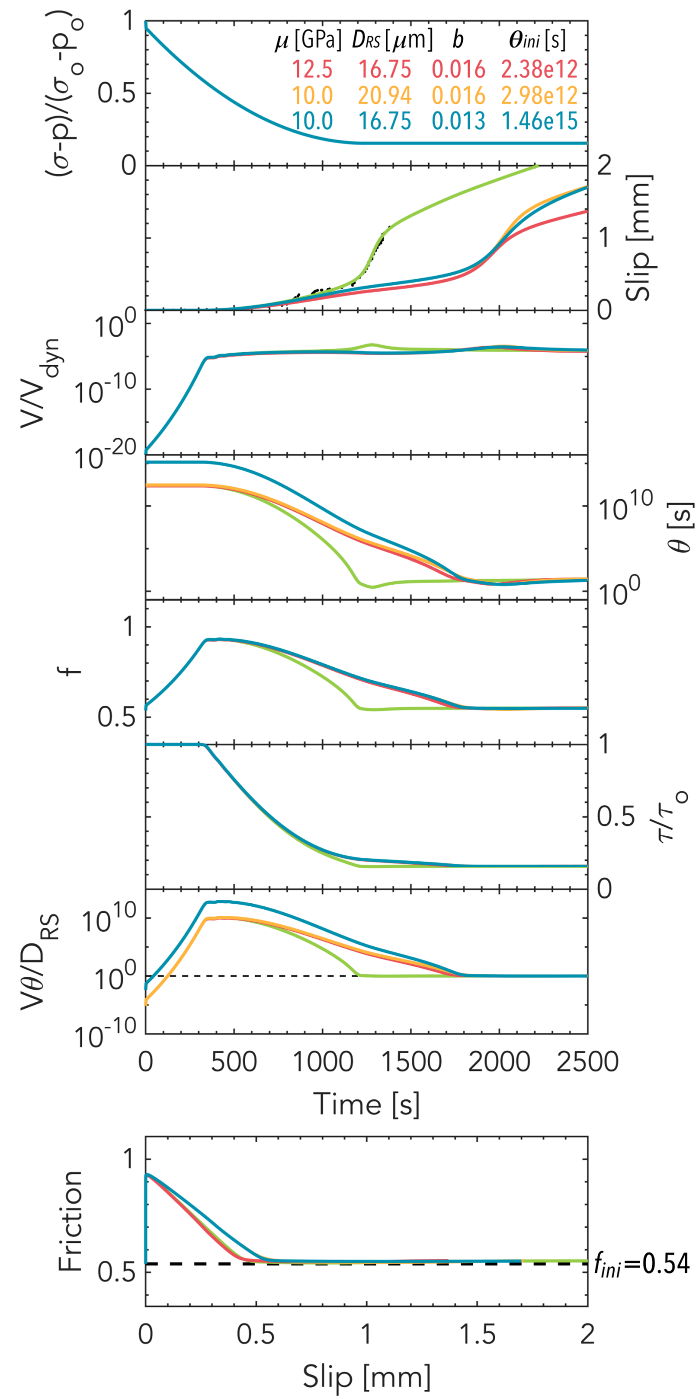

Figure C.12: Temporal evolution of quantities at the injection site and friction vs. slip for prolonged injection but for cases in which the onset of Stage 3 is delayed by increasing μ (pink), increasing D_{RS} (yellow) or decreasing b (turquoise) compared to the intermediate-friction reference case (green). Note the delay in the transient acceleration compared to the reference case. Parameter values modified from the intermediate-friction scenario are listed at the top right corner.

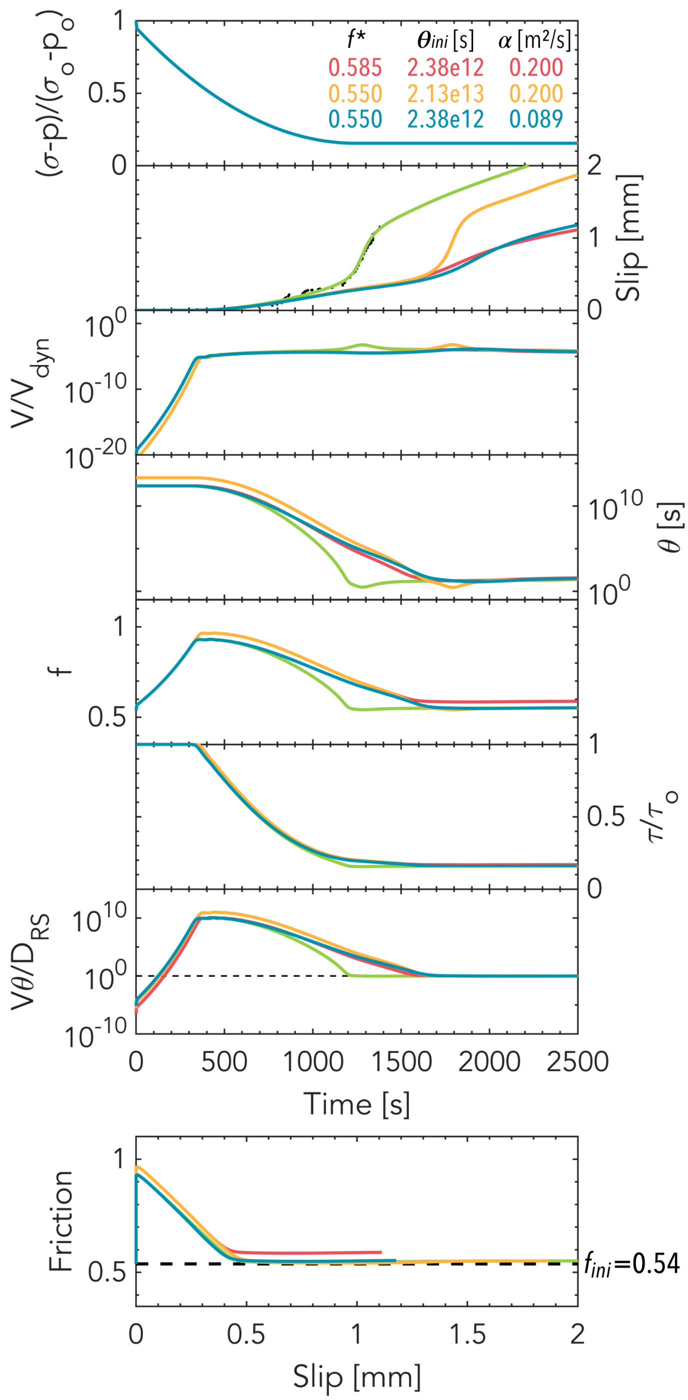

Figure C.13: Temporal evolution of quantities at the injection site and friction vs. slip for prolonged injection but for cases in which the onset of Stage 3 is delayed by increasing f^* (pink), increasing θ_{ini} (yellow) or decreasing α (turquoise) compared to the intermediate-friction reference case (green). Note the delay in the transient acceleration compared to the reference case. Parameter values modified from the intermediate-friction scenario are listed at the top right corner.

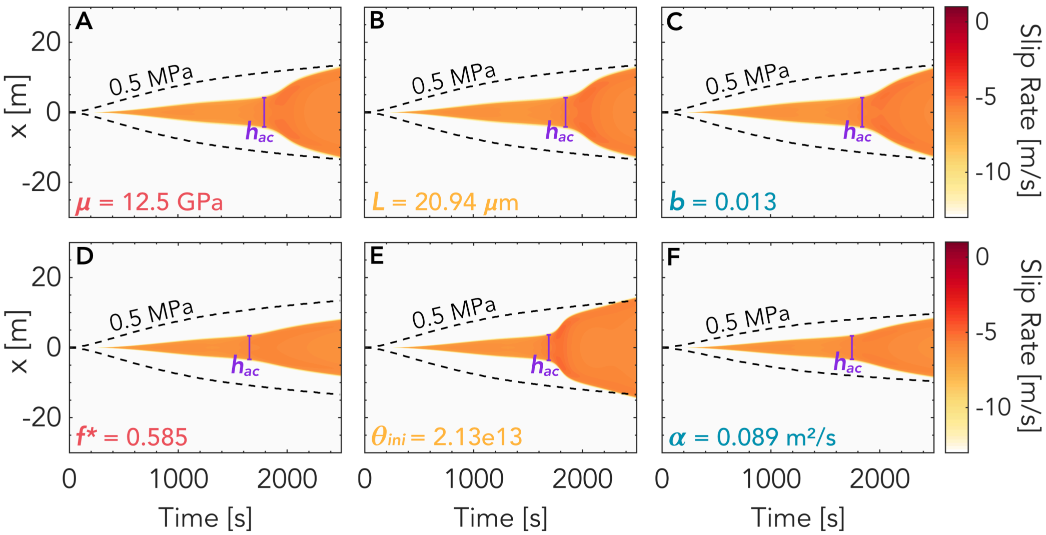

Figure C.14: Spatial and temporal evolution of slip rate for the modified prolonged injection cases shown in Figures C.12 and C.13 in which the onset of Stage 3 is delayed by (A) increasing μ, (B) increasing D_{RS}, (C) decreasing b, (D) increasing f^*, (E) increasing θ_{ini}, (F) decreasing hydraulic diffusivity α. Note that h_{ac} provides a good estimate of the extent of the sliding region before the onset of Stage 3 in all these cases.

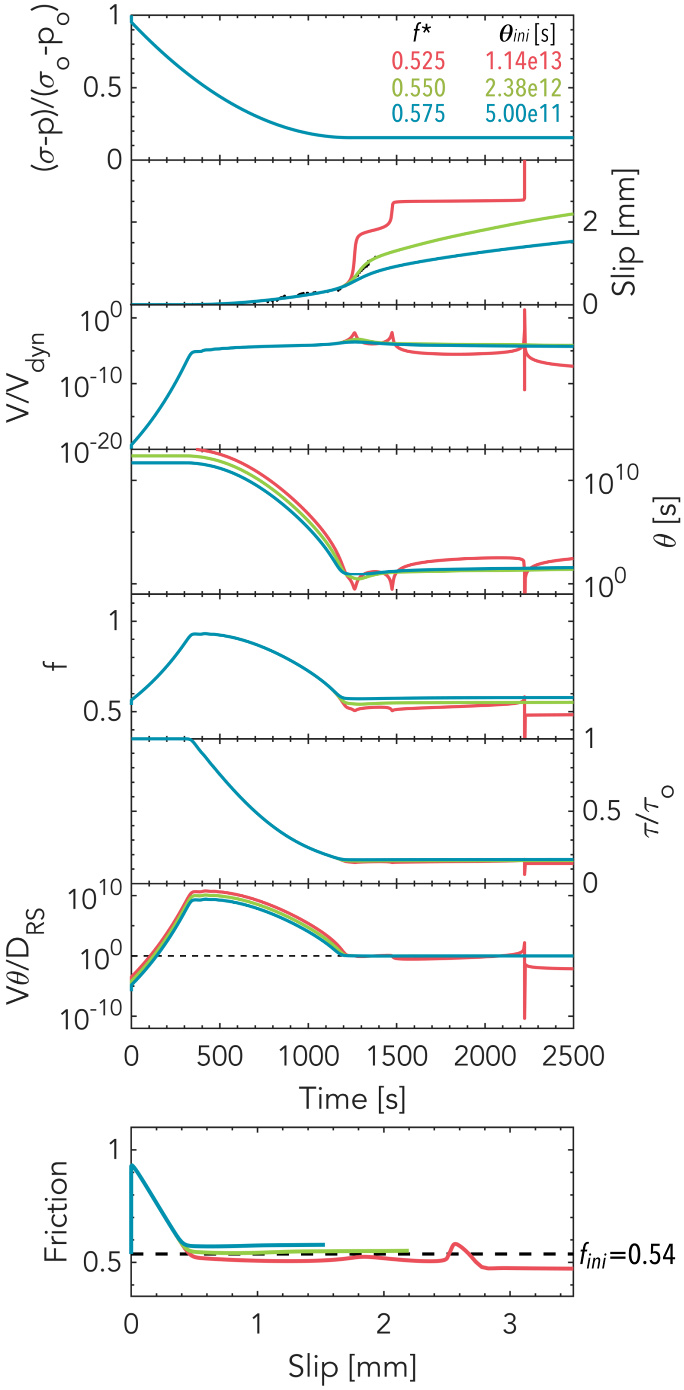

Figure C.15: Temporal evolution of quantities at the injection site and friction vs slip of 2 cases showing the effect of varying f^* while keeping f^p constant. Increasing f^* reduces the amplitude and slope of the transient acceleration. Parameter values modified from the intermediate-friction scenario are listed at the top right corner.

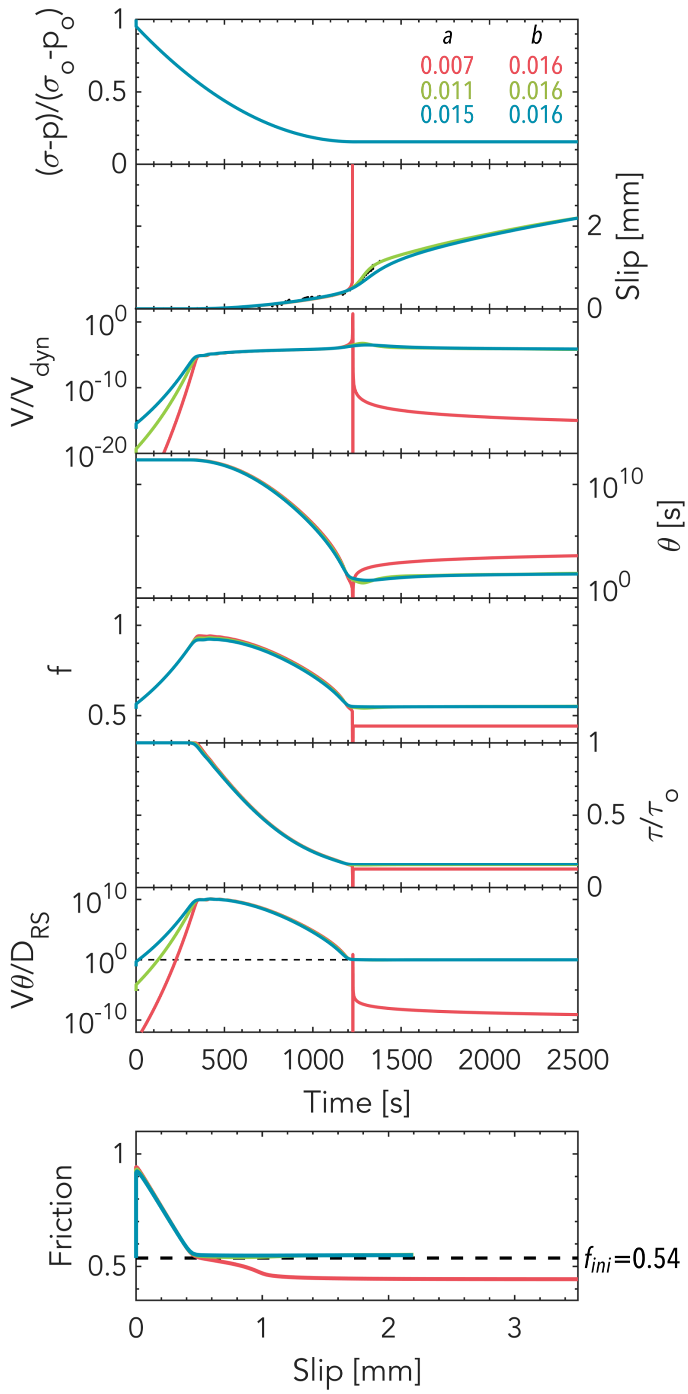

Figure C.16: Temporal evolution of quantities at the injection site and friction vs slip of 2 cases showing the effect of varying a. Increasing a reduces the amplitude and slope of the transient acceleration. Parameter values modified from the intermediate-friction scenario (green) are listed at the top right corner.

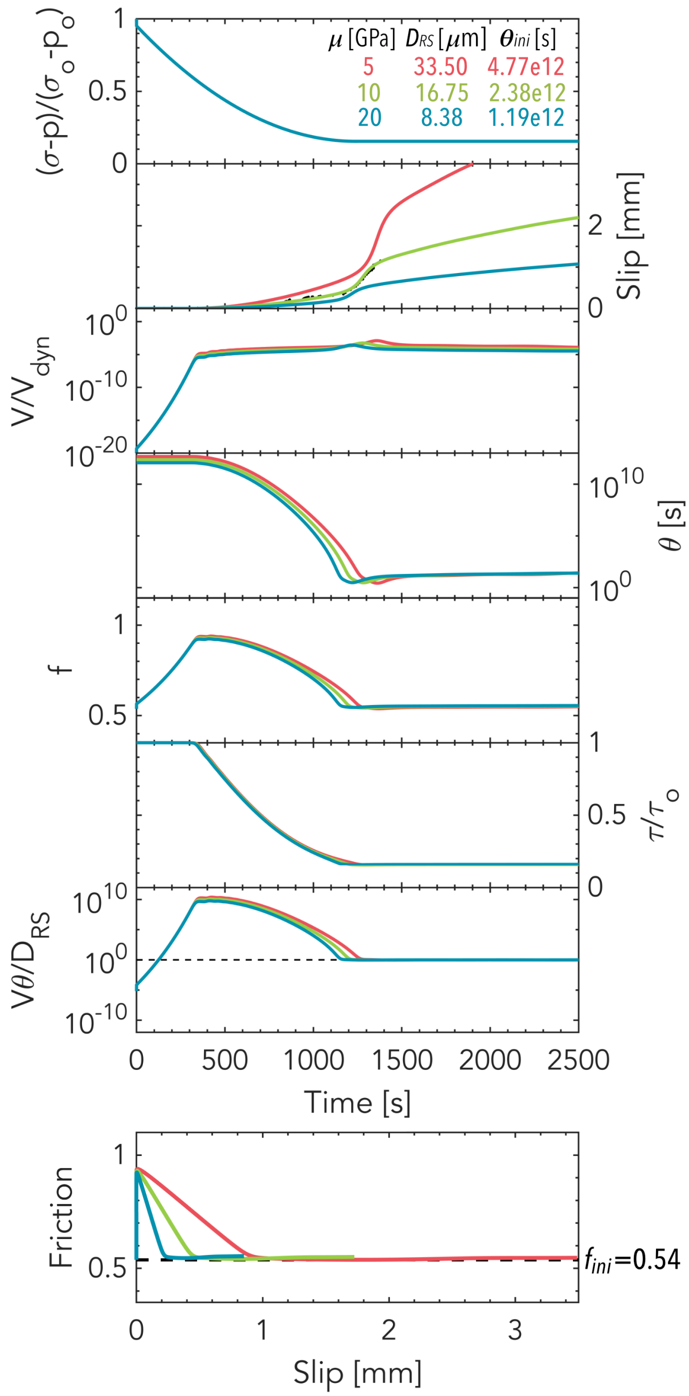

Figure C.17: Temporal evolution of quantities at the injection site and friction vs slip of 2 cases showing the effect of varying μ while keeping h_{ac} and f^p constant. Increasing μ reduces the amplitude and slope of the transient acceleration. Parameter values modified from the intermediate-friction scenario (green) are listed at the top right corner.

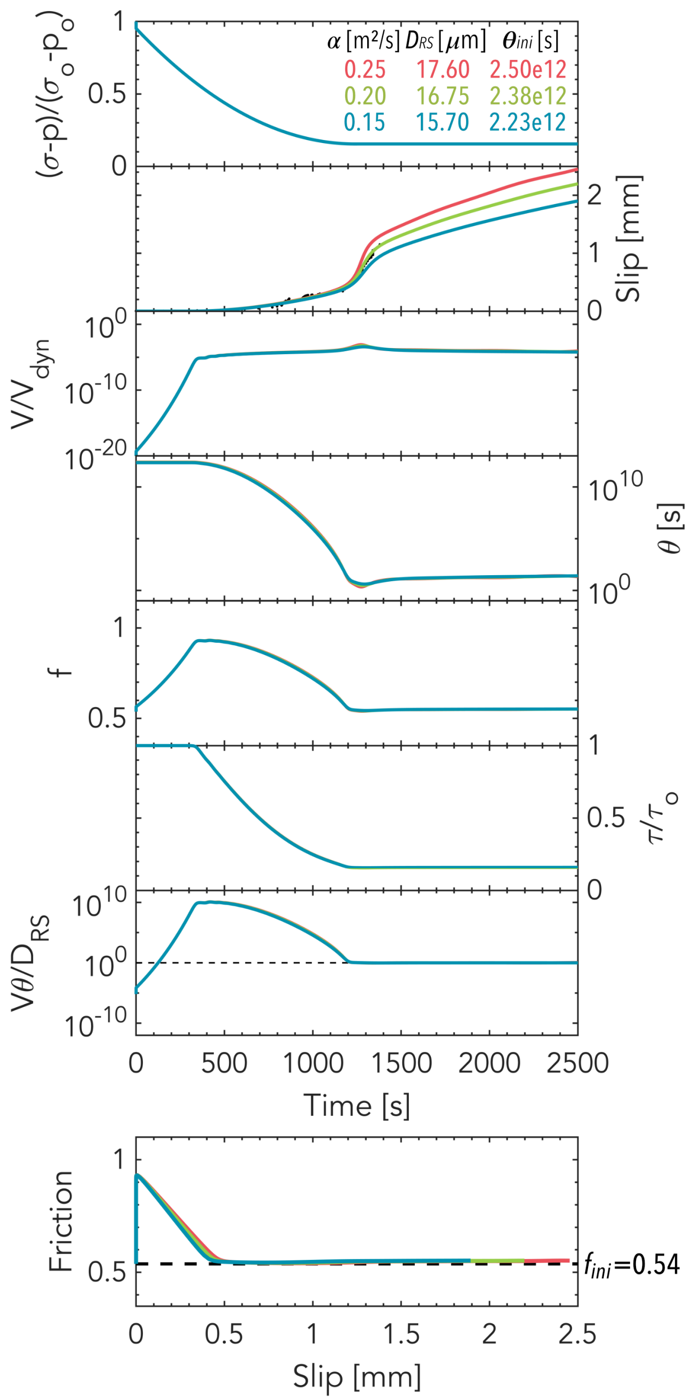

Figure C.18: Temporal evolution of quantities at the injection site and friction vs slip of 2 cases showing the effect of varying α while keeping t_{ac} and f^p constant. Increasing α increases the amplitude and slope of the transient acceleration. Parameter values modified from the intermediate-friction scenario (green) are listed at the top right corner.

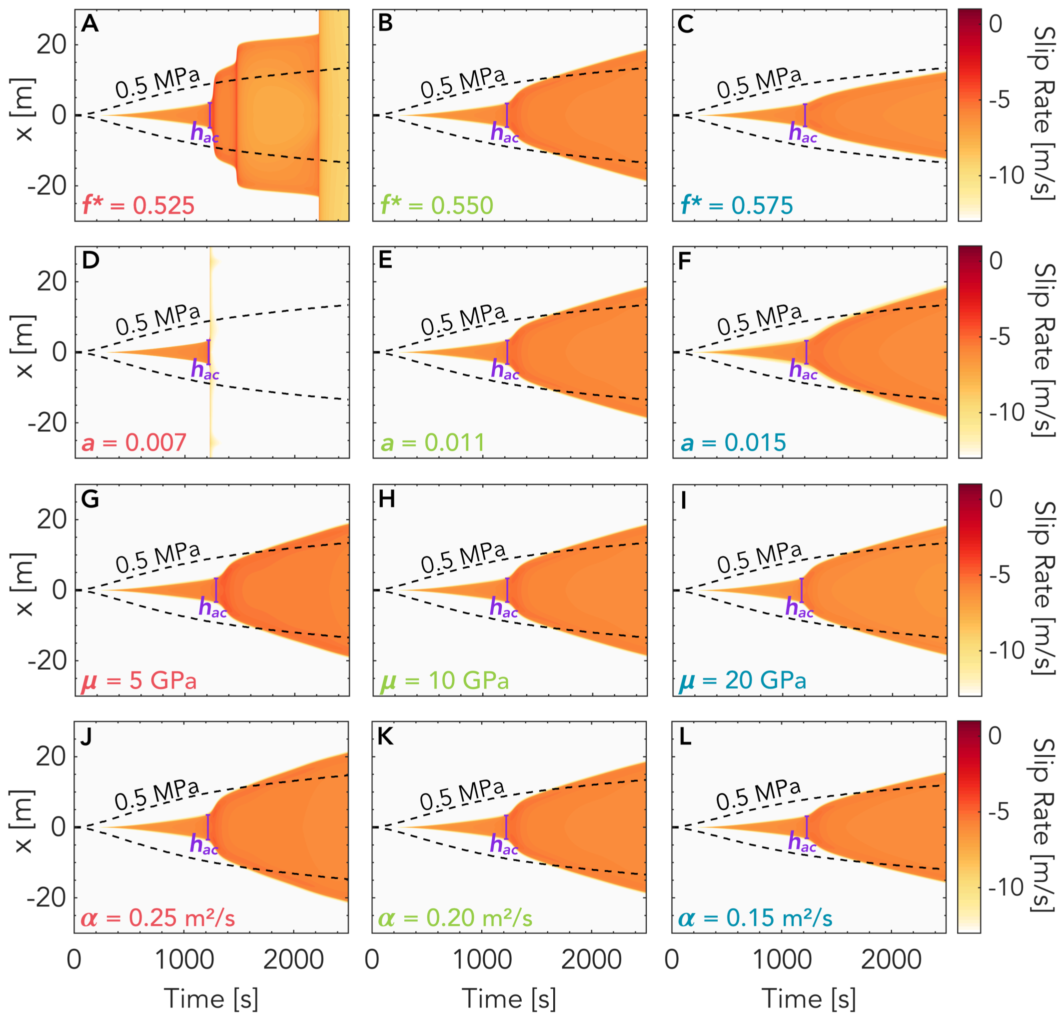

Figure C.19: Spatial and temporal evolution of rate for the cases shown in Figures C.15 – C.18 in which the slope and/or amplitude of the transient acceleration is altered by varying (A,C) f^*, (D,F) a, (G,I) μ and (J,L) α. Panels B, E, H, and K all show the reference intermediate-friction case for comparison purposes.

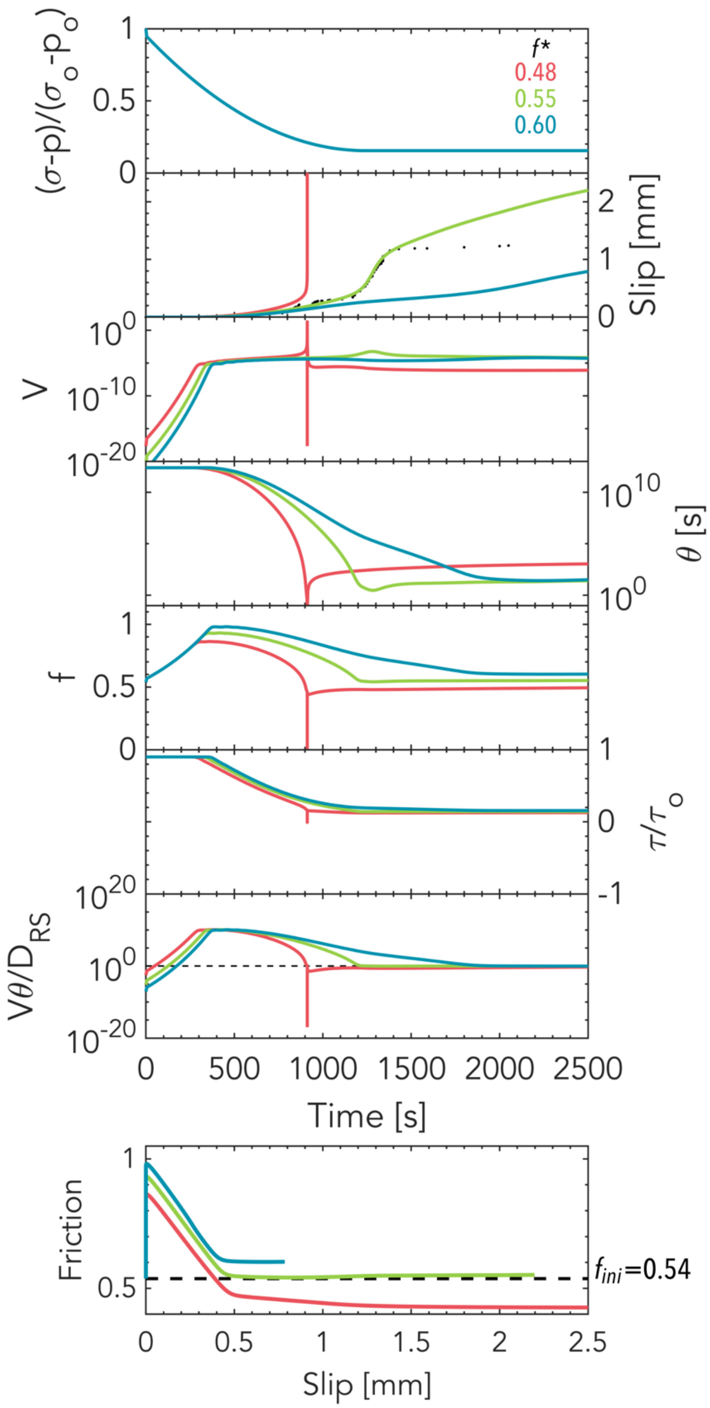

Figures C.20: Simulated temporal evolution of several quantities at the injection site varying f^*, keeping all other parameter values as in the intermediate-friction scenario (green).

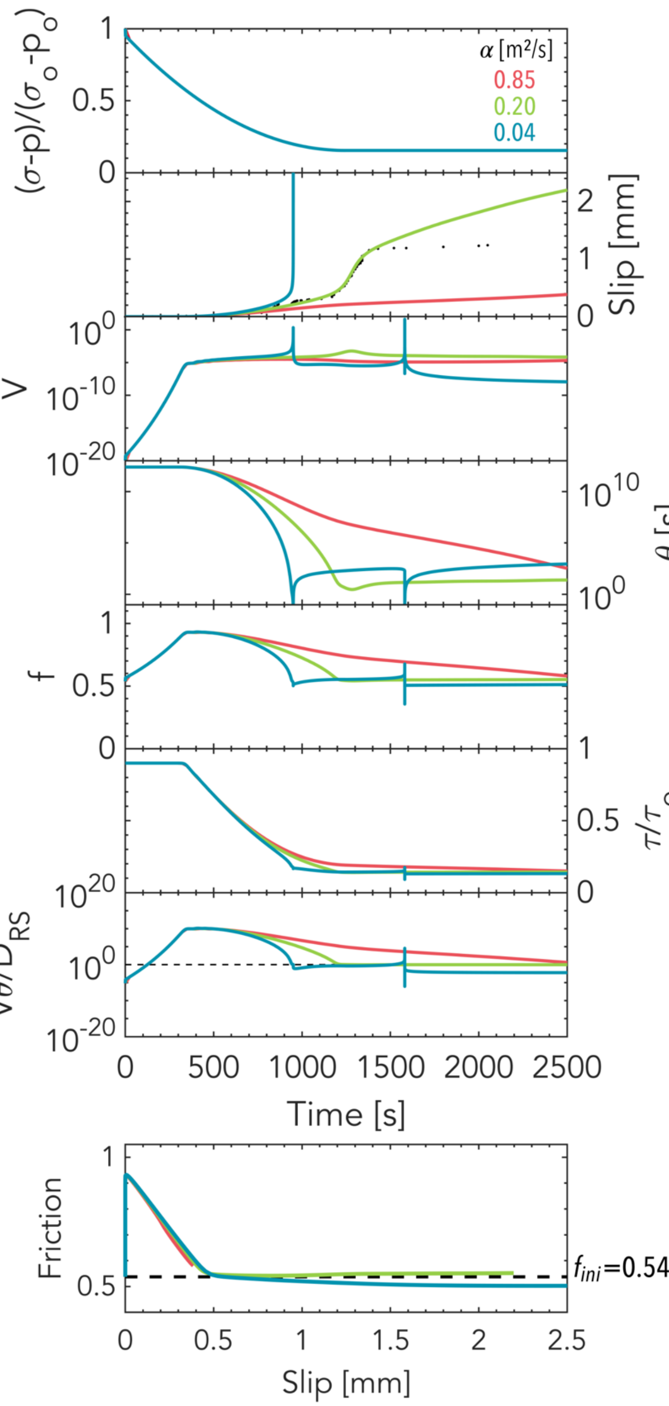

Figures C.21: Simulated temporal evolution of several quantities at the injection site varying α, keeping all other parameter values as in the intermediate-friction scenario (green).

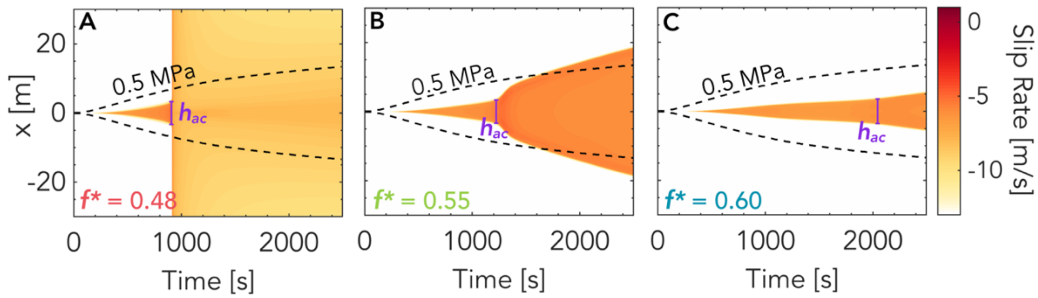

Figure C.22: Spatial and temporal evolution of rate for the cases shown in Figure C.20. Keeping everything else constant, varying f^* affects the spatial extent of the slipping zone compared to the pressurized zone.

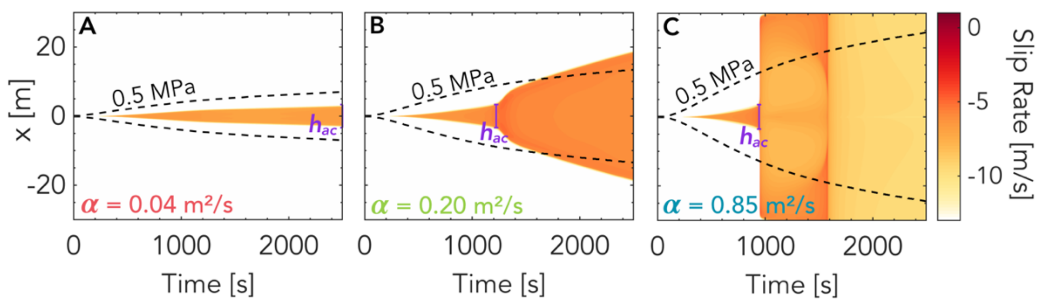

Figure C.23: Spatial and temporal evolution of rate for the cases shown in Figure C.21. Keeping everything else constant, varying α affects the spatial extent of the slipping zone.

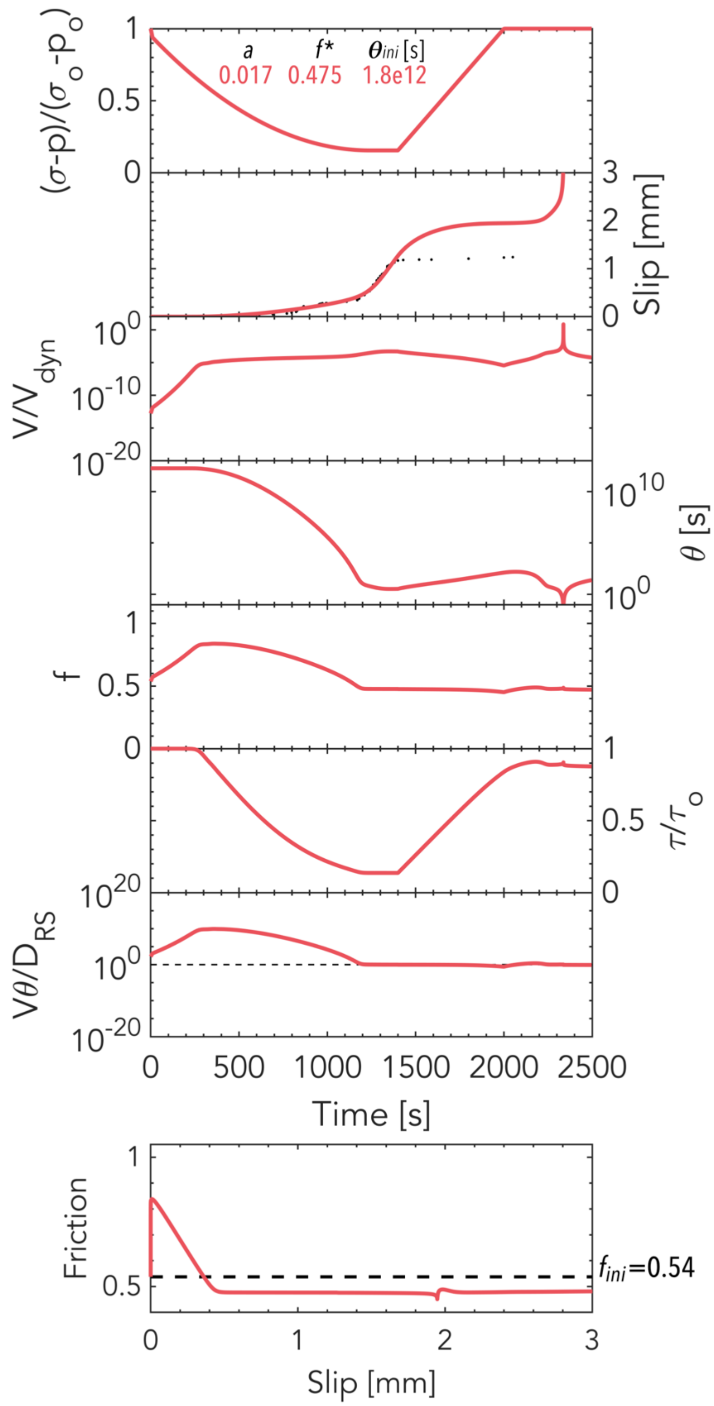

Figure C.24: Simulated temporal evolution of several quantities at the injection site for a scenario similar to the low-friction case in the main text but for a slightly rate-strengthening fault with a = 0.017, b = 0.016, f^* = 0.475 and θ_{ini} = 1.8e12s. Note that in this case an earthquake still nucleates after the injection stopped due to the relatively low residual friction f^r compared to f_{ini}.

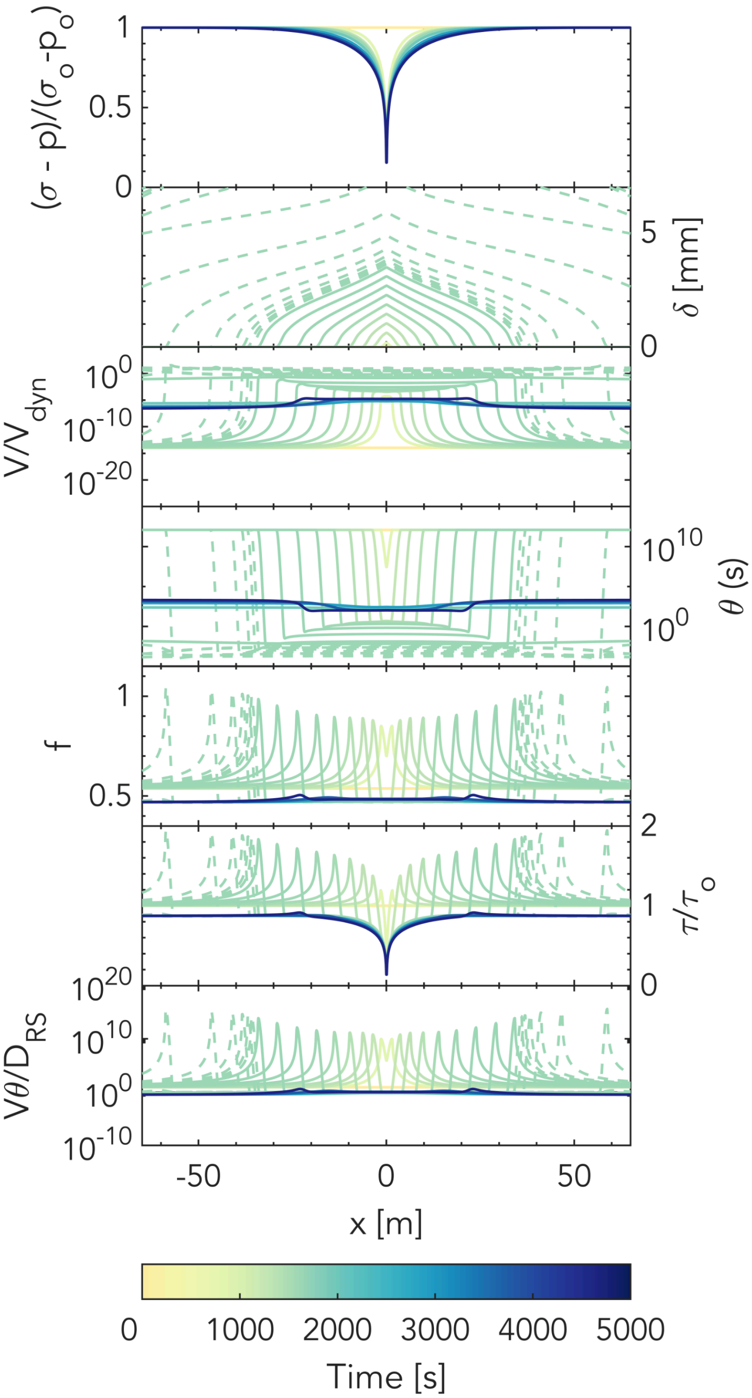

Figure C.25: Spatial and temporal evolution for the low-friction prolonged injection case (plotted every 7000 time steps for $V < V_{dyn}$ and every 2000 time steps for $V > V_{dyn}$).

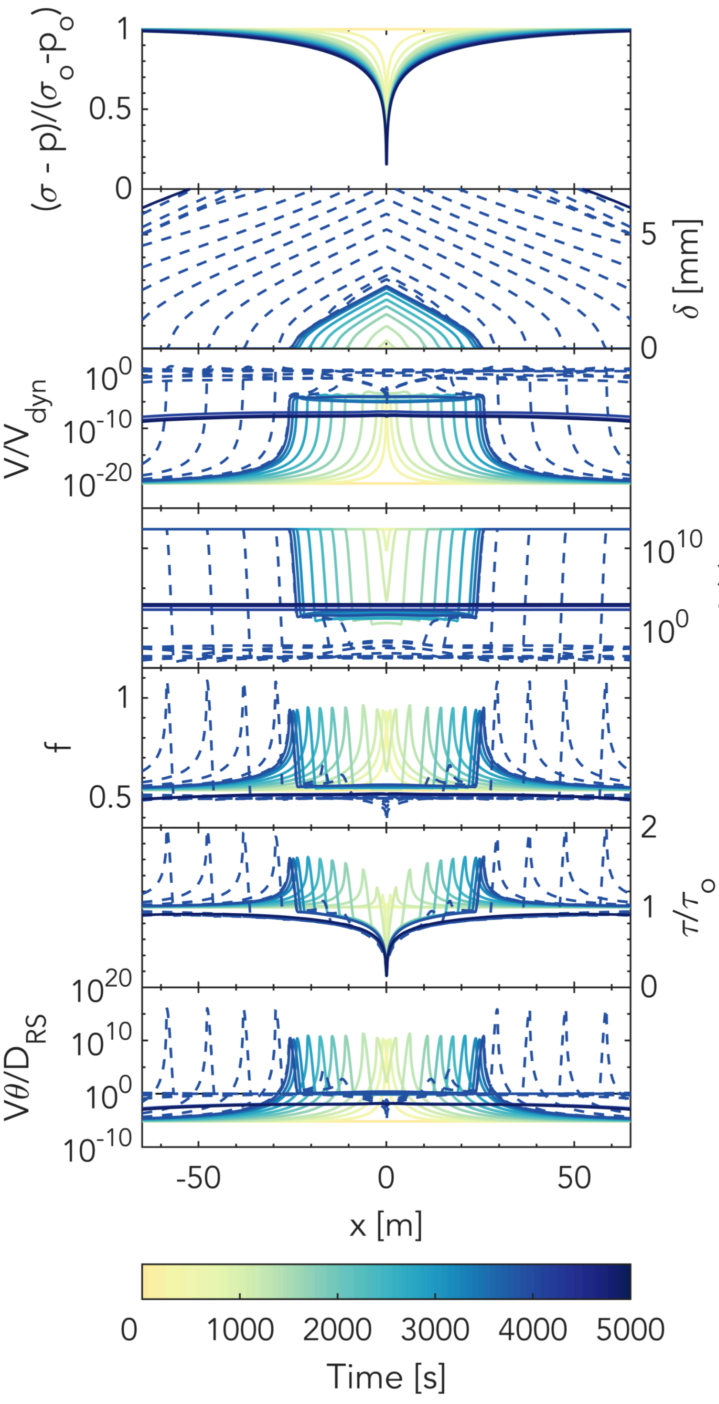

Figure C.26: Spatial and temporal evolution for the intermediate-friction prolonged injection case (plotted every 15000 time steps for $V < V_{dyn}$ and every 1000 time steps for $V > V_{dyn}$).

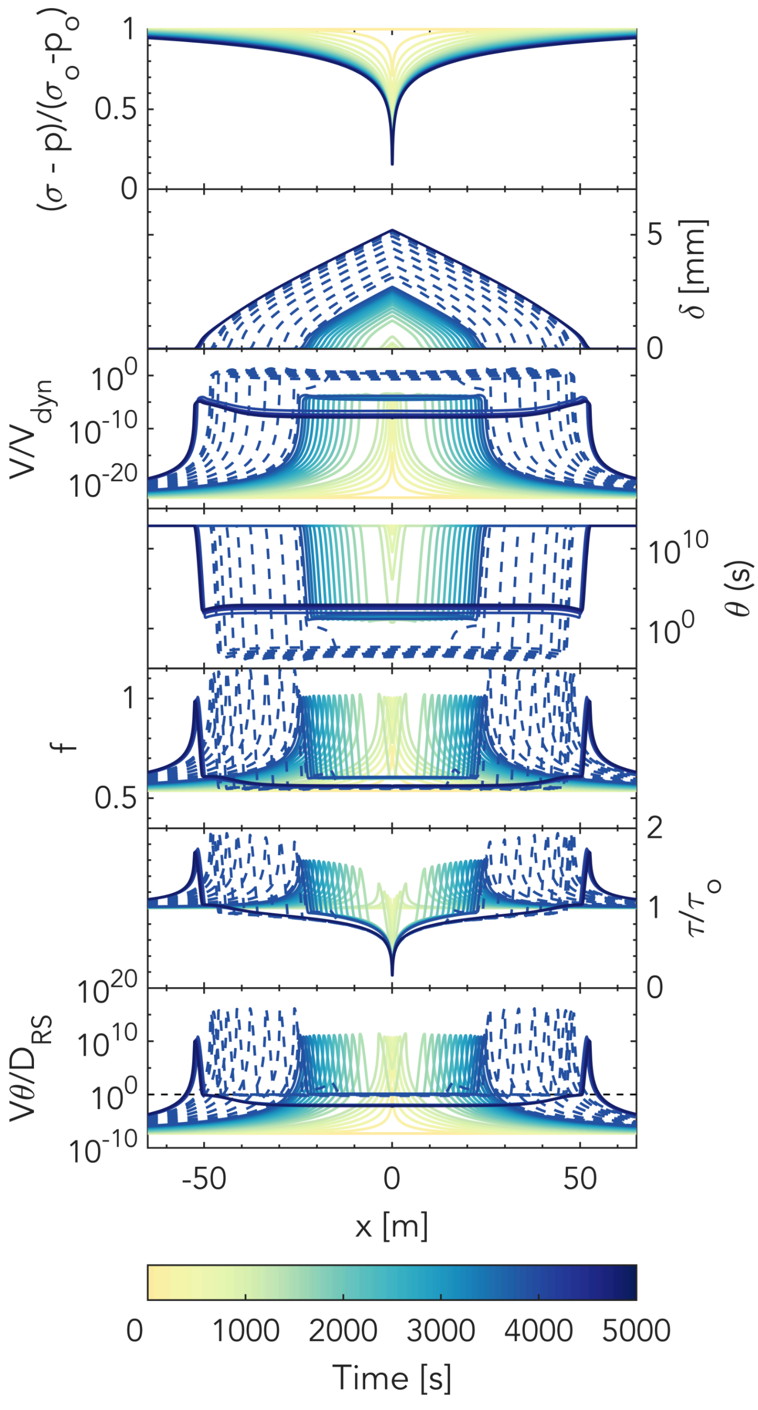

Figure C.27: Spatial and temporal evolution for the high-friction prolonged injection case (plotted every 35000 time steps for $V < V_{dyn}$ and every 750 time steps for $V > V_{dyn}$).

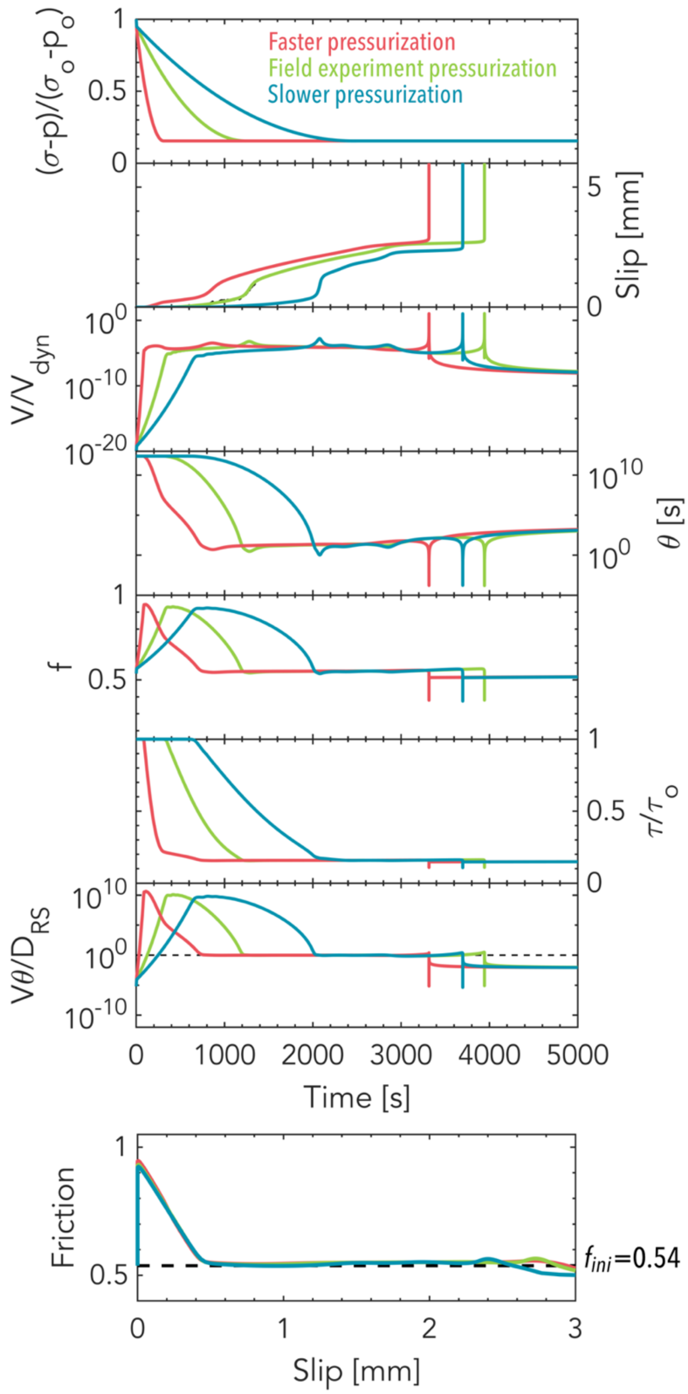

Figure C.28: Effect of varying pressurization rate on the intermediate-friction case. The timing of events is altered but not the overall behavior, i.e., all simulations still show a transient acceleration followed by a run-away dynamic event.

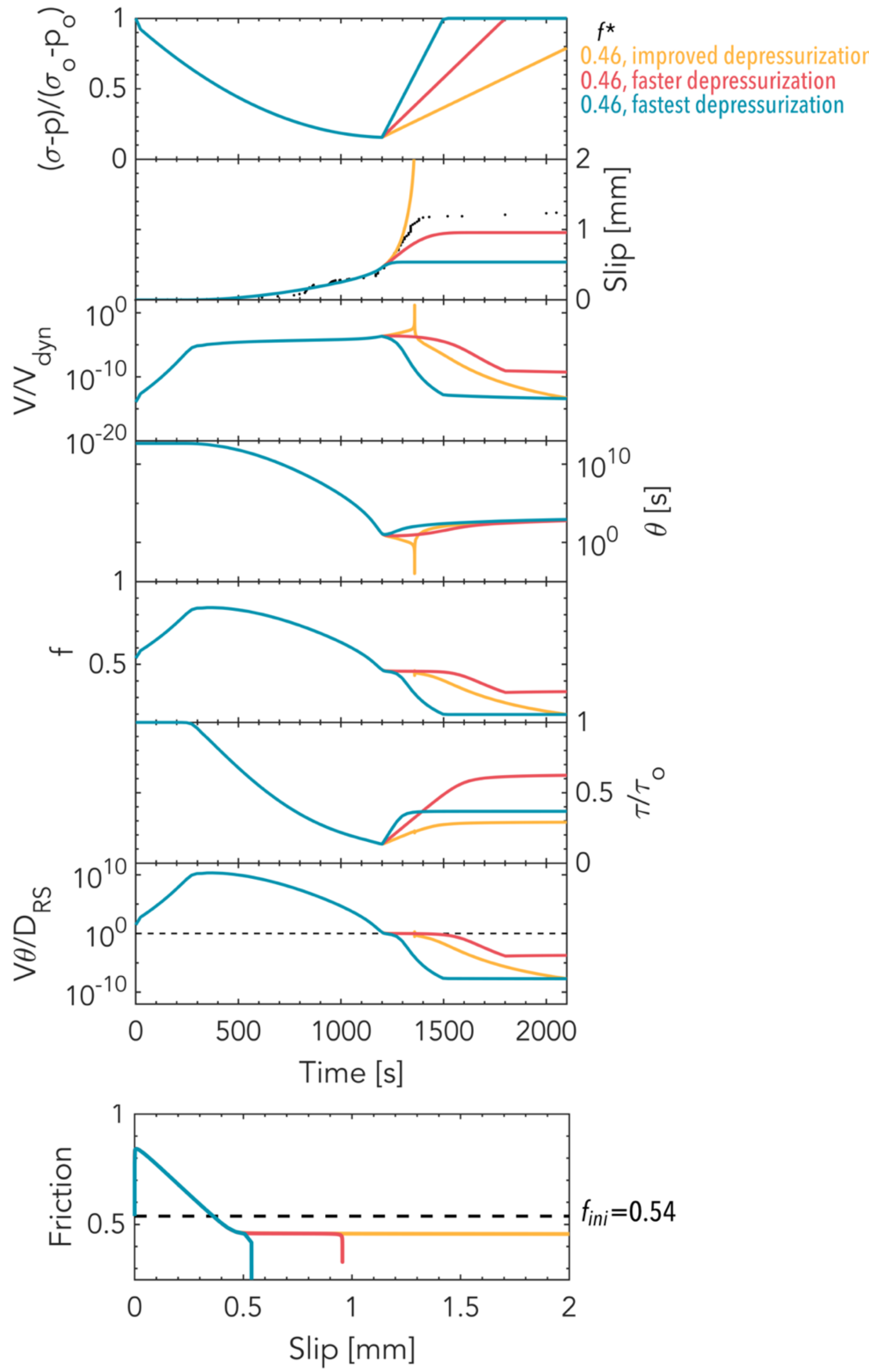

Figure C.29: Effect of varying depressurization rate on a case similar to the low-friction case but with an even lower $f^*$of 0.46. In this case, the depressurization applied as in Figure 2 in the main text is not sufficient to prevent earthquake nucleation (yellow curve). The other two faster depressurization rates successfully suppress the earthquake (pink and turquoise curves).